PROGRESS IN RESEARCH

April 1, 2023 - March 31, 2024

CYCLOTRON INSTITUTE

Texas A&M University

College Station, Texas

PROGRESS IN RESEARCH

APRIL 1, 2023 - MARCH 31, 2024

Prepared By

The Cyclotron Institute Staff

Texas A&M University

College Station, TX 77843-3366

Phone: (979) 845-1411
Fax: (979) 845-1899

Web: https://cyclotron.tamu.edu

August 2024

TABLE OF CONTENTS

SECTION II: HEAVY ION REACTIONS

SECTION III: NUCLEAR THEORY

SECTION IV: SUPERCONDUCTING CYCLOTRON, INSTRUMENTATION AND RIB UPGRADE

Introduction
April 1, 2023 – March 31, 2024

Progress in research and operations at the Texas A&M Cyclotron Institute is summarized in this report for the period April 1, 2023 through March 31, 2024. The CI has had a productive year and I am indebted to the dedicated operations staff that keeps the facility running. The discovery science program continues to produce exciting results as outlined in the chapters that follow. Texas A&M officially became a member of the National Isotope Development Center, as a source of astatine-211.

Longtime Cyclotron Institute professor Carl Gagliardi retired, but continues to remain active as his cycling calendar allows. Additionally, Dr. Akram Zhanov retired after over 20 years as a senior scientist at the Cyclotron Institute. Fortunately, we had very successful faculty searches and will be welcoming Dr. Jonas Karthein as an Assistant Professor and Dr. Baishan Hu as an Assistant Research Professor this coming year.

Congratulations are due to the following students who completed their graduate degrees: Dr. Stefania Dede, Dr. Andrew Hannaman, Ryan Rinderknecht, Dr. Stephen Robicheaux, Dr. Isaac Sarver, Dr. Dustin Scriven, Dr. Arun Sengupta, Zachary Tobin, Dr. Giaogang Wu.

The Texas A&M Cyclotron Institute continues to be the world's premier facility for testing semiconductor chips for resilience to radiation, with over 4386 hours provided to 60 institutions. The third bootcamp for radiation effects testing was successfully held in March, with instructors from the Cyclotron Institute, Renesas Electronics America, NASA GSFC, NASA JPL and NASA JSC.

The faculty at the Texas A&M Cyclotron Institute continue to lead multiple multi-institutional programs including the DOE/NNSA Center of Excellence CENTAUR; the DOE Topical Theory Collaboration Heavy-Flavor Theory (HEFTY); The DOE-IP Horizon Broadening Isotope Production Pipeline Opportunities (HIPPO) program and the DOE-NP Texas Research Enhancing Nuclear Development (TREND) program.

The TREND program and the HIPPO program brought undergraduates to the Cyclotron Institute for summer research. They joined with the 20th class of REU students to form the Tron Summer Scholars program.

During this period, the K500 provided 6192 hours and the K150 provided 4959 hours of beam for both science and radiation-effects testing. Some of the new beams that were developed included transition metal beams, such as Iron and Titanium, produced with the ECRs with Metal Ion Volatile Compounds, or MIVOC. The refurbishment of ECR1 was completed, and ECR1 was used extensively during the latter half of 2023 to provide beam to the K500. The ability to quickly switch from ECR1 and ECR4 on the K500 for either science or radiation effects beams reduced the typical single ECR changeover time by over 200 hours. During the first quarter of 2024, a new filament ion source capable of producing both H^- and He^+

light ion beams was installed for the K150, replacing the previous H- source. This new filament ion source, manufactured by D-Pace, Inc., will allow more intense H and He beams to be accelerated with the K150. The intensity of 4He beam for the production of ^{211}At continues to be improved, with a new maximum intensity of 20μA. The new injection scheme on the light ion guide yielded positive results from the CBECR including the development of ^{89}Nb, ^{89}Zr, ^{114}In, ^{106}In and ^{105}Cd. The re-accelerated radioactive beam of ^{105}Cd was used to study the structure of ^{106}Sn by the resonance elastic scattering p+^{105}In. The CBECR was also outfitted with a sputtering fixture to produce ^{64}Zn(25^{+}) ions which were accelerated to 47 MeV/u by the K500. Progress was made on the first full year of the DoD funded K150 upgrade project. Orders on major components were placed with various vendors such as Pantechnik for the 18 GHz ECR, Alpha Magnetics for the injection line magnets and Negative One-Eighty for the LHe cryopanel cryogenics system. The upgrade project has also procured $400K of replacement legacy items and spare parts including Pfieffer vacuum system equipment, cyclotron power tubes and ECR microwave transmitter repair equipment. Institute scientists remain active in a number of collaborative research efforts around the world. Major programs include: measurements of beta decays with the TRINAT collaboration at TRIUMF; nuclear structure measurements with TexAT at TRIUMF; continued work with the STAR collaboration at RHIC; and participation in the SAMURAI collaboration at RIBF in Tokyo, Japan.

The format of this report follows that of previous years. Sections I through III contain reports from individual research projects. Operation and technical developments are given in Section IV. Section V lists the publications with Cyclotron Institute authors and outside users and the Appendix gives additional information including talks presented by members of the Institute during the past year. Once again, the full volume of this year's Progress in Research is available only on our web site (http://cyclotron.tamu.edu). *Since most of the contributions presented here are truly reports on progress in research, results and conclusions should not be quoted from the report without the consent of the authors.*

I am indebted to Dr. Y.-W. Lui for assembling this report.

S.J. Yennello
Aug 11, 2024

SECTION I

NUCLEAR STRUCTURE, FUNDAMENTAL INTERACTIONS AND ASTROPHYSICS

Measurement of analog-antianalog isospin mixing in ^{47}K β decay

D. Melconian, J. Klimo, B.M. Vargas-Calderon, B. Kootte,[1] J.A. Behr,[1] H. Gallop,[2]
A. Gorelov,[1] C. Luktuke,[2] and J.C McNeil[1]
[1]*TRIUMF, Vancouver, BC, Canada*
[2]*University of Waterloo, Waterloo, ON, Canada*

Many isotopes undergo β minus decay to states of same spin I and parity π, but sometimes decays to the isobaric analog state are energetically forbidden; in these cases, the Gamow-Teller operator dominates, while the Fermi operator linking isobaric analog states is only allowed if some low-lying final state of the same I^π is mixed by an isospin-breaking interaction with the excited isobaric analog. We see such isospin breaking in an $I^\pi = 1/2^+$ state in the ^{47}Ca nucleus 80% fed by the β decay of ^{47}K. Interference between Gamow-Teller and isospin-suppressed Fermi amplitudes produces an asymmetry of the progeny recoil direction with respect to the initial nuclear spin, which we measured with TRIUMF's Neutral Atom Trap for β decay (TRINAT).

Since ^{47}Ca and ^{47}K are near closed shells, the single known ^{47}Ca $1/2^+$ state may contain much of the anti-analog configuration, and is predicted to have a relatively large Coulomb mixing matrix element with the analog. Sensitivity to time reversal-odd parity-even inherently isovector *N-N* interactions through a β-ν-spin correlation is thought to be enhanced in these systems. This is because the small amount of time reversal is referenced to Coulomb rather than strong interactions, which motivates our measurement of isospin breaking in ^{47}K decay.

Using 6×10^6 s^{-1} mass-separated ^{47}K delivered from the TRIUMF-ISAC isotope separator online facility, we trapped on average 500–1000 ^{47}K atoms during the data-taking time. We alternated 2.9 ms trapping with 1.1 ms optical pumping, during which we made the polarized β-decay measurements. The fraction of nuclear polarization achieved for the decaying ^{47}K atoms was $P = \langle I_z \rangle / I = 0.96(4)$. An

electric field collected ^{47}Ca ions produced in ^{47}K β^- decay to an MCP and the shake-off electron(s) on another MCP detector (see Fig. 1); this coincidence condition minimizes backgrounds and decays not originating from trapped atoms, and integrates over all β and ν momenta. The right panel of Fig. 1 shows the observed position spectrum of the recoil ions along the polarization axis (top) and resulting asymmetry (bottom) with this coincidence. The results clearly show a non-zero ratio of Fermi to Gamow-Teller matrix elements, $y \equiv g_V M_F / g_A M_{GT}$. Although not as clean as coincidences with the shake-off

e^- detector, position asymmetries with coincidences in the β-telescopes are also sensitive to y , albeit with larger uncertainties (less events with an increased sensitivity to the electric field and relevant branching ratio). When averaging the two measurements, our final result is y = 0.098(37) . The Gamow-Teller component has been measured to be $g_A M_{GT} = 0.305$ [1], giving $|M_F| = 0.030(11)$ which in turn

leads to a Coulomb matrix element $|H_C|$=101(37) keV. This is a relatively large value, which is in reasonable agreement with the 160 keV predicted by Ref. [2]

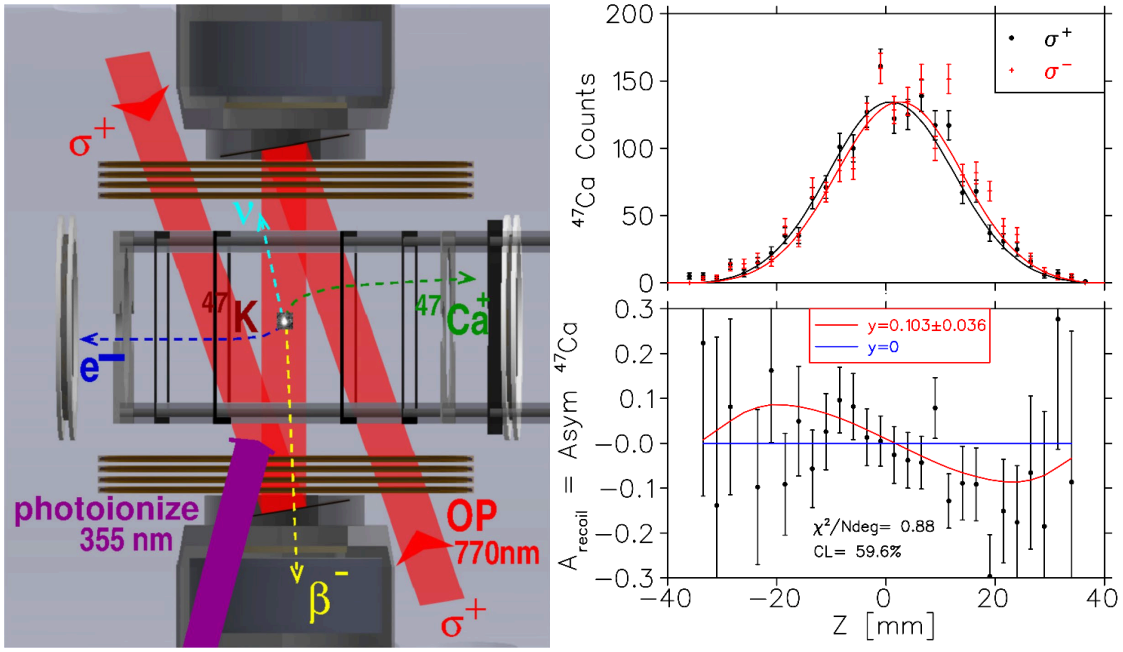

FIG.1. Left: schematic of TRINAT's detection chamber depicting the optical pumping (OP) and photoionization beams, hoops to generate the 650 V/cm field, the two MCP detectors, and the E-ΔE β telescopes. Top-right: distribution of $^{47}Ca^{+2,\ldots,7}$ along the polarization axis in coincidence with shake-off e^- for the two polarizations. Bottom-right: the asymmetry of these distributions A_{recoil}, i.e., the difference divided by the sum of the top distributions. The nonzero asymmetry scales with $y \equiv g_V M_F / g_A M_{GT}$ and directly implies a nonzero Fermi contribution.

The interested reader can find more details in B. Kootte *et al.*, Analog-antianalog isospin mixing in ^{47}K β^- decay, Phys. Rev. C **109**, L052501 (2024).

[1] P. Choudhary, A. Kumar, P. C. Srivastava, and T. Suzuki, Phys. Rev. C **103**, 064325 (2021).
[2] N. Auerbach and M.-L. Bui, Nucl. Phys. **A1027**, 122521 (2022).

Update on improving the fission-product yields of ^{147}Nd, ^{156}Eu and ^{111}Ag

D. Melconian, V.E. Iacob, J. Clark,[1] G. Savard,[1] D.E.M. Hoff,[2] K. Kolos,[2]
N. Scielzo,[2] and M.A. Stoyer[2]
[1]*Argonne National Laboratory, Lemont, Illinois*
[2]*Lawrence Livermore National Laboratory, Livermore, California*

We have submitted a manuscript to Phys Rev C on the ^{147}Nd gamma-ray branching ratios, which was favorably received; it should be published in the next few weeks after we finish addressing the referee comments. Looking ahead, we have high-quality data on the gamma-ray branching ratios of ^{111}Ag and ^{156}Eu. The collaboration decided to pursue completing the analysis of the ^{156}Eu in parallel with analyzing the ^{111}Ag results. Currently, the values for the branching ratios of ^{156}Eu from the most recent evaluation [1] have uncertainties of ranging from 7-14% for the 10 most intense γ rays and up to 30% for the weaker ones. The analysis is proceeding well, however it is difficult due to the sheer number of transitions (~100). Fig. 1 shows the gamma spectrum (in coincidence with a detected beta particle), where all of the observed peaks are attributed to ^{156}Eu except for the one small ^{99}Mo/Tc contaminant peak labelled in the plot. Initial results indicate we will greatly improve the precision of the decay properties.

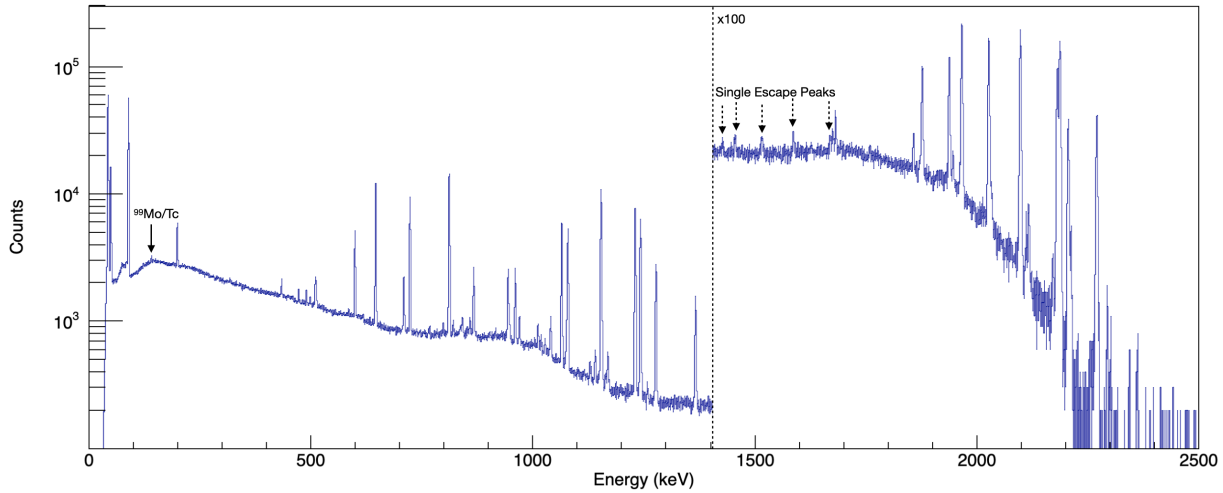

FIG.1. The total γ-ray spectrum from the sample of ^{156}Eu observed during the experiment. The indicated transition show the impurity ^{99}Mo/Tc observed during the second run. All other lines are attributed to the decay of ^{156}Eu.

As an example, our preliminary result for the most intense branch (1153.67 and 1154.08 keV, two transitions we are not able to resolve with our HPGe) is 11.39(12)%, over 5x more precise than the current 11.5(7)%. We will improve the second most intense transition (811.7 keV) from 9.7(8)% to 9.75(8)%, an order of magnitude improvement.

We expect to submit the ^{156}Eu results by fall of 2024 and then will proceed with completing the ^{111}Ag data.

[1] C. Reich, Nuclear Data Sheets **113**, 2537 (2012).
[2] A. F. Kluk, Phys. Rev. C **10**, 1451 (1974).
[3] Y. Iwata, Journal of the Physical Society of Japan **49**, 2114 (1980).

Searching for a candidate for the hypothetical Efimov state in ^{12}C

Antonio Ribeiro Ferreira Guedes De Sousa,[1] Joseph Frost-Schenk,[1] Richard Longland,[2] Lindsay Donaldson,[3] Kevin Li,[4] Jack Bishop,[5] and Philip Adsley[6]

[1]*Department of Physics and Astronomy, University College London, London WC1E 6BT, United Kingdom*

[2]*Department of Physics, North Carolina State University, Raleigh, North Carolina, North Carolina 27695-8202, USA and Triangle Universities Nuclear Laboratory, Durham, North Carolina, North Carolina 27708-0308, USA*

[3]*iThemba Laboratory for Accelerator Based Sciences, Somerset West 7129, South Africa*

[4]*Department of Physics, University of Oslo, N-0316 Oslo, Norway*

[5]*University of Birmingham, Edgbaston B15 2TT, UK*

[6]*Cyclotron Institute, Texas A&M University, College Station, Texas, Texas 77843, USA and Department of Physics and Astronomy, Texas A&M University, College Station, Texas, Texas 77843, USA*

The structure of ^{12}C is of extreme importance for nuclear astrophysics. Notably, the Hoyle state enhances the production of ^{12}C through the 3α process. There is a significant interest in the properties of other states in ^{12}C, such as the possible breathing mode excitation of the Hoyle state [1], the 2^+ Hoyle-state rotational excitation [2] and a hypothetical additional state which could exist in a 3-boson system, known as an Efimov state. Past studies at TAMU and Argonne National Laboratory have cast doubt on the existence of this Efimov state [3] but other measurements, including at LNS Catania have claimed to have observed a signal which may correspond to this state.

A collaboration has been formed to search for the possible Efimov state using other reactions, since beta decay is rather selective and, while unlikely, it is possible that the Efimov state might not have been populated in those experimental studies. At the centre of this collaboration is a new high-resolution study of ^{12}C(p,p') with the Enge SplitPole magnetic spectrometer at the Triangle University Nuclear Laboratory. This reaction provides a high-resolution, low-background population of ^{12}C without strong structural selectivity [4]. This experiment will be combined with already published studies of ^{12}C with the K600 magnetic spectrometer at iThemba LABS and an additional ^{12}C(p,p') dataset from the K600 to provide stringent constraints on the possible energy or cross section for the Efimov state using these different reactions. Proving that the state does not exist is a logical impossibility. Providing data which can be used to confront theoretical models of the Efimov state in terms of its energy and cross section for these different reactions with exceptional energy resolution and background rejection is vital. These data build on the past study by Bishop *et al*. [3], in expanding the number of population mechanisms used to search for this state.

Fig.1 shows the position spectrum from the ^{12}C(p,p') reaction using the TUNL SplitPole magnetic spectrograph. A full calibration of the spectrum has not yet been performed but the strong peak at around channel 2650 is the Hoyle state. Some ^{13}C(p,p') contamination is expected in this spectrum which may be the other small peaks at around channels 450 and 2950.

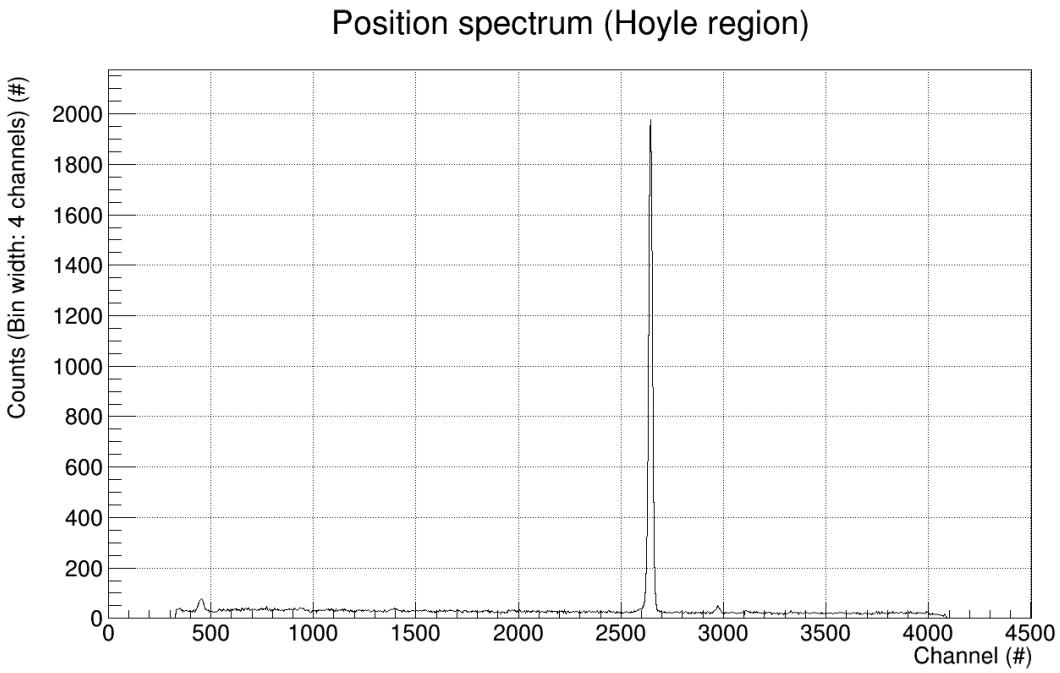

FIG. 1. Position spectrum from the 12C(p,p') reaction.

[1] K.C.W. Li *et al.*, Phys. Lett. B **827**, 136928 (2022).
[2] E. Epelbaum *et al.*, Phys. Rev. Lett. 109, 252501 (2012).
[3] J. Bishop *et al.,* Phys. Rev. C **103**, L051303 (2021).
[4] S. Benamara *et al.*, Phys. Rev. C **89**, 065805 (2014).

Searching for resonance states in ^{22}Ne(p,γ)^{23}Na

D.P. Carrasco-Rojas,[1] M. Williams,[2,3] P. Adsley,[4,5,6,7] L. Lamia,[8,9,10] B. Bastin,[11] T. Faestermann,[12] C. Fougères,[11] F. Hammache,[13] D.S. Harrouz,[13] R. Hertenberger,[14] M. La Cognata,[8] A. Meyer,[13] F. de Oliveira Santos,[11] S. Palmerini,[15,16] R. G. Pizzone,[8]
S. Romano,[8] N. de Séréville,[13] A. Tumino,[8,17] and H.-F. Wirth[14]

[1]*Department of Physics, The University of Texas at El Paso, El Paso, Texas 79968-0515, USA*
[2]*TRIUMF, Vancouver, British Columbia, Canada V6T 2A3*
[3]*Department of Physics, University of York, Heslington, York YO10 5DD, United Kingdom*
[4]*Department of Physics and Astronomy, Texas A&M University, College Station, Texas 77843-4242, USA*
[5]*Cyclotron Institute, Texas A&M University, College Station, Texas 77843-3636, USA*
[6]*iThemba Laboratory for Accelerator Based Sciences, Somerset West 7129, South Africa*
[7]*School of Physics, University of the Witwatersrand, Johannesburg 2050, South Africa*
[8]*Laboratori Nazionali del Sud–Istituto Nazionale di Fisica Nucleare, Via Santa Sofia 62, 95123 Catania, Italy*
[9]*Dipartimento di Fisica e Astronomia "E.Majorana", Università di 64, 95123 Catania, Italy*
[10]*Centro Siciliano di Fisica Nucleare e Struttura della Materia (CSFNSM), 64, 95125 Catania, Italy*
[11]*GANIL, CEA/DRF-CNRS/IN2P3, Bvd Henri Becquerel, 14076 Caen, France*
[12]*Physik Department E12, Technische Universität München, D-85748 Garching, Germany*
[13]*Université Paris-Saclay, CNRS/IN2P3, IJCLab, 91405 Orsay, France*
[14]*Fakultät für Physik, Ludwig-Maximilians-Universität München, D-85748 Garching, Germany*
[15]*Dipartimento di Fisica e Geologia, Università degli Studi di Perugia, via Alessandro Pascoli s/n, 06125 Perugia, Italy*
[16]*Istituto Nazionale di Fisica Nucleare–Sezione di Perugia, via Alessandro Pascoli s/n, 06125 Perugia, Italy*
[17]*Facoltà di Ingegneria e Architettura, Università degli Studi di Enna "Kore", Cittadella Universitaria, 94100 Enna, Italy*

Globular clusters show strong correlations between different elements, such as the well-known sodium-oxygen anticorrelation. One of the main sources of uncertainty in this anticorrelation is the ^{22}Ne(p,γ)^{23}Na reaction rate, due to the possible influence of an unobserved resonance state at E_x = 8862 keV ($E_{r,c.m.}$=68 keV). The influence of two higher-lying resonance states at E_x =8894 and 9000 keV has already been ruled out by direct ^{22}Ne(p,γ)^{23}Na measurements. We studied excited states in ^{23}Na above the proton threshold to determine if the unconfirmed resonance states in ^{23}Na exist using the nonselective proton inelastic-scattering reaction at low energies. Protons scattered from various targets were momentum-analyzed in the Q3D magnetic spectrograph at the Maier-Leibnitz Laboratorium, Munich, Germany. The resonance states previously reported at E_x=8862, 8894, and 9000 keV in other experiments were not observed in the present experiment at any angle. Combined with the non-observation of these resonance states in most other experiments, we have concluded that these proposed states likely do not exist and should be omitted from future evaluations of the ^{22}Ne(p,γ)^{23}Na reaction rate.

Fig.1 shows the excitation-energy spectrum assuming ^{23}Na kinematics. The hollow spectrum is taken with the NaF target and the solid red from the LiF spectrum. Vertical lines show the positions of ^{23}Na excited states. The black lines with blue boxes show the known energies and listed uncertainties, the green dotted lines show the proposed states at E_x = 8862, 8894 and 9000 keV which, on the basis of the available evidence, do not appear to exist and which should be omitted from future evaluations of the ^{22}Ne(p,γ)^{23}Na reaction rate.

This work was supported by TREND.

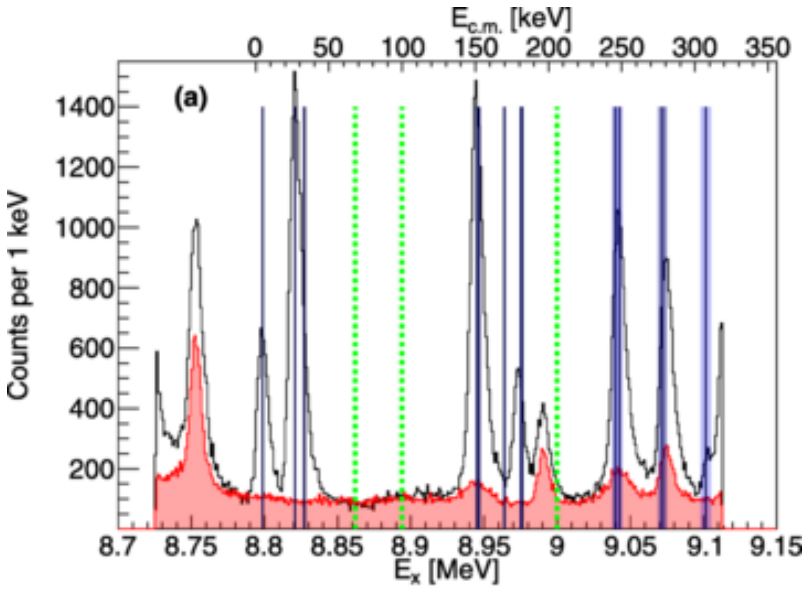

FIG.1. Excitation energy spectrum of the ^{23}Na(p,p') reaction taken of Θ_{Q3D}=70°. Black : NaF target. Red: LiF Target. Blue lines/boxes: Energy of 23Na states with uncertainties. Green:missing ^{23}Na states.

Sensitivity study classical nova synthesis of ^{22}Na and ^{31}P

M. Rashidazad and P. Adsley[1,2]
[1]*Department of Physics and Astronomy, 578 University Drive, College Station, TX, 77843-4242, USA*
[2]*Cyclotron Institute, 120 Spence street, College station, TX, 77843-3366 USA*

Classical novae are explosions taking place on the surface of white dwarfs in binary systems where many nuclear reactions take place and consequently many elements are produced or destroyed, some of which might be ejected into the cosmos. Astronomers are particularly interested in studying the abundance of ^{22}Na, a radioactive isotope with a half-life of 2.6 years, because we can isotopically identify the source of the signal, which is something which cannot be done with elemental absorption lines. Sodium-22 has never been detected in the cosmos, while it has been produced synthetically. The long half-life of Sodium-22 increases its chances of living for long enough that it can be observed following ejection from the nova. Detection of ^{22}Na will give us information about the temperature and the mechanism of a Classical Nova and the reactions that take place during the Nova. The reactions that lead to the production and destruction of ^{22}Na are:

$^{21}\mathrm{Ne} + \mathrm{p} \rightarrow {}^{22}\mathrm{Na} + \boldsymbol{\gamma}$ (proton capture)
$^{22}\mathrm{Mg} \rightarrow {}^{22}\mathrm{Na} + \mathrm{e}^{+} + \boldsymbol{\nu}_{\mathrm{e}} + \boldsymbol{\gamma}$ (beta plus decay)
$^{22}\mathrm{Na} + \mathrm{p} \rightarrow {}^{23}\mathrm{Mg} + \boldsymbol{\gamma}$ (proton capture)
$^{22}\mathrm{Na} \rightarrow {}^{22}\mathrm{Ne} + \mathrm{e}^{+} + \boldsymbol{\nu}_{\mathrm{e}} + \boldsymbol{\gamma}$ (beta plus decay)

We use sensitivity studies to determine the impact of reaction rates on the overall evolution and properties of the astrophysical system, to find the key reactions in nucleosynthesis reaction networks and production of specific isotopes, to determine the abundance of isotopes and elements produced in the nucleosynthesis process, and to help determine the mutual impact of the nuclear rates uncertainties and different astrophysical parameters on each other in different stellar environments.

We use MESA (Modules for Experiment in Stellar Astrophysics), which is an open source one-dimensional general module to simulate the evolution and properties of stars.

By modifying the control parameters and inputs, one can simulate different stellar evolution scenarios. In our case, we have simulated the evolution of a carbon-oxygen (CO) white dwarf in a binary system with a companion star and the occurrence of the classical novae

In Fig. 1, the abundance of ^{22}Na is plotted against time, for different rates of $^{22}\mathrm{Na}(\mathrm{p},\gamma)^{23}\mathrm{Mg}$ reaction. The origin of time is chosen to be the peak of the burst. The peak of the burst is defined as the maximum of T_{max}. The red cross is the maximum of ^{22}Na abundance for each rate. The black diamond is the abundance at the peak of the burst. The 5 green crosses are respectively showing the abundance at 90, 120, 180, 240, 300 minutes after the peak of the burst. As can be seen the abundances of Na decrease by increasing the rate of the reaction, indicating more Na is destroyed and turned into Mg, and vice versa by decreasing the reaction rate.

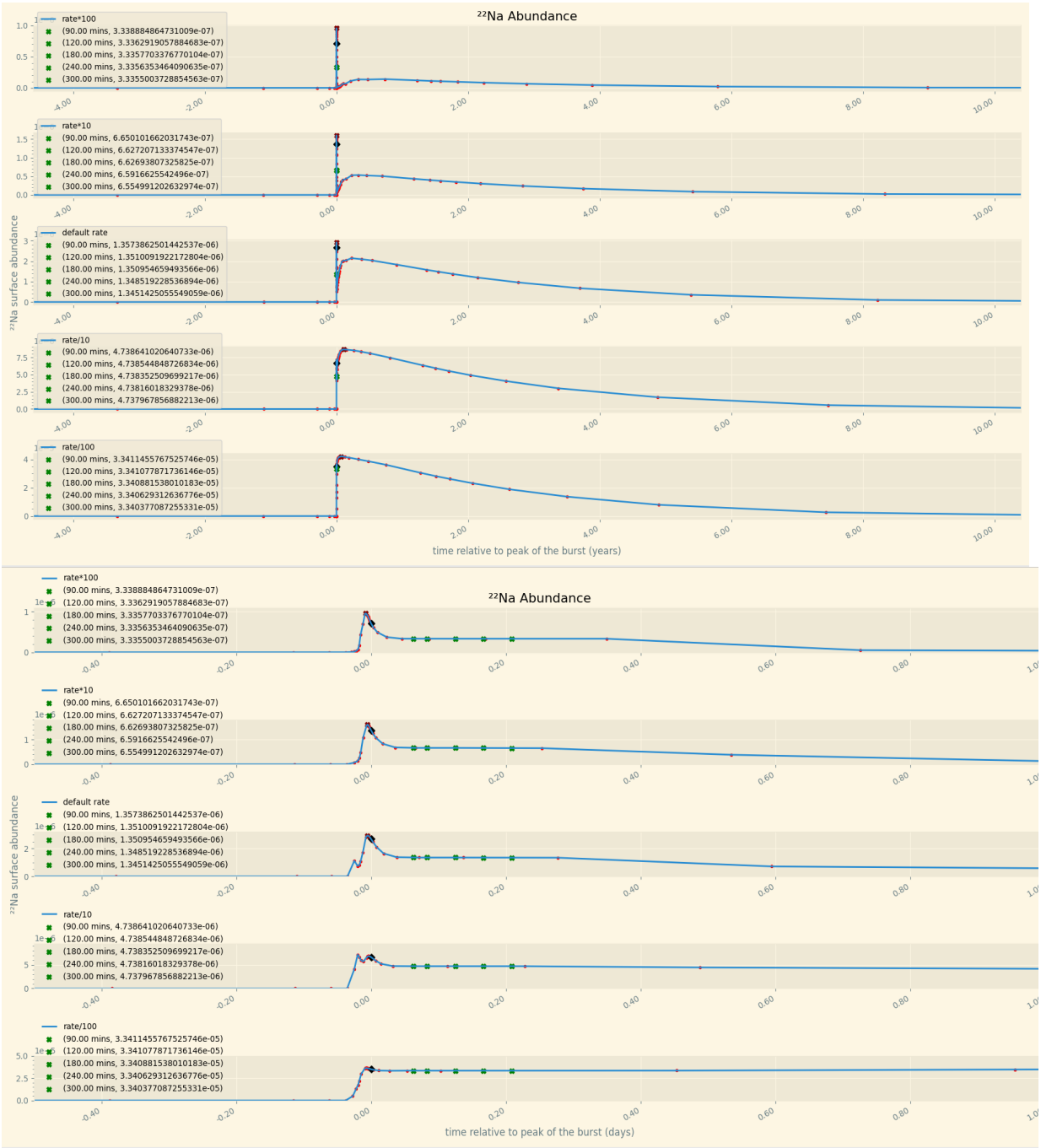

FIG. 1. ^{22}Na+^{23}Na abundances as function of time for different ^{22}Na(p, γ)^{23}Mg reaction rates.

In Fig.1, the abundance of ^{22}Na is plotted against time, for different rates of ^{22}Na(p,γ)^{23}Mg reaction. The origin of time is chosen to be the peak of the burst. The peak of the burst is defined as the maximum of T_{max}. The red cross is the maximum of ^{22}Na abundance for each rate. The black diamond is the abundance at the peak of the burst. The 5 green crosses are respectively showing the abundance at 90, 120, 180, 240, 300 minutes after the peak of the burst. As can be seen the abundances of Na decrease by

increasing the rate of the reaction, indicating more Na is destroyed and turned into Mg, and vice versa by decreasing the reaction rate.

Once the impact of different nuclear reactions on the ^{22}Na abundance have been determined, we plan to extend our studies to the production of phosphorus (^{31}P). According to a recent paper by Bekki and Takuji 2024, the [P/Fe] changes over time are not well explained by core collapse supernovae models while oxygen-neon (ONe) novae on the surface of a white dwarf with a metallicity-dependence rate and a mass greater than 1.25 $M_{\odot}$ is demonstrated to be a good candidate to explain and predict the variation in ^{31}P abundances over time.

Measurement of ^{20}Ne and ^{16}O ground state α-ANCs

E. Harris,[1,2] M. Barbui,[1] J. Bishop,[1] G. Chubarian,[1] E. Koshchiy,[1] Z. Luo,[1,2] C.E. Parker,[1] M. Roosa,[1,2] A. Saastamoinen,[1] D.P. Scriven[1,2] and G.V. Rogachev[1,2]

[1]*Cyclotron Institute, Texas A&M University, College Station, Texas 77843*

[2]*Department of Physics & Astronomy, Texas A&M University, College Station, Texas 77843*

The Asymptotic Normalization Coefficient (ANC) method is a powerful indirect technique often used in experimental nuclear physics to study stellar radiative capture reactions. This method focuses on determining ANCs of nuclear bound states and resonances, which represent the amplitude of the bound-state wave function in the asymptotic region far from the nuclear interior. These coefficients (C) can be extracted experimentally from the differential cross sections of peripheral transfer reactions using the following equation [1]:

$$\left(\frac{d\sigma}{d\Omega}\right)_{exp} = \frac{\left(C^{A}_{a,x}\right)^2}{b_A^2}\frac{\left(C^{B}_{b,x}\right)^2}{b_B^2}\left(\frac{d\sigma}{d\Omega}\right)_{DWBA} \quad (1)$$

This holds for a direct transfer reaction of A + b → B + a, where A = a + x and B = b + x, with x being the transferred particle. Once determined, these ANCs can then be used for the calculation of astrophysical reaction rates. For example, the rate of the well-known α-capture reaction ^{12}C(α,γ)^{16}O has been further constrained by determining the ANCs of states below the α-decay threshold in ^{16}O. This work aims to determine the ANC of the ^{16}O ground state as it currently contributes to the large overall uncertainty of the ^{12}C(α,γ)^{16}O reaction rate.

For this study, we have chosen the α-transfer reaction of ^{12}C(^{20}Ne,^{16}O)^{16}O populating the ground state of both ^{16}O products. The energy of the beam was chosen such that both the entrance and exit channels of this reaction are (nearly) sub-Coulomb. This technique, pioneered by C. Brune [2], has been shown to minimize model dependence and uncertainties of the resulting ANCs. To further reduce model dependence, we employ a ratio of the transfer cross section to the elastic scattering cross section at large angles in the center-of-mass system. This eliminates dependence of the result on beam geometry, target thickness, and detector efficiency, while also lessening sensitivity to the chosen optical potential.

The ^{12}C(^{20}Ne,^{16}O)^{16}O α-transfer experiment was carried out in June of 2021 using the MDM spectrometer and TexPPAC detector system [3]. A low-energy beam of ^{20}Ne at 1.0 and 1.1 MeV/u was produced by the K150 cyclotron and delivered to the scattering chamber where it impinged on a natural ^{12}C target of 22 μg/cm^2 thickness. The ^{16}O reaction products were magnetically filtered through the MDM at an angle of 5° and 15°, and were then detected in the TexPPAC focal plane detector. The position along the X-plane of the detector along with time-of-flight (TOF) between PPACs was used for particle identification of ^{16}O. Utilizing the ^{16}O charge-state fraction determined previously [4], and the number of background-subtracted counts of ^{16}O in TexPPAC, the differential cross section of the α-transfer reaction was determined. The calculation of single-particle ANCs and theoretical cross section were performed using Distorted Wave Born Approximation (DWBA) with the code FRESCO. Equation 1 was then used

to determine the ANCs. Because neither the ^{16}O nor ^{20}Ne ground state α-ANCs are known independently, the final experimental result of this work is the product of the two ANCs.

In addition to our experimental result, three independent theoretical calculations of the ANC product were performed by groups from Louisiana State University, Michigan State University, and Florida State University. All participants were tasked with calculating the product of the ground state α-ANCs of ^{20}Ne and ^{16}O. The three competing theoretical methods applied in this study are the Configuration Interaction Model [5], the No-Core Shell Model [6], and the Lattice Effective Field Theory [7]. An important feature of this study was its double-blind nature, meaning the experimental results were obtained without any knowledge of the theoretical results, and vice versa. All four results were collected by Dr. Sherry Yennello of the Texas A&M University Cyclotron Institute and then revealed to the participants on March 8th, 2024. This comparative study aims to showcase the predictive power of modern theory with respect to cluster configurations of nuclei. A paper discussing the comparison of experimental and theoretical results is currently underway.

[1] A.M. Mukhamedzhanov *et al.*, J. Phys. Conf. Ser. **202**, 012017 (2010).

[2] C.R. Brune, W.H. Geist, R.W. Kavanagh, and K.D. Veal, Phys. Rev. Lett. **83**, 4025 (1999).

[3] E. Harris *et al.*, *Progress in Research*, Cyclotron Institute, Texas A&M University (2021-2022), p. IV-56.

[4] E. Harris *et al.*, *Progress in Research*, Cyclotron Institute, Texas A&M University (2021-2022) p. I-26.

[5] K. Kravvaris and A. Volya, Phys. Rev. Lett. **119**, 062501 (2017).

[6] K.D. Launey, A. Mercenne, and T. Dytrych, Annu. Rev. Nucl. Part. Sci. **71**, 253 (2021).

[7] D. Lee, Prog. Part. Nucl. Phys. **63**, 117 (2009).

R matrix analysis of low energy data on the resonant α+^{18}O scattering

A.K. Nurmukhanbetova,[1,2,] V.Z. Goldberg,[3] A. Volya,[4] D.K. Nauruzbayev,[2,5] G.E. Serikbayeva,[5] and G. V. Rogachev[3,6]

[1]*Energetic Cosmos Laboratory, Nazarbayev University, Astana, 010000, Kazakhstan*

[2]*Nazarbayev University Research and Innovation System, Astana, 010000, Kazakhstan*

[3]*Cyclotron Institute, Texas A&M University, College Station, Texas 77843, USA*

[4]*Department of Physics, Florida State University, Tallahassee, Florida 32306-4350, USA*

[5]*Physics Department, School of Sciences and Humanities, Nazarbayev University, Astana, 010000, Kazakhstan*

[6]*Department of Physics and Astronomy, Texas A&M University, College Station, Texas 77843, USA*

At present the team has finished an analysis of the available information on the resonant α+^{18}O scattering up to 14 MeV excitation energy in ^{22}Ne. The analysis is important because it provides information on properties 22Ne levels important for astrophysics and for a better understanding of nuclear structure. An essential part of this study is a comparison of the results obtained by the classical approach and by the TTIK approach. New developments are prompting the investigation of higher excitation regions in atomic nuclei and the extensive use of rare beams. This necessitates dealing with more and broader resonances, a higher density of states, and several decay channels, making resonance interference increasingly significant. To meet these new challenges, more detailed experimental data (including data from rare beams) and more precise theoretical predictions (including signs of the wave functions of the states) are required. Consequently, we will gain new and more detailed insights into nuclear structure and the influence of the continuum on this structure.

Spectroscopy of ^{12}Be using TexAT

M. Roosa, G. Christian, G. Rogachev, M. Barbui, J. Bishop, E. Harris, E. Koshchiy, Z. Luo, S. Ota, C.E. Parker, and D.P. Scriven

This project aims to develop the capacity to use the TEXas Active Target (TexAT) [KOS20] for transfer reaction studies in inverse kinematics. We plan to demonstrate this capacity by extracting spectroscopic factors to low-lying states in ^{12}Be with the ^{13}B(d,^{3}He)^{12}Be reaction. The structure of these states, in particular the p-wave versus intruder $(sd)^2$ contributions to their wavefunctions, remains an open question [ALB78, FOR94, KAN10, JOH13].

Specifically, this experiment will also help to establish the validity of using an Active Target Time Projection Chamber (AT-TPC) for (d,^{3}He) transfer reaction studies – with the eventual goal of coupling TexAT to the forthcoming TexNEUT p-Terphenyl neutron detector to study neutron-unbound states.

We took data in September of 2022 at the TAMU Cyclotron Institute using the K500 cyclotron and MARS line. A primary beam of ^{15}N at 30 MeV/u was impinged on a 1 mm ^{9}Be target to produce 10^4 pps of ^{13}B at the TexAT window. The total purity was approximately 80% with near equal (10%) contamination from ^{10}Be and ^{8}Li. TexAT's active volume was filled with 100 Torr of Deuterated Methane (CD_4).

As shown in Fig. 1, the active region is surrounded by an array of silicon-cesium iodide

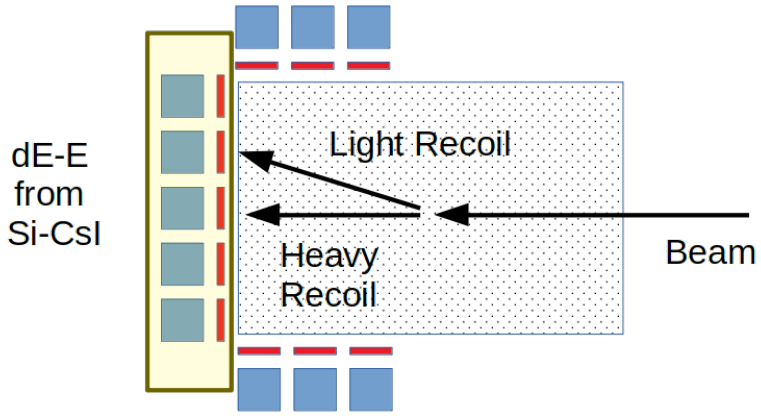

FIG. 1. Cartoon of the TexAT set-up from a top-down perspective showing the Si-CsI telescopes arranged around the micromegas.

telescopes (Si-CsI). These are used to identify the heavy recoil and elastically scattered deuterons with the differential-energy loss (dE-E) method. dE-E plots for heavy- and light-recoil identification are shown in Fig. 2. The isotopic selectivity of the light-recoil identification is not found to be present in the events of interest due to a signal quality problem emerging from the large capacitance of the pads in TexAT's multiplexed side regions. The next iteration of TexAT, the TExas Birmingham Active-Target (TeBAT)

will not feature multiplexing so we are confident this problem will not reemerge in future studies performed by our collaboration.

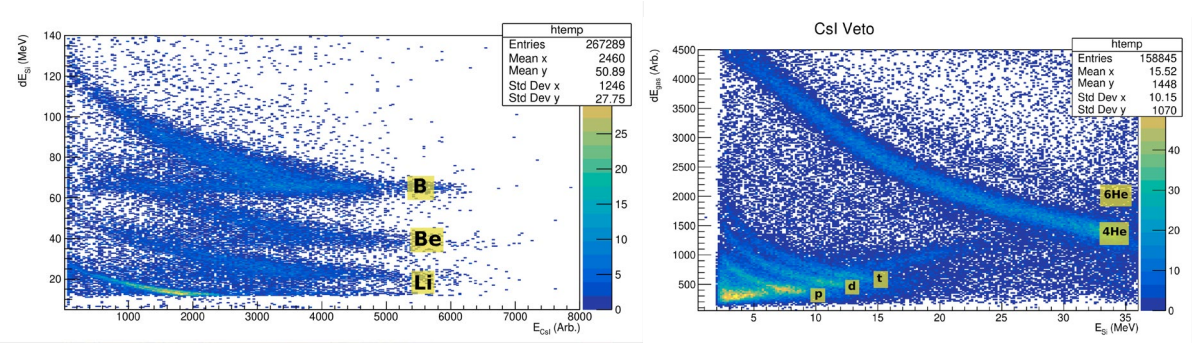

FIG. 2. dE-E plots for heavy-recoil (Left) and light-recoil (Right) identification.

Track reconstruction and missing mass analysis have given the excitation spectrum shown in Fig. 3. The signal quality issues mentioned earlier made upwards of 90% of the data unusable leaving only 9 counts in the region of interest ($E_x(^{12}Be)$ = 0-5 MeV). Data taken with CH_4 was passed through an identical analysis process and produced no counts in the region of interest. Though promising, there were insufficient counts in the CD_4 data to register signal-over-background in the region of interest above a 68% confidence interval.

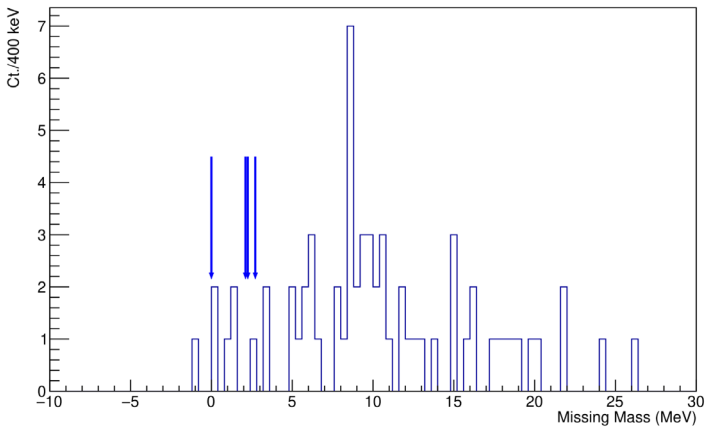

FIG. 3. Excitation spectrum of ^{12}Be with states of interest indicated with arrows.

Analysis of this data has been concluded. Although it is not possible to claim observation (d,^{3}He) from the data taken, we are confident that the insights provided by this study have paved the way for future efforts to make transfer reaction measurements using TexAT-like systems. Specifically, the changed read-out topology TeBAT guarantees that the signal distortion problems seen in this experiment

will not reemerge. When coupled with the isotopic selectivity shown in Fig 2. (Right), (d,^{3}He) spectroscopy in active targets should be well within technical possibility.

[1] E. Koshchiy, *et al*., Nucl. Instrum. Methods Phys. Res. **A957**, 163398 (2020).
[2] D.E. Alburger *et al.*, Phys. Rev. C **17**, 1525 (1978).
[3] H.T. Fortune *et al.*, Phys. Rev. C **50**, 1355 (1994).
[4] R. Kanungo *et al.*, Phys. Lett. B **682**, 391 (2010).
[5] J.G. Johansen *et al.,* Phys. Rev. C **88**, 044619 (2013).

Cyclotron institute evaluation center report: US nuclear structure data program

N. Nica and J.C. Hardy

Nuclear data evaluation is the main activity designed to capitalize the results of nuclear science research. From its beginnings more than a century ago, it became evident that nuclear science evolves over the years in such a way that establishing the "best" parameters at any given time is an important and challenging task. Thus, very early in its development the scientific community became aware, as Marie Curie wrote [1], that "*the need has arisen for the publication of special Tables of the Radioactive Constants*", which she, together with a prestigious group of contemporary scientists, co-authored the first major international nuclear data evaluation paper, titled "*The Radioactive Constants as of 1930*". Moreover, as she continues, "*This responsibility has been assumed by the International Radium Standards Commission chosen in Brussels in 1910 (...)*", which means that, due to its practical importance, this type of activity got institutionalized from its beginnings. Therefore, the origins of what today is known as nuclear data evaluation dates to the dawn of nuclear science itself.

In more recent times, it was recognized that the diversity of published data, not to mention their occasional inconsistencies, demanded that all published results should be assembled and reconciled by a specialized group of experienced scientists. Even collecting the relevant information from all the world's publications, was a nontrivial task, but documented databases were gradually established. This culminated with today's *Nuclear Science Reference* (NSR) database, which is maintained at the National Nuclear Data Center (https://www.nndc.bnl.gov/nsr/). Gradually after several cycles of systematic data analyses the community arrived at "practical standards" of data, which are then revisited periodically to include the continuous updates of newly published data. In this way, nuclear data evaluation has become a new research domain with its own specificity.

A new turning point emerged after the Second World War when the United States got the leading position in the nuclear research field, and consequently the transatlantic nuclear data evaluation changed shores, with the US becoming its main contributor. The United States Nuclear Structure Data Program (USNDP) was started (with its two main subcomponents, one for nuclear reactions and one for nuclear structure), being designed to maintain the so-called Evaluated Nuclear Structure Data File (ENSDF) database, the most extensive nuclear structure data repository in the world. This effort was shared initially among several national institutes and was extended to gradually include a few universities, of which Texas A&M Cyclotron Institute has been one since 2005. It was first funded by a contract with Brookhaven National Laboratory, but in 2017 we started to receive direct funding through the DOE Grant DE-FG02-93ER40773, "Cyclotron-based Nuclear Science". At that time, we became the Texas A&M Cyclotron Institute independent ENSDF Data Evaluation Center, one of the important contributors to the USNDP, as well as to the Nuclear Structure and Decay Data international network hosted by the IAEA Vienna

Between 2005 and 2022, we completed and published the following full mass-chain evaluations: the superheavy A=252 mass chain [2]; the very data-rich mid-mass chains, A=140 [3], A=141 [4], A=147 [5] and A=148 [6]; and the relatively lighter chains, A=97 [7] and A=84 [8], the latter in a large international collaboration. In collaboration with B. Singh and a group of authors from McMaster

University, Canada, we also published the A=77 [9], A=37 [10], A=36 [11], and A=34 [12] mass chains. At the beginning of 2016, we published another large mass chain, A=157, in Nuclear Data Sheets [13]; followed by A=158 in 2017 [14]; the renewed full evaluation of A=140 in 2018 [15]; A=155 in 2019 [16]; A=153 in 2020 [17]; and A=160 in 2021 [18]. We also published the renewed evaluations of A=147 in 2022 [19] (also with Balraj Singh), as well as A=141 in 2023 [20].

In the interval April-September 2023 we worked on the A=148 mass chain, submitted for peer review before the due date of Oct 1, 2023. It is still under review at the time this report is being written.

We also completed the technical review of the A=63 mass chain as assigned by NNDC, in a timely manner, returning the reviewed manuscript of over 400 pages by the end of Feb 2024. It required two months of concentrated effort.

Before the end of 2023, we also completed post-review work for the A=162 mass chain. Following the final editorial review and final preparations for publication, it appeared in Nuclear Data Sheets 195, 1 (2024) (May issue).

After Oct 2023 we started to work on this fiscal year's principal commitment, the A=156 mass chain. This mass chain involves about 1000 experimental publications, of which 136 have been added since our last evaluation. This work is currently in progress and is to be submitted to NNDC by Sept 30, 2024.

In recent years we initiated a process to evaluate several mass chains that are not the official responsibility of our center, but which for different reasons had remained unevaluated for many years: A=162 (since Mar 2007), A=154 (since May 2008), and A=156 (since Mar 2012), in order to improve the currency of the ENSDF database. This initiative is appreciated by the ENSDF community.

[1] M. Curie, A. Debierne, A.S. Eve, H. Geiger, O. Hahn, S.C. Lind, S. Meyer, E. Rutherford, E. Schweidler, Rev. Mod. Phys. **3**, 427 (1931).
[2] N. Nica, Nucl. Data Sheets **106**, 813 (2005).
[3] N. Nica, Nucl. Data Sheets **108**, 1287 (2007).
[4] N. Nica, Nucl.Data Sheets **122**, 1 (2014).
[5] N. Nica, Nucl. Data Sheets **110**, 749 (2009).
[6] N. Nica, Nucl. Data Sheets **117**, 1 (2014).
[7] N. Nica, Nucl. Data Sheets **111**, 525 (2010).
[8] D. Abriola *et al*., Nucl. Data Sheets **110**, 2815 (2009).
[9] B. Singh and N. Nica, Nucl. Data Sheets **113**, 1115 (2012).
[11] N. Nica, J. Cameron, and B. Singh, Nucl. Data Sheets **113**, 1 (2012).
[12] N. Nica and B. Singh, Nucl. Data Sheets **113**, 1563 (2012).
[13] N. Nica, Nucl.Data Sheets **132**, 1 (2016).
[14] N. Nica, Nucl.Data Sheets **142**, 1 (2017).
[15] N. Nica, Nucl.Data Sheets **154**, 1 (2018).
[16] N. Nica, Nucl.Data Sheets **160**, 1 (2019).
[17] N. Nica, Nucl.Data Sheets **170**, 1 (2020).
[18] N. Nica, Nucl.Data Sheets **176**, 1 (2021).
[19] N. Nica, B. Singh, Nucl.Data Sheets **181**, 1 (2022).

[20] N. Nica, Nucl.Data Sheets **187**, 1 (2023).

The data-based research project: Can the concept of a level scheme be of interest for the basic physics research?

N. Nica

Level and decay schemes are par excellence the graphical means to present nuclear structure data. They are used for this purpose by scientific and nuclear data evaluation communities. However, especially for the Evaluated Nuclear Structure Data File (*ENSDF*) evaluation community, level schemes are also of technical interest in order to present the published data in a standard way. Beyond the technical interest, an important question remains: *Can the concept of a level scheme be of interest for the nuclear research itself?*

Level schemes are 2*D* graphs where the information is correlated on the vertical energy scale, accompanied by an arbitrary scale on the horizontal direction, where different bands of a nucleus can be interspersed in a diversity of ways as long their interconnecting transitions are preserved.

To get to the new concept of level scheme, the ensemble of experimental bands' gamma-ray energies as function of spin I can first be described on average as a beam of parallel lines, $2c(2I+k-1)$, with the inertial parameter $c = \hbar^2/2\mathcal{I}$, where is $\mathcal{I}$ the moment of inertia of the nucleus. $2c$ is the constant average slope of the bands and the k integer numbers are the offsets of the bands. We can determine these parameters from a least-squares fit from the $\Sigma(E\gamma(I)/2c-(2I+k-1))^2$=min condition applied simultaneously to all the bands of a nucleus. From $2c$ we can also deduce the effective second order moment of inertia, $\mathcal{I}^{(2)}_{eff} = \frac{\hbar^2}{2c} = const$, that describes the average rotational motion of the real rotational bands.

From the $2c(2I+k-1)$ parametrization we can build the *3D Double Helix discrete geometrical structure, the prototype for the new high-spin level schemes*.

Secondly, the regular experimental gamma-ray energy can be decomposed as $E\gamma=2c(2I+k-1+k'+fn)$, with $(k'+fn)$ being the deviation of the experimental $E\gamma$ value from its $(2I+k-1)$ average value we got from the fit, with k' an integer number and fn a fractional quantity respectively. This can be also written as $E\gamma=2c_{band}(2I+k+k'-1)$ and $2c_{band}=2c[1+fn/(2I+k+k'-1)]$, with $2c_{band}$ and $(2I+k+k'-1)$ real and integer numbers, respectively. Then band second order moment of inertia can be easily obtained, $\mathcal{I}^{(2)}_{band} = \hbar^2/2c_{band}$. This decomposition gets a complete description of the experimental bands of a nucleus.

The $2c_{band}(2I+k+k'-1)$ expression allows the unitary 3*D* representation of decay paths of the rotational bands on the Double Helix, as seen in Fig. 1 for the ^{171}Yb nucleus (data from ref [1]). *Their apparent rotations (precessions) on the Double Helix are due to the combined macroscopic and microscopic nuclear motions.*

Double Helix defines a Semiclassical Meta-Trajectory through the series of $(2I+1)$ generalized discrete angular momentum states available for the rotational motion of the nucleus as a whole for each I value. One can assume that:

On average Nuclear Matter's Motion itself follows the Semiclassical Meta-Trajectory of the Double Helix, on which the actual levels are selected by the rotational bands' paths. Ultimately, Nuclear Matter's Double Helix Motion can be seen as a Semi-Classical Vortex Motion.

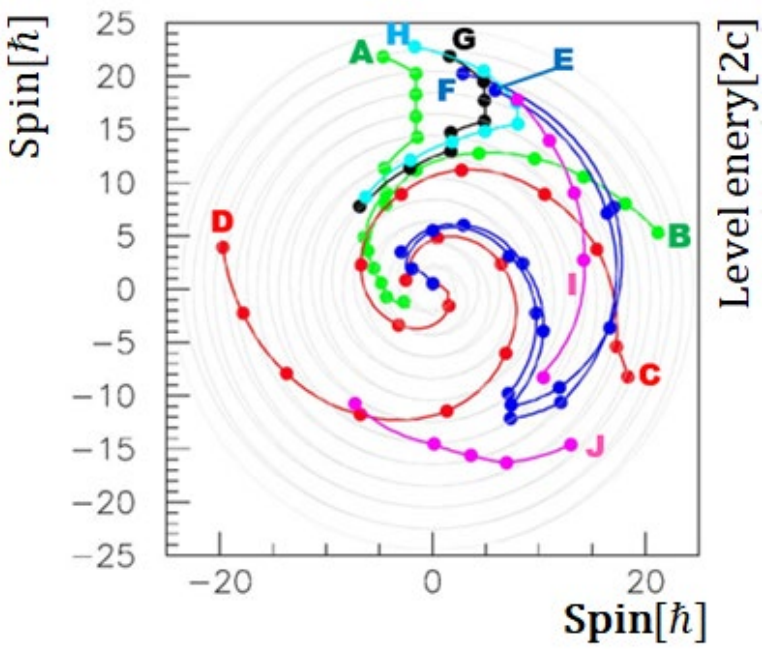

FIG. 1. Double helix level scheme of the rotational bands of the ^{171}Yb nucleus (2D projection view from above)

[1] D.E. Archer *et al.*, Phys. Rev. C **57**, 2924 (1998).

Photoabsorption studies

Aaron Salinas,[1,2] Philip Adsley,[2,3] Lindsay Michelle Donaldson,[4] Diana P. Carrasco-Rojas,[2,5]
John Santucci,[2,3] and Benjamin Shemiah Wellons[2,3]
[1]*Texas Lutheran University, Seguin, 78155*
[2]*Cyclotron Institute, Texas A&M University, College Station, 77843-3366, Texas*
[3]*Department of Physics & Astronomy, Texas A&M University, College Station, 77843-4242, Texas*
[4]*iThemba Laboratory for Accelerator Based Science, Somerset West, 7219, Western Cape, South Africa*
[5]*Department of Physics, The University of Texas at El Paso, El Paso, 79968-0515, Texas*

Photoabsorption reactions, in which a nucleus responds to an external electric field, can tell us many interesting things about the behaviour of nuclei, including probing the symmetry energy - the cost of exchanging protons for neutrons in nuclear matter - and how likely neutron-capture reactions are to take place in nuclear reactors or stars. In recent years, there was an interesting result which found that photoabsorption reactions are modified by the shell structure of the nuclei of interest, notably that the dipole polarisability, a measure of nuclear diffuseness, showed structures at certain nuclear shell closures [1]. However, based on concerns expressed over the results of photoneutron reactions in recent IAEA reports and other papers [2], we decided to reinvestigate this effect to determine if it could be an experimental artefact rather than a physics effect. To this end, we have redetermined the dipole polarisabilities of a number of nuclei using updated experimental data or re-evaluations of past experimental results. Our preliminary finding is that we do not reproduce the magnitude of the previously observed drop in the dipole polarisability at the neutron shell closures but that there may still be some evidence for a shell structure effect but additional validation of the data must be carried out to ensure that the results are robust.

Fig. 1 shows the ratio of dipole polarisability parameter (the σ_{-2}) to a systematic trend $\sigma_{-2} = 2.4\ A^{5/3}$ mb/MeV across a range of nuclei, and with various different sources for the photoabsorption strength. These results are still being finalised due to some inconsistencies in the description of the shapes of the isovector giant dipole response for some systems.

This project was performed, in part, by two Research Experience for Undergraduate students (A.S., D.P., C-R) under the Texas Researchers Enhancing Nuclear Diversity (TREND) project. This project is supported by DOE Grant DE-SC0024208.

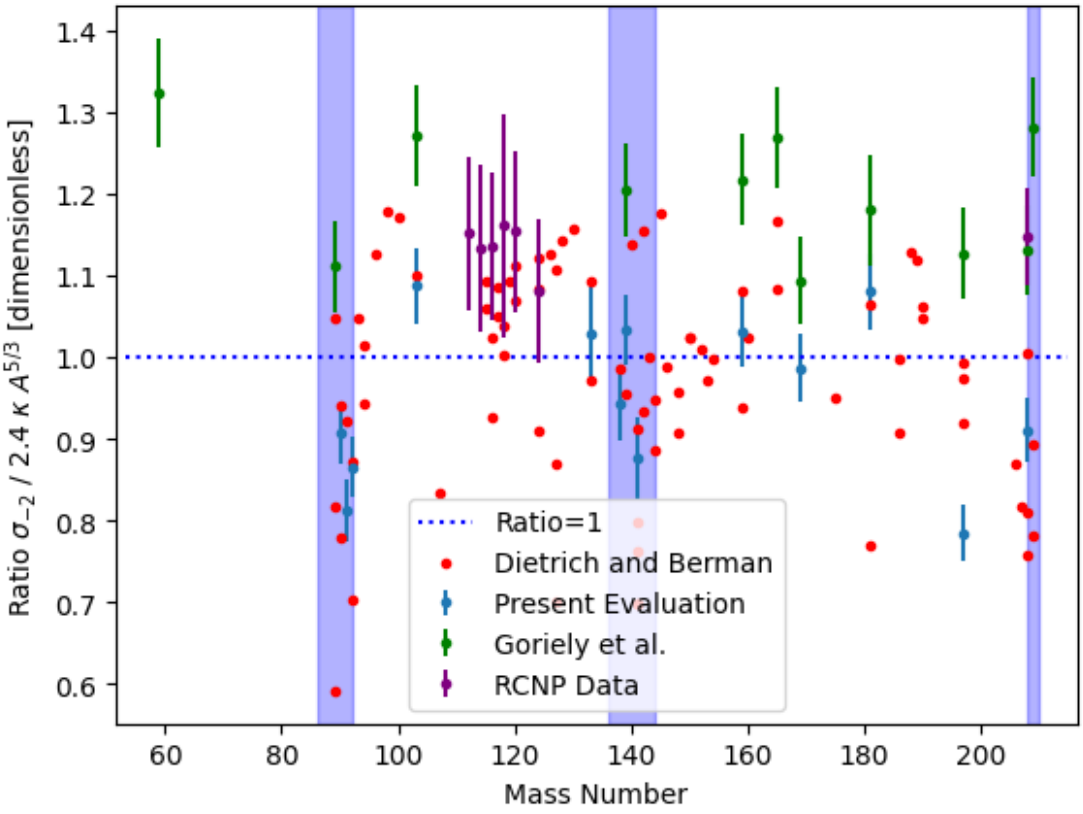

FIG. 1. Ratio of σ_{-2} from data vs systematic $\sigma_{-2} = 2.4\ (1)\ \kappa\ A^{5/3}$ mb/MeV trend with data from various different sources.

[1] C. Ngwetsheni and J.N. Orce, Phys. Lett. B **792**, 335 (2019).

[2] T. Kawano *et al.*, Nuclear Data Sheets **163** 109 (2020); V.V. Varlamov *et al.*, Euro. Phys. J. A **54,** 74 (2018).

Study of the resonant elastic scattering of the first cyclotron institute light ion guide cocktail beam (A=105) on hydrogen

M. Barbui,[1] R.G. Bartsch,[1] A. Lestone,[1] A. Alafa,[1] A. Alvarez,[1] V.Z. Goldberg,[1]
E. Harris,[1] E. Koshchiy,[1] G. Tabacaru,[1] B.T. Roeder,[1] M. Roosa,[1] J. Santucci,[1] and G.V. Rogachev[1,2]
[1]*Cyclotron Institute, Texas A&M University, MS3366 College Station, Texas 77843*
[2]*Department of Physics & Astronomy, Texas A&M University, College Station, Texas 77843*

We performed a first commissioning experiment using a cocktail beam of ^{105}Cd, ^{105}In, and ^{105}Ag provided by the Cyclotron Institute Light Ion Guide (LIG) [1]. The beam intensity was about 100 particles per second. A 7-um plastic scintillator upstream of the reaction chamber measured the incoming beam during the experiment. The beam composition was measured periodically during the run using the beam diagnostics upstream of the scattering chamber. The^{105}In was about 35% of the total beam intensity. The In/Cd ratio was about 50%. The ^{105}Ag was accumulating in the LIG gas cell as a decay product of ^{105}Cd. The beam also contained a 2% contamination of mass 94. The initial energy of the beam was 12 MeV/nucleon.

We measured the resonant elastic scattering of the provided beam on Hydrogen in inverse kinematics. We wanted to investigate the existence of low-lying resonances in ^{106}In/^{106}Sn and test our capability to reproduce the observed cross-section using a Koning-Delaroche (KD) nuclear potential [2].

Fig. 1 shows a picture of the experimental setup. The scattering chamber was filled with pure H_2

FIG. 1. Picture of the experimental setup. The picture shows the scattering chamber and the three Si-CsI(Tl) telescopes (labeled as 1, 2, 3) at the end of the gas volume. A PCB board used for the signals read out is also visible.

gas at an average pressure of 1725 mbar, sufficient to stop the beam a few centimeters before the silicon detectors. A 4-um-Havar window isolated the scattering chamber from the beam line under vacuum. We measured the scattered protons with three Si-CsI(Tl) telescopes placed at the end of the chamber at a minimum distance of 44.5 cm from the window. The silicon detectors had an active area of 5x5 cm^2 (divided into four quadrants) and a thickness of 500 um. The CsI(Tl) had the same surface and a thickness of 4 cm.

Figure 2 shows the preliminary excitation function measured in the angular ranges covered by our silicon detectors. Since ^{105}Cd was the dominant isotope in the cocktail beam, we reconstructed the center-of-mass energy using the kinematics of the elastic scattering ^{105}Cd+p.

The Figure also shows ^{105}Cd+p Rutherford cross-sections and the cross-sections from the KD potential. The insert in Figure 2 shows the cross-sections corresponding to the protons that punched through the silicon detector.

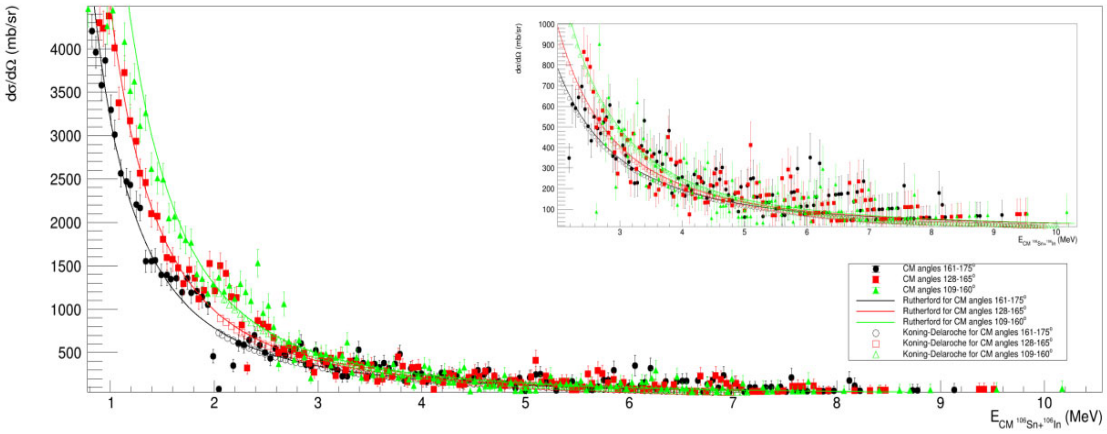

FIG. 2. Excitation function for the resonant elastic scattering on Hydrogen. See the text for details.

At center-of-mass energies from 2 to 5.5 MeV, the cross-sections from the KD potential agree well with the Rutherford cross-sections; at energies higher than 5.5 MeV, the KD cross-sections are slightly smaller than the Rutherford cross-sections.

The experimental data agree well with the Rutherford cross-sections at center-of-mass energies lower than 2 MeV. The data in the insert of Figure 2 show some possible structures with cross-sections exceeding the Rutherford cross-section by at least one sigma. This excess of cross-section suggests the presence of resonances. Larger statistics are required to investigate these structures further. Moreover, the limited statistics accumulated with a beam composition without ^{105}In are insufficient, at this time, to disentangle the contribution to the cross-section due to ^{105}Cd and ^{105}Ag from that due to ^{105}In.

[1] G. Tabacaru et al. Proceedings of ECRIS2010, Grenoble, France (2010) and
https://cyclotron.tamu.edu/facilities/light-ion-guide/
[2] A.J. Koning and J.P. Delaroche, Nucl. Phys. **A713**, 231 (2003).

Cold QCD physics with STAR at RHIC

B.E. Aboona, C.A. Gagliardi and the STAR Collaboration

Our group continues to play a major role in the STAR spin physics program. Over the past year, our analysis efforts have focused on three measurements: the Collins effect in 200 GeV p+Au collisions, the Collins effect in 510 GeV pp collisions, and an investigation of the contribution from diffractive processes to the large transverse single-spin asymmetry, A_N, that is seen for forward rapidity electromagnetic jets (EM-jets) in 200 GeV pp collisions. In addition, group members have continued to carry a wide range of administrative responsibilities for STAR.

Our graduate student B. Aboona is analyzing data that STAR recorded during 2015 to determine the size of the Collins effect in $\sqrt{(s_{NN})}$ = 200 GeV p+Au collisions. This will provide unique insight into the possible factorization breaking that has been predicted for transverse-momentum-dependent phenomena in hadronic collisions, in addition to a spin-dependent probe of the hadronization mechanism in cold nuclear matter.

High-quality particle identification (PID) is an important step in the Collins analysis. It requires a detailed understanding of the response of the PID quantities commonly used in STAR analyses. PID from the time projection chamber (TPC) is obtained using a quantity known as n_σ. This quantity returns the difference between the measured and the calculated dE/dx of a track in units of resolution, σ. For example, a reconstructed track whose $n_\sigma(\pi)$~0 is very likely to be a pion. Each track has four n_σ values: $n_\sigma(\pi)$, $n\sigma\ (K)$, $n_\sigma(p)$, and $n_\sigma(e)$. Similarly, PID from the time of flight (TOF) system is obtained using $n_{\sigma,TOF}$. Here, the quantity returns the difference between the measured and the calculated TOF of a given track divided by the TOF resolution. Eqs 1 and 2 summarize the model functions for n_σ and $n_{\sigma,TOF}$, respectively, where the details of how these functional forms have been obtained are discussed in last year's report. A two-dimensional functional form can be achieved by the product of $g(x)$ and $h(y)$, which results in a functional form where b, α, μ_2, and σ_2 are constants.

$$g(x) = Ae^{-\frac{1}{2}\left[\frac{x-\mu}{\sigma+b(x-\mu)}\right]^2} \qquad (1)$$

$$h(y) = A_1\left[e^{-\frac{1}{2}\left(\frac{y-(\langle y\rangle-0.085)}{\sigma_1}\right)^2} + \alpha e^{-\frac{1}{2}\left(\frac{y-(\langle y\rangle-0.085+\mu_2)}{(\sigma_1+\sigma_2)}\right)^2}\right] \qquad (2)$$

We produce momentum (p) and pseudorapidity (η) binned two-dimensional histograms of $n_\sigma(\pi, K, p)$ vs. $n_{\sigma,TOF}(\pi, K, p)$ for all the tracks in jets of interest to our analysis and utilize the two-dimensional functional model to fit the histograms. Fig. 1 is a sample two-dimensional fit. The p and η binning results in 2880 two-dimensional histograms, each requiring a two-dimensional likelihood fit with 15 or 20 free parameters. These multi-peak, two-dimensional likelihood fits are computationally intensive, and some can be unstable. Optimization steps have been implemented to address these issues.

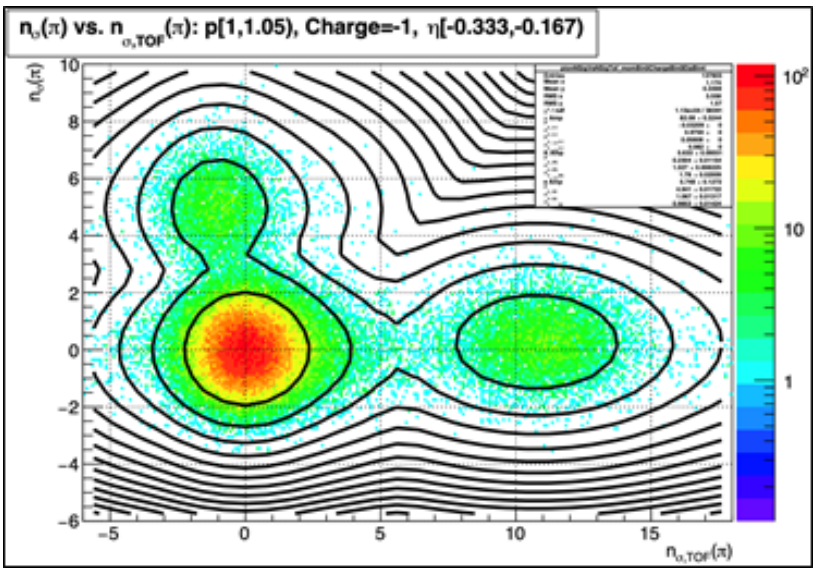

FIG. 1. A sample fitted $n_\sigma(\pi)$ vs. $n_{\sigma,TOF}(\pi)$ distribution in the momentum range $1 < p < 1.05$ GeV/c and $\boldsymbol{\eta}$ range $-0.33 < \eta < -0.167$. At this momentum, the proton peak is far off the right-hand side of the plot.

We analytically calculate the $n_{\sigma,TOF}$ mean difference between two particle peaks. This is made possible by knowing the mean p and η of the particle species, as well as the geometry of the STAR detector. We then compare the analytical calculations to the $n_{\sigma,TOF}$ mean differences from data. Fig. 2a illustrates the good agreement between the analytical calculations and data. Given that pions are the highest statistic peak, we utilize the calculated $n_{\sigma,TOF}$ mean differences to fix the $n_{\sigma,TOF}$ means of K, p, and e with respect to the pion peak, thus reducing the number of free parameters in the fit.

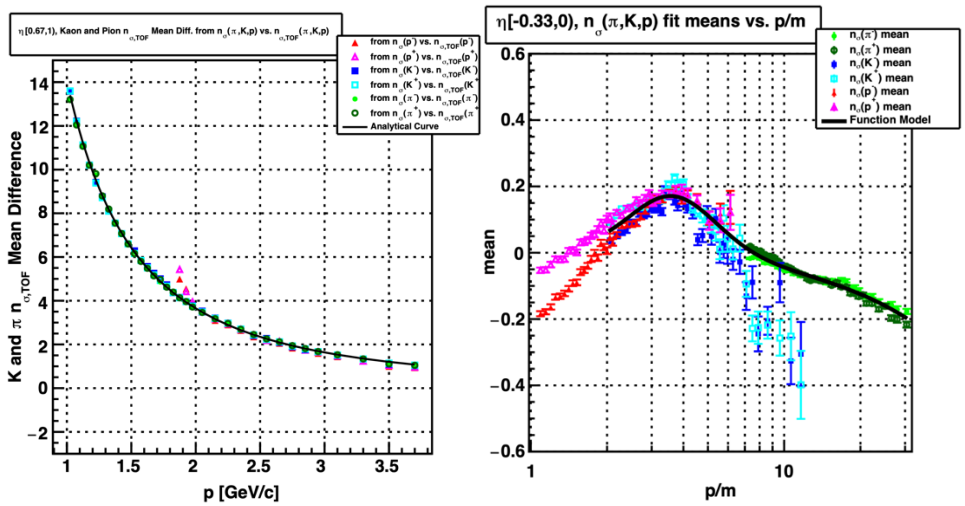

FIG. 2. (a) Data points show the difference between the $\boldsymbol{K}$ and $\boldsymbol{\pi}$ $\boldsymbol{n_{\sigma,TOF}}$ means from data, and the black curve shows the result of calculating the difference analytically. (b) Data points are the means of $\boldsymbol{n_\sigma(\pi, K, p)}$ vs. $\boldsymbol{p/m}$ from data, and the black curve shows the result of the model fit function.

We further reduce the number of free parameters in the fits by modeling the means and sigmas of n_σ and $n_{\sigma,TOF}$ for the signal peak in each fit. As an example to illustrate this point, Fig. 2b shows the mean of $n_\sigma(\pi, K, p)$ vs. p/m, where m is the respective particle mass. The black curve is a model function that fits the data above $p/m \sim 2$. This model function is then used to analytically calculate the mean of $\pi, K,$ and p for a given value of p/m when $\pi, K,$ and p are the signal peaks during the fitting process. The region below $p/m = 2$ corresponds to well-isolated protons, and therefore only a single peak needs to be fitted and model calculations are unnecessary there.

Using information from the two-dimensional fits, we can calculate particle fractions for a given p and η bin by calculating the ratio of integrated particle yields (A_i). Eq. 3 shows an example of how A_π can be calculated, where N_i is the integral of the two-dimensional fit function using the appropriate parameters for the respective particle peak in a given kinematic bin and $i = \pi,\ K,\ p,$ or e. The focus particle of each two-dimensional fit can be any one of the four particle species. A sample comparison between the kaon yield for "pion-centric" versus "kaon-centric" fits is shown in Fig. 3. Below ~2 GeV/c, both the pion-centric and kaon-centric A_K values are similar. Beyond ~2 GeV/c, A_K values from the kaon-centric two-

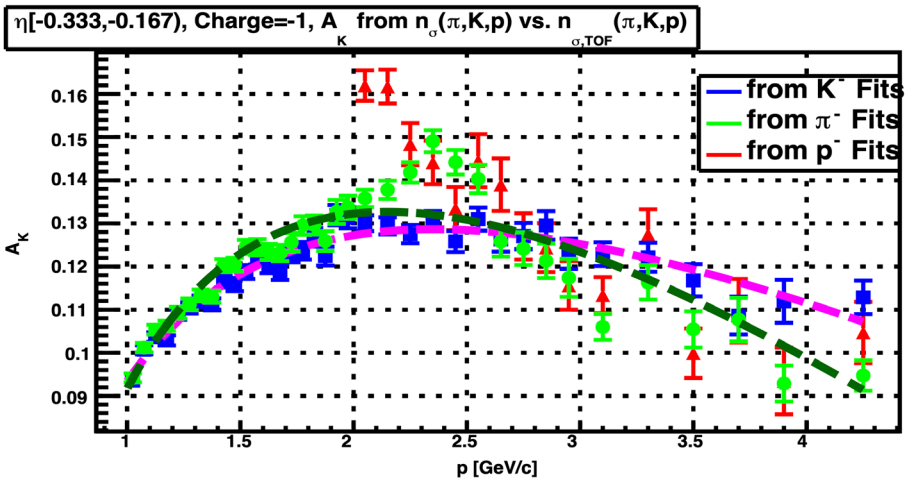

FIG. 3. Comparison between "kaon-centric" and "pion-centric" $\boldsymbol{A_K}$ yields, each of which is fitted with a model function.

dimensional fits are more "well-behaved" when compared to the pion-centric A_K values. This stems from the difference between how the pion and kaon fits are handled. In the pion-centric fit, all the fit parameters for the pion peak are fixed except for the amplitude. The $n_{\sigma,TOF}(K)$ mean is determined with respect to the $n_{\sigma,TOF}(\pi)$ peak, which allows the kaon peak to be easier to fit, but it is still challenging at higher momenta. On the other hand in a kaon-centric fit, all fit parameters for the kaon peak are fixed except for the amplitude, which makes the job of the fitter easier, especially at higher momenta. All parameters corresponding to the pion peak are free, but the pion peak is the highest statistic peak and the fitter is able to locate it easily. Therefore, these differences between the ways the fits are handled lead to the different A_K values between the two fits. We have adopted the fractional yields from kaon-centric fits for the Collins PID procedure. The difference between the kaon-centric and pion-centric yields is assigned as the systematic uncertainty associated with PID.

$$A_\pi = \frac{N_\pi}{N_\pi + N_K + N_p + N_e} \qquad (3)$$

During 2017, STAR recorded a transversely polarized *pp* dataset at $\sqrt{s}$ = 510 GeV with 16 times the figure of merit of the previous measurement [1]. Fig. 4 shows a comparison of the preliminary Collins asymmetries found in the 2017 data with our previous measurements in 200 GeV *pp* collisions [2]. No energy dependence is observed within uncertainties. This sets a stringent limit on evolution effects for transverse-momentum-dependent fragmentation functions. A paper describing these results is being written at present, with Dr. Gagliardi as one of the five principal authors.

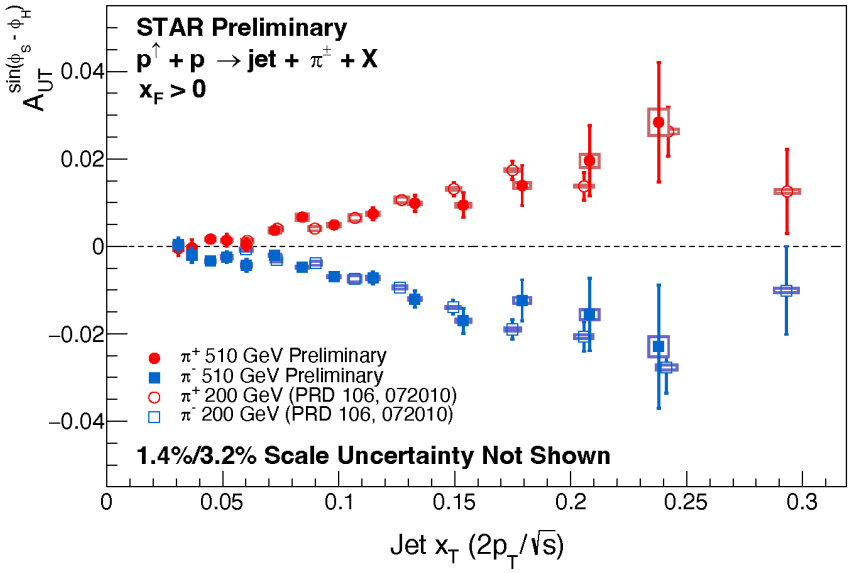

FIG. 4. Comparison of preliminary STAR Collins asymmetry measurements in 510 GeV *pp* collisions with previous results from 200 GeV *pp* collisions [2].

Recently, STAR published measurements of forward π^0 and EM-jet A_N [3] that indicate the large transverse single-spin asymmetries that have been seen for inclusive hadron production at forward rapidities are unlikely to arise from either the Collins or Sivers effects. This led to the question whether the large asymmetries might arise from diffractive processes. The UC-Riverside group began a study of EM-jets observed in *pp* data at $\sqrt{s}$ = 200 GeV that STAR recorded during 2015 to explore this question, and asked Dr. Gagliardi to join the effort. Two different processes have been investigated. In one case, A_N has been measured for the case where a moderate to high-p_T EM-jet and a low-p_T, near-beam momentum proton are both observed at forward rapidity, with the summed energy of the EM-jet and proton consistent with the initial beam energy. The observed asymmetry is found to be negative, which is opposite in sign to the inclusive EM-jet asymmetry. In the other case, EM-jets that arise from single diffraction are being studied by measuring the probability that beam-like protons are seen in the opposite hemisphere. In this case, the observed spin asymmetries are consistent within statistics with those for EM-jets from non-diffractive collisions. Two papers are being written at present. The first will provide a detailed multi-dimensional (x_F,

p_T, photon multiplicity) map of the inclusive EM-jet asymmetries over the pseudo-rapidity range $1 < \eta < 4$. The other will report the comparison of the spin asymmetries found for diffractive processes with those for inclusive EM-jets. Dr. Gagliardi is one of the seven principal authors for both papers.

Finally, we continue to carry various administrative responsibilities for STAR. Dr. Gagliardi was a member of the Trigger Board for Run 23, and is serving again for Run 24. He served as the chair of the god-parent committee for one publication [4] and as a member of the god-parent committee for four others [5-8]. He also made important, but informal, contributions to three other STAR papers [9-11]. In parallel, Mr. Aboona has served as the code-QA representative on the god-parent committee for one paper [9].

[1] L. Adamczyk *et al*. (STAR Collaboration), Phys. Rev. D **97**, 032004 (2018).
[2] M.S. Abdallah *et al*. (STAR Collaboration), Phys. Rev. D **106**, 072010 (2022).
[3] J. Adam *et al*. (STAR Collaboration), Phys. Rev. D **103**, 092009 (2021).
[4] M.I. Abdulhamid *et al*. (STAR Collaboration), Phys. Rev. D **109**, 012004 (2024).
[5] M.I. Abdulhamid *et al*. (STAR Collaboration), JHEP **06**, 176 (2023).
[6] STAR Collaboration, Phys. Rev. C (2023) (submitted); arXiv:2309.00145.
[7] STAR Collaboration, Phys. Rev. Lett. (2023) (submitted); arXiv:2309.00156.
[8] STAR Collaboration, Nature (2023) (submitted); arXiv:2310.12674.
[9] STAR Collaboration, Phys. Rev. Lett. (2023) (submitted); arXiv: 2305.10359.
[10] STAR Collaboration, Phys. Rev. Lett. (2023) (submitted); arXiv:2311.13637.
[11] STAR Collaboration, Phys. Rev. C (2023) (submitted); arXiv:2311.13632.

SECTION II

HEAVY ION REACTIONS

Application of nuclear forensics methodology to americium

I.W. Haynes[1,2] and C.M. Folden III[1,2]
[1]*Department of Chemistry, Texas A&M University, College Station, Texas 77843*
[2]*Cyclotron Institute, Texas A&M University, College Station, Texas 7784*

The elements U and Pu are the primary focus of academic nuclear forensics research, with minor actinides and other radioactive materials underrepresented. Am, the primary contaminant in Pu sources and the daughter of $^{241, 243}$Pu, is one such underrepresented material that happens to be widely proliferated. Used at scale by private industry [1] and widely available to the general public in small quantities contained in smoke detectors [2], Am receives little direct nuclear forensic attention despite its potential for proliferation [3, 4]. This project aims to expand the capability of nuclear forensics *vis-à-vis* Am by adapting an existing source-reactor type discrimination method for plutonium, based on radiochemical measurements of actinide and intra-elemental fission product isotopic ratios. We will also work with Dr. Sunil S. Chirayath at Oak Ridge National Laboratory to apply the existing methodology to Am samples.

First, the needed mass of Am must be determined. Previous work in the Folden group estimated the mass of Pu needed for a reactor-type discrimination method was 4–40 g [5]. This estimate may not be accurate for Am because purity standards for Am used by the Department of Energy are less stringent than those for Pu [6], and common Pu reprocessing schemes see Am go into the same streams as most fission products, leading to a possible concentration effect. The starting mass of americium required for an investigation is inversely proportional to the concentration of trace fission products, such that milligrams of Am would be needed if the concentration of fission products per mass of americium were in the ppb range [7]. Alternatively, if concentrations were at the legal limit of the Department of Energy's guidance to the former Rocky Flats plant [6], nanograms of Am would contain fission product levels measurable by mass spectrometry [7]. Conservatively estimated, tens of milligrams of Am may be needed, which corresponds with up to 100 mCi of activity. The concentration of fission products is inversely related with the quality and quantity of purifications performed throughout a sample's history, which in a forensic investigation is typically unknown.

We have begun a collaboration with Pacific Northwest National Laboratory to study legacy Am samples that may have forensic value. For these legacy samples, no information on sample history is available and the possibility that these estimates are not conservative enough cannot be discounted. Designs that minimize the danger of handling these levels of activity have been made with input from EHS experts at Texas A&M and collaborators at PNNL.

This project will adapt previous work at Texas A&M that developed a source-reactor type discrimination method for purified Pu samples, using intra-elemental isotopic ratios, and apply it to Am samples. These ratios are taken on a suite of elements including any present actinides (Pu, Am) and key fission products, including Cs and multiple lanthanide elements (Sm, Eu); the method is flexible enough to incorporate some additional fission product elements, if present in a sample. If measured, these ratios can be used in conjunction with a library of reactor simulations to determine reactor-type, burnup, and time since irradiation. A critical step to this process is the partitioning of the lanthanides, as they exhibit isobaric interferences that cannot be resolved in traditional mass spectrometers. However, Am and

lanthanides behave similarly in most chemical systems due to similar oxidation state preferences (+3) and atomic radii [8, 9]. The primary challenge to adapting the reactor-type discrimination method to Am samples is the separation of high activities of Am from trace fission products, to enable the partitioning of the lanthanides in a safe manner.

We are developing two research plans for the extraction of lanthanide fission products from the Am sources at PNNL. The preferred method is a modification of a rapid liquid-liquid extraction method [9]. Under strong oxidizing conditions, Am has access to a +5-oxidation state that the select lanthanide fission products of value do not have. Using the tridentate extracting ligand TODGA that strongly extracts +3 oxidation state elements mixed with a strong oxidizer such as Bi (V), the fission products are extracted into an organic phase and Am remains in the aqueous. This method has been shown to have extremely high separation factors in single contact-cycles lasting under 60 seconds. Development of a method for the back-extraction of lanthanide elements from this TODGA extractant system is currently underway. An alternative method using a TEVA column chromatography resin with a ammonium thiocyanate eluent system is also being considered [10].

Either route achieves the separation of trace analytes from Am at PNNL facilities, yielding fractions ready for lanthanide partitioning via α-HIB column chromatography [5], followed by quantification via ICP-MS. Intra-elemental ratios of fission products, Am, and Pu will then be used in the reactor-type discrimination library methodology, ultimately yielding information on the source-reactor type that initially created PNNL's legacy Am.

[1] C. D. Ferguson, T. Kazi, and J. Perera, James Martin Center for Nonproliferation Studies, 2003, available at https://www.nonproliferation.org/wp-content/uploads/2016/09/op11.pdf.

[2] "Backgrounder on Smoke Detectors." United States Nuclear Regulatory Commission, (NRC Library, 2020). Available at www.nrc.gov/reading-rm/doc-collections/fact-sheets/smoke-detectors.html.

[3] "Nuclear Material Control and Accountability." U.S. Department of Energy, Report #DOE M 470.46, (Office of Security and Safety Performance Assurance, 2005)

[4] C. G. Bathke *et al.*, Nucl. Technol. **179**, 5 (2012). doi:10.13182/NT10-203

[5] K. J. Glennon, E. M. Bond, T. A. Bredeweg, S. S. Chirayath, and C. M. Folden III, J. Radioanal. Nucl. Chem. **327**, 143 (2021). doi:10.1007/s10967-020-07448-3

[6] J. D. Navratil, Report #6321166, (Office of Scientific and Technical Information, 1984). Available at https://www.osti.gov/servlets/purl/6321166-AOgODc/. doi:10.2172/6321166

[7] A. Vesterlund and H. Ramebäck, J. Radioanal. Nucl. Chem. **322**, 941 (2019);doi:10.1007/s10967-019-06795-0

[8] W. W. Schulz, *Chemistry of americium* (Office of Scientific and Technical Information, 1976); doi:10.2172/7232133

[9] Z. Wang, J.-B. Lu, X. Dong, Q. Yan, X. Feng, H.-S. Hu, S. Wang, J. Chen, J. Li, and C. Xu, J. Am. Chem. Soc. **144**, 6383 (2022); doi:10.1021/jacs.2c00594.

[10] J. Mahmoud, M. Higginson, C. Gilligan, P. Thompson, F. Livens, and S. L. Heath, J. Radioanal. Nucl. Chem. **331**, 1353 (2022); doi:10.1007/s10967-022-08190-8.

Development of a procedure for the radiochronometric analysis of a mock ^{224}Ra sample: towards a nuclear forensic analysis of a historical ^{226}Ra pigment sample

J.R. Garcia[1,2] and C.M. Folden III[1]
[1]*Department of Chemistry, Texas A&M University, College Station, TX 77840*
[2]*Los Alamos National Laboratory, Nuclear and Radiochemistry Group, Los Alamos NM 87544*

^{226}Ra was identified as a potential threat in nuclear terrorism events by the International Atomic Energy Agency in 2008 for usage in radiological dispersive devices [1]. In the field of nuclear forensics, literature pertaining to ^{226}Ra radiological samples is nonexistent. This work aims to develop a methodology for the nuclear forensic analysis of ^{226}Ra pigment samples, a common product of the early 1900s from the watch dial industry [2]. As part of this analysis, the pigment sample age, or "time since purification," will be determined by measuring absolute quantities of ^{210}Pb and ^{210}Po (daughters in the ^{226}Ra decay chain) relative to ^{226}Ra. To perform a radiochronometric analysis, the solid pigment sample must be quantitatively dissolved, separated via chromatographic methods, and assayed by the respective radiation detector. Preliminary results of the dissolution and separation procedure will be discussed.

A mock ^{224}Ra pigment sample comprised of ZnS (>99% w/w) and a ^{224}Ra salt (<1% w/w) [2-4] was used to develop all procedures for dissolution and separation. Other radiotracer salts such as ^{133}Ba, ^{212}Pb, ^{209}Po, ^{207}Bi, and ^{65}Zn (where ^{65}Zn was chemically incorporated into the lattice structure of ^{nat}ZnS) were incorporated into the pigment. The mock pigment sample was dissolved using a mixture of 0.8 M tetrakis(hydroxymethyl)phosphonium chloride (THPC) solution and 2 M NH_4Cl solution stirred at ~85 °C for 2 h. A small quantity of mock pigment (~0.005 g) was dissolved using 5 mL of the dissolution solution, and radionuclide quantities were assayed by gamma spectrometry with an HPGe detector. The dissolution efficiencies for $^{133}BaCl_2$ (γ = 356 keV), $^{224}RaCl_2$ (γ = 240 keV), $^{212}PbCl_2$ (γ = 238 keV), and ^{65}ZnS (γ = 1115 keV) were 103 ± 8%, 100 ± 3%, 103 ± 3%, and 100 ± 2%, respectively. Mixed solutions of THPC and NH_4Cl have proven effective for the quantitative dissolution of the mock ^{224}Ra pigment sample.

There is significant literature on column chromatography of many elements and their behaviors with various resin and acid systems [5]. However, THPC and NH_4Cl are uncommon reagents, so the literature is very sparse. In this case, removing all elements from the THPC/NH_4Cl matrix and converting to a more commonly studied medium (such as HCl or HNO_3) is advantageous. Batch studies were performed to determine the chemical behavior of Ra, Ba, Pb, Bi, Po, and Zn in the THPC/NH_4Cl matrix. Chelex-100 was the selected resin due to its effective ability to remove metal ions from dilute salt solutions [6]. Weight distribution coefficient values, D_w, were measured to be ≥ 1000 for all studied elements in dilute solutions of THPC/NH_4Cl (0.008 M and 0.02 M, respectively) indicating retention onto the resin under these conditions. Next, the common ion in the matrix is Cl^-, so it was desirable to switch to HCl media for elemental separation after retention on Chelex-100. Batch studies were performed for all elements between 0.01 M and 10 M HCl on Chelex-100 resin. These data showed retention of all elements under dilute conditions (0.01 M HCl). Furthermore, 1 M HCl allowed for the desorption of Ra, Ba, Pb, and Zn and retention of Bi on the resin; Bi was recovered using 10 M HCl. Using this information, a separation scheme was determined. Starting from dissolution, a 500 µL cocktail mixture of

known quantities of ^{244}Ra, ^{133}Ba, ^{212}Pb, ^{207}Bi, and ^{65}Zn dissolved in H_2O was added to a round bottom flask containing a 5 mL solution of THPC and NH_4Cl (0.008 M and 0.02 M, respectively). A 0.3 g Ni foil was added to the mixture to simulate the auto-deposition of ^{209}Po for its separation from the solution. After 2 h of heating (~75 °C) and stirring, 100 µL was removed and diluted to 10 mL with H_2O. The pH of the resulting solution was adjusted to 4.5 using a 1.0 M solution of NaOH. After 30 min, this solution was loaded onto the reverse preconditioned (10 M HCl, 1 M HCl, 0.01 M HCl, and diluted THPC/NH_4Cl solution, in that order) Chelex-100 column (8 mm diameter; 3 cm bed height). The column was rinsed with 5 mL of 0.01 M HCl to retain ^{224}Ra, ^{133}Ba, ^{212}Pb, ^{207}Bi, and ^{65}Zn to switch from THPC/NH_4Cl media to HCl. Next, the column was rinsed with 5 mL of 1 M HCl to elute ^{224}Ra, ^{133}Ba, ^{212}Pb, and ^{65}Zn. Finally, the column was rinsed with 5 mL of 10 M HCl to recover ^{207}Bi. The results of this experiment are shown in Fig. 1.

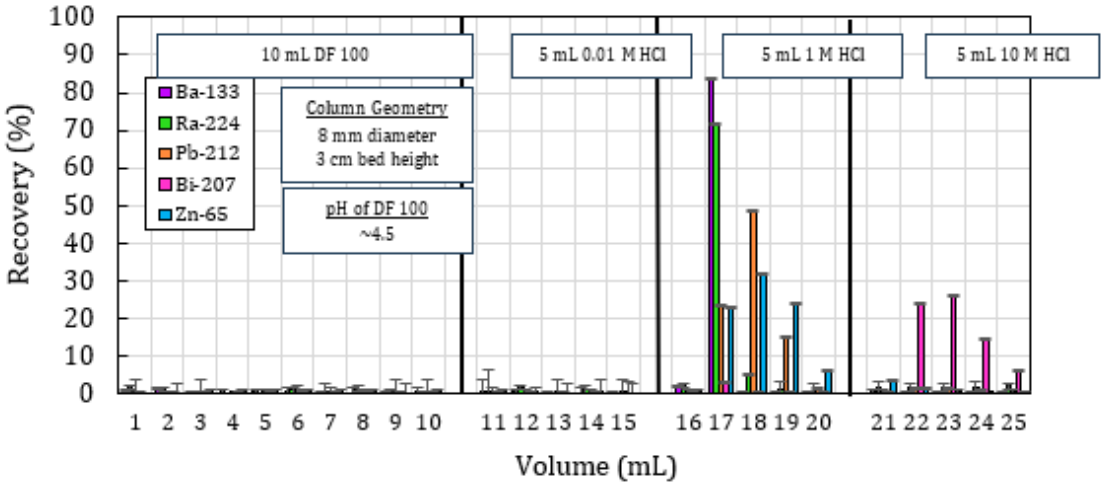

FIG.1. Chromatographic separation of ^{224}Ra, ^{133}Ba, ^{212}Pb, ^{207}Bi, and ^{65}Zn using Chelex-100 resin. The load solution of diluted THPC/NH_4Cl (dilution factor, DF, of 100) was adjusted to pH 4.5 and equilibrated for 30 min before separation. Each element appeared in their anticipated fractions according to batch study experiments.

Overall, according to the batch study experiments, this experiment has shown recovery of all elements that appear in the anticipated fractions. In addition, all elements could be recovered from the THPC/NH_4Cl matrix, making alpha spectrometry a feasible assay technique (THPC/NH_4Cl previously formed a residue that inhibited α particles from reaching the detector [7]).

In future work, ^{209}Po will be incorporated into the dissolution and separation procedures to confirm its auto-deposition and removal from THPC/NH_4Cl matrices. Additionally, milligram quantities of ^{nat}ZnS will be used for the combined dissolution and separation procedure to ensure possible separation even with large quantities of Zn. These procedures will ultimately be applied to the mock ^{224}Ra pigment sample for the radiochronometric determination of the known sample age. Finally, these procedures will be used to age date a historical ^{226}Ra pigment sample.

A dissertation based on the results discussed above is currently being written.

[1] S. Friedrich, R. Stan, and Z. Lyudmila, AIP Conference Proceedings **1034**, 3 (2008). doi:10.1063/1.2991254
[2] D.I. Harvie, Endeavour **23**, 100 (1999). doi:10.1016/S0160-9327(99)01201-6
[3] G.F. Kunz, Luminous composition, patent number:US789811A (1905). available at https://patents.google.com/patent/US789811A/en (Accessed 3.21.24)
[4] S. Norquest, A. Kile, and D. Peters, OSGP **22**, 169 (2016). available at https://resources.culturalheritage.org/osg-postprints/wp-content/uploads/sites/8/2015/05/osg022-11.pdf (Accessed 07.01.23)
[5] R.A. Silva, K. Hawboldt, and Y. Zhang, Miner. Process. Extr. Metall. Rev. **39**, 395 (2018). doi:10.1080/08827508.2018.1459619
[6] S. Faucher, C. Moreau, P. Chéry, and G. Lespes, J. Anal. Chem. **75**, 468 (2020). doi:10.1134/S1061934820040024
[7] J.R. Garcia, C.M. Folden III, and E.M. Bond, *Progress in Research*, Cyclotron Institute, Texas A&M University (2022-2023), p. II-22, available at https://cyclotron.tamu.edu/progress-reports/2022-2023/cyclotron_progress_2023.pdf (Accessed 5.30.24)

Preparation for online superheavy element homolog experiments using functionalized detector surfaces

A. S. Kirkland,[1,2] R. Eichler,[3,4] J. R. Garcia,[1,2] I. W. Haynes,[1,2]
J. A. Mildon,[1,2] P. Steinegger,[3,5] E. E. Tereshatov,[1] G. Tiebel,[3,5]
V. Zakusilova,[1] and C. M. Folden III[1,2]
[1]*Cyclotron Institute, Texas A&M University, College Station, Texas 77843*
[2]*Department of Chemistry, Texas A&M University, College Station, Texas 77843*
[3]*Laboratory of Radiochemistry, Center for Nuclear Engineering and Sciences, Paul Scherrer Institute, Forschungsstrasse 111, Villigen PSI, CH-5232, Switzerland*
[4]*Department of Chemistry, Biochemistry and Pharmaceutical Sciences, University of Bern, Freiestrasse* 3, Bern, CH-3012, Switzerland
[5]*Laboratory of Inorganic Chemistry, Department of Chemistry and Applied Biosciences, ETH Zürich, Leopold-Ruzicka-Weg 4, Zürich, CH-8093, Switzerland*

Superheavy elements (SHEs) characteristically have short half-lives and low production cross sections. This makes studying the chemistry of SHEs difficult, and improvements in experimental techniques are necessary in order to expand the understanding of SHE chemistry. A promising new technique for doing so is the use of self-assembled monolayers (SAMs) on the surface of gold-coated detectors. Recent work has shown that imidazole-based SAMs on the surface of gold chips can be used offline to selectively sorb rhodium (Z=45) and iridium (Z=77), homologs of meitnerium (Z=109), from solution [1]. Cyclotron-based experiments producing ^{176}Ir show promising results [2]. The current work describes a new system utilizing polonium (Z=84), an expected homolog of livermorium (Z=116).

Polonium was chosen due to the desirable decay properties of its isotopes and its relative availability. ^{216}Po ($t_{1/2}$ = 144 ms, α-branching ratio: 100%) can be extracted in the gas-phase from a ^{228}Th source utilizing a recoil transfer chamber (RTC) [3], which makes it viable to use for offline testing. Recent experiments by our group have also tested several nuclear reactions to determine the optimal conditions for producing suitable isotopes of Po in cyclotron-based experiments with the AGGIE gas-filled separator, and preliminary results are reported here.

These experiments were performed using the K150 cyclotron at Texas A&M University Cyclotron Institute. ^{40}Ar^{11+} with an energy of 6.9 MeV/u was passed through a 15 μm Al window and various Al degraders, as well as a 2 μm Ti target backing. The targets used were 835 μg cm^{-2} ^{160}Dy and 347 μg cm^{-2} ^{162}Dy. The products were separated using the AGGIE gas-filled separator, which was set for a magnetic rigidity of 1.6 T m for both targets. The products were then focused onto two double sided silicon detectors (DSSDs).

The nuclear reactions performed include ^{160}Dy(^{40}Ar, xn)$^{200-x}$Po and ^{162}Dy(^{40}Ar, xn)$^{202-x}$Po. The latter is the most promising reaction, and an example spectrum, as well as the production rates as a function of the compound nucleus excitation energy are shown in Fig. 1. There are several isotopes produced, including ^{197}Po ($t_{1/2}$ = 84 s, α-branching ratio: 44%), ^{196}Po ($t_{1/2}$ = 5.8 s, α-branching ratio: 98%), and ^{195m}Po ($t_{1/2}$ = 1.92 s, α-branching ratio: 98%).

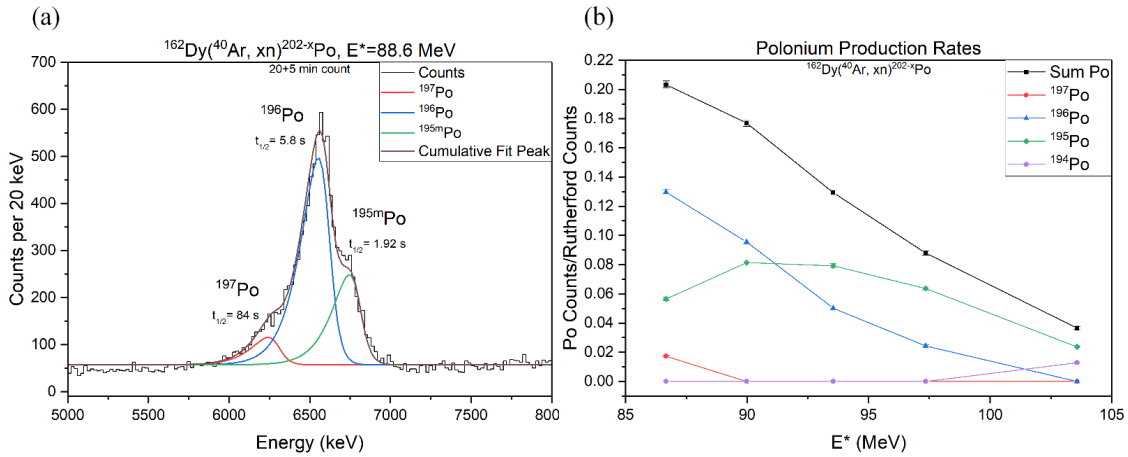

FIG.1. (a) Preliminary example α-spectrum of three isotopes of Po using ^{162}Dy(^{40}Ar, xn)$^{202-x}$Po; "20+5 min" refers to 20 min of irradiation followed by a 5 min measurement without the ion beam on target to allow radionuclides to decay. (b) Preliminary excitation function for the same nuclear reaction; Rutherford counts refer to events collected on a pair of scattering detectors positioned ±30° respective to the ion beam axis, after it passes through any degraders and the target, scaling linearly with the luminosity (beam x target). Lines are drawn to guide the eye.

Since production of Po has been established, preparations have shifted towards the preparation of a well-organized SAM. The chosen monolayer is 1,9-nonanedithiol (NDT; see Fig. 2(a)), which has a known thickness of 1.3 nm [4]. This is ideal for α-spectroscopy, since negligible amounts of energy will be lost in the monolayer. However, dithiol SAMs are prone to oxidation, which can complicate the self-assembly process and form disorganized multilayers [5]. Optimization of the deposition process is ongoing. Using spectroscopic ellipsometry, the measured layer thickness is 2.27 ± 0.031 nm (see Fig. 2(b)), which is indicative of a bilayer. Improvements to the deposition process are being considered, including changing the long alkyl chain to a more rigid phenyl-based backbone, and adding a reducing agent to the solution to prevent the oxidative coupling of the dithiol monolayer.

These experiments will continue with an online experiment to test the sorption of Po on the NDT SAM being planned for Fall 2024.

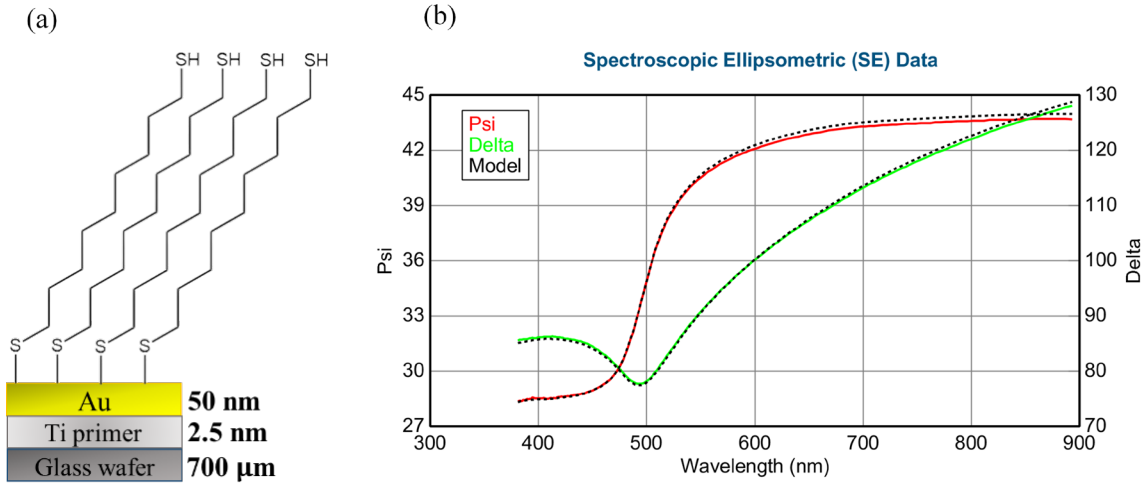

FIG.2. (a) Expected structure of 1,9-nonanedithiol (NDT) on an Au-coated glass wafer. (b) Spectroscopic ellipsometry data of NDT SAMs deposited from a 5 mM NDT solution in deoxygenated hexanes, corresponding to a NDT SAMs thickness of 2.27 ± 0.031 nm. This thickness is determined by measuring the phase difference (Δ) and amplitude difference (Ψ) of polarized light passing through the thin film, and a Cauchy model is used to determine the thickness.

[1] V. Zakusilova, E.E. Tereshatov, M. Boltoeva, and C.M. Folden III, Appl. Surf. Sci. **642**, 158356 (2024); doi:10.1016/j.apsusc.2023.158356

[2] V. Zakusilova, PH.D. Thesis, University of Strasbourg, 2022, available at https://www.theses.fr/2022STRAE020.

[3] M.C. Alfonso, E.E. Tereshatov, M.J. DeVanzo, J.A. Sefcik, M.E. Bennett, D.A. Mayorov, T.A. Werke, and C.M. Folden III, Nucl. Instrum. Methods Phys. Res., **A798**, 52 (2015); doi:10.1016/j.nima.2015.07.004

[4] A.T. Kelley, J.N. Ngunjiri, W.K. Serem, S.O. Lawrence, J.-J. Yu, W.E. Crowe, and J.C. Garno, Langmuir **26**, 3040 (2010); doi:10.1021/la9026128

[5] H. Hamoudi and V.A. Esaulov, Ann. Phys. **528**, 242 (2016); doi:10.1002/andp.201500280

An evaluation of the possible effect of tetra-neutron production on ternary fission yields

H. Pais,[1] G. Roepke,[2] and J. B. Natowitz[3]
[1]*CFisUC, Department of Physics, University of Coimbra, 3004-516 Coimbra, Portugal.*
[2]*Institut fűr Physik, Universit¨at Rostock, D-18051 Rostock, Germany.*
[3]*Cyclotron Institute, Texas A&M University, College Station, Texas 77843, USA*

Ternary fission of actinides occurs in the neck region between the two heaviest fission fragments and probes the state of the nucleus at scission. In a previous publication [1] we explored the ternary fission in the ^{238}Pu(nth,f) reaction. Based upon the comparisons of theoretical yields to experimental yield we concluded that the neck region could be characterized by a temperature of 1.29 MeV, a density of 6.7 x 10^{-5} fm-3 and a proton fraction 3.5 x 10^{-2}.

The possible existence of tetra-neutrons has long been postulated. The current most credible evidence of tetra-neutron formation appears to be that of Duer *et.al.* [2] who reported evidence for a resonant four neutrons state with an energy of $E4n = 2.37 \pm 0.38(\text{stat}) \pm 0.44(\text{sys})$ MeV and a width of $\Gamma = 1.75 \pm 0.22(\text{stat}) \pm 0.30(\text{sys})$ MeV. The role that such a tetra-neutron could play in neutron star matter has been addressed in Pais *et al.* [3]. Given the extreme neutron richness found for the ternary fragment region in fission it is natural to ask whether the production of tetra-neutrons might exist and be reflected in the ternary fragment yields. We are presently carrying out exploratory calculations using the techniques described in Refs [1,3].

In Fig. 1 we present yield ratios comparing yields calculated for the ternary fission neck matter with and without inclusion of the tetra-neutron characterized by the Duer *et al.* parameters. Very clear effects are seen indicating yield modifications induced by inclusion of the tetra-neutron. However, these effects occur at densities higher than those derived in Ref. [1]. It is clear that these results are sensitive to he assumed parameters of the matter explored as well as those reported for the tetra-neutron. We are currently evaluating a range of temperatures, densities, proton fractions and tetra-neutron binding energies to understand under which conditions the effects of tetra-neutron production might be reflected at higher densities, temperatures and proton fractions which might be accessible in the laboratory, e.g, in the neck regions of deep inelastic collisions.

[1] J.B. Natowitz *et al.*, Phys. Rev. C **107**, 014618 (2023).
[2] H. Pais *et al.*, Astron.& Astrophys. **679**, A113 (2023).
[3] M. Duer et al., Nature **606**, 678 (2022).

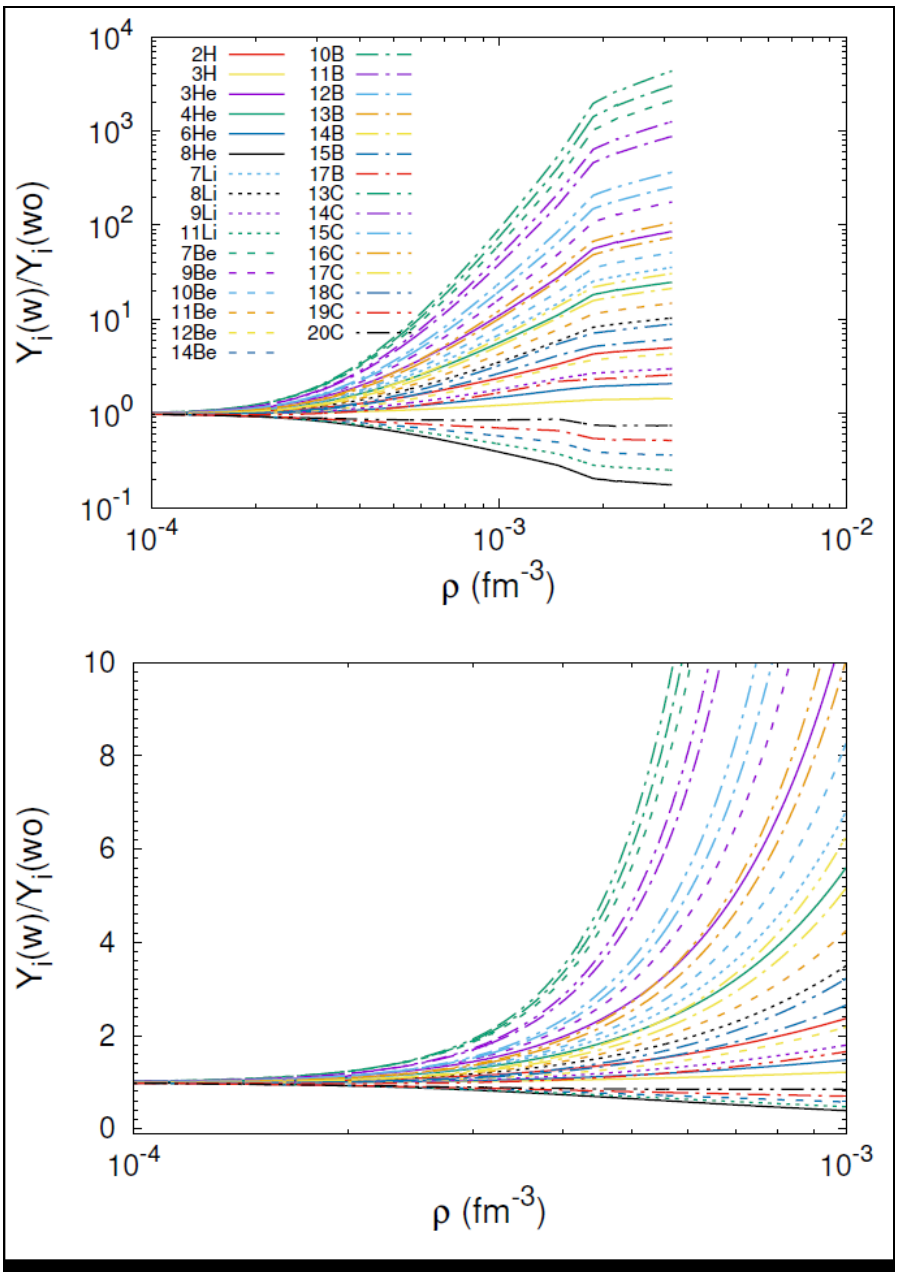

FIG.1. Yield ratios for ternary fission fragments observedin the reaction ^{238}Pu(nth,f). Ratios of yields caculated with and without inclusion of tetra-neutrons (see text) are shown. Top-full results. Bottom – expanded scale.

Analysis techniques for investigating decay pathways in excited light nuclei

B.M. Harvey, T. Hankins, A.B. McIntosh, K. Hagel, and S.J. Yennello

Light nuclei are known to exhibit clusterization when excited. This clusterization of these nuclei is often correlated to how they decay through the emission of alpha particles and what subsequent nuclei are formed. The quintessential example of this is the Hoyle state in ^{12}C, which is known to dominantly decay through sequential emission of alpha particles [1], forming the unbound ground state of ^{8}Be in the process.

These light nuclei and their decay pathways have been studied in some detail over the past few decades but there are still many open questions. The techniques used to study ^{12}C can be explored in recent data collected from a variety of nuclei with the Forward Array Using Silicon Technology (FAUST) detector array [2] at Texas A&M University.

FAUST allows for precise measurements of momentum and particle type with reasonably large angular coverage (~1.5° - ~45°). The array consists of 68 ΔE-E telescopes assembled from a thin (300 um) Si detector, backed by a thick CsI(Tl) detector. The Si detector has resistive surfaces on both faces allowing for precise incident position to be ascertained event-by-event. Over several experiments, data were collected at 35 MeV/u for the following beams all on natural carbon: ^{16}O, ^{20}Ne, ^{24}Mg, ^{28}Si, ^{32}S, and ^{36}Ar. The normal kinematic system ^{12}C + ^{28}Si was also studied.

There are several analyses which can be performed on this dataset, the foundation of which is the ability to reconstruct decay pathways of the excited states of the nuclei through their initial excitation energies and those of their constituent particles. If one can assign decay pathways, one can study branching ratios and angular correlations of the decay products which aids the understanding of the clusterization of nuclei.

As an example to the statistical power these data hold, one can look at the excitation of ^{12}C in ^{12}C + ^{28}Si @ 35 MeV/u. In events where three alpha particles are measured, their relative energy to the 3^- alpha center of mass can be determined and associated with an excitation in ^{12}C by the following equation:

$$E^* = \sum_i K_{i,c.m.} - Q_{rxn}$$

The resulting spectra is shown in the first following figure in black points. Several features are immediately apparent. From left to right, the Hoyle state appears at 7.654 MeV, and the next excited state in ^{12}C (a 3^- state) appears just above 9 MeV. Above this, many more states appear, each of which can be compared to literature. One can also look at the energy spectra of every combination of two alpha particles in the events which had three, resulting in Fig. 2.

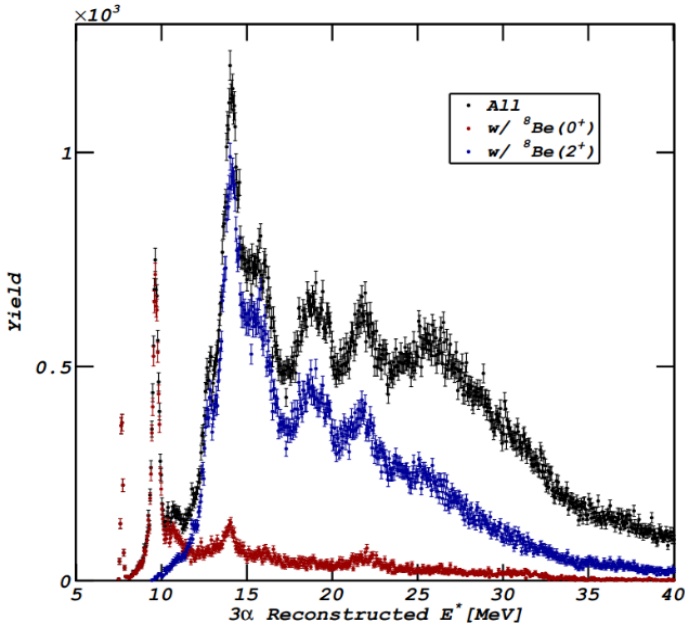

FIG.1. Alpha reconstructed energy, gated on nothing (black), events with a measured Be-8(gs) (red) and gated on states with a measured Be-8(2+) (blue).

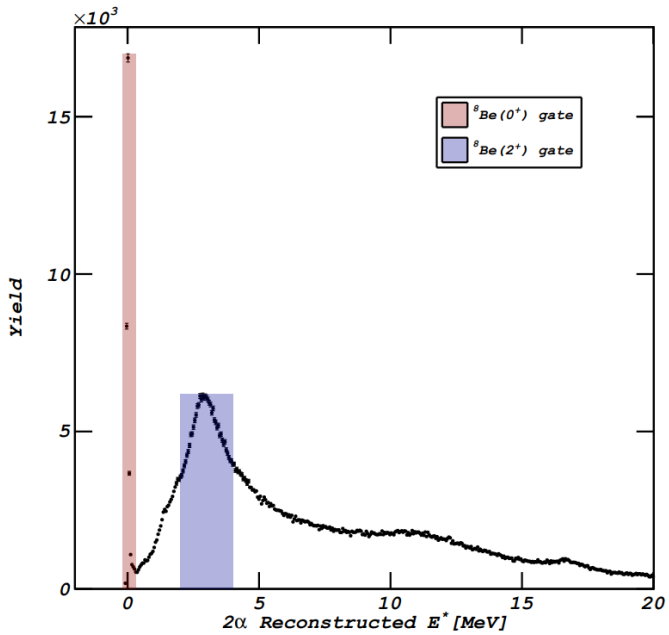

FIG. 2. Alpha reconstructed excitation energy showing gates on different states.

When ^{12}C decays via alpha emission, the remaining residue is an ^{8}Be which promptly decays by second alpha emission. The second spectrum shows which states are populated as an intermediate step from the ^{12}C decays; the very narrow ground state and the much broader 2^+ first excited state in ^{8}Be are shown in red and blue, respectively. It is therefore possible to gate on three alpha events where one alpha-

alpha pair in the breakup possesses an E* within either shaded region; these gated spectra are shown in the first plot as the red and blue data, respectively. Immediately, one can see that the Hoyle state virtually always decays through the ^{8}Be ground state, as does the ^{12}C 3^{-} state. However, as the ^{12}C excitation energy increases, the relative contribution from the 2^{+} state in ^{8}Be also increases. This technique demonstrates good agreement to reported data and is flexible to study other decay pathways of larger and more complex decay mechanisms in other nuclei going forward.

[1] https://journals.aps.org/prl/pdf/10.1103/PhysRevLett.119.132501
[2] https://doi.org/10.1016/j.nima.2023.168130.

DAPPER: PSF forward analysis on ^{58}Fe using d,p reaction in inverse kinematics

M. Q. Sorensen,[1,2] A. Abbott,[1,2] A. B. McIntosh,[1] A. Alvarez,[1,3] A. Couture,[4] K. Hagel,[1] J. Gauthier,[1] S. Ota,[5] G. Potel,[6] A. Richards,[7] and S.J. Yennello[1,2,3]

[1]*Cyclotron Institute, Texas A&M University, College Station, TX 77843*

[2]*Department of Chemistry, Texas A&M University, College Station, TX 77843*

[3]*Department of Physics, Texas A&M University, College Station, TX 77843*

[4]*Los Alamos National Laboratory, Los Alamos, NM 87545*

[5]*Brookhaven National Laboratory, Upton, NY 11973*

[6]*Lawrence Livermore National Lab, Livermore, CA 94550*

[7]*Ohio University, Athens, OH 45701*

The photon strength function (PSF) is important in describing photon emission probabilities and thus it plays a role in radiative neutron capture reactions. Experiments have shown an enhancement in the PSF at low energy for some nuclei. This low energy enhancement (LEE) could have a large effect on r-process nucleosynthesis, where many nuclei with unmeasured neutron capture cross sections are produced in nature. Experiments have shown an LEE in both ^{56}Fe and ^{57}Fe nuclei [1-3]. A measurement of ^{58}Fe's PSF could see if this trend continues. In addition, doing a measurement of ^{58}Fe's PSF helps to prepare for a future measurement of ^{60}Fe's PSF, which will require a radioactive beam. DAPPER (Detector Array for Photons, Protons, and Exotic Residues) probes PSFs using inverse kinematics (d,p) reactions. DAPPER consists of 128 BaF_2 detectors, to detect the gamma rays with high efficiency, and one S3 Annular Silicon detector, to detect the proton. A beam experiment was done on August 2nd, 2021, to measure ^{58}Fe's PSF. The analysis methodology that I am using to constrain the photon strength function is known as the forward method [4].

The forward method works by simulating the gamma ray cascade assuming a certain PSF and nuclear level density (NLD), and then comparing the simulation to the experimental results. In order to compare the simulated data to the experimental ones, the simulated cascades must be subject to the same experimental constraints as the experimental data. To do this we have chosen to use GEANT4 to simulate DAPPER's response. In addition to the GEANT4 simulation the initial spin of the ^{58}Fe nucleus must also be accounted for. For each PSF and NLD, multiple initial spins states must also be sampled, and their contributions then must be weighed by a predicted spin distribution as a function of excitation energy. Dr. Potel provided some theoretical predictions of how much spin state contributes to the (d,p) reaction, allowing us to predict the yield as a function of excitation energy for each of the different J states [5].

Extensive work has been done to compare multiple models to experimental results. To select on more statistical initial state population higher excitation energy regions are used in this analysis. Given this concern the region gated on is the 9 to 9.5 MeV region. One model that was explored is the quasiparticle random-phase approximation (QRPA) PSF provided by PSF database [6] coupled with Hartree-Fock-Bogolyubov (HFB) NLD [7] sourced from RIPL3. The QRPA-PSF model agrees well with earlier measurements of ^{56}Fe and ^{57}Fe PSFs at higher gamma ray energy but differ at lower energy values where the LEE has a large effect. Using the nominal values for the QRPA-PSF and the HFB NLD,

DICEBOX simulations were run and then compared to experimental results in Fig. 1. Overall decent agreement was found with the reduced chi square calculated for each spectrum.

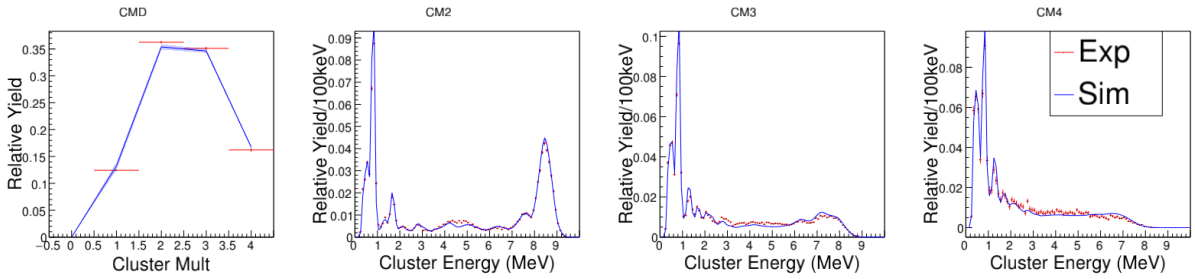

FIG.1. Comparison between simulation (blue) and experiment (red), gating on the 9 to 9.5 MeV E* region. Each spectrum is normalized to areas of 1 for both simulation and experiment. Only statistical errors are shown and are typically small for the simulation. Only events with the Esum within 300 keV of the excitation energy were included (Total Sum Gate (TSG) gate).

The QRPA-PSF provided by the PSF database has several phenomenological corrections applied to it. One of these terms is for the LEE, which is modeled as an exponential decay from zero energy. To see the effect on the Sim-Exp agreement the constant value (Cval) for that exponential was tweaked and then the simulations were run again. The reduced chi square was then re-evaluated for each of these new LEE strengths to yield the trends seen in Fig. 2. The cluster multiplicity distribution shows a trend of

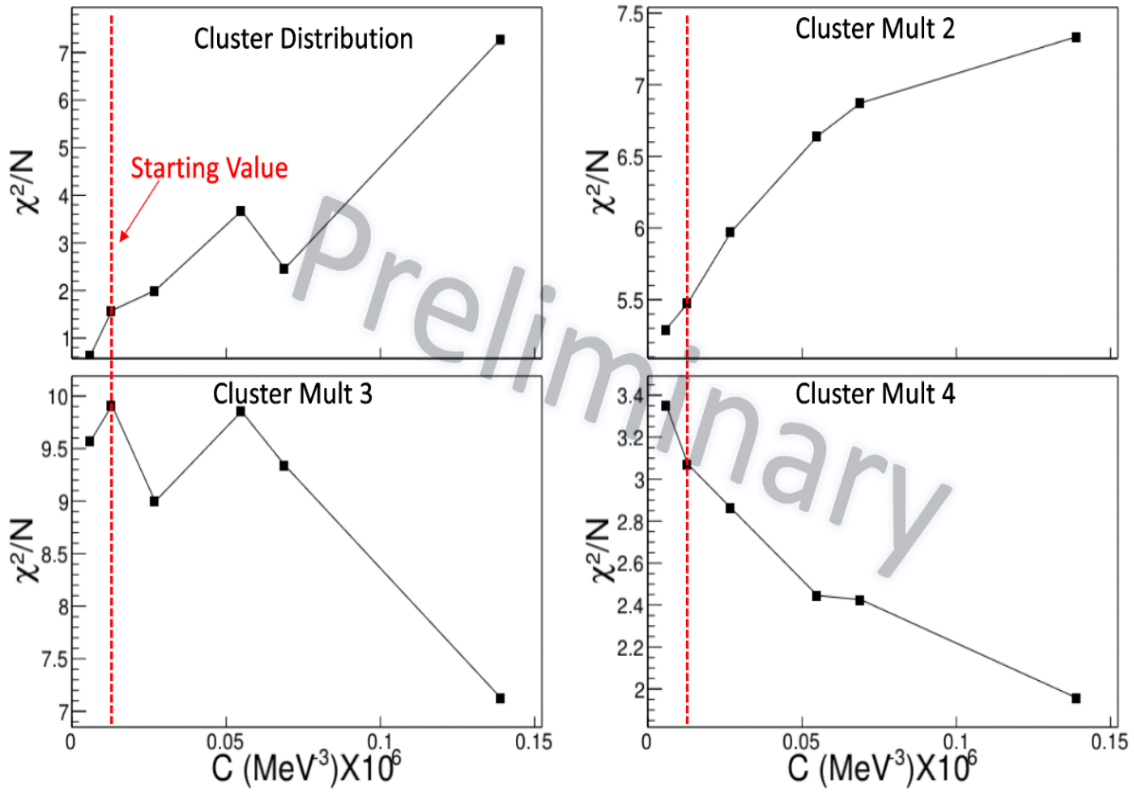

FIG.2. Reduced Chi2 evaluation for each spectrum evaluated as a function of the LEE constant value. Once more the region evaluated is between 9 to 9.5 MeV E* with the total sum gate.

having worse agreements as the LEE is increased, which is also seen in the cluster mult 2 energy

distribution. The cluster mult 3 energy distribution only shows better agreement for an extreme value of the LEE, while the cluster mult 4 energy distribution exhibits the opposite trend as seen for the cluster mult 2 energy distribution. If the LEE was the only source of disagreement between the simulation and the experiment all the distributions should show similar chi square minima. Since this is not observed other sources of discrepancies need to be explored within the chosen model space.

Many models have been simulated, and a comprehensive evaluation of the trends is being prepared. For the sake of brevity, only an example MSC plot for the cluster mult 2 energy distribution is shown in Fig. 3. This demonstrates the effect of changing the models used in the DICEBOX simulation. Substantial changes in the simulated energy shape can be seen in the middle energy region. The CT-Oslo-EBFG NLD coupled with the QRPA PSF approximates the results from Austin's thesis and shows good agreement in the central region. This gives some evidence that the Forward and Oslo analysis method can corroborate each other. The BSFG-GLO and CT-SLO model used in Dr. Bennet's study of ^{58}Fe's PSF [8] over predict the observed energy distribution in the middle energy region. Publication on the final results will likely occur within one to two years.

[1] A. Voinov *et al.*, Phys. Rev. Lett. **93**, 142504 (2004).

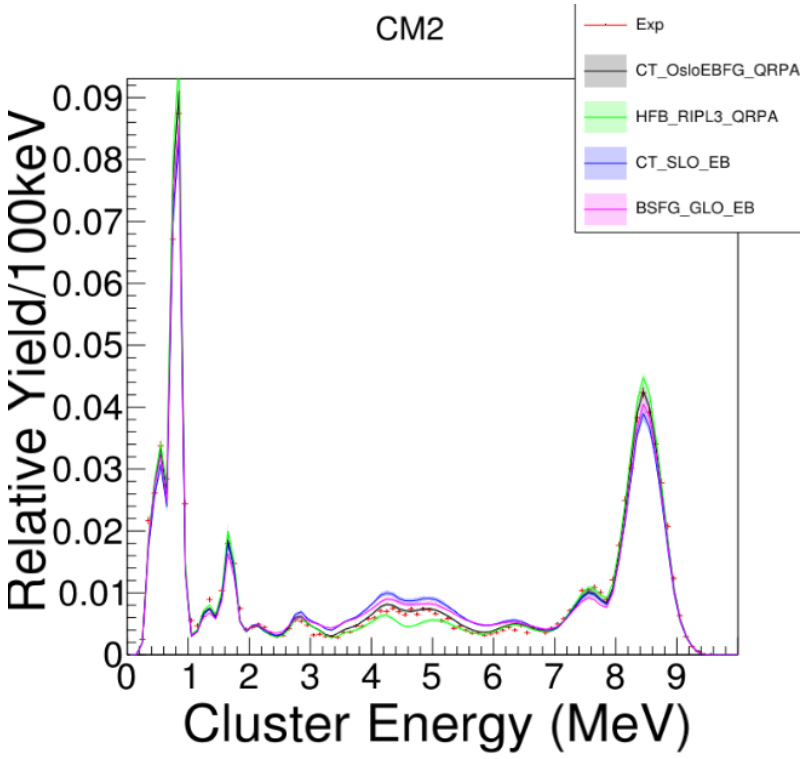

FIG.3. Cluster multiplicity 2 energy comparison between the experiment (red) and various models. In black is a model using Austin's Oslo CT NLD with the EBFG normalization with the QRPA PSF with from the PSF database corresponding to 10 MeV excitation energy, in green is the HFB RIPL3 NLD with the QRPA PSF, blue is the constant temperature NLD with a simple Lorentzian model adopted in Dr. Bennet's dissertation on ^{58}Fe's PSF, and in pink is a simulation using a BSFG NLD with a GLO PSF also used in Dr. Bennet's work.

[2] E. Algin *et al.*, Phys. Rev. C **78**, 054321 (2008).

[3] A.C. Larsen *et al*., Phys. Rev. Lett. **111**, 242504 (2013).
[4] F. Becvar, Nucl. Instru. Methods Phys. Res. **A417**, 434 (1998).
[5] G. Potel, F. M. Nunes, and I. J. Thompson, Phys. Rev. C **92**, 034611 (2015).
[6] S. Goriely, P. Dimitriou, M. Wiedeking, T. Belgya, T. M. Sprouse, R. Firestone, J. Kopecky, M. Krtiˇcka, V. Plujko, R. Schwengner, S. Siem, H. Utsunomiya, S. Hilaire, S. Péru, *et al*, Eur. Phys. J. A **55**, 172 (2019).
[7] S. Goriely, S. Hilaire, and A. J. Koning, Phys. Rev. C **78**, 064307 (2008).
[8] E. Bennett, PhD Thesis, Texas A&M University, 2020.

Forward angle proton energy spectra in the ^{64}Zn + ^{112}Sn reaction at 47 MeV/u

A. Fentress, A. McIntosh, K. Hagel, M. Sorensen, T. Hankins, B. Harvey, A. Alvarez,
N. Shaffett, R. Wada, and S.J. Yennello

Forward proton spectra acquired with NIMROD [1] in the first campaign in 2001 using 47 MeV/u ^{64}Zn projectiles exhibit intriguing high energy tails up to 200 MeV. In order to confirm that these are, indeed, high energy protons and not an artifact of non-physics effects, ie double hits where two protons enter the CsI at the same time and are identified as a proton with the apparent energy being the sum of the two protons, we decided to mount a simple experiment that discriminates against double hits and can confirm or refute these interesting high energy protons.

47 MeV/u ^{64}Zn ions were accelerated using the K500 Cyclotron at the Cyclotron Institute at Texas A & M University. The Zn ions were incident on a ^{112}Sn target. A single Ring 2-3 module from NIMROD was placed in a chamber at the same distance from the target as it is in NIMROD. To discriminate against double hits, we installed a 6mm thick CsI detector with the phototube detecting the CsI light from the side rather than the back like the NIMROD CsIs. In this way we can in principle obtain particle identification from each of the CsI detectors using pulse shape analysis as well as using the signals from each to obtain particle identification information from the ΔE vs E map.

Fig. 1 shows the particle identification map of the hydrogen isotopes. The horizontal axis shows the CsI fast signal from the front ΔE detector and the vertical axis shows the CsI fast signal from the back detector. Excellent separation between protons, deuterons and tritons are observed. This technique allows to discriminate against double hit protons as the ΔE signal will be on a different line from the proton line if two protons enter the front CsI in the same event.

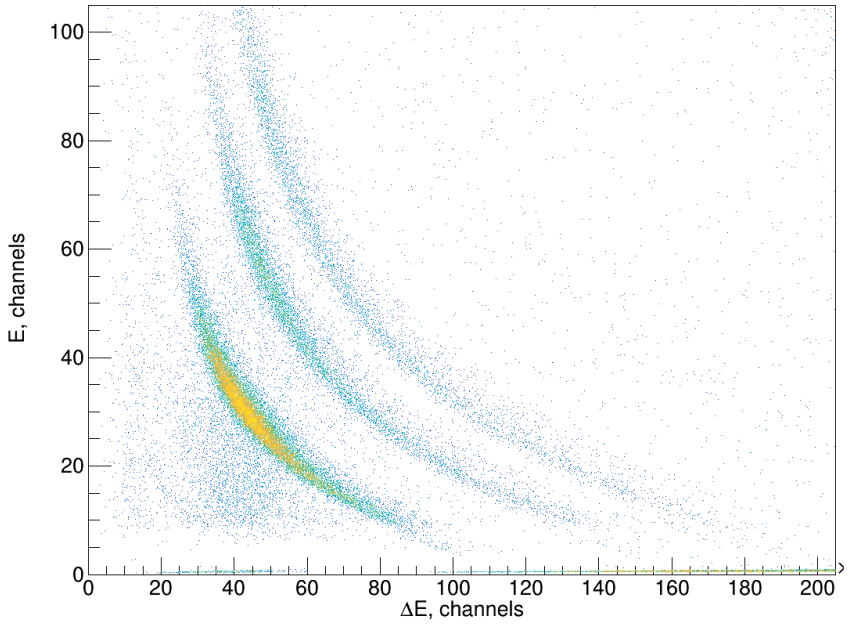

FIG. 1. E vs ΔE distribution of hydrogen isotopes.

Fig. 2 shows the slow vs fast map of the ΔE CsI detector. Excellent proton, deuteron and triton separation is achieved as well. The leftmost line includes cosmic muons that travel through the detector, gamma rays and neutrons as well as, importantly, protons that have passed through the ΔE into the E detector.

The particles were linearized using the now standard NIMROD linearization software [1]. Linearizations were performed on the particle identification map shown in figure 1 as well as the slow vs fast of the front ΔE CsI. The system was calibrated by using a 55 MeV H2 beam from the K500. Several peaks were observed that were used as calibration points. The primary peak was from beam that passed through the target. There was another peak that corresponded to beam that passed through the target frame. Finally there were events where two protons from the beam passed through the target in a double hit scenario and they appeared to the right of the deuteron line in the CsI dE vs E particle identification map demonstrating the discrimination against double hits that this setup provided.

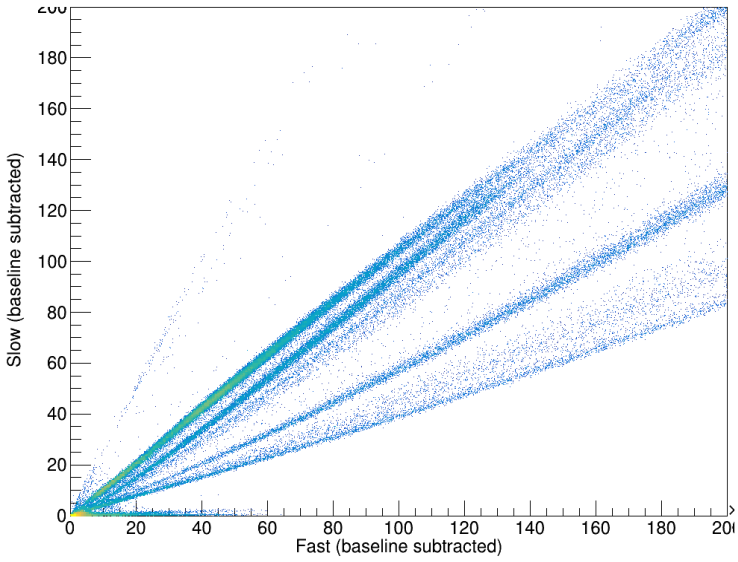

FIG. 2. CsI ΔE Slow vs Fast.

The histogram in Fig. 3 shows the calibrated protons spectrum that was obtained from this experiment. The high threshold is seen because only identified protons that entered the E detector are shown. Since we used only one module of NIMROD, this spectrum is a minimum bias spectrum. The earlier experiment [2] did not have a minimum bias trigger whose spectra are currently accessible. Data from this experiment were separated into bins of centrality with bin 1 being the most peripheral and bin 4 being the most central (violent). We chose proton spectra from bin 2 as having the most representative spectra relating to min bias. The closed circles represent the differential multiplicity proton data from bin 2. The present experiment was normalized at the peak to make the comparison. We observe good agreement in the peak and high energy tail of the experiment indicating that the high energy tails observed in that and other similar experiments do not result from double hit protons.

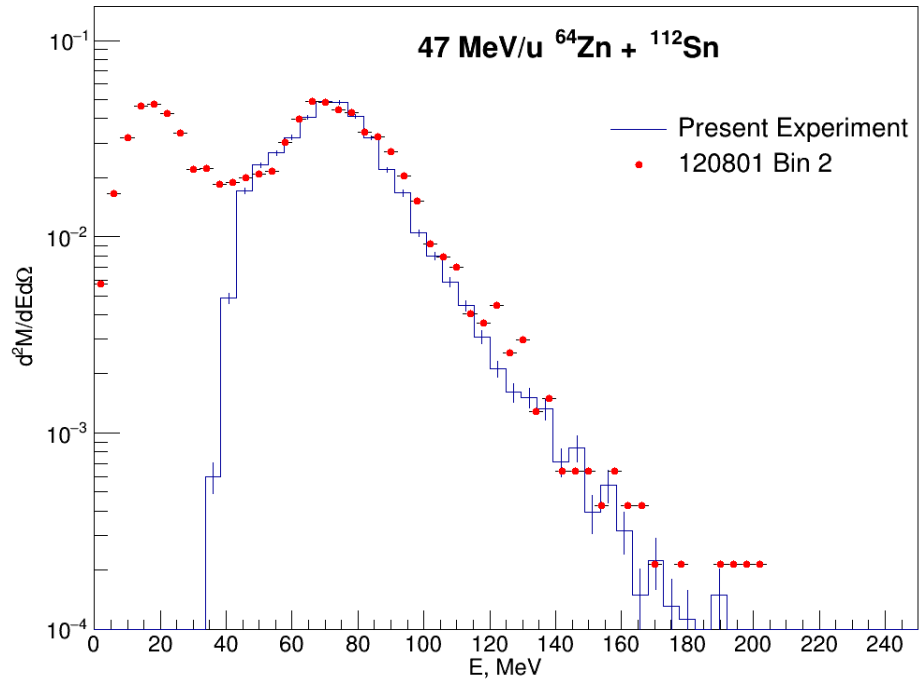

FIG. 3. Blue histogram: NIMROD Ring 2 proton spectrum from the present experiment. Only protons that entered into the E detector are shown resulting in the high threshold due to the 6mm CsI ΔE detector. Red closed circles: NIMROD Ring 2 proton spectrum from the previous experiment [2].

[1] S. Wuenschel *et al*., Nucl. Instrum. Methods Phys. Res. **A604,** 578 (2009).

[2] L. Quin *et al.*, *Progress in Research*, Cyclotron Institute, Texas A&M University (2003-2004), p. II-31.

Preliminary analysis towards ^{55}Fe photon strength function using ^{54}Fe (d, p)^{55}Fe reactions with DAPPER

A. Alvarez, A. B. McIntosh, J. Gauthier, K. Hagel, A. Abbott, M. Sorensen, A. Couture, T. King, S. Ota, S. Pain, S. Regener, A. Richard, and S. J. Yennello

Fall 2023

The Detector Array for Photons, Protons, and Exotic Residues (DAPPER) was assembled for the measurement of ^{55}Fe photon strength function. DAPPER is composed of an annular silicon detector(S3) for capturing protons emitted at backwards angle and 128 barium fluoride scintillators to measure gamma ray energies from the de-excitation of residues [1]. Photons strength functions serve an important role in constraining neutron capture reaction models for advancements in nucleosynthesis, stockpile science, and reactor design. During the DAPPER campaign the experiment was split into two modes, stable beam and radioactive beam mode. Stable beam mode would run DAPPER similar to previous campaigns using a high intensity beam on a deuterated polyethylene (CD2) target for high statistics on the silicon and barium fluoride detectors. Radioactive beam mode would utilize the fast Ionization Chamber (IC) from the GODDESS array while attenuating the beam for an optimal intensity for both the silicon detector and the IC. The attachment of the GODDESS ionization chamber allows for particle identification and the energy of the residues [2].

FIG. 1. A picture of DAPPER assembled during the experiment in stable beam mode.

Spring 2024

Review of the data collected in Fall 2023, the calibration of detectors has begun using an array of sources with known energies for both the silicon and barium fluoride during the experiment. Fig. 2

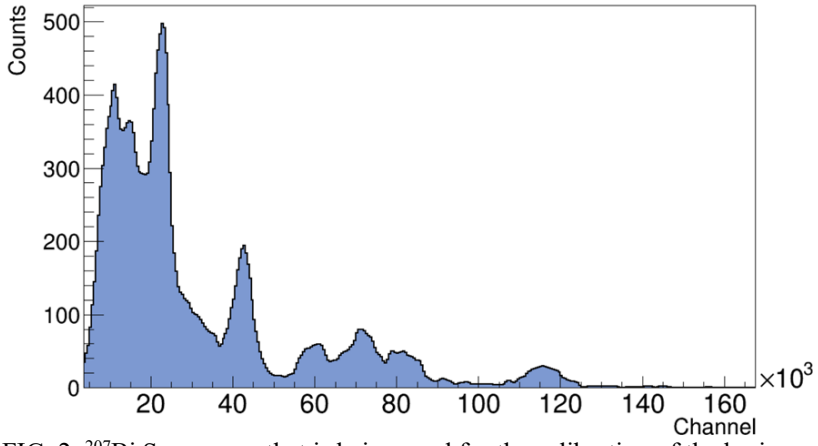

FIG. 2. ^{207}Bi Source run that is being used for the calibration of the barium fluoride detectors.

shows a ^{207}Bi source run for the barium fluoride detectors with the peaks at 20,000 and 40,000 channels, which are known gamma rays, also peaks between 60,000 to 120,000 are known alphas. At the moment there are still corrections needed for both the silicon and the barium fluoride detectors either in gain or calibration. The barium fluoride detectors suffer from gain offsets due to changing temperatures in the surrounding environment, however by using the internal alpha radiation from the radium contaminant, gain corrections can be done as a function of time. The silicon detector calibration was done using an alpha source, but needs slight gain corrections due to heating of pre-amps. Fig. 3 shows excitation energy vs angle calculated using inverse kinematics from the protons detected by the silicon detector for ^{55}Fe, however jags and offsets in the plot show a need for corrections in gain. Fig. 4 from the IC we get waveforms showcasing single and higher order hits close in time. Following the fitting of single hits, the plan is to find suitable

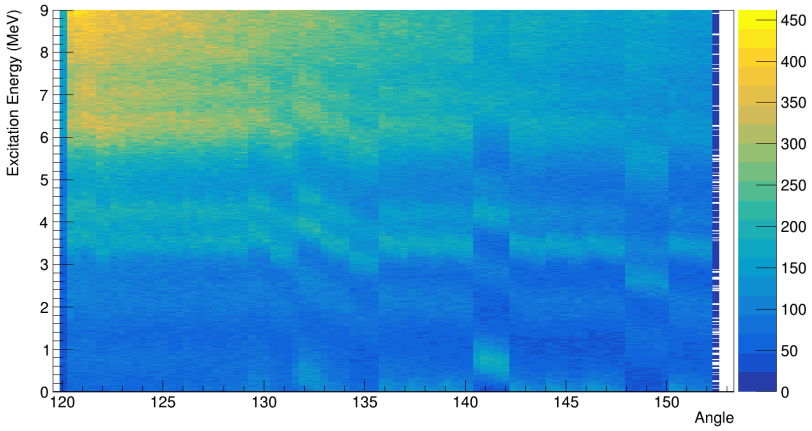

FIG. 3. Excitation energy vs angle for ^{55}Fe from the silicon detector.

methods that can allow for the disentanglement of multi-pulse waveforms. This fitting and disentanglement will allow us to extract the energy of single hits and multi-hits.

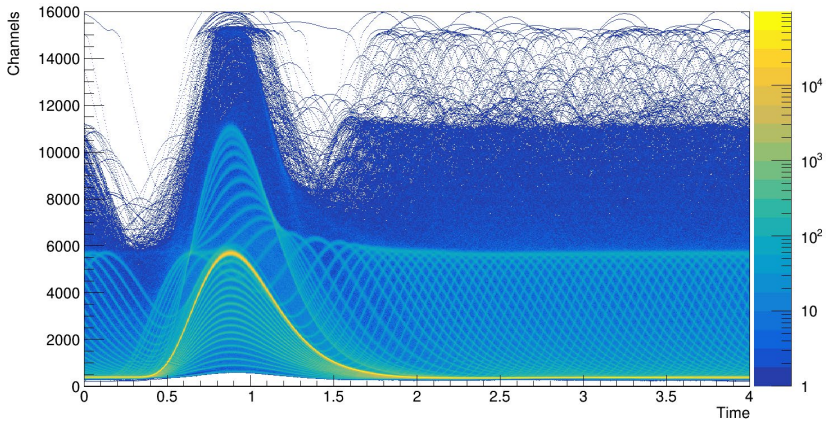

FIG. 4. Waveforms collected by the ionization chamber during the experiment.

[1] S3, https://www.micronsemiconductor.co.uk/product/s3/.

[2] S.D. Pain *et al.*, Physics Procedia **90**, 455 (2017).

The Photon strength function of ^{58}Fe via the inverse Oslo and shape methods

A. Abbott,[1,2] M. Q. Sorensen,[1,2] A. B. McIntosh,[1] A. Alvarez,[1,3] A. Couture,[4]
K. Hagel,[1] J. Gauthier,[1] S. Ota,[5] A. Richards,[6] and S. J. Yennello[1,2,3]
[1]*Cyclotron Institute, Texas A&M University, College Station, TX 77843*
[2]*Department of Chemistry, Texas A&M University, College Station, TX 77843*
[3]*Department of Physics, Texas A&M University, College Station, TX 77843*
[4]*Los Alamos National Laboratory, Los Alamos, NM 87545*
[5]*Brookhaven National Laboratory, Upton, NY 11973*
[6]*Ohio University, Athens, OH 45701*

The photon strength function (PSF) is a statistical property of the nucleus describing gamma-ray emission probabilities and is an essential quantity for calculating neutron-capture cross sections within the Hauser-Feshbach formalism. It has been shown to exhibit a low-energy enhancement (LEE) at low gamma-ray energies for other iron isotopes (^{56,57}Fe) from previous measurements [1,2,3] which could have significant impact in nucleosynthesis [4]. Due to the importance of these reactions for nuclear astrophysics, nuclear waste transmutation, and nuclear energy and the difficulty of direct measurements on short-lived nuclei, the Detector Array for Photons, Protons, and Exotic Residues (DAPPER) [5] was constructed to make measurements of the statistical properties of nuclei using indirect methods. Using the (d,p) reaction in inverse kinematics, the PSF for ^{58}Fe was extracted from particle-gamma coincidence data obtained using an S3 annular silicon detector and 128 BaF_2 scintillators to determine the excitation energy from the emitted proton and the gamma-ray energies, respectively. The Oslo method provides both the PSF and the nuclear level density (NLD) using a normalization procedure [6] while the Shape method provided a functional form of the PSF in a model-independent way [7]. Four separate coincidence matrices are explored: (a) excitation energy versus crystal gamma-ray energies, (b) excitation energy versus cluster gamma-ray energies (Compton add-back routine), (c) excitation energy versus crystal gamma-ray energies in events with total gamma-ray energy collection (total sum gate TSG), and (d) excitation energy versus cluster gamma-ray energies with the TSG.

Following the procedure for the Oslo methods, the raw particle-gamma coincidence data was unfolded [8] using the detector response generated with GEANT4 and then an iterative subtraction procedure was implemented [9] to extract the first-generation gamma-rays. The Oslo method proceeds with a chi-square fit across a statistical region of the primary matrix [6] to obtain functional forms of the NLD and PSF which are then constrained using the known discrete level density, the s-wave neutron level spacing parameter at the neutron separation energy ($D_0(S_n)$) and the average s-wave radiative width at the neutron separation energy ($\langle\Gamma_\gamma\rangle(S_n)$). Two separate statistical regions were explored, both sharing excitation energy cuts from 5.5-9.5 MeV and one with a low gamma-ray energy region at 3.5 MeV and another at 2.0

MeV. Given possible issues originating from over-subtractions resulting from strongly populated states at low excitation energies, the 2 MeV gamma-ray cuts are not discussed further here [10]. Fig. 1 shows the extracted NLDs from the Oslo method; panels (a) and (b) agree well with the known level density for ^{58}Fe and join smoothly with a constant temperature (CT) model interpolation from the calculated level density at the separation energy ($\rho(S_n)$). The data in panels (c) and (d) using the TSG show an over-estimate of the low-energy discrete regions possibly resulting from the preferential selection on low multiplicity events. The total error bands

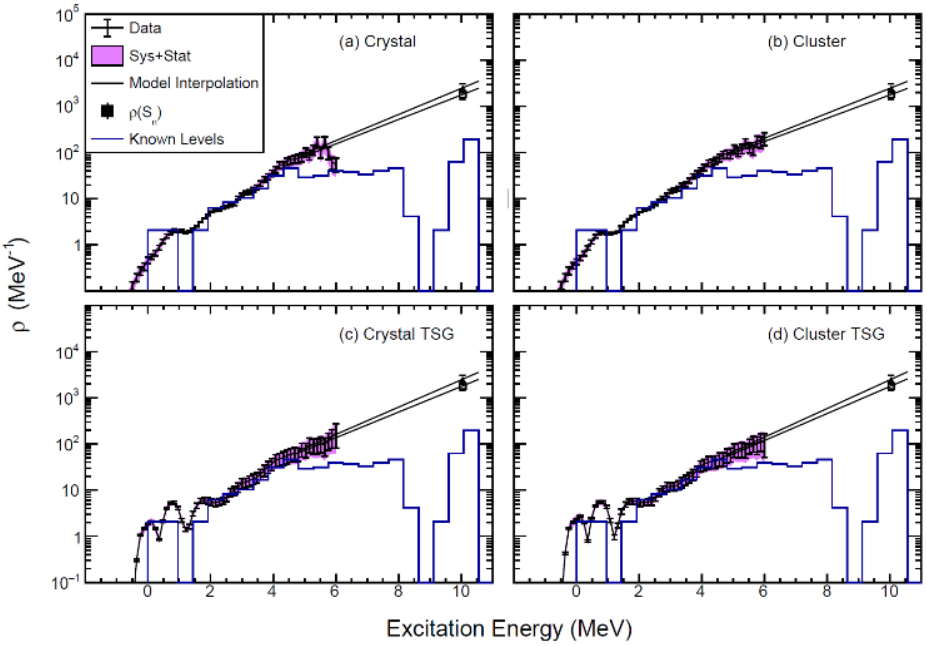

FIG.1. NLDs obtained from the Oslo analysis on each of the coincidence matrices. The known levels are indicated by the binned blue line, the calculated $\rho(S_n)$ by the points, and the CT model interpolation as the thin black line. The two calculated $\rho(S_n)$ are determined using separate models and make up upper and lower bounds.

include systematic errors originating from reported uncertainties in the previously mentioned normalization parameters. The extracted PSF in Fig. 2 panel (a) agrees well with two theoretical predictions (QRPA and SMLO [11]) while panels (b), (c), and (d) appear to possess lower strength at lower gamma-ray energies. This discrepancy could result from uncertainties in the unfolding and primary methods not properly accounting for the impact of the clustering algorithm and the TSG.

The Shape methods proceeds with a selection of two final state populations in the primary matrix, in this case the 810 and 1675 keV first and second excited states. These two states are both 2^+ which simplifies the calculation. The TSG matrices provide clear final state diagonals in the primary matrices and so are the focus of the Shape method analysis. For each excitation energy bin in the statistical region (5.5-

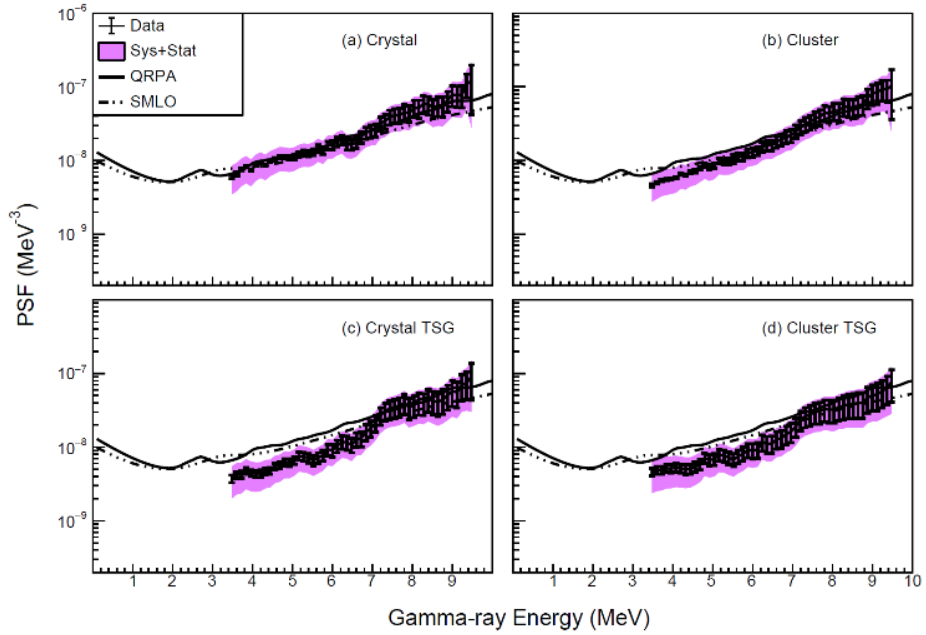

FIG. 2. PSFs obtained from the Oslo analysis for each of the coincidence matrices. The solid and dotted-dashed black lines are two theoretical predictions for the PSF of ^{58}Fe.

9.5 MeV) the strength can be estimated by the yield of primary gamma-rays and an internal normalization provides a functional shape of the PSF for ^{58}Fe. This method requires no constraint to external data. A scaling of the PSF acquired from the Shape method can then be compared to the results from the Oslo method and has been done so in Fig. 3. The agreement is very good with the crystal data, and slightly in

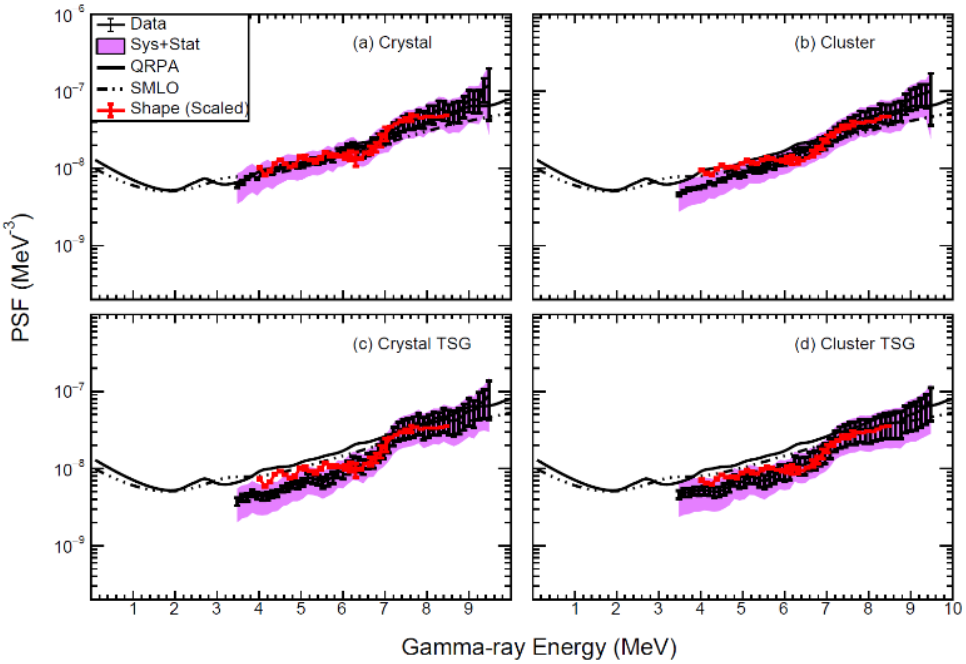

FIG. 3. Same Oslo PSFs from Figure 2, but with the Shape method results added (red points). Very good agreement is achieved in panel (a). Slight low-energy discrepancies for panels (b), (c), and (d) may arise from uncertainties associated with the clustering and TSG

disagreement at lower gamma-ray energies compared to the data in panels (b), (c), and (d) likely for the reasons previously mentioned. Given the good agreement between the crystal data Oslo PSF with the Shape method PSF obtained from a separate matrix, it is then compared to the previously measured Oslo iron data in Fig. 4. The agreement in slope and magnitude is quite good. No LEE is reported in ^{58}Fe in this data set given the presence of strongly populated low-energy excited states.

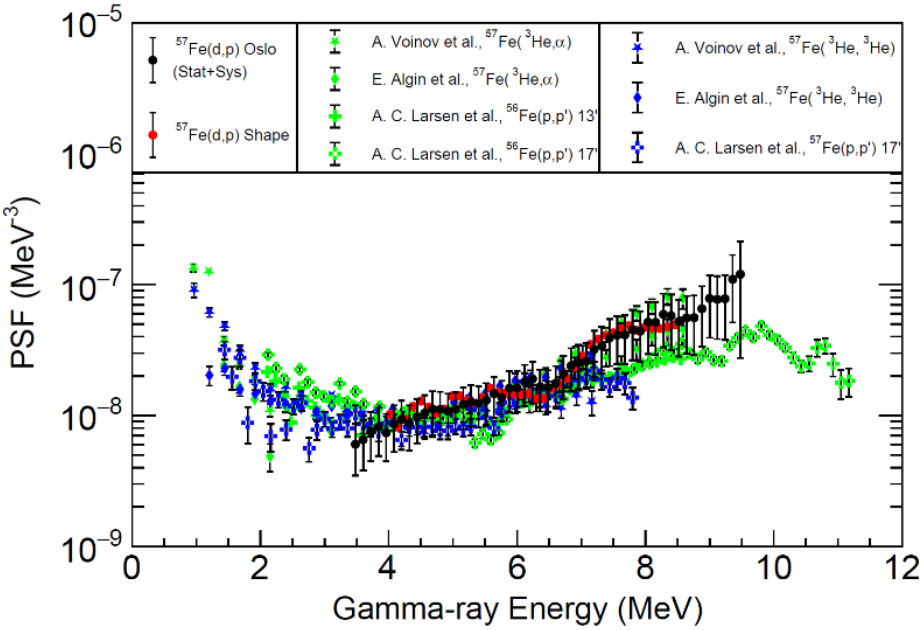

FIG. 4. Crystal results from this data set (black (Oslo) and red (Shape) points) compared to previous Oslo method measurements on 56,57Fe. For the 58Fe data, systematic errors are included. In the previous measurements only statistical errors are reported. Consistent magnitude and slope are obtained, though a LEE is not probed in this work due to the presence of systematic issues (see text).

[1] A. Voinov *et al.*, Phys. Rev. Lett. **93**, 142504 (2004).

[2] E. Algin *et al.*, Phys. Rev. C **78**, 054321 (2008).

[3] A.C. Larsen *et al.*, Phys. Rev. Lett. **111**, 242504 (2013).

[4] A.C. Larsen and S. Goriely, Phys. Rev. C **82**, 014318 (2010).

[5] A.B. McIntosh, M. Sorensen, and A. Abbott, Nucl. Instrum. Methods Phys. Res. A (in preparation).

[6] A Schiller *et al.,* Nucl. Instrum. Methods Phys. Res. **A447**, 498 (2000).

[7] M. Wiedeking, M. Guttormsen, A.C. Larsen, F. Zeiser, A. Görgen, S.N. Liddick, D. Mücher, S. Siem, and A. Spyrou, Phys. Rev. C **104**, 014311 (2021).

[8] M. Guttormsen, T.S Tveter, L Bergholt, F Ingebretsen, and J Rekstad, Nucl. Instrum. Methods Phys. Res. **A374**, 371 (1996).

[9] M. Guttormsen, T. Ramsøy, and J. Rekstad, Nucl. Instrum. Methods Phys. Res. **A255**, 518 (1987).

[10] A. Abbott, PhD Thesis, Texas A&M University, 2024.

[11] S. Goriely *et al.*, Eur. Phys. J. A **55**, 172 (2019).

Updates to NIMROD for low density nuclear matter studies, and new potting method for feedthroughs

N. Shaffett and K. Hagel

A reliable understanding of the nuclear Equation of State (EOS) at various densities and temperatures is a vital component to understanding various nuclear and astrophysical phenomena. In particular, studies of temperatures of several MeV and densities below normal nuclear matter density $n_B^0 \sim 0.15$ fm−3 are necessary in the study of core collapse supernovae [1]. Previous research into this field has been done at Texas A&M using "The Neutron Ion Multi-detector for Reaction Oriented Dynamics" (NIMROD) and upgrades to this array will aid in future research [1,2].

NIMROD is a 4π array of detectors built to study reaction mechanisms in heavy ion reactions [3]. It consists of a 166 segment charged particle array set in a neutron ball. The Array is arranged in 12 rings of Si-CsI telescopes or single CsI detectors arranged concentrically around the beam axis as shown in Fig.1. The CsI detectors are 1-10 cm thick TI doped crystals read by photomultiplier tubes, with a pulse shape discrimination method being employed to identify light particles in the CsI [4]. Previous work with NIMROD to study low density nuclear matter has employed coalescence model methods to extract the source size, and by extinction the density [1,2]. However an alternative method of determining source size is to use correlation functions [5-7]. Extracting correlation functions using NIMROD will require improved position data, leading to the current work of replacing some of NIMROD's quadrant detectors with strip detectors.

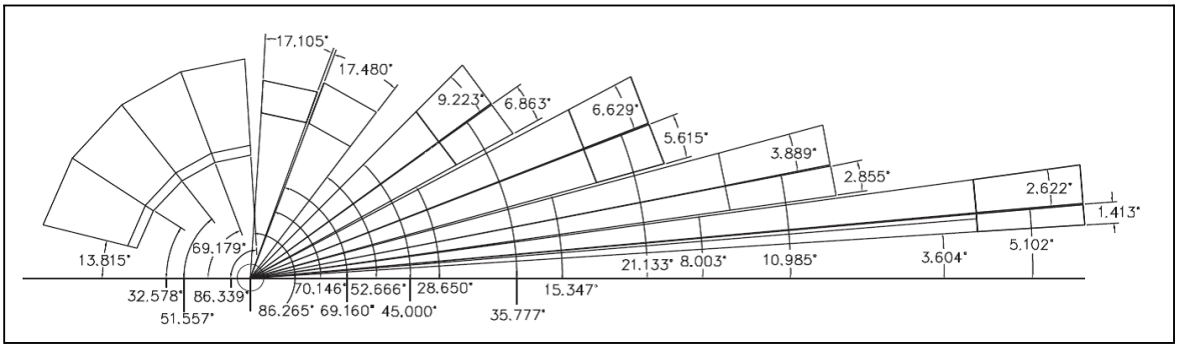

FIG. 1. Angular configuration of the NIMROD detectors.

The current focus is on the modules in ring 8-9 since this angular range highlights the intermediate velocity source while minimizing contributions from secondary decays of projectile like and target like sources [2]. In order to replace the quadrant detectors, which each have 5 signals (4 front and one back), with strip detectors, which each have 17 signals (16 front and one back), the current setup of 13 cables per module will need to be modified to 37 cables per module. Thinner cables and new boards have been ordered for this purpose and assembly is currently beginning. To accommodate these changes the feedthroughs for ring 8-9 need to be replaced. In order to prevent excess leaking in the feedthroughs a new potting method has been tested and will be implemented in the production of the feedthroughs. The method and results of the test will take up the remainder of this report.

Two spare feedthroughs, like the one shown in Fig. 2, were potted by mixing equal amounts of the epoxy resin and hardener and then applying it to the feedthrough using a 5mL syringe. The tip of the syringe was cut off to allow larger beads of epoxy to be applied and tape was used to prevent epoxy getting into the o-ring slots of the feedthrough.

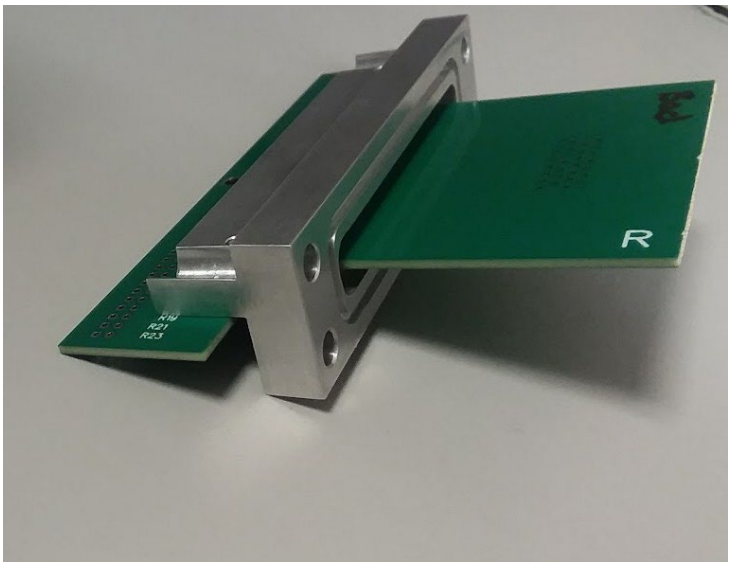

FIG. 2. Feedthrough before potting.

The new aspect of this method was to release any trapped air bubbles in the epoxy by placing it under a vacuum. The feedthroughs were placed in a vacuum chamber and the pressure was dropped so that the epoxy started to expand outwards releasing the trapped air. After letting it sit for a few moments the chamber was brought back up to air and the epoxy settled back into place. Any cavities in the top layer of epoxy caused by the popped bubbles were smoothed out and the feedthrough was left to dry for 36 hours.

FIG. 3. Feedthrough after potting.

After drying, the potted feedthroughs were placed on a small test chamber which was brought down to vacuum. The amount of epoxy needed was slightly overestimated leading to a small overflow preventing a seal from completely forming during leak testing, but this was easily fixed by using a knife to shave off the excess epoxy. An example of a finished feedthrough can be seen in Fig. 3. Overall the new potting method showed decent results and is planned to be applied to the new NIMROD feedthroughs that are being designed.

[1] M. Hempel, K. Hagel, J. Natowitz, G. Röpke, and S. Typel, Phys. Rev. C **91**, 045805 (2015), doi: 10.1103/PhysRevC.91.045805.

[2] L. Qin *et al.*, Phys. Rev. Lett. **108**, 172701 (2012), doi: 10.1103/PhysRevLett.108.172701.

[3] "NIMROD Multipurpose charged particle array at Texas A&M University." Accessed: May 18, 2024. [Online]. Available: https://cyclotron.tamu.edu/nimrod/

[4] S. Wuenschel *et al.*, Nucl. Instrum. Methods Phys. Res. **A604**, 578 (2009), doi: 10.1016/j.nima.2009.03.187.

[5] G. Verde, Braz. J. Phys., **37**, 885 (2007), doi: 10.1590/S0103-97332007000600005.

[6] G. Verde, D. A. Brown, P. Danielewicz, C. K. Gelbke, W. G. Lynch, and M. B. Tsang, Phys. Rev. C, **65**, 054609 (2002), doi: 10.1103/PhysRevC.65.054609.

[7] G. Verde, A. Chbihi, R. Ghetti, and J. Helgesson,Eur. Phys. J. A 30, 81 (2006), doi :10.1140/epja/i2006-10109-6.

Work toward measuring transfer reaction particle correlations to improve stellar models

T. Hankins, A.B. McIntosh, P. Adsley, B.M. Harvey, and S.J. Yennello

The $^{12}C(\alpha,\gamma)^{16}O$ reaction in stellar nucleosynthesis is considered one of the most important aside from the triple-α process as it directly impacts the $^{12}C/^{16}O$ ratio and the properties of stars past helium burning [1]. Even after decades of research, however, the uncertainty associated with the reaction cross section at stellar energies remains large due to difficulties with direct measurements and the presence of two dominant multipolar contributions. Estimation of the cross section via extrapolation is currently the only viable technique which proceeds using models constrained by resonance properties of ^{16}O. As a result, a comprehensive understanding of $^{16}O^*$ as a function of the excitation energy is needed for accuracy.

One of the most significant uncertainties is that associated with the relative contributions of the E1 and E2 transitions for excitation energies near the stellar regime. Conventional measurements of this ratio often make use of the angular correlation technique, in which the two are disentangled by measuring the transition intensity at an angle with respect to the de-exciting residue where the E2 contribution is zero. Generally, the de-exciting residue is measured near zero degrees in the center-of-mass, resulting in cylindrical symmetry for the emission pattern. This simplifies the correlation, which is often necessary for small acceptance instruments, such as spectrometers. With the proper apparatus and reaction, however, a more comprehensive measurement of the correlation can be performed.

Indirect methods, such as the α-transfer technique, are often used to supplement the direct reaction. In the context of this work, (^{7}Li, t) has been investigated. The resulting reaction is a "mirror" of the true (α, γ), and as a result, reaction properties can be extracted similarly. The full process studied is an inverse kinematic α-transfer between ^{12}C and ^{7}Li with coincidence measurements made between the triton, α, and ^{12}C following de-excitation of the $^{16}O^*$.

A test experiment of the aforementioned reaction was conducted at 15 MeV/u with the Forward Array Using Silicon Technology (FAUST) and an added annular S3 silicon detector; the details of this, in addition to preliminary simulations, are given in [2]. A ^{12}C beam was supplied from the TAMU CI K150 cyclotron and impinged upon a ~5 μm metallic Li foil with an intensity such that the highest rate seen by the innermost forward detectors in FAUST averaged 300 Hz; this was maintained for approximately two days. Following the experiment, preliminary calibrations were performed, and the data of interest were extracted using the techniques detailed in [2]; the α-^{12}C relative energy spectrum from this experiment is shown in Fig. 1. In this plot, the relative energies of the α and ^{12}C detected in relevant events were calculated as if originating from a de-exciting $^{16}O^*$. The distribution is largely featureless within statistical error except for the clear excess at $E_{rel.}$ = 3.2 MeV which corresponds to the E* = 10.36 MeV state in ^{16}O.

The original intent of this work was to investigate relative energies less than 3.0 MeV, but as can be seen, the population of these energies is low. To continue the preliminary analysis, attention was turned

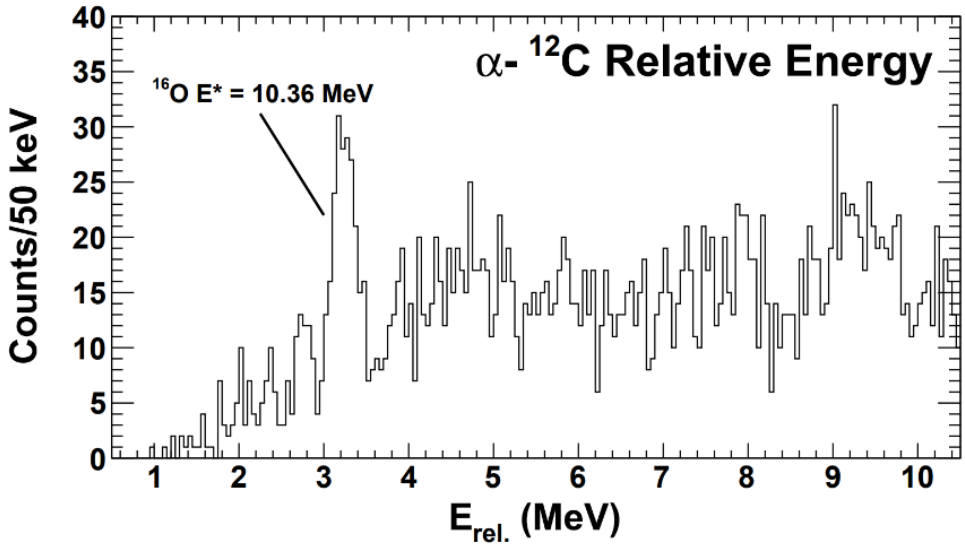

FIG. 1. α-^{12}C relative energy spectrum. The spectrum is largely featureless within statistical uncertainty, except for the excess at $E_{rel.}$ = 3.2 MeV corresponding to the E* = 10.36 MeV state in ^{16}O.

to the E* = 10.36 MeV state. First, with experimental data in hand, estimating yield with a lower beam energy became possible. Using the reaction code FRESCO [3], integrated cross sections for the 10.36 MeV state were calculated using optical model parameters (OMPs) from literature [4]. This information is summarized in Fig. 2a; each red point corresponds to a cross section calculated using OMPs extracted from data at the corresponding beam energy. However, with so few points for a broad span, the cross sections for intermediate energies were also calculated. These are given by the black points, and the lines connecting them to the red points indicate which OMPs were used for the associated calculation. As can be seen, the differing OMPs may yield cross sections differing by as much as a factor of three, but a general trend is clear. Comparing the cross sections for the 10.36 MeV population at 15 MeV/u (~180

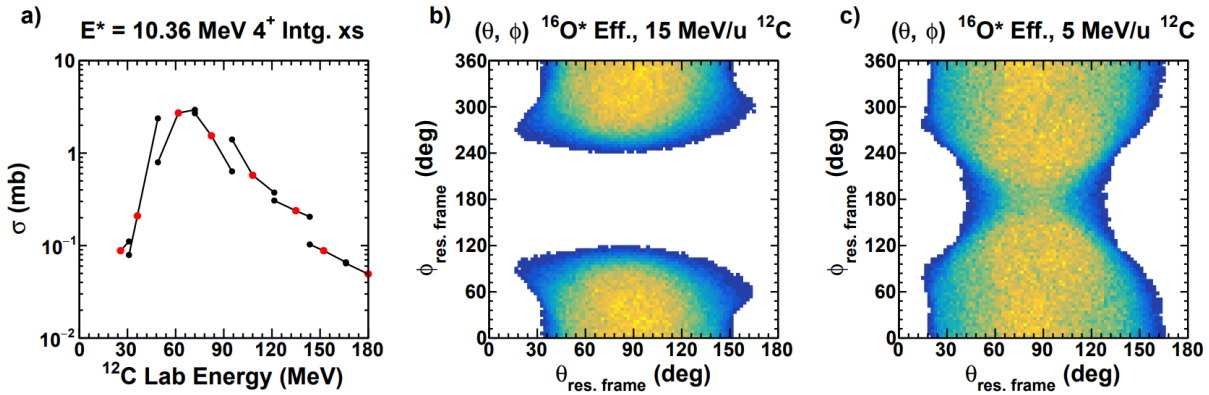

FIG. 2. Summarized simulation results. a) FRESCO integrated cross section calculations for the E* = 10.36 MeV ^{16}O* state as a function of incident ^{12}C beam energy. The Q4 2023 experiment was conducted at 180 MeV. b) (θ, φ) detection map for simulated isotropic decay of ^{16}O* in the frame of the ^{16}O with a ^{12}C beam energy of 15 MeV/u. c) Same as b), but at 5 MeV/u.

MeV TKE) and the maximum (~6.0 MeV/u, ~72 MeV TKE), the optimized yield boost is roughly a factor of 60. This is estimated to increase to about 150-200 once folding in detection efficiency (see below).

Reducing the beam energy leads to two closely related problems. The original energy was chosen such that ^{12}C elastic scatter would punch through the ~300 μm silicon detectors, as stopping in the detector causes significant damage; with a corresponding punchthrough energy of ~11.2 MeV/u, energies near or less than this result in a large amount of stopping. Additionally, reducing the beam energy results in an increase in the elastic scatter cross section at a given lab θ; reducing to the "ideal" energy of 6.0 MeV/u results in a factor of six increase to the cross section. The only solution to mediate this problem, aside from using a different instrument for the measurement, is to transition to thinner silicon detectors. This has been considered as an avenue, although no progress has been made on this front at the time of writing.

To begin preparing to make the final angular correlation measurement, the phase-space simulation originally used for coincidence and yield estimations [2] was configured to include breakup correlations in the frame of the decaying $^{16}O^*$. The simplest configuration, isotropic decay, was first simulated to estimate detection efficiency in preparation for the true measurement. Through this simulation, however, it was discovered that FAUST is kinematically insensitive to a large portion of the α-^{12}C (θ, φ) map at 15 MeV/u; this can be seen in Fig. 2b. This figure shows the detected (θ, φ) map from isotropic decay (source θ ∝ sin(θ), source φ ∝ const.) of the $^{16}O^*$; FAUST is insensitive for decays near φ = 180°. This corresponds to in-plane or near-in plane emission of the α toward the beam axis, often missing FAUST acceptance. The detection efficiency improves with decreasing beam energy, however, as the magnitude of the Lorentz boost becomes smaller, and the transverse "pop" becomes relatively larger. To illustrate, the (θ, φ) map for isotropic decay at 5 MeV/u is also provided in Fig. 2c. In this regime, FAUST becomes sensitive for decays near φ = 180°, as the relative energy "kick" for in-plane emissions is now proportionally large enough to send the particle to the other side of the array for detection.

Based on the results of the (θ, φ) simulations detailed in Fig. 2, it is hypothesized that the lower energy states that were not populated in Fig. 1 were simply kinematically inaccessible at 15 MeV/u but might become measurable at lower energies. Follow-up simulations to confirm this are to be performed in the near future. It is important to note that losing sensitivity to the full (θ, φ) is not entirely problematic; preliminary simulations extracting a sample density matrix using only the sensitive region corresponding to Fig. 2c were successful with as little as 25,000 entries. However, having the intermediate region is critical; a sensitivity map analogous to Fig. 2b is insufficient for extraction of the matrix elements.

Due to the beam energy and yield requirements, alternate reaction mechanisms for probing this with FAUST are being investigated. Alternate α-transfer candidates, as well as inelastic excitation mechanisms have been considered, but nothing has been definitively decided at the time of writing.

[1] M. Fey, *et al.* Nucl. Phys. **A718**, 131 (2003).
[2] T. Hankins, *et al.*, *Progress in Research*, Cyclotron Institute, Texas A&M University (2022-2023) p. II-13.
[3] I.J. Thompson, Comput. Phys. Rep. C **7**, 167 (1988), http://www.fresco.org.uk.
[4] J. Cook, At. Data Nucl. Data Tables **26**, 1 (1981).

Demonstration of zero-degree axial field ionization counter for measuring heavy residues for use with DAPPER

A.B. McIntosh and S.D. Pain[1]
[1]*Oak Ridge National Laboratory, Oak Ridge, Tennessee 37830*

The Detector Array for Photons, Protons, and Exotic Residues (DAPPER) has been commissioned and used to measure reactions of ^{57}Fe(d,pγ)^{58}Fe @ 7.5 MeV/u which is calibrated, analyzed to extract the photon strength function and level density; the results are in preparation for publishing.

In preparation for use of DAPPER with rare isotope beams, a zero-degree detector is needed to separate, event by event, reactions with the beam species of interest from reactions with contaminants in the beam. In the past, we have investigated PPACs, diamond detectors, and YAP scintillators with no detector passing all of our qualifications. Sufficient energy (or timing) resolution is needed to distinguish adjacent elements in the Fe/Co region even at rates of at least 300,000 particles per second.

In collaboration with S. Pain of ORNL and colleagues, we have tested a fast axial-field segmented IC with a cocktail beam of Fe and Co at 7.5 MeV/u. This is the current IC used with the GODDESS array. There are grids of thin 0.0007" wires of gold-plated tungsten. The distances between the grids is about 0.5". Each grid has a wire spacing of 2mm, giving 99% transmission through each grid, and the wires in each grids are designed to shadow the wires in successive grids to maximize transmission. The grids alternate in potential; electrons and ion have little distance to travel before being collected. All cathode grids wires from all planes are electrically tied to provide a single signal proportional to the total energy. The first anode grid treats individual wires separately to provide position sensitivity; the second anode grid provides position sensitivity in the orthogonal direction. The subsequent seven anode grids can be tied together into up to three groups by jumpers on the preamp board to provide energy loss measurements. All signals are amplified with Zeptosystems charge sensitive amplifiers with the highest gain (nominally 15 mV/MeV), and with the feedback resistor modified to half its value to decrease the output signal fall time. The CSA output are sent to MSCF shaping amplifiers with minimal shaping time (0.25us) and low gain on the input stage amplifier (higher gain on the input stage saturates the current buffer at a lower rate and temporarily disables the buffer while baseline is restored). The short shaping time causes the amplifier to run in ballistic deficit, but the modest loss in energy resolution is tolerated in exchange for the ability to run to high rate. Pressure of just over 100 Torr isobutane was used to stop the beam comfortably before the end of the IC. The gas in the IC is static, not flowing, allowing for a constant gas mass, minimizing change in IC stopping power with temperature. The Anode 0 channel was selected to include the first four anode planes to select energy loss before the Bragg peak to maximize Fe/Co discrimination.

Fig. 1 shows the yield vs Anode 0 vs Cathode signal for moderately high rate (~70,000 pps as measured with an LED on the fast output of the shaper). The two most intense spots correspond to the Fe (lower anode amplitude) and Co (higher). These are well separated at this rate, and good separation is observed even at a measured beam rate of 600,000 pps. In fact, it is certain this rate is under-counting the actual beam rate due to pile up in the shaper pulse; this may be as bad as a factor of two or three. It is

likely possible to correlate the observed change in the leakage current in the IC bias supply to determine the beam rate, though the resolution of this method is not firmly established. Other features of Fig. 1 are due to stopping in the wires (spots left and diagonal down from the main peaks) energy loss in the wires (continuum line toward lower energy) and pile-up pulses corresponding to double hits in the IC. The proportion of double hits naturally increased as a function of beam intensity.

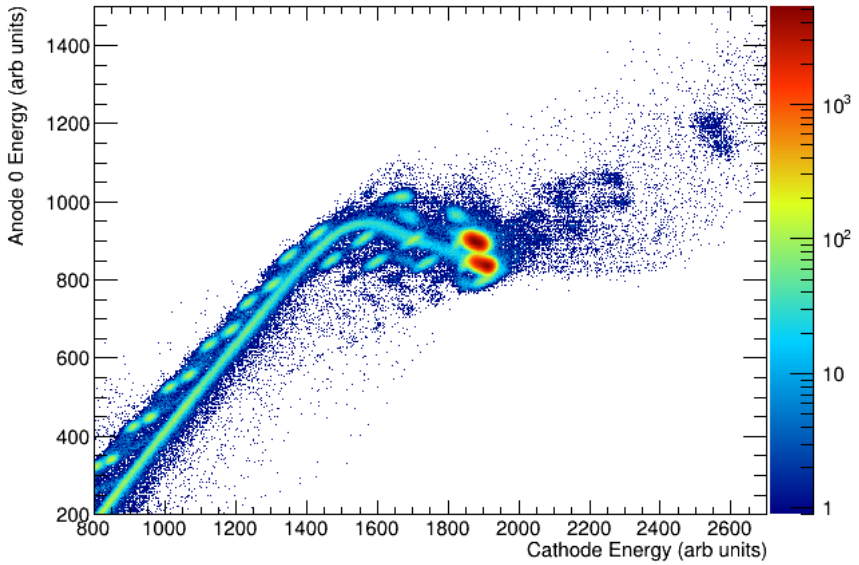

FIG. 1. Energy loss vs total energy observed for Fe/Co cocktail at a rate of 70kpps, run 186, October 2023, (102723).

Deconvolution of the pileup pulses may be possible through preservation of the waveform of the shaper pulse. Following this demonstration in October, the physics run in December included measurement of the waveforms from the IC for products from ^{54}Fe(d,pγ)^{55}Fe. The pileup from particles in discrete beam bursts is clear, and work is ongoing to disentangle the pulse amplitudes.

Toward understanding relativistic heavy-ion collisions with the STAR detector at RHIC

S. Mioduszewski, N. Sahoo, J. Tyler, and the STAR Collaboration

High-energy heavy-ion collisions produced at RHIC produce a dense partonic matter called quark gluon plasma (QPG). The goal of this project is to study the properties of this material by comparing per-trigger yields of recoil jets produced in Au+Au and p+p collisions. Two papers were recently submitted to Physical Review Letters and Physical Review C [1,2], respectively. A third paper on medium-induced acoplanarity of recoil jets in central Au+Au collisions is in preparation to be submitted to Physical Review Letters. In these papers, the recoil jets were reconstructed with charged particles only and are referred to as "charged jets". Current efforts are ongoing to reconstruct the "full jets", which include the neutral energy as well.

In a γ-jet event, the trigger provides a calibrated baseline for the total energy of the jet particles on the recoil side of the trigger (opposite azimuth). The inclusion of the Barrel Electromagnetic Calorimeter (BEMC) provides a more accurate measurement of the total energy of jet particles on the recoil side of the event. The BEMC covers an area of $|\eta| < 1$ and full azimuth. It uses lead-scintillator towers to capture electromagnetic showers of up to 60 GeV [3]. The inclusion of an additional detector in the jet reconstruction requires additional quality assurance work, checking for hot towers and additional bad runs. In this analysis, a tower is considered hot if it registers a hit frequency greater than 5 standard deviations away from the average in set energy ranges for a given dataset. After the hot-tower check, 97% of the detector had valid towers in the dataset we intend to analyze.

The Run-9 dataset in p+p collisions and its corresponding embedding was used as a test of our method of unfolding jet spectra. Full-jet reconstruction was performed using the anti-k_T algorithm from the Fastjet package [4]. In this analysis, charged tracks with transverse momentum p_T between 0.2 and 30 GeV/c, as well as BEMC towers with transverse energy E_T above 0.2 GeV are considered as constituents. A fiducial cut is made on the pseudorapidity of the jet axis, $|\eta_{\text{jet}}| < (1 - R_{\text{jet}})$, where R_{jet} is the jet resolution parameter associated with the radial size of the jet. Two values of jet resolution parameter are considered, R_{jet} =0.2 and R_{jet} =0.5. Fig. 1 shows a comparison of the (raw) charged vs. full jet p_T spectrum on the recoil side of a p^0 trigger with E_T=9-11 GeV, before unfolding.

The Run-9 embedding sample is composed of PYTHIA di-jet events embedded into zero-bias p+p data. Jets were reconstructed as in data, for both simulated (PYTHIA) and detector-level (where the detector response is from a full GEANT simulation) events. Jets at the PYTHIA level are matched to jets at the detector level by requiring their centroids be within a certain distance in $\eta - \varphi$ space. This distance is 0.1 for a jet radius of 0.2 and 0.2 for a jet radius of 0.5. The response matrix for full jets with a π^0 trigger with E_T= 9-11 GeV, with a match closest in $\eta - \varphi$ space are shown in Fig. 2. PYTHIA jets which did not have a corresponding match at the detector level were considered an inefficiency, a correction applied after unfolding the jet p_T spectrum.

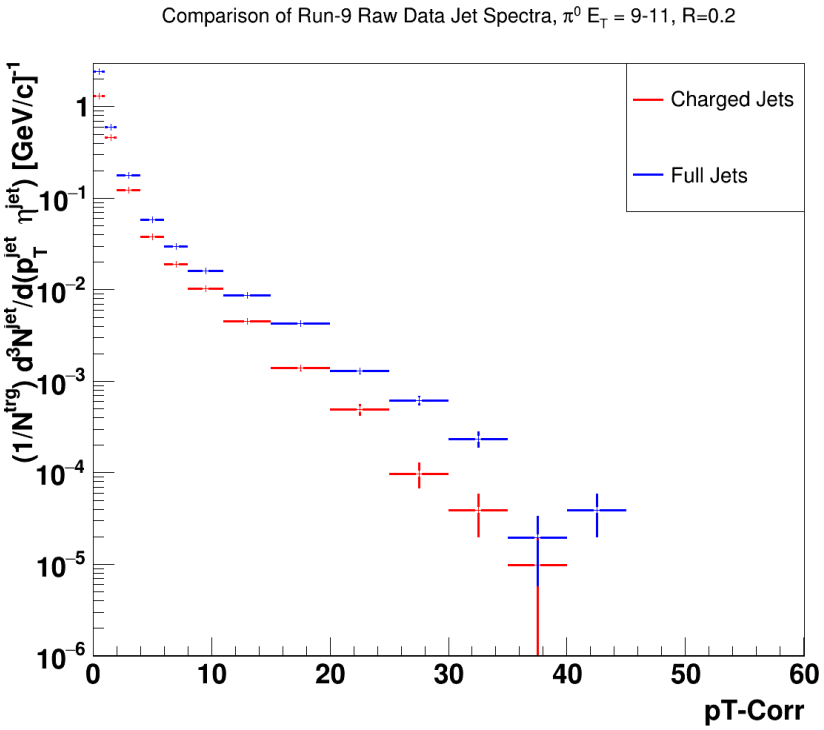

FIG.1. The semi inclusive jet p_T spectrum, on the recoil side of a π^0 trigger with E_T between 9 and 11 GeV, for full vs. charged jets. The jet resolution parameter is 0.2.

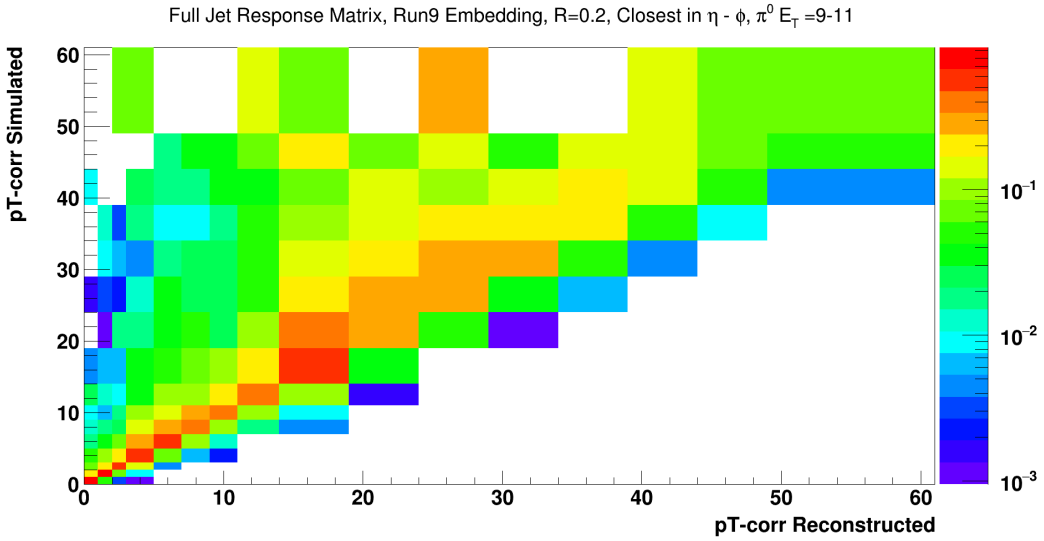

FIG. 2. The Run-9 embedding response matrix for full jets, on the recoil side of a π^0 trigger with E_T between 9 and 11 GeV. The jet resolution parameter 0.2. The matches closest in $\eta - \varphi$ space are selected.

The unfolding was handled by RooUnfold, a framework for deconvoluting particle physics data [5]. The iterative "bayesian" unfolding method was utilized. To test the closure of this method, the

embedding was separated into two subsamples. The response matrix and efficiency were generated from the first subsample as described above. The reconstructed spectrum was generated from the second subsample and was then unfolded using the first subsample's response matrix and efficiency. Fig. 3 shows a comparison of the reconstructed spectrum, simulated spectrum, and unfolded spectrum in this so-called "closure test". The closure test indicates that this method provides closure for a range of $6 < p_{T,jet} < 35$ GeV/c. Closure means that the corrected detector-level spectrum agrees with the original PYTHIA-level spectrum, which validates the unfolding procedure.

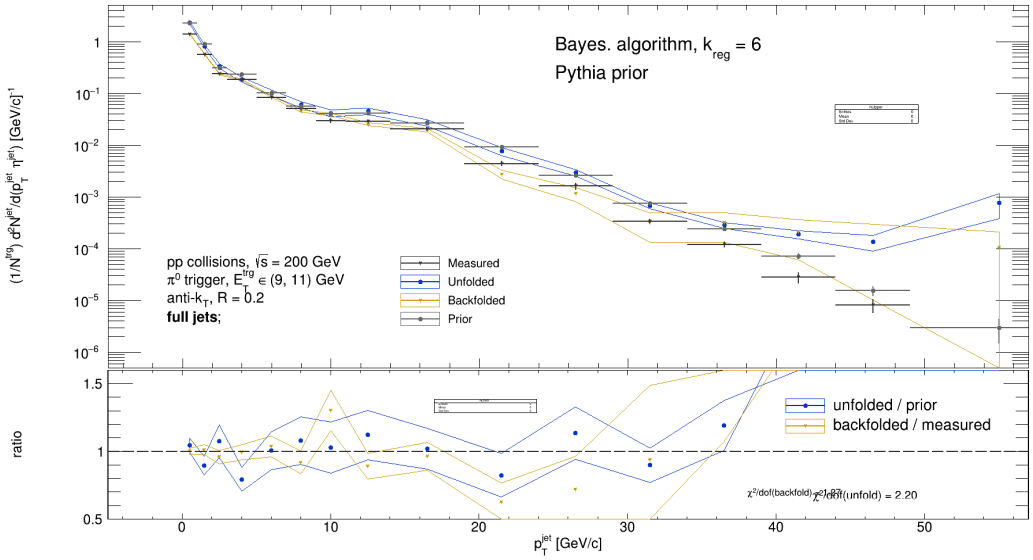

FIG. 3. "Closure Test", as described in the text. The denominator shows the ratio of the corrected spectrum (labeled as "unfolded") to the original PYTHIA spectrum (labeled as "prior"). The ratio being consistent with 1 shows that closure is achieved.

[1] STAR Collaboration. (2023). arXiv:2309.00156

[2] STAR Collaboration. (2023). arXiv:2309.00145.

[3] STAR Collaboration (2003). Nucl. Instrum. Methods Phys. Res. **A499(2-3)**, 725 (2003).

[4] M. Cacciari and G. Salam, Phys. Lett. B **641**, 57 (2006); M. Cacciari, G. Salam and G. Soyez, J. High Energy Phys. **0804** 005 (2008), http://fastjet.fr.

[5] T. Adye, arXiv:1105.1160 (2011).

Revisit to experimental search for high-spin isomers in inverse collisions of ^{28}Si+^{12}C at 35 MeV/nucleon using FAUST array

R. Wada, A. McIntosh, K. Hagel, J. B. Natowitz and FAUST collaboration

In our previous work of Ref. [1], we reported three possible candidates with estimated cross sections of 30-50μb for toroidal high-spin isomer states at high excitation energies in ^{28}Si in the 7α decay channel, using inverse kinematic collisions of ^{28}Si+^{12}C at 35 MeV/nucleon with the NIMROD 4π array.

To verify the results with higher energy resolution and better statistics, the same reaction was studied with the upgraded FAUST array. As reported in Ref.[2], no strong evidence wes observed for such resonances above the 20μb range and precluded smaller peaks as statistical fluctuations. In the 1μb range, however, strong correlations are observed among peaks in the excitation energy distribution of the subsets of 7α events. In Fig.1, the deviation from the average yield and their standard deviations are

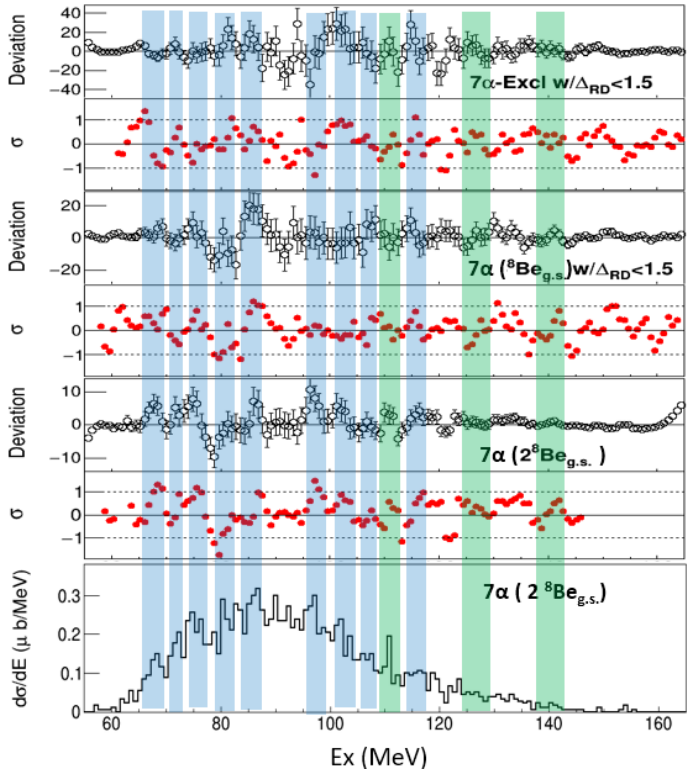

FIG. 1. Candidate resonance peaks. (Top 6) Each two figures from the top shows the deviation from the averaged excitation energy distribution and their statistical standard deviation values (top 2) for exclusive 7α events under a condition of Δ_{RD}<1.5, where events decaying through any cluster formation are excluded, (middle 2) for 7α events decaying through one ^{8}Be(gs) under a condition of Δ_{RD}<1.5, (bottom 2) for 7α events decaying through two-^{8}Be(gs). (Bottom) The excitation energy distribution of 7α events decaying through two-^{8}Be(gs). Blue bars indicates the location of the resonance peaks assigned in this work and green indicates those from Ref.[1]. For a description of the method of calculating the deviations and their standardization, see Ref. [2].

shown for the 7α sub-event sets with a condition of $\Delta_{RD} \leq 1.5$, with decaying trough ^{8}Be(gs) + $\Delta_{RD} \leq 1.5$, and with two ^{8}Be(gs). $\Delta_{RD} \leq 1.5$ condition is set to select events with larger angular momentum. Δ_{RD} is the distance from the rod-disk line in a sphericity-coplanarity plot. As one can see, many peaks are correlated each other at a given excitation energy. Note that events in all three sub-event sets are exclusive from each other.

Utilizing a shape analysis method [3], simulated event sets are generated in two steps to characterize these candidate resonance peaks, focusing on their physical shapes and angular momentum. In the first step, different shapes of 7α initial nuclei are generated using EQMD [4]. More than 5M ^{28}Si 7α initial nuclei are generated. Fluctuation in their cooling process generates different shapes. In order to determine their physical shape, a shape analysis method in their coordinate space is utilized. About 80% of the generated initial nuclei have a disk shape. 15% are categorized as spherical. 1% are in a rod shape. The nuclei with a toroidal shape are made from the disk shape nuclei, by excluding nuclei which has α (or αs) within a radius of 1.5fm from the Z axis (XY is the disk plane). Similarly, tube-shaped nuclei (non-linear chain) are made from the rod-shape nuclei excluding those with α(s) within a distance 1.5fm from the Z-axis. Less than a few % remains in the latter two treatments. All shapes are made symmetric around the Z-axis.

The second step is to give kinetic energy to α's in the simulated event set with a given shape at a given excitation energy. Note that α's in the initial nuclei made by EQMD do not have any kinetic energy. For a resonance at the excitation energy E_x, the available energy for the kinetic energy is given by $E_{av} = E_x - Q$. This kinetic energy is divided into two parts, thermal energy and rotational energy. They are distributed among 7α's in two steps.

(1) Thermal energy E_{th} for simulated event sets is set from 1 MeV to E_{av} in every 1 MeV energy step. For each E_{th}, the rotation energy E_{rot} is given by $E_{rot} = E_{av} - E_{th}$. To add the kinetic energy to 7α, their momentum increases gradually using random vector in a small step (0.1 MeV/c) till the thermal energy of 7α reaches to E_{th}. In order to make a clear separation between the thermal and rotation energies, the total angular momentum L is required $|L| < 2$ at the end of this procedure.

(2) Rotational energy is given by rotating the whole 7α system around the Z axis, adjusting L_z to get E_{rot}. For a given E_{rot}, L_z becomes different for different shapes, since their moments of inertia are different.

Each set of the simulated events is compared to the events under a candidate peak to determine their shape and L_z one by one. Three observables are used for this purpose, α kinetic energy E_α, distance Δ_{RD} from the rod-disk line and distance from disk-sphere line Δ_{DS} from the momentum shape analysis. Δ_{RD} is closely related to L_z. Smaller Δ_{RD} corresponds to larger L_z . Δ_{DS} relates to the shape. Spherical shapes show smaller values and rod shape gives larger values. The shape and L_z from the simulated data set at the best χ^2 fit are assigned to each candidate resonance peak.

In Fig.2 an example of the χ^2 fit is shown for the candidate resonance at Ex=87.5 MeV. Here a tube shape is used instead of rod, which results a better fit than that of a rod in all cases. On the left, the fit results at the minimum χ^2 value are shown. E_α, Δ_{RD}, Δ_{DS} and L_z spectra are plotted from left to right and those for sphere, disk, tube and toroid are plotted from the top to the bottom. On the right, χ^2 values are plotted as a function of E_{th}. In this example the preference of the tube shape is observed. Note that

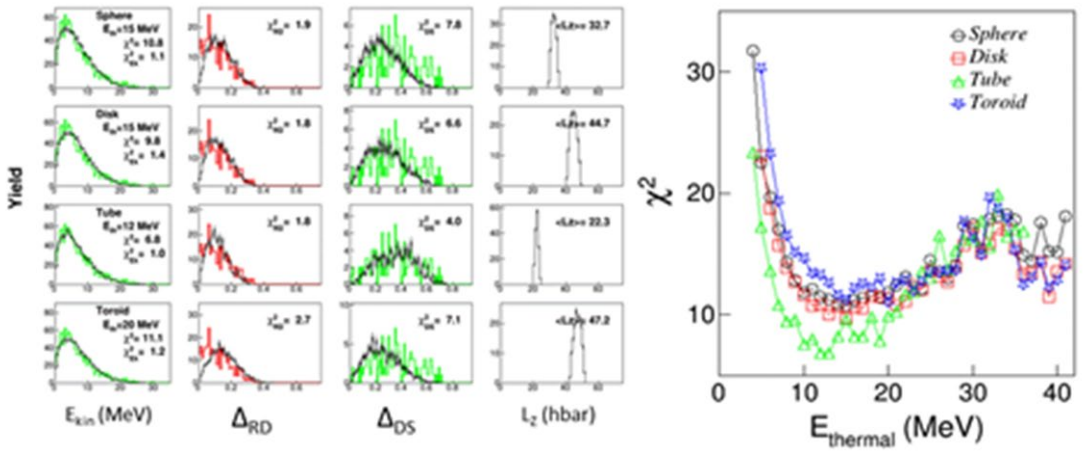

FIG. 2. An example of the χ2 fit for the candidate resonance at 87.5 MeV. (left) Colored spectra are from the experiment and black ones from the simulation. $\chi 2 = \chi 2_{Ek} + \chi 2_{\Delta RD} + \chi 2_{\Delta DS}$. <Lz> is the extracted average angular momentum. (right) χ2 value distribution as a function of Eth for different shapes.

this preference mainly originates from the shape of Δ_{DS} in the third column. The best χ^2 fit search is made for all candidate peaks. For the first four candidate peaks from the lowest up to 85.5 MeV, no preference for the shape is observed, indicating their angular momentum is small (L_z<20). In such cases the momenta are distributed randomly, resulting a distribution around the center in the momentum shape independent of the shapes. However those at higher excitation energy at E_x > 87.5 MeV, similar preferences of the tube shape are observed and L_z value is determined for each candidate resonant peak. This fact is consistent with the possibility that the candidate resonances are high-spin isomer states. They are summarized in Fig.3. The extracted L_z values show a good agreement with those of the theoretically

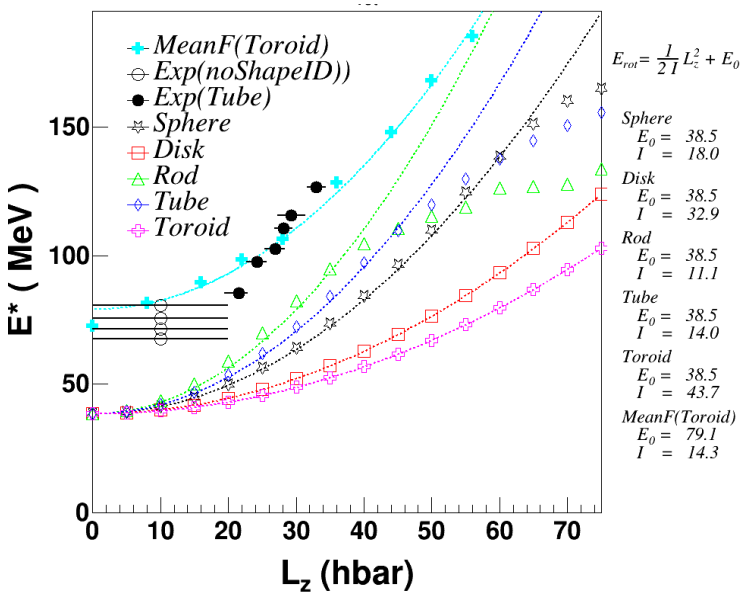

FIG. 3. Summary plot. Experimentally determined resonances are shown by open and closed circles. Open circles represent those with no shape assignment and tentatively L_z < 20 is given. Closed circles represent the preference of a tube shape with extracted L_z value. Light blue symbols are results from the mean filed calculation of Ref.[5]. Other symbols are yrast line for each given shape. Fit function E_{gs} and the moments of inertia are listed on the right.

predicted by Ren et al. in their mean field calculation [5], although their calculations are made for toroidal shapes, not for tube shapes.

[1] X.G. Cao *et al.*, Phys. Rev. C **99**, 014606 (2019).
[2] A. Hannaman *et al.*, Phys. Rev. C **109**, 054615 (2024).
[3] J.P. Bondorf *et al.*, Phys. Lett. B **240**, 28 (1990).
[4] T. Maruyama *et al.*, Phys. Rev. C **53**, 297 (1996).
[5] Z. X. Ren *et al.*, Nucl. Phys. **A996**, 121696 (2020).

SECTION III

NUCLEAR THEORY

An imaginary-time study of carbon burning in stellar conditions

T. Depastas, S.T. Sun, H. Zheng and A. Bonasera

The carbon burning reaction is a fundamental step of stellar evolution and involves the depletion and production of chemical elements important for the formation of life. In this work [1], we use the molecular dynamics Hybrid α-Cluster (HαC) [2] approach, as well as an analytical theory, to study the $^{12}C+^{12}C$ fusion towards zero energy. The calculation of the sub-barrier cross section is performed in the framework of the imaginary time method (ITM) [3], which is based on the Feynman Path Integrals.

We obtain the values of the cross sections and astrophysical S*-factors, which we correlate to collective motion of the monopole and dipole type. We additionally include a calculation for the reaction with a carbon in its 2^+ state above the threshold and discuss a possible experimental investigation. Our results confirm direct experimental and theoretical results close to the barrier and suggest possible 2^+ mixtures in the indirect experimental data [4]. Our study offers an accurate view of the burning process in the somewhat unexplored low energy region.

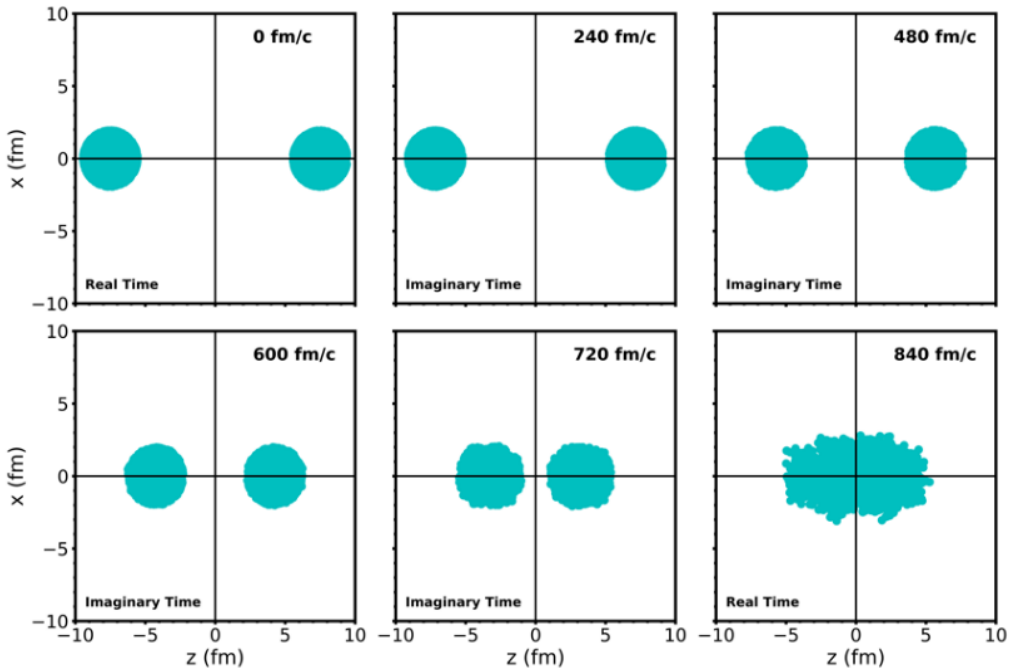

FIG. 1. (Color online) Evolution of the 12C+12C fusion in the xz plane with EC.M. = 3.5 MeV. The cyan points are the densities of the alpha particles from 300 event calculations with the HαC model, while the reaction axis is defined to be the z-axis.

[1] T. Depastas, S.T. Sun, H. Zheng and A. Bonasera, Phys Rev C **108**, 035806 (2023).

[2] H. Zheng and A. Bonasera, Symmetry **13**, 1777 (2021).

[3] A. Bonasera and V. Kondratyev, Phys. Lett. B **339**, 207 (1994).

[4] A. Tumino *et al.*, Nature (London) **557**, 687 (2018).

Pseudo-rapidity distributions of charged particles in asymmetric collisions using Tsallis thermodynamics

J.Q. Tao,[1] H.B. He,[2] H. Zheng,[2] W.C. Zhang,[2] X.Q. Liu,[3] L.L. Zhu,[4] and A. Bonasera

[1]*Key Laboratory of Quark & Lepton Physics (MOE) and Institute of Particle Physics, Central China Normal University, Wuhan 430079, China*

[2]*School of Physics and Information Technology, Shaanxi Normal University, Xi'an 710119, China*

[3]*Institute of Nuclear Science and Technology, Sichuan University, Chengdu 610064, China*

[4]*Department of Physics, Sichuan University, Chengdu 610064, China*

The pseudo-rapidity distributions of the charged particles produced in the asymmetric collision systems p+Al, p+Au and ^{3}He+Au at $\sqrt{s_{NN}}$ = 200 GeV are evaluated in the framework of a fireball model with Tsallis thermodynamics [1]. The fireball model assumes that the experimentally measured particles are produced by fireballs following the Tsallis distribution and it can effectively describe the experimental data, e.g., see Fig. 1. Our results as well as previous results for d+Au collisions at $\sqrt{s_{NN}}$= 200 GeV and p+Pb collisions at $\sqrt{s_{NN}}$=5.02 TeV validate that the fireball model based on Tsallis thermodynamics can provide a universal framework for pseudo-rapidity distribution of the charged particles produced in

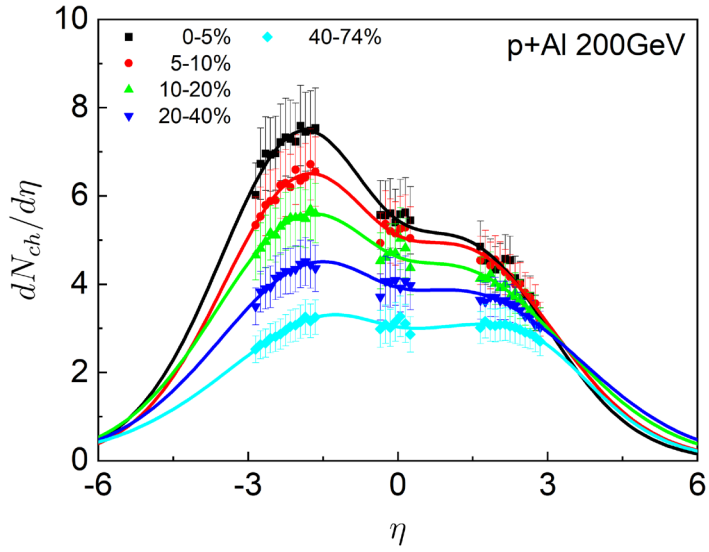

FIG. 1. (Color online) The pseudo-rapidity distributions of the charged particles produced in p+Al collisions at $\sqrt{s_{NN}}$= 200 GeV for different centralities. The symbols are experimental data taken from [2]. The curves are the results from the fireball model with Tsallis thermodynamics.

asymmetric collision systems. We predict the centrality dependence of the total charged particle multiplicity in the p+Al, p+Au, and ^{3}He+Au collisions. Additionally, the dependences of the fireball model parameters (y_{0a}, $y_{\_0A}$, σ_a and σ_A) on the centrality and system size are studied, e.g., see Fig. 2.

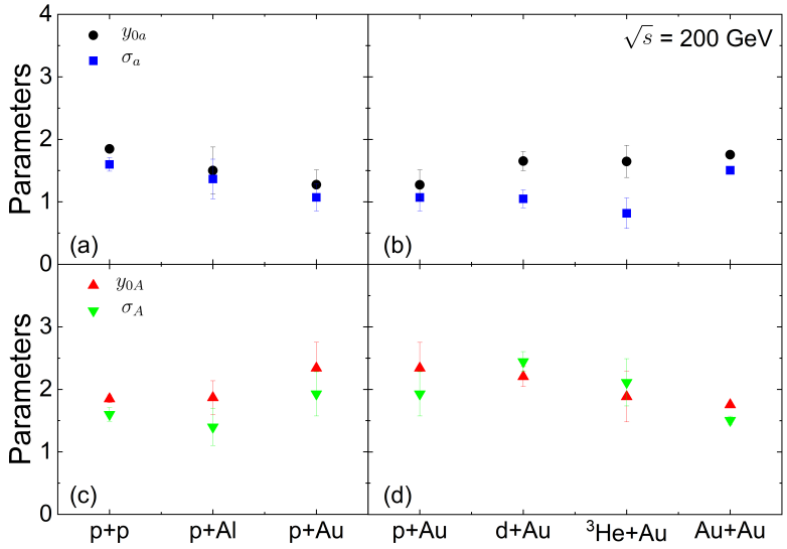

FIG. 2. (Color online) Collision system size dependence of model parameters y_{0a}, $y_{\_0A}$, σ_a and σ_A for p+p, p+Al (0-5%), p+Au (0-5%), d+Au (0-20%), ^{3}He+Au (0-5%) and Au+Au (0-6%) collisions at $\sqrt{s_{NN}}$=200 GeV.

[1] J.Q. Tao, H.B. He, H. Zheng, W.C. Zhang, X.Q. Liu, L.L. Zhu and A. Bonasera, Nucl. Sci. Tech. **34**, 172 (2023).

[2] A. Adare, C. Aidala, N.N. Ajitanand *et al.* (PHENIX Collaboration), Phys. Rev. Lett. **121**, 222301 (2018).

Revisiting the 3α reaction rates in helium burning stars

T. Depastas, S.T. Sun, H.B. He, H. Zheng and A. Bonasera

Helium burning is one of the most fundamental steps of stellar nucleosynthesis, as it describes the formation of the life-determining element of carbon, while it plays a key role in the evolution of Red Giant, accreting White Dwarfs and Neutron Stars. In this work [5], we develop a generalized statistical theory for the 3α reaction, which is based on the use of the Imaginary Time Method [3], along with the semi-classical Hybrid α-Clustering (HαC) [2] and Neck Model (NM) [6] frameworks. The results are compared to the methodology and data of the NACRE collaboration [7], following in several orders of magnitude discrepancies, especially at low temperatures. This may be crucial for the early dynamics of helium burning stars.

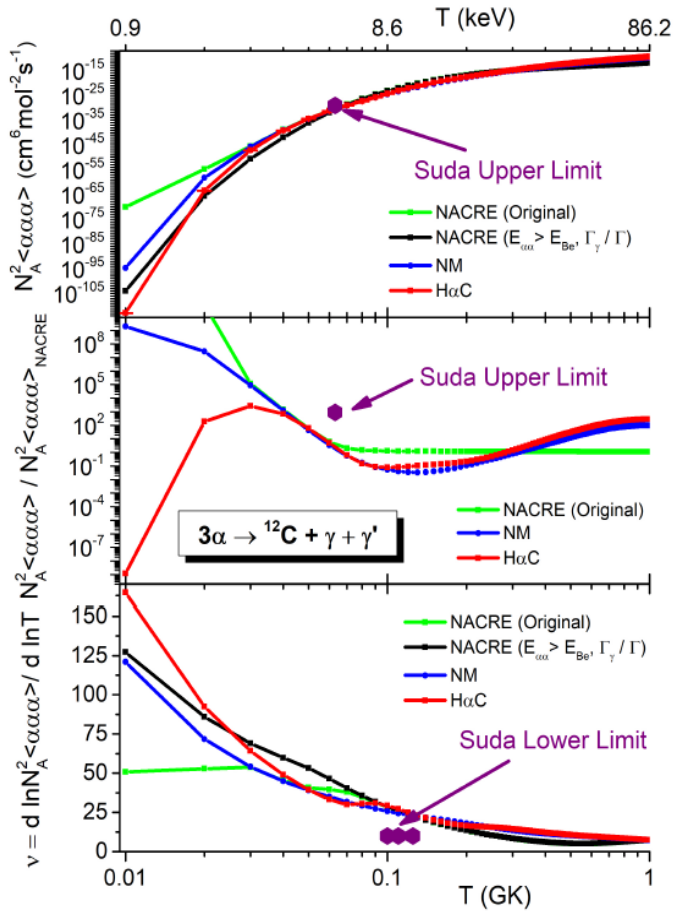

FIG. 1. (Color online) The reaction rate per α triplet (top), the same quantity normalized by the corrected NACRE data (middle) and the temperature dependence (bottom). The original (Angulo et al. (1999)) and corrected NACRE data, as well as the HαC and NM results are shown, according to the key. We also emphasize the astronomical constraints by Suda et. al (Suda et al. (2011)) with purple points.

[1] T. Depastas, S.T. Sun, H. Zheng and A. Bonasera, Phys Rev C **108**, 035806 (2023).
[2] H. Zheng and A. Bonasera, Symmetry **13**, 1777 (2021).
[3] A. Bonasera and V. Kondratyev, Phys. Lett. B **339**, 207 (1994).
[4] A. Tumino *et al.*, Nature (London) **557**, 687 (2018).
[5] T. Depastas, S.T. Sun, H.B. He, H. Zheng, A. Bonasera, Phys Lett B (2024) submitted.
[6] A. Bonasera, G. Bertsch, E. El-Sayed, E., Phys. Lett. B **141** (1984).
[7] C, Angulo *et al.*, Nuclear Physics A **656**, 3–183 (1999).

Thermodynamic properties at the kinetic freeze-out in the Au+Au and Cu+Cu collisions at the RHIC using the Tsallis distribution

W.H. Wu,[1] J. Q. Tao,[2] H. Zheng,[1] W.C. Zhang,[1] X.Q. Liu,[3] L.L. Zhu,[4] and A. Bonasera

[1]*School of Physics and Information Technology, Shaanxi Normal University, Xi'an 710119, China*

[2]*Key Laboratory of Quark & Lepton Physics (MOE) and Institute of Particle Physics, Central China Normal University, Wuhan 430079, China*

[3]*Institute of Nuclear Science and Technology, Sichuan University, Chengdu 610064, China*

[4]*Department of Physics, Sichuan University, Chengdu 610064, China*

Event-by- The thermodynamic properties of charged particles, such as the energy density, pressure, entropy density, particle density, and squared speed of sound at the kinetic freeze-out in the Au+Au collisions from the relativistic heavy ion collider (RHIC) beam energy scan program ($\sqrt{s_{NN}}$=7.7--200 GeV) and in the Cu+Cu collisions at $\sqrt{s_{NN}}$=62.4, 200 GeV are studied using the thermodynamically consistent Tsallis distribution [1]. The energy density, pressure, and particle density decrease monotonically with the collision energy for the same collision centrality; These properties also decrease monotonically from the central to peripheral collisions at the same collision energy. While the scaled energy density ε/T^4 and scaled entropy density s/T^3 demonstrate the opposite trend with the collision energy for the same collision centrality. There is a correlation between ε/T^4 and s/T^3 at the same centrality, see Fig. 1. In addition, the

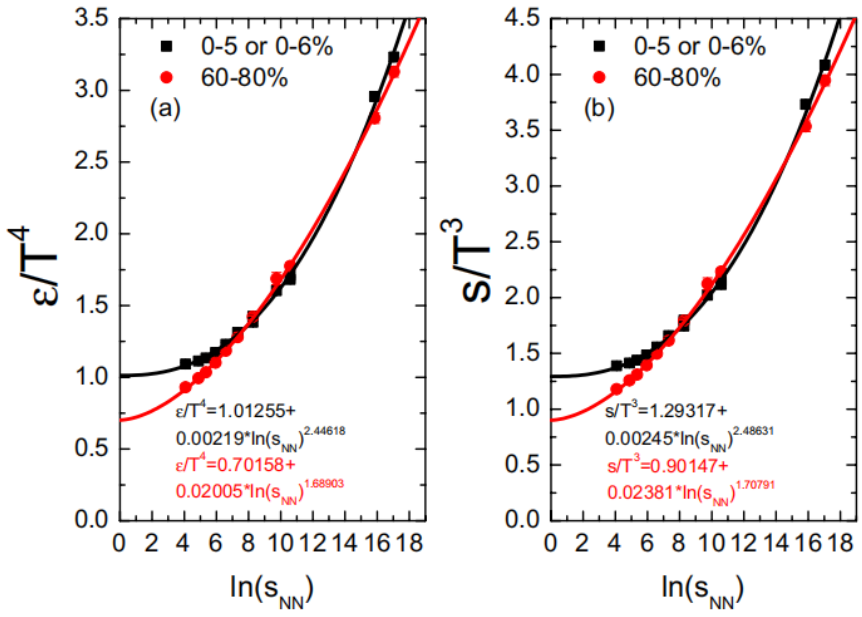

FIG. 1. (Color online) The scaled ε/T^4 and s/T^3 for the most central (black) collision and most peripheral (red) collision in the Au+Au collisions at $\sqrt{s_{NN}}$==7.7-200 GeV, and in the Cu+Cu collisions at $\sqrt{s_{NN}}$==62.4, 200 GeV, as a function of $ln(s_{NN})$. The lines are fitted with the expressions shown at the bottom of the figure. The parameters used to calculate the thermodynamic quantities for the Pb+Pb collisions are obtained from Ref. [2].

squared speed of sound was calculated to determine that all the collision energies share nearly the same value at different collision centralities.

[1] W.H. Wu, J.Q. Tao, H. Zheng, W.C. Zhang, X.Q. Liu, L.L. Zhu and A. Bonasera, Nucl. Sci. Tech. **34**, 151 (2023).
[2] M.D. Azmi, T. Bhattacharyya, J. Cleymans, M. Paradza, J. Phys. G: Nucl. Part. Phys. **47**, 045001 (2020).

Effects of short-range correlations on proton densities using the Wood-Saxon potential

T. Ma and S. Shlomo

Jastrow approach has long been used to describe short-range correlations within the nucleus. But unless the number of nucleons in the nucleus is very small, it is not possible to calculate the proton density and form factor exactly by employing the Jastrow wave function. To deal with this case, Iwamoto and Yamada have developed the Cluster Expansion method [1] and M. GAUDIN et al. have applied that method to nuclei with simple correlation factor $e^{-\beta^2 r^2}$ [2]. Here we first discuss a new method [3] to calculate the effect on the proton density caused by short-range correlation that can be applied to heavier nuclei. In this report we will provide the result produced by this method for the proton density, especially in the high Z, N≠Z method.

Under the independent particle approximation, the shell model many body wave function is given by the Slater determinant of the occupied single particle wave functions $\psi_i(\boldsymbol{r_j})$:

$$\psi_{SM} = \frac{1}{\sqrt{A!}} \det\left(\psi_1(\boldsymbol{r_1}) \dots \psi_A(\boldsymbol{r_A})\right)$$

To account for the short range correlation, we use Jastrow wave function:

$$\psi_{corr} = \frac{N}{\sqrt{A!}} \prod_{1\le i<j}^{A} f_{ij}(|\boldsymbol{r_i} - \boldsymbol{r_j}|) \det\left(\psi_1(\boldsymbol{r_1}) \dots \psi_A(\boldsymbol{r_A})\right)$$

In which N is normalize factor. In long range limit f_{ij} goes to 1.

Therefore, we can assume that for g_{ij}=f_{ij}-1, which is not negligible only when $\boldsymbol{r_i} - \boldsymbol{r_j}$ is small, we can use,

$$\prod_{1\le i<j}^{A} f_{ij}(|\boldsymbol{r_i} - \boldsymbol{r_j}|) = \prod_{1\le i<j}^{A} (1 + g_{ij}(|\boldsymbol{r_i} - \boldsymbol{r_j}|))$$

We also note that the chance that more than 3 nucleons are all close to each other is small, and therefore we can neglect all the diagrams [3] that involves more than 3 nucleons. Thus, we can get for the correlated density ρ(**r**)

$$\rho(\mathbf{r}) = \rho0(\mathbf{r}) + \int g(\mathbf{r}-\mathbf{r1})\left(\rho0\mathrm{sum}(\mathbf{r1})\rho0(\mathbf{r}) - \rho0(\mathbf{r},\mathbf{r1})\rho0(\mathbf{r1},\mathbf{r})\right)d\mathbf{r1} -$$
$$\int g(\mathbf{r1}-\mathbf{r2})\left(\rho0(\mathbf{r},\mathbf{r1})\rho0(\mathbf{r1},\mathbf{r})\rho0\mathrm{sum}(\mathbf{r2}) - \rho0(\mathbf{r},\mathbf{r1})\rho0(\mathbf{r1},\mathbf{r2})\rho0(\mathbf{r2},\mathbf{r}')\right)\ d\mathbf{r1}d\mathbf{r2}, \quad (1)$$

where ρ0(**r**) and $\rho0(\mathbf{r},\mathbf{r1})$ are the shell model one-body density matrix for proton or neutron with a certain spin state, and $\rho0\mathrm{sum}(\mathbf{r1})$ is the sum of the density of both kinds of nucleons (proton and neutron of all spin states) within the shell model.

Under the method that we developed, if we set $g(\boldsymbol{r_i}-\boldsymbol{r_j})=-e^{-\beta^2|r_i-r_j|^2}$ we can calculate the nucleon density distribution for all the spherical symmetric nucleus, especially heavier one. How well it works? Here is an example:

We use the Wood-Saxon potential: $V=(\frac{50}{1+e^{\frac{r-1.25A^{\frac{1}{3}}}{(0.6-1.2A)fm}}}(1+0.72\frac{N-Z}{A})+V_{columb})$ MeV, in which V_{columb}=1.44Z/r MeV for r>r_o=$1.25A^{\frac{1}{3}}$ and $1.44Z(\frac{3r_0^2-r^2}{2r_0^2})$ MeV for r<r_o, for neutron the potential is $V=(\frac{50}{1+e^{\frac{r-1.25A^{\frac{1}{3}}}{(0.6-1.2A)fm}}}(1+0.72\frac{Z-N}{A})$ MeV. For the correlation factor we use $g(\boldsymbol{r_i}-\boldsymbol{r_j})=-e^{-1.4^2|r_i-r_j|^2}$. The calculated proton root-mean-square (RMS) radii are given in Table I and the shell model and the correlated proton density distributions are shown in Figs 1 and 2.

Table I. Calculated proton root-mean-square (RMS) radii.

nucleus	4He	16O	28Si	32S	40Ca	60Ni	90Zr	140Ce	208Pb
shell model radius	1.616	2.530	3.059	3.190	3.330	3.756	4.150	4.787	5.448
radius with correlation(fm)	1.737	2.677	3.182	3.330	3.484	3.857	4.283	4.905	5.542
radius change	7.47%	5.81%	4.02%	4.37%	4.62%	2.66%	3.19%	2.46%	1.73%

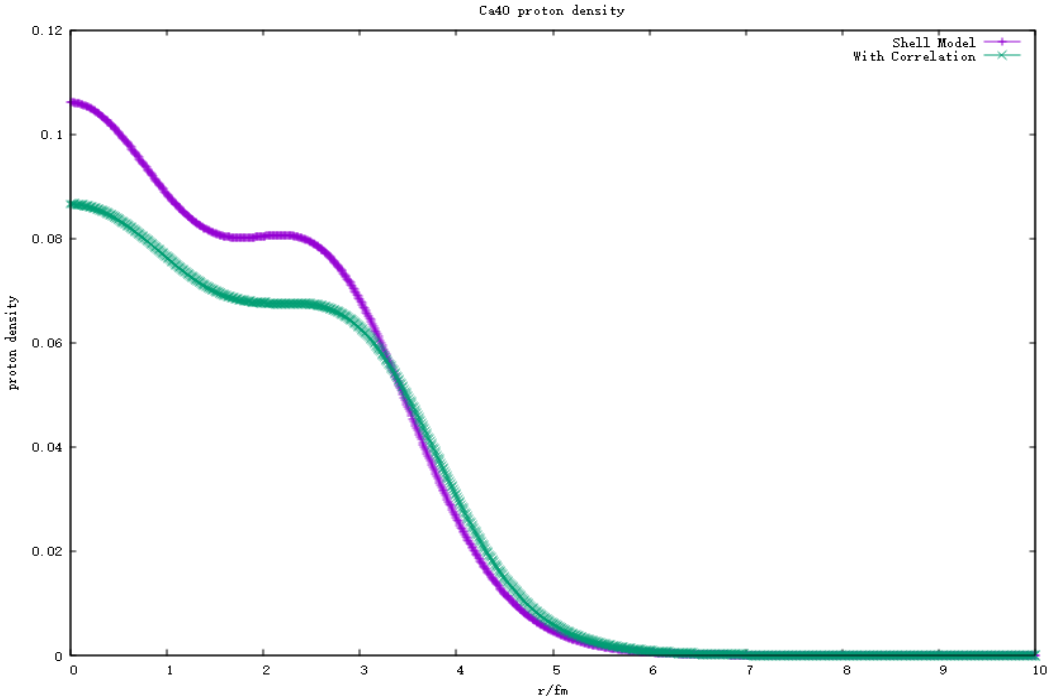

FIG. 1. The shell model (red line) and the correlated (blue line) proton density distributions of ^{40}Ca.

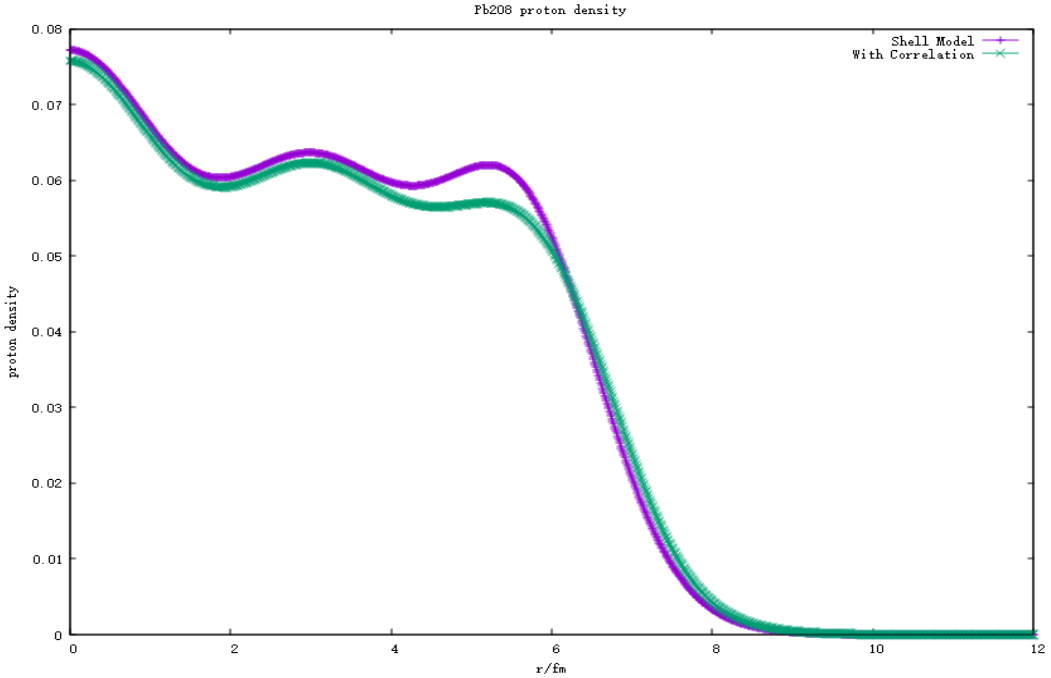

FIG. 2. The shell model (red line) and the correlated (blue line) proton density distributions of ^{208}Pb.

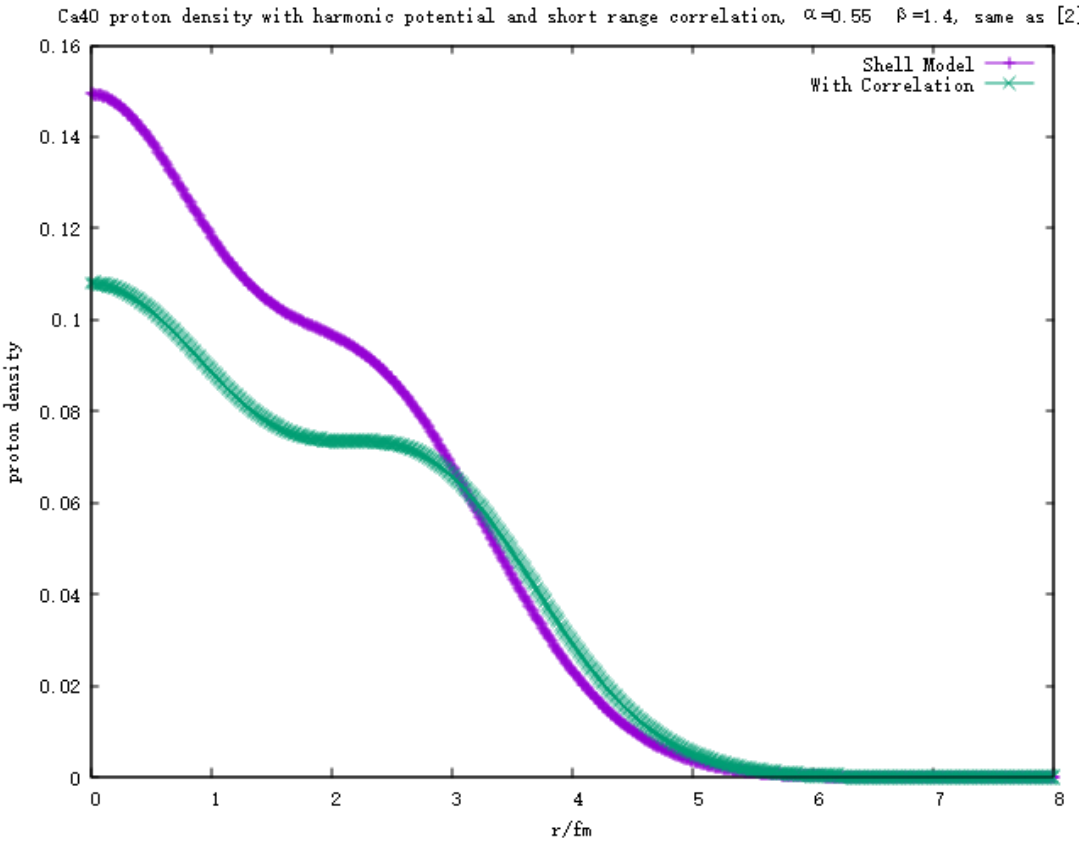

FIG. 3. Proton density for ^{40}Ca with harmonic potential [2] and short range correlation.

In order to confirm the correctness of my calculaion, I used my method for the case provided in [2]: Ca40 with harmonic shell model α=0.55fm-1 and short-range correlation factor β=1.4fm-1, and the result withCorrelation is shown in Fig. 3.

[1] F. Ywamoto and M. Yamada, Progr. Theor. Phys. **17**, 543 (1957).
[2] M. Gaudin, J. Gillespie, G. Ripka, Nucl. Phys. **A176**, 217 (1971).
[3] Tianyang Ma and Shalom Shlomo (to be published).

On properties of isoscalar giant multipole resonances in medium-heavy spherical nuclei

M.L. Gorelik,[1], S. Shlomo, B.A. Tulupov,[2] and M.H. Urin[3]
[1]*Moscow Economic School, Moscow, Russia;*
[2]*Institute for Nuclear Research, RAS, Moscow 117312, Russia*
[3]*National Research Nuclear University "MEPhI", Moscow, Russia*
E-mail: gorelik@theor.mephi.ru

In recent years, a large volume of theoretical studies of properties of Isoscalar (T = 0) Giant Multipole (L = 0 - 3) Resonances (ISGMPRs) in medium-heavy spherical nuclei has been performed [1, 2]. Within the Particle-Hole Dispersive Optical Model (PHDOM), main relaxation modes of high-energy particle-hole-type nuclear excitations associated with Giant Resonances (GRs) in medium-heavy closed-shell nuclei are together taken into account. For this reason, PHDOM has unique abilities in describing such characteristics of various GRs in nuclei, as the strength function, transition densities, and probabilities of direct one-nucleon decay (Ref. [2] and references therein). In the present work, studies of Ref. [2] related to ISGMPRs in ^{48}Ca, ^{90}Zr, ^{132}Sn, and ^{208}Pb are supplemented by the following points. (i) The strength distributions deduced from an analysis of (α, α')-reaction of ISGMPR excitation [3,4] are compared with the respective strength functions calculated within PHDOM. (ii) The method of evaluating, within PHDOM, partial branching ratios of GR direct one-nucleon decay is specified to make more adequate the comparison with experimental data of Ref. [5]. (iii) The extended PHDOM version, in which nucleon pairing in open-shell spherical nuclei is approximately taken into account, is implemented to evaluate the strength function of Isoscalar Monopole GR in the chain of even $^{114\text{-}124}$Sn isotopes. The results are compared with the experimental data of Ref. [6]. In a whole, the obtained results in PP. (i)-(iii) calculation are in a reasonable agreement with the respective experimental data.

[1] U. Garg and G. Colo, Progr. Part. Nucl. Phys. **101**, 55 (2018).
[2] M.L. Gorelik, S. Shlomo, B.A. Tulupov and M.H. Urin, Phys. Rev. C **103**, 034302 (2021); https://arxiv.org/abs/2201.04202.
[3] Y.K. Gupta, K.B. Howard, U. Garg, J.T. Matta *et al*., Phys. Rev. C **97**, 064323 (2018).
[4] A. Bahini, R. Neveling, P. von Neumann-Cosel, J. Carter *et al.*, Phys. Rev. C **107**, 034312 (2023).
[5] M. Hunyadi, A.M. Van den Berg, B. Davids, M.N. Harakeh *et al.*, Phys. Rev. C **75**, 014606 (2007).
[6] T. Li, U. Garg, Y. Liu, R. Marks *et al.*, Phys. Rev. C **81**, 034309 (2010).

Pairing correlations in statistical level densities within the micro-macroscopic approach

A.G. Magner,[1,2] A.I. Sanzhur,[1] S.N. Fedotkin,[1] A.I. Levon,[1] U.V. Grygoriev,[1,3] and S. Shlomo
[1]*Institute for Nuclear Research, National Academy of Sciences of Ukraine, Kyiv, Ukraine*
[2]*Cyclotron Institute, Texas A&M University, College Station, USA*
[3]*University of Groningen, Groningen, Netherlands*

In this report we present results for the statistical level density $\rho(E,N,Z)$ for several magic nuclei as function of the total energy E, and number of neutrons N and protons Z within the micro-macroscopic approach (MMA) [1], with main focus on pairing correlations. This level density ρ was improved at low excitation energy U [1]. The density ρ was derived as function of the excitation energy U, $\rho \propto S^{-\nu} I_\nu(S)$, in terms of the system entropy, $S = 2(aU)^{1/2}$, where a is the level density parameter, and $I_\nu(S)$ is the modified Bessel function of order ν. The orders $\nu = 2$ and $\nu = 3$ correspond to the cases of neglecting (MMA1) and dominating (MMA2) shell contributions, respectively. Taking into account the particle number fluctuations beyond the Bardeen-Cooper-Schrieffer (BCS) theory, the pairing gap Δ_0 can be considered as a smooth function of the particle number A. For the condensation energy E_c and the critical excitation energy U_c for a superfluid-normal phase transition, one can, respectively, use the well-known approximations, $E_c = 3a\Delta^2/(2\pi^2)$ and $U_c = aT_c^2 + \Delta^2/(4G)$, where $T_c = e^C\Delta_0/\pi$, with the Euler constant C, and G is the mean matrix element of residue interaction.

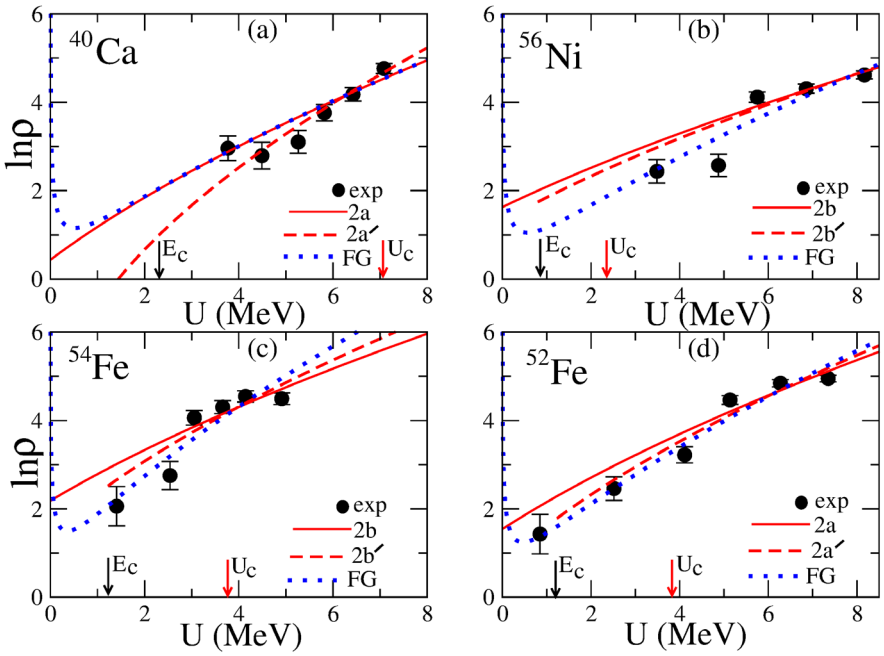

FIG. 1. Level density (in logarithms) as a function of excitation energy $\boldsymbol{U}$ for low energy states in the magic (close-shell) ^{40}Ca (a) and ^{56}Ni (b), semi-magic ^{54}Fe (c), and non-magic (open-shell) ^{52}Fe (d) nuclei. Solid lines show the results of the MMA approach for minimal values of LMS errors $\boldsymbol{\sigma}$ with pairing condensation being neglected. Dashed lines are the same but taking into account the pairing effect through the found condensation energy $\boldsymbol{E_c}$. Blue dotted lines present the results of the Fermi gas approach. Experimental close circles are obtained from the ENSDF excitation energy data.

Fig. 1 presents a comparison between the results of the MMA approaches for relatively small excitation energies U, below neutron resonances, in four nuclei, ^{40}Ca (a), ^{56}Ni (b), ^{54}Fe (c), and ^{52}Fe (d), and the experimental data obtained from the database http://www.nndc.bnl.gov/ensdf, ENSDF. Close points with errors are obtained by using the energies and spins of excited states (with spin degeneracies) by the macroscopic sample method [1]. The results for MMA2a level density approach (with dominating contributions of shell and pairing corrections from [2]) in magic nucleus ^{40}Ca ($E_c = 2.3$ MeV, $U_c = 7.1$ MeV) with the least mean square fit (LMSF) error $\sigma = 1.3$ agrees well with the experimental data obtained by least mean square (LMS) fitting using one physical parameter – the inverse level density parameter $K = A/a$. Those for the MMA2b approach (also with dominating contributions of these corrections but due to their large derivatives of the shell corrections over the chemical potential) in magic nucleus ^{56}Ni ($E_c = 0.8$ MeV, $U_c = 2.5$ MeV, $\sigma = 2.2$) are less in agreement with the experimental data when using similar LMS fitting. Pairing effects are larger for ^{40}Ca (a), see the difference between dashed and solid lines, in contrast to the ^{56}Ni (b) case. Condensation energies E_c and superfluid-normal phase transition energies U_c are marked by black and red arrows, respectively. The range between arrows for, ^{40}Ca, overlaps whole excitation energies while for the nickel, ^{56}Ni, there is no such an overlap. Therefore, we may predict that the pairing effects are easier to detect in ^{40}Ca than in ^{56}Ni. In contrast to these close-shell results, one has an intermediate situation for semi-magic ^{54}Fe (c) and open-shell ^{52}Fe (d) nuclei.

[1] A.G. Magner, A.I. Sanzhur, S.N. Fedotkin, A.I. Levon, U.V. Grygoriev, S. Shlomo, arxiv:2308.07784, submitted to Eur. J. Phys. A, **60**, 6 (2024).

[2] P. Möller, A.J. Sierk, T. Ichikawa, H. Sagawa, Atomic Data and Nuclear Data Tables **109-110**, 1 (2016).

Studying caloric curves of nuclear matter

A.I. Sanzhur,[1] and S. Shlomo[2]
[1]*Institute for Nuclear Research, National Academy of Sciences of Ukraine, Kyiv, Ukraine*
[2]*Cyclotron Institute, Texas A&M University, College Station, Texas, 77840*

Caloric curves measurements in heavy-ion collisions [1] have shown signs of a liquid-vapour phase transition in nuclear matter. The plateau region of the caloric curve, that is, the dependence of temperature, T, on excitation energy per particle $\varepsilon_{\rm ex}$, gives the signal of phase transition [2]. For finite nuclear systems composed of a limited number of neutrons N and protons Z (small system), the extension of concepts as applied in the case of infinite matter is possible [3]. Generally, the liquid-vapour phase transition is accompanied by an increase of energy and particle number fluctuations. In this context it is of interest to consider fluctuations for thermodynamic states along the caloric curve. Here we address this issue within the grand canonical ensemble formulation.

The grand partition sum Ξ and grand potential Ω for the system driven by the corresponding environmental variables are written as,

$$\Xi(\lambda_0,\lambda_1,V,T)=\iint dA_0 dA_1 \exp\left[\left(\lambda_0 A_0+\lambda_1 A_1-F(A_0,A_1,V,T)\right)/T\right], \quad \Omega=-T\ln(\Xi). \qquad (1)$$

Here, the integration is carried out over possible values of total number of nucleons $A_0=N+Z$ and neutron excess $A_1=N-Z$. In Eq. (1), $F=F(A_0,A_1,V,T)$ stands for the free energy, λ_0 and λ_1 are, respectively, the isoscalar and isovector chemical potentials, V is the system volume, and T is the temperature. In order to calculate the average quantities and fluctuations, the probability distribution function $p(A_0,A_1)=\exp[(\lambda_0 A_0+\lambda_1 A_1-F)/T]\,/\Xi$ is introduced. Using this distribution function the average values of particle number, $\langle A_0\rangle$, neutron excess, $\langle A_1\rangle$, pressure, $\langle P\rangle$, and energy, $\langle E\rangle$, are reduced to the first derivatives of the grand potential (1) for λ_0,λ_1,V and T, respectively,

$$\langle A_0\rangle=-\left(\frac{\partial\Omega}{\partial\lambda_0}\right)_{\lambda_1,V,T}, \quad \langle A_1\rangle=-\left(\frac{\partial\Omega}{\partial\lambda_1}\right)_{\lambda_0,V,T}, \quad \langle P\rangle=-\left(\frac{\partial\Omega}{\partial V}\right)_{\lambda_0,\lambda_1,T},$$

$$\langle E\rangle=\Omega-T\left(\frac{\partial\Omega}{\partial T}\right)_{\lambda_0,\lambda_1,V}-\lambda_0\left(\frac{\partial\Omega}{\partial A_0}\right)_{\lambda_1,V,T}-\lambda_1\left(\frac{\partial\Omega}{\partial A_1}\right)_{\lambda_0,V,T}. \qquad (2)$$

The excitation energy per particle $\varepsilon_{\rm ex}$, needed for determination of the caloric curve, $T(\varepsilon_{\rm ex})$, is obtained from Eq. (2) as

$$\varepsilon_{\rm ex}=(\langle E\rangle-E_{gs})/\langle A_0\rangle, \qquad (3)$$

where E_{gs} is the ground state energy at $T=0$. One should note that, for the considered small system, the energy $\langle E\rangle$ is not linear homogeneous function of entropy $\langle S\rangle$, volume V, and $\langle A_0\rangle$, $\langle A_1\rangle$ numbers, in contrast to the macroscopic limit $V\to\infty$ (within the habitual thermodynamics for infinite nuclear matter)

when all extensive properties become functions of λ_0, λ_1, and T only. Nevertheless, for the certain set of environment variables, like λ_0, λ_1, V and T in our case, the thermodynamics of small system can be built [4]. Along with "differential" pressure $\langle P \rangle$, see Eq. (2), the "integral" pressure $\hat{P} = -\Omega/V$ is introduced, and the average energy takes the form $\langle E \rangle = T\langle S \rangle - \langle P \rangle V + \lambda_0 \langle A_0 \rangle + \lambda_1 \langle A_1 \rangle + \mathcal{E}$, with $\mathcal{E} = \left(\langle P \rangle - \hat{P}\right)V$ being the correction term for the small system which disappears in the macroscopic limit, i.e. $-(\partial\Omega/\partial V)_{\lambda_0,\lambda_1,T} = -\Omega/V = \hat{P} = \langle P \rangle$ (see Ref. [4]).

We have calculated the isobaric caloric curve, using $\hat{P} = 0.05$ MeV/fm^3, for the small nuclear system having on the average $\langle A_0 \rangle = 200$ and $\langle A_1 \rangle = 40$ and the asymmetry parameter $X = \langle A_1 \rangle / \langle A_0 \rangle = 0.2$. Calculation was carried out for the temperature interval $T = 5 \div 12$ MeV using KDE0v1 Skyrme effective nucleon-nucleon interaction [5]. At each chosen temperature the values of λ_0, λ_1, and V were determined to provide the above mentioned values of $\langle A_0 \rangle$, $\langle A_1 \rangle$, and $\hat{P}$. The result is shown in Fig. 1 by the dotted line. With the aim of comparison, the calculation at the same pressure and asymmetry parameter was carried out for infinite asymmetric nuclear matter (solid and dashed lines in Fig. 1). Comparing the dotted line with the solid one in Fig. 1 it is seen that the temperature in the middle of plateau region for the small system is lower than that for infinite matter by about of 0.2 MeV.

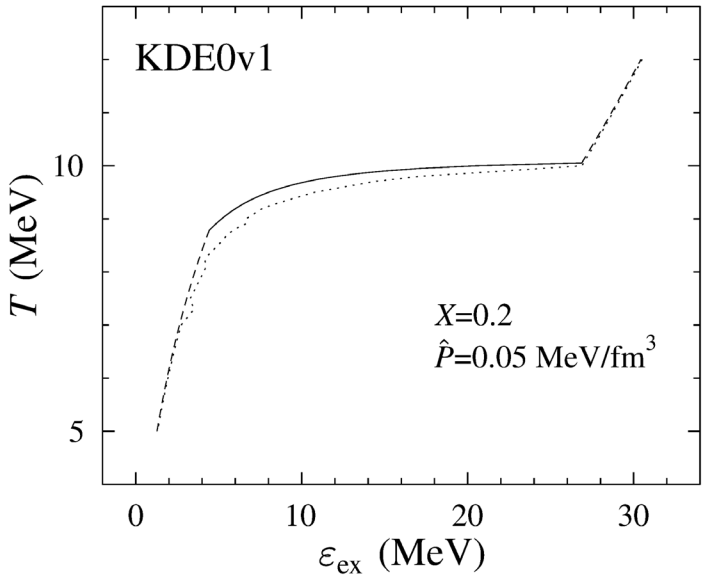

FIG. 1. Isobaric caloric curves $\boldsymbol{T(\varepsilon_{ex})}$. Dotted line presents the result at pressure $\boldsymbol{\hat{P} = 0.05\ MeV/fm^3}$ for small nuclear system with $\boldsymbol{\langle A_0 \rangle = 200}$, $\boldsymbol{\langle A_1 \rangle = 40}$. Solid and dashed lines shows the result in the case of infinite matter for the same pressure and asymmetry parameter. Dashed line correspond to a single phase, solid line is obtained for phase coexistence region. Calculations were carried out using KDE0v1 Skyrme nucleon-nucleon effective interaction [5].

We also obtained the relative fluctuations of the nucleon number, δ_0, and the neutron excess, δ_1, by means of the following expressions

$$\delta_0 = \frac{\left(\langle A_0^2\rangle - \langle A_0\rangle^2\right)^{1/2}}{\langle A_0\rangle} = -\frac{\sqrt{-T\left(\frac{\partial^2\Omega}{\partial\lambda_0^2}\right)_{\lambda_1,V,T}}}{\left(\frac{\partial\Omega}{\partial\lambda_0}\right)_{\lambda_1,V,T}} \quad , \quad \delta_1 = \frac{\left(\langle A_1^2\rangle - \langle A_1\rangle^2\right)^{1/2}}{\langle A_1\rangle} = -\frac{\sqrt{-T\left(\frac{\partial^2\Omega}{\partial\lambda_1^2}\right)_{\lambda_0,V,T}}}{\left(\frac{\partial\Omega}{\partial\lambda_1}\right)_{\lambda_0,V,T}} \, . \qquad (4)$$

The calculation of the dispersion and, consequently, the fluctuation (absolute or relative) of A_0 and A_1 requires the value of the second derivative of the grand potential Ω with respect to the corresponding chemical potential. Fig. 2 presents the relative fluctuations δ_0 and δ_1 for small nuclear system $\langle A_0\rangle = 200$, $\langle A_1\rangle = 40$ as functions of excitation energy per particle. Fig. 2 demonstrates the increase of fluctuations in the two-phase region of excitation energies. Such an increase, together with the plateau region in caloric curve $T(\varepsilon_{\rm ex})$, gives the signature of the occurring phase transition.

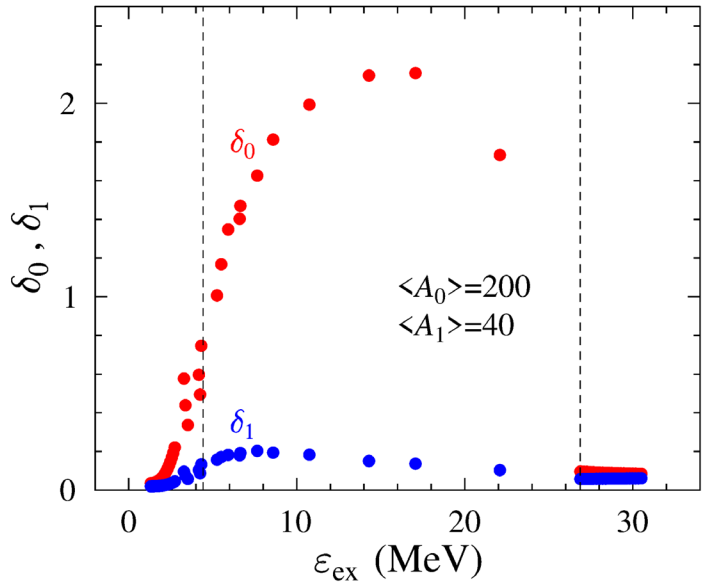

FIG. 2. Relative fluctuations of the nucleon number $\boldsymbol{\delta_0}$ (red dots) and neutron excess $\boldsymbol{\delta_1}$ (blue dots) versus the excitation energy per nucleon $\boldsymbol{\varepsilon_{ex}}$, see Eqs. (3), and (4). Results are obtained for small nuclear system with $\boldsymbol{\langle A_0\rangle = 200}$ and $\boldsymbol{\langle A_1\rangle = 40}$ along the caloric curve, see Fig. 1. The range of $\boldsymbol{\varepsilon_{ex}}$ between vertical dashed lines corresponds to coexistence of liquid and vapour phases for the case of infinite nuclear matter.

In spite of the presented results for small nuclear system do not include the effects of Coulomb interaction and nuclear surface, they still can be valuable to give an idea on the excitation energy range where to expect the observation of liquid-vapour phase transition.

[1] J.B. Natowitz *et al.*, Phys. Rev. C **65**, 034618 (2002).

[2] V.M. Kolomietz, S. Shlomo. *Mean field theory* (Singapore: World Scientific, 2020) p. 565.

[3] Tapas Sil *et al*., Phys. Rev. C **69**, 014602 (2004).

[4] Terrell L. Hill. *Thermodynamics of Small Systems* (New York: Dover Publications, 2013) p. 416.

[5] B.K. Agrawal, S. Shlomo, V. Kim Au. Phys. Rev. C **72**, 014310 (2005).

Asymptotic normalization coefficients for $\alpha + {}^{12}C$ synthesis and the *S*-factor for ${}^{12}C(\alpha, \gamma){}^{16}O$ radiative capture

A.M. Mukhamedzhanov, R.J. DeBoer, B.F. Irgaziev, L.D. Blokhintsev, A.S. Kadyrov, and D.A. Savin

The $^{12}C(\alpha,\gamma)^{16}O$ reaction, determining the survival of carbon in red giants, is of interest for nuclear reaction theory and nuclear astrophysics. A specific feature of the ^{16}O nuclear structure is the presence of two subthreshold bound states, (6.92 MeV, 2^+) and (7.12 MeV, 1^-), that dominate the behavior of the low-energy S-factor. The strength of these subthreshold states is determined by their asymptotic normalization coefficients (ANCs), which need to be known with high accuracy. Recently, using a model-independent extrapolation method, Blokhintsev *et al.* [1] determined the ANCs for the α-particle removal taking into account three subthreshold states in ^{16}O.

The goal of this work is to address four main problems elucidating the impact of the subthreshold ANCs on the low-energy S-factor. Firstly, we analyze the connection between variations of the subthreshold ANCs and the low-energy S-factor, in particular, at the most effective energy of 300 keV. Secondly, we calculate contributions to the S(300 keV)-factor from the subthreshold 1^- and 2^+ resonances, that are controlled by the subthreshold ANCs. We also evaluate the contribution of the uncertainties of the subthreshold ANCs to the budget of the S(300 keV)-factor uncertainty. Thirdly, we analyze interference of the subthreshold resonances with higher resonances and with the E1 and E2 direct captures to the ground state. Finally, we investigate a correlated effect of the subthreshold and ground-state ANCs on the low-energy S-factor and, in particular, on the S(300 keV)-factor. The S-factors are calculated within the framework of the R-matrix method using the AZURE2 code.

Our total S-factor takes into account the E1 and E2 transitions to the ground state of ^{16}O of the interfering subthreshold and higher resonances, which also interfere with the corresponding direct captures, and cascade radiative captures to the ground state of 16O through four subthreshold states: 0^+, 2^+, 3^-, 2^+ and 1^-. Since our ANCs are higher than those used by deBoer *et al.* [2], the present total S-factor at the most effective astrophysical energy of 300 keV is higher, 174 keVb versus 137 keVb of that work. The contribution to the total E1 and E2 S-factors from the corresponding subthreshold resonances at 300 keV are (71−74)% and (102 − 103)%, respectively. The correlation of the uncertainties of the subthreshold ANCs with the E1 and E2 S(300 keV)-factors is found. The E1 transition of the subthreshold resonance 1^- does not depend on the ground-state ANC but interferes constructively with a broad (9.585MeV; 1^-) resonance giving (for the present subthreshold ANC) an additional 26% contribution to the total E1 S(300 keV)-factor. Interference of the E2 transition through the subthreshold resonance with direct capture is almost negligible for small ground-state ANC of 58 fm−1/2. However, the interference with direct capture for higher ground-state ANC of 337 fm−1/2 is significant and destructive, contributing −27%. The interference between the E2 transition of the SR 2+ and direct capture is minimal when the ground-state ANC is small, but becomes destructive at higher ground-state ANC, resulting in a contribution of −27%. The low-energy SE2(300 keV)-factor experiences a smaller increase when both subthreshold and the ground-state ANCs rise together due to their anticorrelation, compared to when only the subthreshold ANCs increase.

This paper is submitted to Phys. Rev. C

[1] L.D. Blokhintsev, A.S. Kadyrov, A.M. Mukhamedzhanov and D.A. Savin, Eur. Phys. J. A **59**, 162 (2023).
[2] R.J. DeBoer *et al.*, Rev. Mod. Phys. **89**, 035007 (2017).

Determination of asymptotic normalization coefficients for the channel $^{16}O \rightarrow \alpha + ^{12}C$. II. Excited states $^{16}O(3^-, 2^+, 1^-)$

L.D. Blokhintsev A.S. Kadyrov, A.M. Mukhamedzhanov,and D.A. Savin

Asymptotic normalization coefficients (ANC) determine the overall normalization of cross sections of peripheral radiative capture reactions. In a recent paper [Blokhintsev et al., Eur. Phys. J. A 58, 257 (2022)], we considered the ANC C0 for the virtual decay $^{16}O(0^+; 6.05MeV) \rightarrow \alpha + ^{12}C(g.s.)$. In the present paper, which can be regarded as a continuation of the previous, we treat the ANCs Cl for the vertices $^{16}O(J\pi) \rightarrow \alpha + ^{12}C(g.s.)$ corresponding to the other three bound excited states of ^{16}O ($J\pi = 3^-, 2^+, 1^-, l = J$). ANCs Cl ($l = 3, 2, 1$) are found by analytic continuation in energy of the α-^{12}C l-wave partial scattering amplitudes, known from the phase-shift analysis of experimental data, to the pole corresponding to the ^{16}O bound state and lying in the unphysical region of negative energies. To determine Cl, the scattering data are approximated by the sum of polynomials in energy in the physical region and then extrapolated to the pole. For a more reliable determination of the ANCs, various forms of functions expressed in terms of phase shifts were used in analytical approximation and subsequent extrapolation.

The paper has been published in Eur. Phys. J. A (2023).

[1] Blokhintsev *et al.*, Eur. Phys. J. A **58**, 257 (2022).

Determination of the astrophysical factor of the ^{3}He(α,γ)^{7}Be down to zero energy using the asymptotic normalization coefficient method

M. LaCognata, R.E. Tribble and A.M. Mukhamedzhanov

The observation of neutrinos emitted in the pp chain and in the CNO cycle can be employed to test the Standard Solar Model. The ^{3}He(α, γ)^{7}Be reaction is the reaction of the 2nd and 3rd branch of the pp chain, so the indetermination of its cross section significantly affects the predicted ^{7}Be and 8B neutrino fluxes. Notwithstanding its relevance and the great deal of experimental and theoretical papers, information of the reaction cross section at energies of the core of the Sun (15 keV - 30 keV) is sparse and additional experimental work is necessary to attain the target (3%) accuracy. The precise understanding of the external capture component to the ^{3}He(α, γ)^{7}Be reaction cross section is pivotal for the theoretical assessment of the reaction mechanism. In this work, the indirect measurement of this external capture component using the Asymptotic Normalization Coefficient (ANC) technique is discussed. To extract the ANC, the angular distributions of deuterons yielded in the ^{6}Li(^{3}He,d)^{7}Be alpha-transfer reaction were detected with high precision at $E_{^{3}He}$=3.0 MeV and 5.0 MeV. The ANCs were then deduced from the juxtaposition of DWBA and CC calculations with the experimental angular distributions and the zero energy astrophysical S-factor for ^{3}He(α, γ)^{7}Be reaction was calculated to equal 0.534 keVb. Both our experimental and theoretical approaches were tested through the analysis of the ^{6}Li(p,γ)^{7}Be astrophysical implications.

The paper was published in J. Phys. Conference Series **2586**, 012093 (2023).

Resonances in low-energy nuclear processes and nuclear astrophysics and asymptotic normalization coefficients: a review

A.M. Mukhamedzhanov

This work is continuation of the previous review by Mukhamedzhanov and Blokhintsev [Mukhamedzhanov and Blokhintsev, [Eur. Phys. J. A 58, 29 (2022)] in which the ANC of a bound state was addressed. However, the ANC is important characteristics not only of bound states but also resonances. The role of the ANCs in resonance processes is addressed. Among various topics considered here are Gamow–Siegert resonance wave functions for charged particles and their normalization, relationship between ANCs and resonance widths. Significant part is devoted to the R-matrix approach for resonance processes. The resonance wave functions, internal and external and their projections on the two-body channel are given. Important ingredients of the R-matrix method for resonance states are also discussed. Elastic resonance scatterings are analyzed and extended for subthreshold resonances. It is shown how the notion of the subthreshold resonance works in practical analysis. To this end, the $^{13}C(\alpha,n)^{16}O$ reaction, which is considered to be the main neutron supply to build up heavy elements from iron-peak seed nuclei in AGB stars, is analyzed. Important part of the review is analysis of the relationship between resonance width and ANC of mirror resonance and bound states using the Pinkston–Satchler equation and the Wronskian method. Practical examples are given.

Among important parts of the theoretical research is the theory of transfer reactions populating resonance states. Comparative analysis of prior and post-form DWBA amplitudes shows that the prior form is preferable over the post form due to faster convergence over rnA. Calculations of the stripping to resonance reaction $^{16}O(d, p)^{17}O(1d3/2)$ performed using the prior form of the CDCC method. A special attention is given to resonance astrophysical processes. Useful equations for internal and external radiative widths are given. Radiative capture through subthreshold resonance is considered. In particular, radiative capture reactions $^{11}C(p, \gamma)^{12}N$ and $^{15}N(p, \gamma)^{16}O$ and the role of the ANC is addressed in detail.

The paper has been published in Eur. Phys. J. A (2023).

[1] Mukhamedzhanov and Blokhintsev, Eur. Phys. J. A **58**, 29 (2022).

Nuclear Theory – Nuclear astrophysics

J.W. Holt

I. Introduction

The structure, phases, and dynamics of nuclear matter are crucial to understand stellar explosions, the origin of the elements, patterns in observed gravitational waves, and the composi-tion of the densest observable matter in the universe. The appropriate tool to study strongly inter-acting matter at the typical scales relevant in nuclear astrophysics (well below the scale of chiral symmetry breaking $\Lambda\chi\approx1$ GeV) is chiral effective field theory [1-3]. In recent years, chiral effective field theory has become a cornerstone of the modern approach to nuclear many-body dynamics that provides a systematic framework for describing realistic mi-crophysics, such as multi-pion exchange processes and three-body forces, within a well-defined organizational hierarchy. The long and intermediate-range parts of the nuclear potential result from one- and two-pion exchange processes, while short-distance dynamics, not resolved at the wavelengths corresponding to typical nuclear Fermi momenta, are introduced as contact interac-tions between nucleons. Chiral effective field theory is unique in its multichannel methods for quantifying uncertainties and especially in its ability to estimate the importance of missing physics.

II. Neutrino reactions in warm, neutron-rich matter

Neutrinos dominate the transport of energy, momentum, and lepton number in extreme astrophysical settings, such as core-collapse supernovae [4,5], newly born neutron stars [6,7], and neutron star mergers [8,9]. Both neutral-current elastic scattering processes and charged-current absorption processes affect the total neutrino and anti-neutrino opacities in these environments. In a dense medium, the free-space elastic scattering and absorption cross sections are modified due to nuclear mean fields and correlations. These effects are encoded in dynamical structure functions that can be obtained from the imaginary part of nu-clear response functions. Previously, nuclear matter response functions have been studied using a variety of nuclear interactions and many-body approximations, including nonrelativistic and rela-tivistic mean field models [10,11], Fermi liquid theory [12,13], the virial expansion [14]. Recent studies [15,16] have highlighted the important role of nuclear mean fields for calculating charged-current reactions in the supernova neutrinosphere. Here the large asymmetry between proton and neutron densities leads to a strong splitting of the proton and neutron mean fields that enhances neutrino absorption and suppresses anti-neutrino absorption. This, in turn, affects the composition of matter ejected from supernovae and neutron star mergers as well as neutrino flavor and energy distributions that terrestrial neutrino detectors may observe.

In recent work [17], we have employed nuclear forces based on chiral effective field theory to investigate beyond-mean-field corrections to spin and density response functions of nu-clear matter under ambient conditions typical of supernova and neutron star merger neutrino-spheres, where the nucleon number density varies in the range $0.001\ n0<n<0.1\ n0$, with $n0=0.16$ fm^{-3} the nuclear matter saturation density, and the temperature varies in the range $5\text{ MeV}<T<10\text{ MeV}$. Specifically, we calculated Hartree-

Fock mean field corrections as well as re-summed particle-hole vertex corrections in the random phase approximation (RPA). In Fig. 1 we show the inverse mean free paths for electron neutrino (blue) and

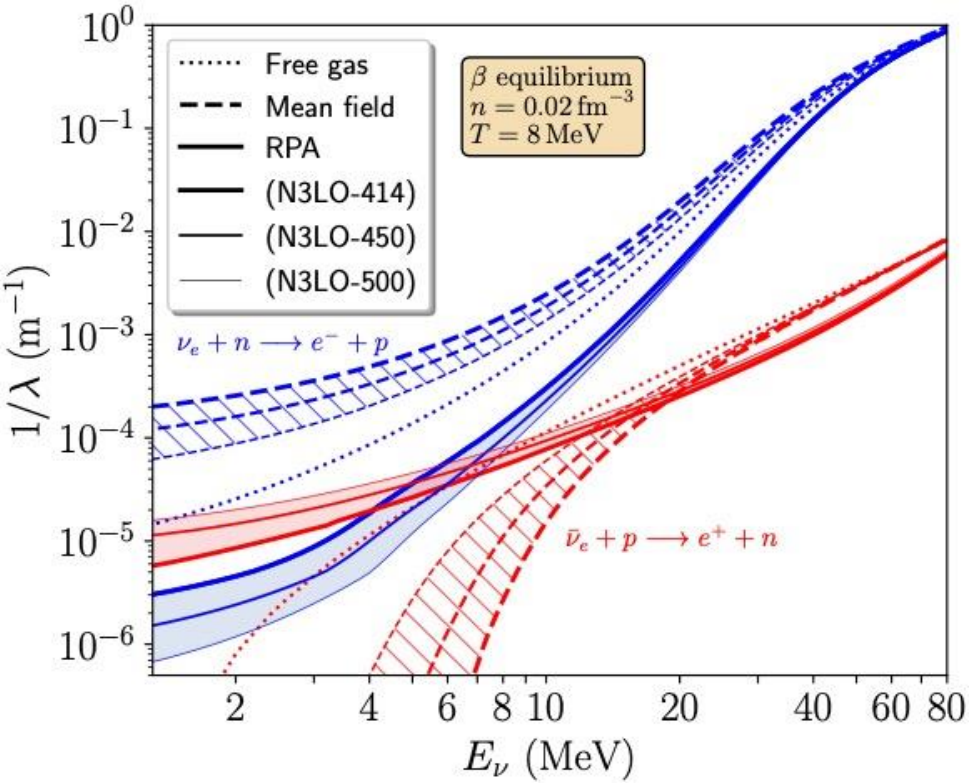

FIG. 1. Electron neutrino (blue) and antineutrino (red) inverse mean free paths as a function of energy for beta-equilibrium nuclear matter at density $\boldsymbol{n = 0.02}$ fm^{-3} and temperature $\boldsymbol{T = 8}$ MeV. The dotted lines denote results for noninteracting nucleons, the dashed curves denote results including nuclear mean fields at the Hartree-Fock level, and solid lines represent results including both mean fields and random phase approximation vertex corrections. The shaded bands denote uncertainties due to the choice of nucleon-nucleon potential.

antineutrino (red) absorption as a function of the incident energy for beta-equilibrium nuclear matter at density $n = 0.02$ fm^{-3} and temperature $T = 8$ MeV. The dynamic structure functions are computed from the associated charged-current spin response functions in three approximations. First, the inverse neutrino mean free paths neglecting interactions between nucleons are shown by the dotted curves. Second, we show as the dashed lines the effect of introducing proton and neutron mean fields in the Hartree-Fock approximation. Finally, the solid curves show the combined effects of nucleon mean fields and vertex corrections obtained in the random phase approximation. We employ three different chiral nucleon-nucleon interactions: N3LO-414, N3LO-450, and N3LO-500.

In all cases, we find that the mean-field effects significantly enhance the electron neutrino absorption cross-section and suppress the electron antineutrino absorption cross-section across all energies considered, in agreement with previously published studies. The effects are largest for the most perturbative chiral potential, N3LO-414. In contrast, RPA correlations redistribute strength to the vicinity of a positive-energy collective mode. This significantly reduces the outgoing electron energy into a region where Pauli

blocking suppresses the reaction. This redistribution of strength due to a broad collective mode shifts the response to higher energy and undoes the enhancement of the inverse mean free path due to mean-field effects. Remarkably, correlations suppress the electron neutrino absorption cross-sections over the entire energy range and are especially large for low-energy neutrinos. Whereas the inclusion of nuclear mean fields resulted in a clear splitting of the electron neutrino absorption cross section with varying nuclear potential, the fact that the order and relative magnitude of the splitting remains intact after the inclusion of RPA correlations suggests these effects are less sensitive to the choice of NN potential. In particular, RPA correlations suppress the inverse mean free path by approximately two orders of magnitude for all three chiral potentials.

III. Generative modeling of the nucleon-nucleon interaction

Developing high-precision models of the nuclear force and propagating the associated uncertainties in quantum many-body calculations of nuclei and nuclear matter remain key challenges for ab initio nuclear theory. In recent work [18], we have demonstrated that generative machine learning models, specifically the Generative Flow ("Glow") model, can construct novel instances of the nucleon-nucleon interaction when trained on existing potentials from the literature. In particular, we modified and trained the Glow model on nucleon-nucleon potentials derived at second and third order in chiral effective field theory and at three different choices of the resolution scale. We then showed that the model can be used to generate samples of the nucleon-nucleon potential drawn from a continuous distribution in the resolution-scale parameter space. This work provides an important step toward a comprehensive estimation of theoretical uncertainties in nuclear many-body calculations that arise from the arbitrary choice of nuclear interaction and resolution scale.

In Fig. 2 we show neutron-proton scattering phase shifts in selected partial-wave channels (1S0, 3S1, 3P0, 3P1, 3P2, 1D2, 3D1, 3D2, 3D3) predicted from nuclear potentials generated by the Glow model. The samples are generated over a continuum of resolution scales defined by the value of the cutoff scale Λ

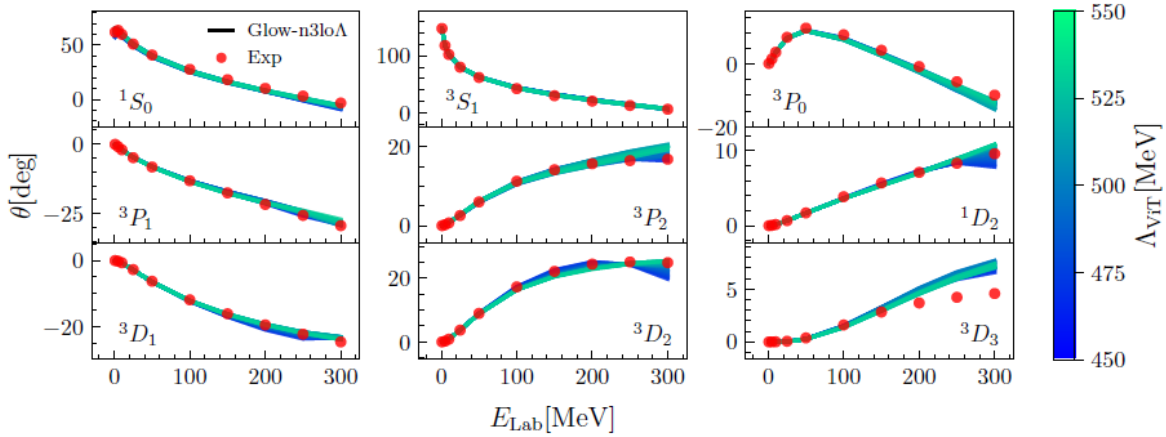

FIG. 2. Neutron-proton scattering phase shifts in selected partial-wave channels computed from Glow-generated nuclear potentials. The colors of the solid lines represent the values of the high-momentum cutoff **Λ**, which can take on a continuum of values. The red dots correspond to the phase shift analysis of nucleon-nucleon scattering data in [19].

used to regulate the high-momentum components of the nucleon-nucleon potential. The red dots correspond to the phase shift analysis in Ref. [19]. One sees that the Glow model is capable of generating realistic nucleon-nucleon potentials that produce high-quality scattering phase shifts. One can also observe that although the potentials are generated uniformly over the interval $450\,\mathrm{MeV} < \Lambda < 550\,\mathrm{MeV}$, the associated phase shift values are not uniformly distributed. This indicates the presence of complicated correlations between Λ and observables, highlighting the need for general statistical uncertainty analysis tools that are presently unavailable in the literature.

[1] S. Weinberg, Physica A **96**, 327 (1979).
[2] E. Epelbaum, H.-W. Hammer and U.-G. Meissner, Rev. Mod. Phys. **81**, 1773 (2009).
[3] R. Machleidt and D. R. Entem, Phys. Rep. **503**, 1 (2011).
[4] A. Burrows and R. F. Sawyer, Phys. Rev. C **59**, 510 (1999).
[5] T. Melson, H.-T. Janka, R. Bollig, F. Hanke, A. Marek, and B. Mueller, Astrophys. J. Lett. **808**, L42 (2015).
[6] J.A. Pons, S. Reddy, M. Prakash, J.M. Lattimer, and J.A. Miralles, Astrophys. J. **513**, 780 (1999).
[7] L.F. Roberts and S. Reddy, Phys. Rev. C **95**, 045807 (2017).
[8] Y. Sekiguchi, Class. Quant. Grav. **27**, 114107 (2010).
[9] S. Wanajo, Y. Sekiguchi, N. Nishimura, K. Kiuchi, K. Kyutoku, and M. Shibata, Astrophys. J. Lett. **789**, L39 (2014).
[10] R.F. Sawyer, Phys. Rev. C **40**, 865 (1989).
[11] S. Reddy, M. Prakash, and J.M. Lattimer, Phys. Rev. C **58**, 013009 (1998).
[12] N. Iwamoto and C.J. Pethick, Phys. Rev. D **25**, 313 (1982).
[13] A. Burrows and R.F. Sawyer, Phys. Rev. C **58**, 554 (1998).
[14] C.J. Horowitz and A. Schwenk, Phys. Lett. B **642**, 326 (2006).
[15] G. Martinez-Pinedo, T. Fischer, A. Lohs, and L. Huther, Phys. Rev. Lett. **109**, 251104 (2012).
[16] L.F. Roberts, S. Reddy, and G. Shen, Phys. Rev. C **86**, 065803 (2012).
[17] E. Shin, E. Rrapaj, J.W. Holt and S.K. Reddy, Phys. Rev. C **109**, 015804 (2024).
[18] P. Wen, J.W. Holt and M. Li, arXiv:2306.13007.
[19] R. Navarro Prez, J.E. Amaro, and E. Ruiz Arriola, Phys. Rev. C **89**, 064006 (2014).

Comparing pion production in transport simulations of heavy-ion collisions at 270A MeV under controlled conditions

J. Xu,[1] H. Wolter,[2] M. Colonna,[3] D. Cozma,[4] P. Danielewicz,[5] and
C. M. Ko *et al*. (TEMP Collaboration)
[1]*School of Physical Science and Engineering, Tongi University, Shanghai 200092, China*
[2]*Faculty of Physics, University of Munich, D-85748, Garching, Germany*
[3]*INFN-LNS, Laboratori Nazionali del Sud, 95123 Catania, Italy*
[4]*IFIN-HH, 077125 Magurele-Bucharest, Romania*
[5]*FRIB and Department of Physics and Astronomy,*
Michigan State University, East Lansing, Michigan 48824,

Within the Transport Model Evaluation Project (TMEP), we have carried out a detailed study of the performance of different transport models in Sn + Sn collisions at 270*A* MeV, which are representative reactions used to study the equation of state at supra-saturation densities [1]. We have put particular emphasis on the production of pion and Delta resonance, which have been used as probes of the nuclear symmetry energy. Our study aims to understand the differences in the results of different codes for a given physics model to estimate the uncertainties of transport model studies in the intermediate energy range. With a common and rather simple physics model, we have followed in detail the results of four Boltzmann-Uehling-Uhlenbeck (BUU) models [2-5] and six quantum molecular dynamics (QMD) models [6-11]. It is found that the nucleonic evolution of the collision and the nucleonic observables in these codes do not completely converge, but the differences among the codes can be understood as being due to several reasons: the basic differences between BUU and QMD models in the representation of the phase-space distributions, computational differences in the mean-field evaluation, and differences in the adopted strategies for the Pauli blocking in the collision integrals. For pion observables, we have found that a higher maximum density leads to an enhanced pion yield and a reduced π^-/π^+ yield ratio, while a more effective Pauli blocking generally leads to a slightly suppressed pion yield and an enhanced π^-/π^+ yield ratio. We have specifically investigated the effect of the Coulomb force and found that it increases the total π^-/π^+ yield ratio but reduces the ratio at high pion energies, although differences in its implementations do not have a dominating role in the differences among the codes. Considering only the results of codes that strictly follow the homework specifications, we have found a convergence of the codes in the final charged-pion yield ratio to a 1σ deviation of about 5%. However, the uncertainty is expected to be reduced to about 1.6% if the same or similar strategies and ingredients, i.e., an improved Pauli blocking and calculation of the nonlinear term in the mean-field potential, are similarly used in all codes. As a result of this work, we have identified the sensitive aspects of a simulation with respect to the pion observables and suggested optimal procedures in some cases. Our study has provided benchmark calculations of heavy-ion collisions to be complemented in the future by simulations with more realistic physics models, which include the momentum-dependence of isoscalar and isovector mean-field potentials and pion in-medium effects.

[1] J, Xu, H. Wolter, M. Colonna, D. Cosma, P. Danielewicz, C.M. Ko *et al.* (TEMP Collaboration), Phys. Rev. C **109**, 044609 (2024).

[2] H.S. Wang, J. Xu, B.A. Li, and W.Q. Shen, Phys. Rev. C **98**, 054608 (2018); J. Xu and W.T. Qin, *ibid.* **102**, 024306 (2020).
[3] P. Danielewicz, Nucl. Phys. **A673**, 375 (2000).
[4] T. Song and C.M. Ko, Phys. Rev. C **91**, 014901 (2015).
[5] M. Colonna, M. Di Toro, A. Guarnera *et al.*, Nucl. Phys. **A642**, 449 (1998); A. Guarnera, M. Colonna, and Ph. Chomaz, Phys. Lett. B **373**, 267 (1996); M. Colonna, Phys. Rev. Lett. **110**, 042701 (2013).
[6] J. Su, F.S. Zhang, and B.A. Bian, Phys. Rev. C **83**, 014608 (2011); J. Su and F.S. Zhang, *ibid.* **87**, 017602 (2013); J. Su, K. Cherevko, W. J. Xie, and F. S. Zhang, *ibid.* **89**, 014619 (2014).
[7] Z.Q. Feng, Phys. Rev. C **84**, 024610 (2011); **85**, 014604 (2012).
[8] Ch. Hartnack, R.K. Puri, J. Aichelin, J. Konopka, S.A. Bass, H. Stöcker, and W. Greiner, Eur. Phys. J. A **1**, 151 (1998).
[9] N. Ikeno, A. Ono, Y. Nara, and A. Ohnishi, Phys. Rev. C **93**, 044612 (2016); **97**, 069902(E) (2018).
[10] D.T. Khoa, N. Ohtsuka, M.A. Matin *et al.*, Nucl. Phys. **A548**, 102 (1992); V. Uma Maheswari, C. Fuchs, A. Faessler *et al.*, *ibid.* **628**, 669 (1998); K. Shekhter, C. Fuchs, A. Faessler, M. Krivoruchenko, and B. Martemyanov, Phys. Rev. C **68**, 014904 (2003); M.D. Cozma, Y. Leifels, W. Trautmann, Q. Li, and P. Russotto, *ibid.* **88**, 044912 (2013).
[11] J. Yang, Y. Zhang, N. Wang, and Z. Li, Phys. Rev. C **104**, 024605 (2021).

Hadronic effects on Lambda hyperon polarization in relativistic heavy ion collisions

H. Sung,[1] C. M. Ko, and S. H. Lee[1]

[1]*Department of Physics and Institute of Physics and Applied Physics, Yonsei University, Seoul 03722, Korea*

We have studied the effect of hadronic scatterings on the spin polarization of Lambda hyperon in Au-Au collisions at $\sqrt{s_{NN}} = 7.7$ GeV in a schematic kinetic approach by using thermally averaged Λ spin flip and non-flip cross sections [1]. These cross sections, shown in the left window of Fig.1, are calculated by including contributions from both the *s*-channel process through the $\Sigma^*(1358)$ resonance and the *t*-channel process via the exchange a scalar sigma meson. Although the thermally averaged cross sections due to the *t*-channel process is about a factor of 1.3 larger than those of the *s*-channel process, as shown in the middle window of Fig. 1, the ratio of the spin flip to non-flip cross sections is negligibly small compared to that from the s-channel process, which has a constant value of 1/3.5 [2]. Because of the latter small value, the spin polarization of Lambda hyperon is found to decrease by only about 7% during the hadronic stage of these collisions as shown in the right window of Fig. 1. Our result thus justifies the assumption in theoretical studies of Lambda hyperon polarization that compare its value calculated at the chemical freeze out to the measured one at the kinetic freeze out [3,4].

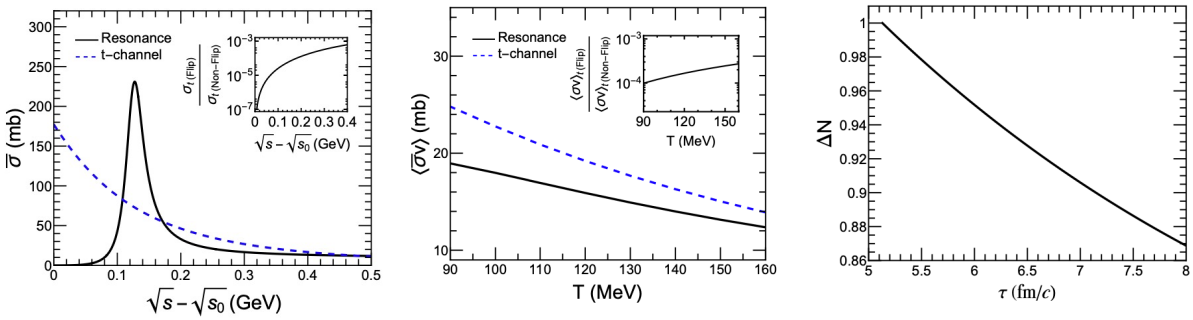

FIG. 1. Left window: Energy dependence of spin averaged $\boldsymbol{\Lambda + \pi \rightarrow \Lambda + \pi}$ cross section for the *s*-channel process through the $\boldsymbol{\Sigma^*(1358)}$ resonance (solid line) and the *t*-channel process via the exchange a scalar sigma meson (dashed line). Also shown in the inset is the ratio of spin flip to non-flip cross sections for the *t*-channel process. Middle window: Thermally averaged $\boldsymbol{\Lambda - \pi}$ scatting cross section in *s*-channel (solid line) and t-channel (dashed line) as functions of temperature. Also shown in the inset is the ratio of thermally averaged Lambda spin flip to non-flip cross sections as a function of temperature. Right window: Time evolution of the normalized number difference between spin up and spin down Lambda hyperons in Au-Au collisions at $\boldsymbol{\sqrt{s_{NN}} = 7.7}$ GeV.

[1] H. Sung, C.M. Ko, and S.H. Lee, arXivv:2404.15890 [nucl-th].

[2] C.M. Ko, EPJ Web Conf. **276**, 06001 (2023).

[3] I. Karpenko and F. Becattini, Eur. Phys. J. C **77**, 213 (2017).

[4] H. Li, L.-G. Pang, Q. Wang, and X.-L. Xia, Phys. Rev. C **96**, 054908 (2017).

K_1/K^* enhancement in heavy-ion collisions and the restoration of chiral symmetry

H. Sung,[1] S. Cho,[2] C. M. Ko, S. H. Lee,[1] and S. Lim[3]

[1]*Department of Physics and Institute of Physics and Applied Physics, Yonsei University, Seoul 03722, Korea*

[2]*Division of Science Education, Kangwon National University, Chuncheon 24341, Korea*

[3]*Department of Physics, Pusan National University, Pusan 46241, Korea*

We have extended the recent study of K_1/K^* enhancement as a signature of chiral symmetry restoration in heavy ion collisions at the CERN Large Hadron Collider via the kinetic approach [1] to include the effects due to non-unity hadron fugacity during the evolution of produced hadronic matter and the temperature-dependent K_1 mass [2]. It is found that including non-unity pion and kaon fugacity (middle window of Fig. 1) reduces slightly the K_1/K^* enhancement found in previous study due to chiral symmetry restoration but adding temperature-dependent K_1 mass (left window of Fig. 1) leads to a substantial further reduction of the K_1/K^*enhancement. However, the final K_1/K^* ratio still shows a factor of 2.4 and 1.3 enhancement, respectively, in peripheral and midcentral collisions compared to the case without chiral symmetry restoration as shown in right window of Fig. 1, confirming its use as a good signature for chiral symmetry restoration in the hot dense matter produced in relativistic heavy ion collisions.

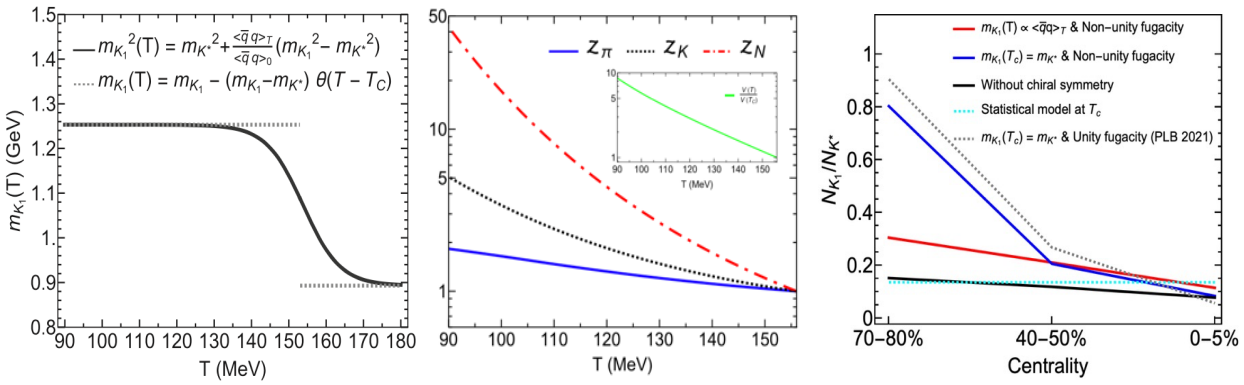

FIG. 1. (Left window) Temperature dependence of $\boldsymbol{K_1}$mass. Solid line is from the QCD sum rule calculations of Ref. [3], while dotted line is the one assumed in Ref. [1] with $\boldsymbol{T_C = 156}$ MeV. (Middle window) Temperature dependence of the pion (solid line), kaon (dotted line), and nucleon (dash-dotted line) fugacity as well as the volume ratio of hadronic matter (solid line in the inset). (Right window) The $\boldsymbol{K_1/K^*}$ yield ratio in Pb-Pb collisions at $\sqrt{\boldsymbol{s_{NN}}}$= 5.02 TeV at three centralities of 0–5%, 40–50%, and 70–80% for various scenarios of K_1 mass and hadronic matter property.

[1] H. Sung, S. Cho, J. Hong, S.H. Lee, S. Lim, and T. Song, Phys. Lett. B **819**, 136388 (2021).

[2] H. Sung, S. Choo, C.M. Ko, S.H. Lee, and S. Lim, Phys. Rev C **109**, 044911 (2024).

[3] S.H. Lee, Symmetry **15**, 799 (2023).

Kinetic approach to light-nuclei production in intermediate-energy heavy-ion collisions

R. Wang,[1,2] Y.G. Ma,[1,3] L.W. Chen,[4] C.M. Ko, K.J. Sun,[1,3] and Z. Zhang[5]

[1]*Key Laboratory of Nuclear Physics and Ion-beam Application (MOE), Institute of Modern Phys, Fudan University, Shanghai 200433, China*

[2]*Shanghai Institute of Applied Physics, Chinese Academy of Sciences, Shanghai 201800, China*

[3]*Shanghai Research Center for Theoretical Nuclear Physics, NSFC and Fudan University, Shanghai 200438, China*

[4]*School of Physics and Astronomy, Shanghai Key Laboratory for Particle Physics and Cosmology, and Key Laboratory for Particle Astrophysics and Cosmology (MOE), Shanghai Jiao Tong University, Shanghai 200240, China*

[5]*Sino-French Institute of Nuclear Engineering and Technology, Sun Yat-Sen University, Zhuhai 519082, China*

We have developed a kinetic approach to the production of light nuclei up to mass number $A \leq 4$ in intermediate-energy heavy-ion collisions by including them as dynamic degrees of freedom [1]. The conversions between nucleons and light nuclei during the collisions are incorporated dynamically via the breakup of light nuclei by a nucleon and their reverse reactions. We have also included the Mott effect on light nuclei [2,3], i.e., a light nucleus will no longer be bound if the phase-space density of its surrounding nucleons is larger than the cutoff parameter $f_A^{\rm cut} \geq \int f_N\left(\frac{\boldsymbol{P}}{A}+\boldsymbol{p}\right)\rho_A(\boldsymbol{p})d^3\boldsymbol{p}$, where $\rho(\boldsymbol{p})$ denotes the

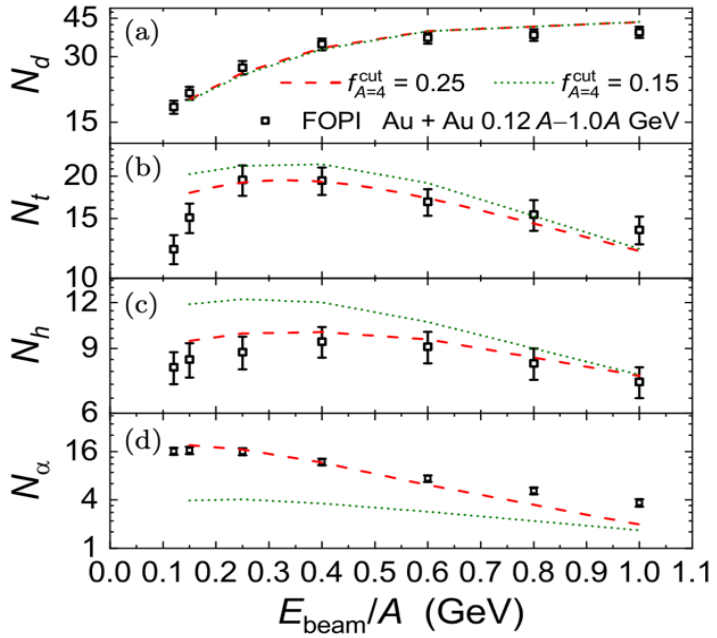

FIG. 1. Incident-energy dependence of light-nuclei yields from kinetic approach with $\boldsymbol{f_{A=2}^{\rm cut}=0.11}$, $\boldsymbol{f_{A=3}^{\rm cut}=0.16}$, and $\boldsymbol{f_{A=4}^{\rm cut}=0.25}$. The results for a smaller $\boldsymbol{f_{A=4}^{\rm cut}=0.15}$ are also included for comparison. The experimental data are from the FOPI Collaboration [4,5].

nucleon momentum distribution inside a light nucleus consisting of A nucleons and f_N is the nucleon phase-space distribution in the medium with $\boldsymbol{P}$ being the total momentum of the A nucleons. With this kinetic approach, we have obtained a reasonable description of the measured yields of light nuclei in central Au + Au collisions at energies of 0.25A GeV-1.0A GeV by the FOPI Collaboration [4,5], as shown in Fig. 1. Our study also indicates that the observed enhancement of the alpha-particle yield at low incident energies can be attributed to a weaker Mott effect on the alpha particle, which makes it more difficult to dissolve in nuclear medium, because of its much larger binding energy.

[1] R. Wang, Y.G. Ma, L.W. Chen, C.M. Ko, K.J. Sun, and Z. Zhang, Phys. Rev. C **108**, L031601 (2023).

[2] G. Röpke, L. Münchow, and H. Schulz, Nucl. Phys. **A379**, 536 (1982).

[3] G. Röpke, M. Schmidt, L. Münchow, and H. Schulz, Nucl. Phys. **A399**, 587 (1983).

[4] FOPI Collaboration, Nucl. Phys. **A848**, 366 (2010).

[5] R. Bougault, B. Borderie, A. Chbihi, Q. Fable, J. D. Frankland, E. Galichet, T. Genard, D. Gruyer, M. Henri, M. La Commara, N. Le Neindre, I. Lombardo, O. Lopez, M. Pârlog, P. Pawłowski, G. Verde, E. Vient, and M. Vigilante, Symmetry **13**, 1406 (2021).

Quantum mechanical softening of the hypertriton transverse momentum spectrum in heavy-ion collisions

D.-N. Liu,[1, 2] C. M. Ko, Y.-G. Ma,[1, 2] F. Mazzaschi,[3] M. Puccio,[4] Q.-Y. Shou,[1, 2]
K.-J. Sun,[1, 2] and Y.-Z. Wang[1, 2]

[1]*Key Laboratory of Nuclear Physics and Ion-beam Application (MOE), Institute of Modern Physics, Fudan University, Shanghai 200433, China*

[2]*Shanghai Research Center for Theoretical Nuclear Physics, NSFC and Fudan University, Shanghai 200438, China*

[3]*Dipartimento di Fisica dell'Universita and Sezione INFN, Turin, Italy*

[4]*Experimental Physics Department, CERN, CH-1211 Geneve23, Switzerland*

We have investigated hypertriton production in Pb-Pb collisions at $\sqrt{s_{NN}} = 5.02$ TeV using the coalescence model with kinetic freeze-out nucleons and Λ hyperons from a microscopic hybrid approach [1] based on the MUSIC hydrodynamic model [2,3] and the UrQMD hadronic transport model [4]. We have found that the halo structure of hypertriton with a large $\Lambda - d$ distance of approximately 10 fm leads to not only a suppression of ${}^{3}_{\Lambda}\mathrm{H}$ yield but also a softening of its transverse momentum spectrum with a weak centrality dependence as shown in Fig. 1. In particular, the mean transverse momentum of ${}^{3}_{\Lambda}\mathrm{H}$, shown in Fig. 2, is found to be significantly smaller than that of helium-3 even in the most central

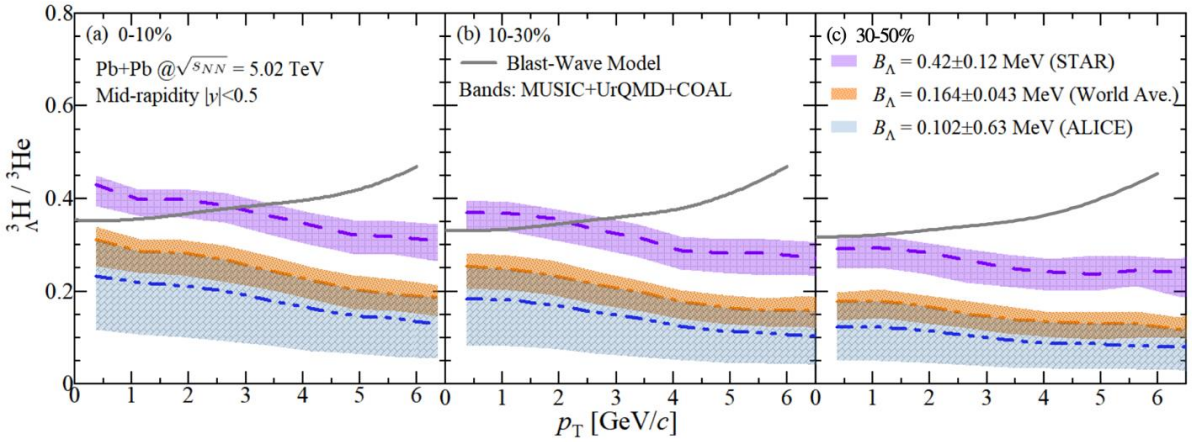

FIG. 1. The yield ratio of hypertriton to helium-3 as a function of transverse momentum in Pb-Pb collisions at $\sqrt{s_{NN}} = 5.02$ TeV for 0-10% (a), 10-30% (b), and 30-50% (c) centralities. Results from the coalescence approach (MUSIC+UrQMD+COAL) and blast-wave model are denoted by shaded regions and solid lines, respectively.

collisions, which is in sharp contrast with the prediction of the blast-wave model [5]. Such a quantum mechanical softening of the (anti-)hypertriton spectrum is a general feature and a natural outcome of the hypertriton wave function used in the final-state coalescence model, which can be readily tested in high-energy experiments with different beam energies and collision systems, providing thus a good opportunity to unravel the production mechanism of (anti-)hypernuclei in high-energy nuclear collisions and also to obtain constraints on the Λ-nucleon interaction.

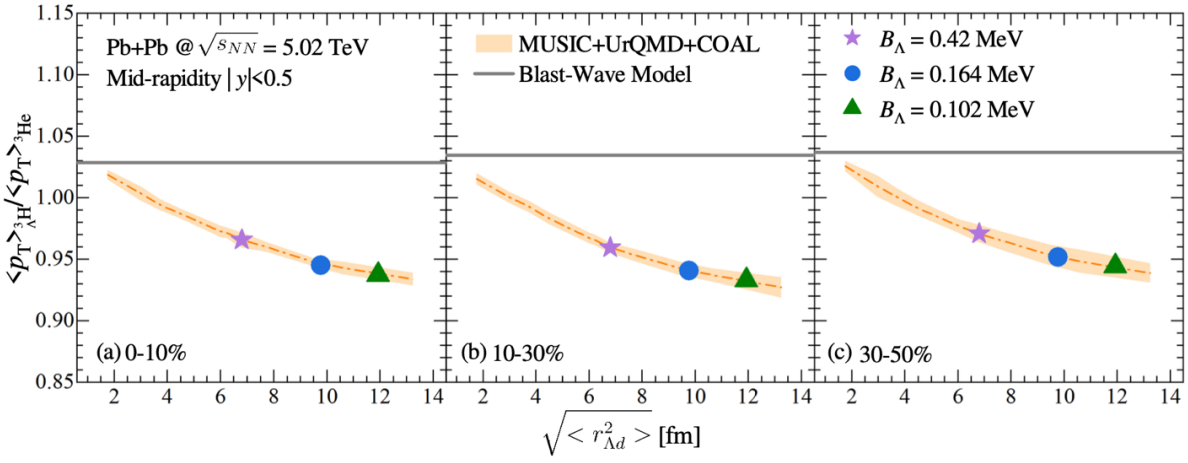

FIG. 2. Ratio of hypertriton to helium-3 mean transverse momentum as a function of $\boldsymbol{\Lambda - d}$ distance in Pb-Pb collisions at $\sqrt{\boldsymbol{s_{NN}}} = \mathbf{5.02}$ TeV for 0-10% (a), 10-30% (b), and 30-50% (c) centralities. The solid lines denote the prediction of the blast-wave model, whereas the shaded bands denote the prediction from the coalescence model. The solid symbols correspond to results obtained for various values of the $\boldsymbol{\Lambda}$ separation energy $\boldsymbol{B_\Lambda}$.

[1] D.N. Liu, C.M. Ko, Y.G. Ma, F. Mazzschi, M. Pucci, Q.Y. Shon, K.J. Sun, and Y.Z. Wang, arXiv:2404:02701 [nucl-th].

[2] A. Monnai, B. Schenke, and C. Shen, Phys. Rev. C **100**, 024907 (2019).

[3] C. Shen and S. Alzhrani, Phys. Rev. C **102**, 014909 (2020).

[4] S. A. Bass *et al.*, Prog. Part. Nucl. Phys. **41**, 255 (1998).

[5] E. Schnedermann, J. Sollfrank, and U.W. Heinz, Phys. Rev. C **48**, 2462 (1993).

Unveiling the dynamics of little-bang nucleosynthesis

K.J. Sun,[1,2] R. Wang,[1,3] C.M. Ko, Y.G. Ma,[1,2] and C. Sen[4,5]

[1]*Key Laboratory of Nuclear Physics and Ion-beam Application (MOE), Institute of Modern Phys, Fudan University, Shanghai 200433, China*

[2]*Shanghai Research Center for Theoretical Nuclear Physics, NSFC and Fudan University, Shanghai 200438, China*

[3]*Shanghai Institute of Applied Physics, Chinese Academy of Sciences, Shanghai 201800, China*

[4]*Department of Physics and Astronomy, Wayne State University, Detroit, MI 48201, USA.*

[5]*RIKEN BNL Research Center, Brookhaven National Laboratory, Upton, NY 11973, USA*

We have shown in a recent study via the relativistic kinetic approach that the post-hadronization dynamics plays an important role in the little-bang nucleosynthesis during high-energy heavy-ion collisions [1]. Specifically, we have found, as shown in Fig. 1, that the triton number produced from the created QGP

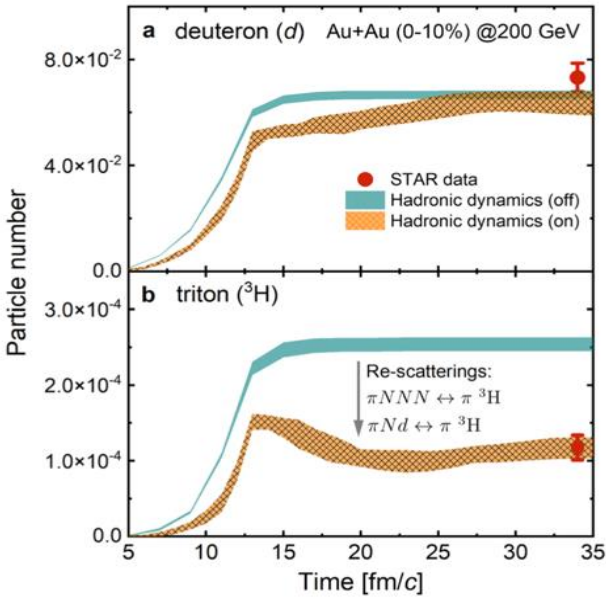

FIG. 1. Time dependence of deuteron (a) and triton (b) numbers in mid-rapidity ($|\boldsymbol{y}| < \mathbf{0.5}$). Experimental data with combined statistical and systematic uncertainties from Refs. [2,3] are denoted by filled symbols, while theoretical results with statistical uncertainties are shown by shaded bands.

in central Au + Au collisions is reduced by about a factor of 1.8 during the subsequent hadronic matter expansion, although the deuteron number is essentially not affected. These distinct hadronic effects on deuteron and triton production are in excellent agreement with recent measurements by the STAR Collaboration at RHIC [2,3] as shown in Fig. 2 and are further supported by the latest measurement by the ALICE Collaboration at the LHC [4,5] as shown in Fig. 3. Our study thus shows the inadequacy of the statistical hadronization model for understanding triton production in these collisions [6]. In contrast to the

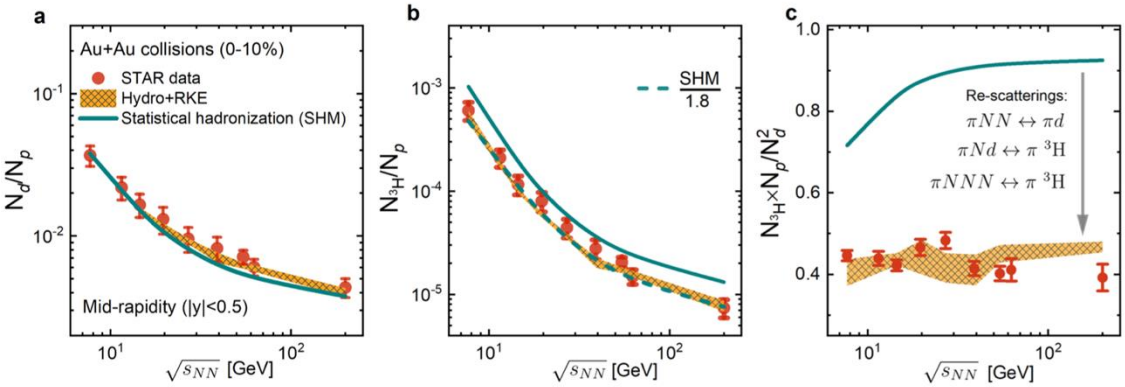

FIG. 2. Collision energy dependence of hadronic re-scattering effects on light nuclei yield ratios $\mathbf{N_d/N_p}$ (a), $\mathbf{N_{3He}/N_p}$ (b) and (c). Theoretical results with and without hadronic dynamics are from Hydro + RKE (shaded bands) and SHM [5] (lines), respectively. Experimental data points with combined statistical and systematic uncertainties are from the STAR Collaboration [2,3].

big-bang nucleosynthesis, in which photonuclear reactions dominate its dynamics, our model-to-data comparison unveils the importance of pion-catalyzed multi-body reactions on the dynamics of the little-bang nucleosynthesis in relativistic heavy- ion collisions.

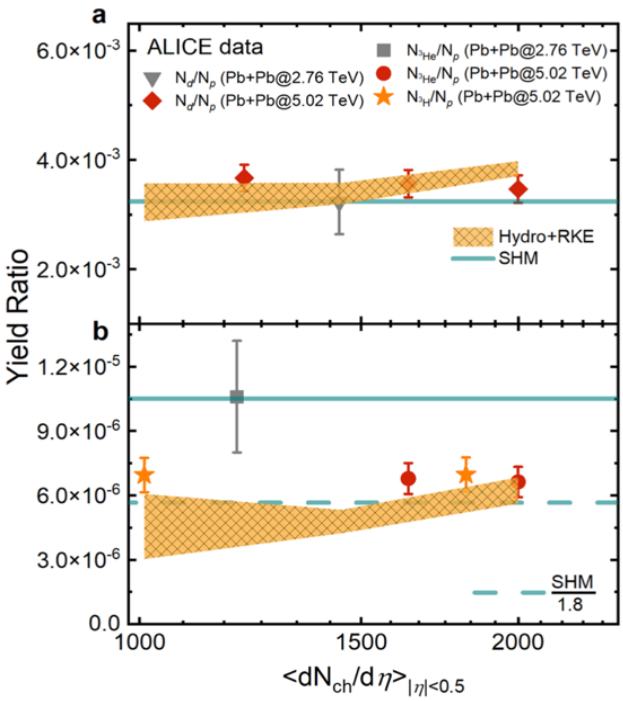

FIG. 3. Charged-particle multiplicity ($\mathbf{dN_{ch}/d\eta}$) dependence of hadronic re-scattering effects on light nuclei yield ratios $\mathbf{N_d/N_p}$ (a), $\mathbf{N_{3He}/N_p}$ and $\mathbf{N_{3H}/N_p}$ (b). Theoretical results with and without hadronic dynamics are from Hydro+RKE (shaded bands) and SHM [6] (lines), respectively. Experimental data points with combined statistical and systematic uncertainties are from the ALICE Collaboration [4,5].

[1] K.J. Sun, R. Wang, C.M. Ko, Y.G. Ma, and C. Sen, Nature Comm. **15**, 1975 (2024).
[2] M. Abdulhamid *et al.*, Phys. Rev. Lett. **130**, 202301 (2023).
[3] J. Adam *et al.*, Phys. Rev. C **99**, 064905 (2019).
[4] S. Achary *et al.*, Phys. Rev. C **107**, 064904 (2023).
[5] J. Adam *et al.*, Phys. Rev. C **93**, 024917 (2016).
[6] A. Andronic, P. Braun-Munzinger, K. Redlich, and J. Stachel, Nature **561**, 321 (2018).

Analytic and semi-analytic solutions to classical color glass models

R.J. Fries and S. Robicheaux

The initial phase of a collision of two nuclei at very high energy is thought to be described by the dynamcis of color glass condensate (CGC) [1,2]. Color glass condensate refers to the fact that the wave function of highly boosted nuclei is expected to be dominated by gluons with transverse polarization and at occupation numbers large enough to enable classical field concepts to apply. The first viable model of CGC became known as the McLerran-Venugopalan (MV) model [2]. Nuclear collisions can be computed as collisions of sheets of CGC, leading to a state usually called glasma. The output of such calculations can then be used to initialize calculations of the subsequent stages of a nuclear collision, in particular the approach to kinetic equilibrium and the following near-equilibrium fluid dynamic evolution of the system.

The IP-glasma model [3] offers a numerical implementation of the MV model which has been successfully used over the past decade in a variety of phenomenological calculations. Analytic solutions to the MV-model have been offered in [1] based on a series expansion in proper time. However, the convergence of the series is poor and only the earliest features, like the onset of radial flow in the glasma, can be studied analytically.

In the current project we have computed the energy momentum tensor of the glasma in the MV model analytically for all times in the weak field limit. Weak-field limit here means that all non-abelian terms after the initial non-abelian interaction of the sheets of color glass are dropped from the calculation. Technically this means that the fields we consider are of order g^3A^2 where g is the coupling constant of the strong force, and A generically denotes a gauge potential in one of the colliding nuclei. The restriction to weak fields allows for the analytic solution to be obtained. Collisions of lead nuclei at the Large Hadron Collider are strictly speaking outside of the applicability of the weak field limit. Thus, while valuable insights can be obtained from analytic solutions, their applicability to real collision system will have to be carefully investigated.

We find that the energy momentum tensor in the simplest case of nuclei of homogeneous average color charge densities $\langle\rho^2\rangle \sim \mu_1, \mu_2$ in nucleus 1 and 2, resp., is given by Meijer-G functions. For example, the energy density from longitudinal fields is [4]

$$\langle E_z^2 + B_z^2 \rangle = \frac{2\pi\alpha_s^3 N_c}{N_c^2 - 1} \mu_1 \mu_2 \frac{M(4m^2\tau^2)}{\tau}$$

where $N_c = 3$ is the number of colors, $\alpha_s = g^2/4\pi$, and M is a linear combination of three Meijer-G functions. The averaging here is over all color charge densities that are allowed for given μ_1, μ_2. The McLerran-Venugopalan model suffers from infrared (IR) and ultraviolet (UV) divergences which require ad-hoc regularizations. The former is indicated by the presence of an IR cutoff m in the result above, which is chosen to be implemented as an effective gluon mass in the Green's function for the gluon field. Fig. 1 shows a comparison of our results for the reduced longitudinal and transverse pressure with a numerical calculation using the publically available IP glasma code. The two calculations agree over most of the time

but differ for times from around 0.1 to 0.4 fm. Some disagreement is to be expected as scales would have to be carefully matched between the discretized numerical solution and our analytic solution. However, agreement is reached in the long time limit.

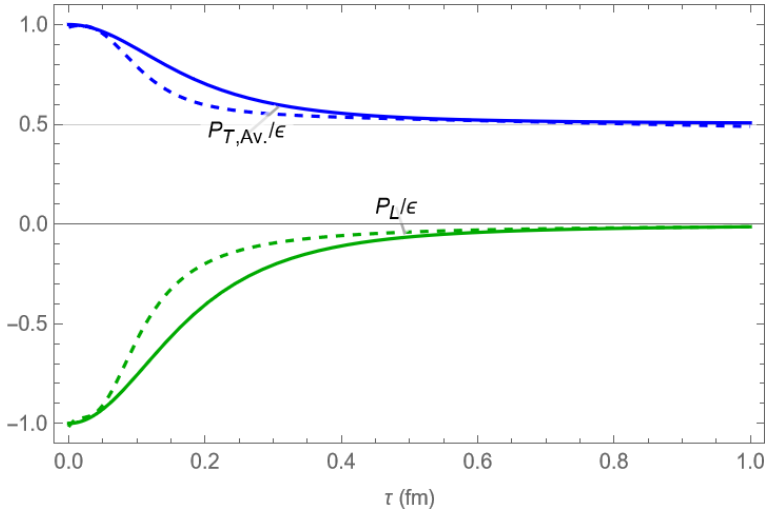

FIG. 1. Ratios of transverse pressure $\boldsymbol{p_T}$ and longitudinal pressure $\boldsymbol{p_L}$ over the energy density $\boldsymbol{\epsilon}$ as functions of proper time $\boldsymbol{\tau}$ in the McLerran-Venugopalan model [4]. Solid lines: analytic result. Dashed line: numerical solution using the IP glasma code [3].

The divergences in the MV-model have motivated us to propose a new model which is called the improved Gaussian model. It removes UV-divergences by smearing the initial charge distribution on small but finite length scales. It also implements global color neutrality which considerably softens (but not completely removes) the IR divergences. The improved Gaussian model is more challenging to handle in analytic calculations, but we have computed expressions for the energy momentum tensor of the glasma up to one integral which remains to be done numerically [4].

This work was support by the U.S. National Science Foundation under awards 1812431 and 2111568.

[1] G. Chen, R. J. Fries, J. I. Kapusta, Y. Li, Phys. Rev. C **92**, 064912 (2015).
[2] L. D. McLerran, R. Venugopalan, Phys. Rev. D **49**, 2233 (1994).
[3] B. Schenke, P. Tribedy , R. Venugopalan, Phys. Rev. Lett. **108**, 252301 (2012).
[4] S. Robicheaux and R. J. Fries, (2024) submitted.

The JETSCAPE collaboration: Hybrid hadronization updates and studies of hadronic rescattering

R.J. Fries with JETSCAPE Collaborators

In previous versions of this report we have discussed the continuing work of the JETSCAPE collaboration. JETSCAPE is a multi-disciplinary collaboration, supported by NSF, which is tasked to develop a software framework for simulations of high energy nucleus-nucleus and other collisions. In this reporting period, both products of the JETSCAPE collaboration, the JETSCAPE framework and the XSCAPE framework, underwent major updates with members of the Texas A&M group playing an outsize role [1]. The largest change included in the updates to JETSCAPE 3.6 and XSCAPE 1.1, respectively, concern the Hybrid Hadronization model which was developed at Texas A&M. With the help of members of Hannah Elfner's group in Frankfurt, in particular through the efforts of Hendrik Roch, significant improvements to Hybrid Hadronization were made.

These improvements include: increased stability, in particular by processing string configurations which are too complex for PYTHIA 8 to fragment; precise net baryon number conservation by eliminating several bugs in the handling of string junctions; better treatment of beam partons; for the first time, the possibility to hadronize parton "holes" in quark gluon plasma that are tracked by some shower Monte Carlo codes; stricter enforcement of energy and momentum conservation; more precise determination of the final positions of hadrons from string fragmentation; a more complete spectrum of excited meson states that partons can recombine into, including all quark model states from the particle data book; compatibility of output with the hadronic transport model SMASH.

The last improvement unlocks a new ability for the JETSCAPE and XSCAPE frameworks. Hadrons from hard processes can now be fed into SMASH to compute hadronic final state interactions for jets both in vacuum and in a medium. SMASH had previously only been used as an afterburner for output from fluid dynamic simulations, i.e. in the soft sector of high energy nuclear collisions. Preliminary studies were carried out to test the new functionality, and a systematic study of the effects of hadronic final state rescattering in the vacuum was begun.

Fig. 1 shows preliminary results from simulations of electron-position collisions at the Z-pole energy of 91.2 GeV. This collision system is the experimentally and theoretically cleanest test of our understanding of jet physics. Interestingly, we see significant (up to 15%) percent effects on hadron spectra. Hadronic rescattering seems to lead to some kind of self-quenching in which the higher momentum hadrons are slightly depleted and the fraction of very low momentum hadrons increases. This preliminary result provides ample motivation to study these effects carefully even for vacuum systems. We expect the hadronic rescattering to be even more impactful in nucleus-nucleus collisions, where the system is surrounded by a thick "corona" of hot hadron matter which can be simulated by SMASH.

This work was support by the U.S. National Science Foundation under award 2004571, and by the ExtreMe Matter Institute EMMI at the GSI Helmholtzzentrum für Schwerionenforschung, Darmstadt, Germany.

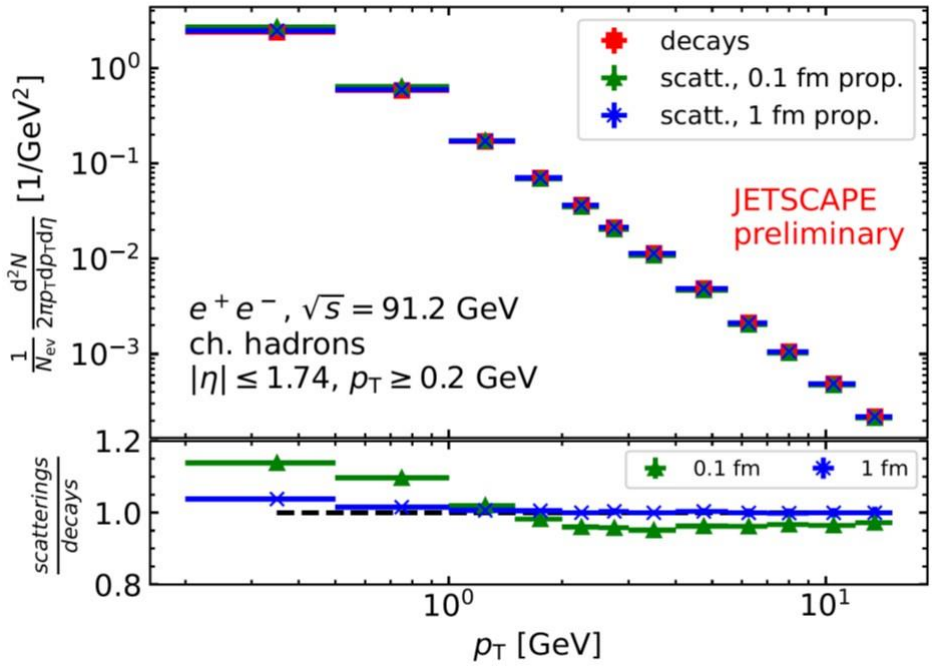

FIG. 1. The spectrum of charged hadrons in e+e- collisions at an energy of 91.2 GeV. Results are shown for hadron decays only in SMASH, and two scenarios with hadronic rescattering in SMASH with hadrons propagating for a proper time of 0.1 or 1 fm/c, respectively. The bottom panel shows the ratio of the latter two result with the decays only case. Hadronic rescattering has an effect even in this very dilute system.

[1] The JETSCAPE 3.6x and XSCAPE 1.1.x packages, https://github.com/JETSCAPE

$\psi(2S)$ Transport in heavy-ion collisions at the LHC

B. Wu and R. Rapp

I. Introduction

The production of charmonia in ultra-relativistic heavy-ion collisions (URHICs) has been an active area of research for four decades. The initially proposed J/ψ suppression signature of quark–gluon plasma (QGP) formation [1] has developed into more comprehensive transport models that account for regeneration mechanisms as dictated by the principle of detailed balance. This ensures that the abundances of charmonia approach their pertinent equilibrium limits, see, e.g., Refs. [2, 3] for reviews. Recent pioneering ALICE measurements [4] of $\psi(2S)$ production at low transverse momenta (p_T) are providing critical constraints to model calculations and can be used to test a "sequential regeneration" of J/ψ and $\psi(2S)$ mesons [5].

II. Methods

We provide an update of our semi-classical transport approach [6, 7] for quarkonium production in URHICs, focusing on J/ψ and $\psi(2S)$ mesons in 5.02 TeV Pb-Pb collisions at the Large Hadron Collider (LHC) [8]. We have employed the most recent charm-production cross sections reported in pp collisions, which are pivotal for the magnitude of the regeneration contribution, and their modifications due to cold-nuclear-matter (CNM) effects. We have also utilized an improved input for the in-medium charmonium binding energies to ensure an approximately constant J/ψ mass, consistent with our bottomonium calculations [9]. This update was rather mild and has a very small net effect on the total production. We have further reassessed the relevance of inelastic-scattering versus gluo-dissociation mechanisms, confirming them to be rather negligible.

III. Results

In our applications to phenomenology, we specifically elaborate on predictions for recent ALICE data on $\psi(2S)$ production in 5.02 TeV Pb-Pb collisions at the LHC [4]. Multi-differential observables are calculated in terms of nuclear modification factor (R_{AA}) as a function of centrality, transverse momentum, and rapidity, including the contributions from feeddown from bottom hadron decays. Our predictions for $\psi(2S)$ production, both in terms of the nuclear modification and the ratio relative to J/ψ production, are in good agreement with the data, see Fig. 1. Specifically, the $\psi(2S)/J/\psi$ ratio is significantly larger than what one would expect from the equilibrium values at a given temperature. This originates from the fact that the $\psi(2S)$ is regenerated much later in the fireball evolution than the more strongly bound the J/ψ, due to its much smaller binding energy. The mechanism of sequential regeneration relative to the more strongly bound J/ψ meson thus plays an important role in interpreting recent ALICE data.

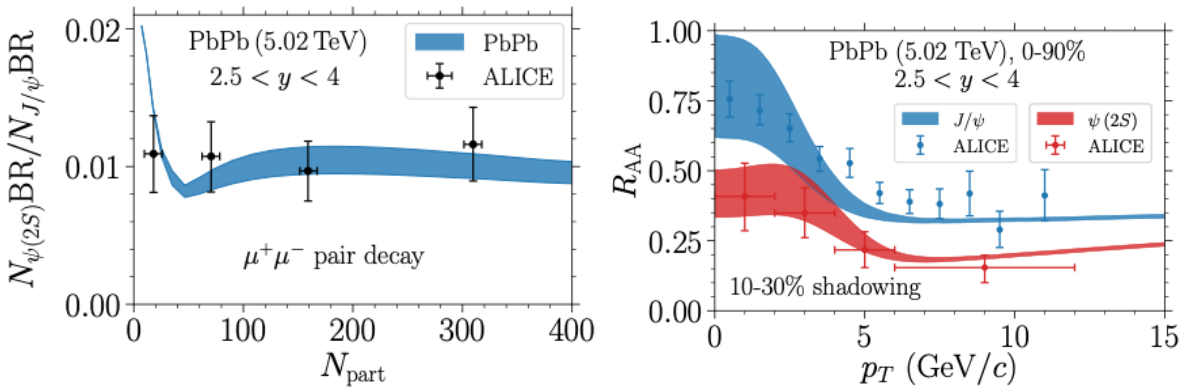

FIG. 1. Left: the ratio of $\boldsymbol{\psi(2S)}$ over $\boldsymbol{J/\psi}$ as a function of centrality ($\boldsymbol{N_{part}}$) in Pb-Pb (5.02 TeV) collisions at forward rapidity, compared to ALICE data [4]. The bands indicate the uncertainty of the $\boldsymbol{\psi(2S)}$ dissociation temperature around the mixed phase, $\boldsymbol{T_{diss}}$ =179–180 MeV. Right: nuclear modification factor ($\boldsymbol{R_{AA}}$) as a function of transverse momentum ($\boldsymbol{p_T}$) for inclusive $\boldsymbol{J/\psi}$ (blue) and $\boldsymbol{\psi(2S)}$ (red) production at forward rapidity in 0–90% Pb-Pb (5.02 TeV) collisions, compared to ALICE data [4]. The bands indicate the uncertainty due to nuclear shadowing.

[1] T. Matsui and H. Satz, Phys. Lett. B **178**, 416 (1986).

[2] R. Rapp, D. Blaschke, and P. Crochet, Prog. Part. Nucl. Phys. **65**, 209 (2010).

[3] A. Andronic *et al.*, Eur. Phys. J. A **60**, 88 (2024).

[4] S. Acharya *et al.*, Phys. Rev. Lett. **132**, 042301 (2024).

[5] X. Du and R. Rapp, Nucl. Phys. **A943**, 147 (2015).

[6] L. Grandchamp and R. Rapp, Nucl. Phys. **A709**, 415 (2002).

[7] X. Zhao and R. Rapp, Phys. Rev. C **82**, 064905 (2010).

[8] B. Wu and R. Rapp, Universe **10** (6), 244 (2024).

[9] X. Du, R. Rapp, and M. He, Phys. Rev. C **96**, 054901 (2017).

T-matrix analysis of static Wilson line correlators from lattice QCD at finite temperature

Z. Tang, S. Mukherjee, P. Petreczky and R. Rapp

The microscopic description of quark-gluon plasma (QGP), a strongly interacting medium where quarks and gluons are deconfined, is a fundamental objective in studying the phases of matter emerging from Quantum Chromodynamics (QCD). Heavy-flavor (HF) particles, i.e., charm and bottom quarks, are excellent probes for investigating the properties of QGP in ultrarelativistic heavy-ion collisions [1-3]. In particular, the in-medium properties of quarkonia, bound states of heavy quarks and antiquarks, offer unique insights into the QGP because they are closely related to the QCD force [4-6]. Toward this end, recent lattice-QCD (lQCD) studies have provided novel data on the Wilson line correlators (WLCs) (correlation functions of a static quark-antiquark pair) at finite temperature [7], which can be analyzed using theoretical models for the interactions between particles in QGP. It turns out that these lQCD results cannot be described by perturbative approaches [7], calling for non-perturbative methods like the thermodynamic T-matrix approach.

The T-matrix approach is a quantum many-body formalism that enables a self-consistent calculation of 1- and 2-body correlation functions in a strongly coupled QGP [8-10], encompassing both

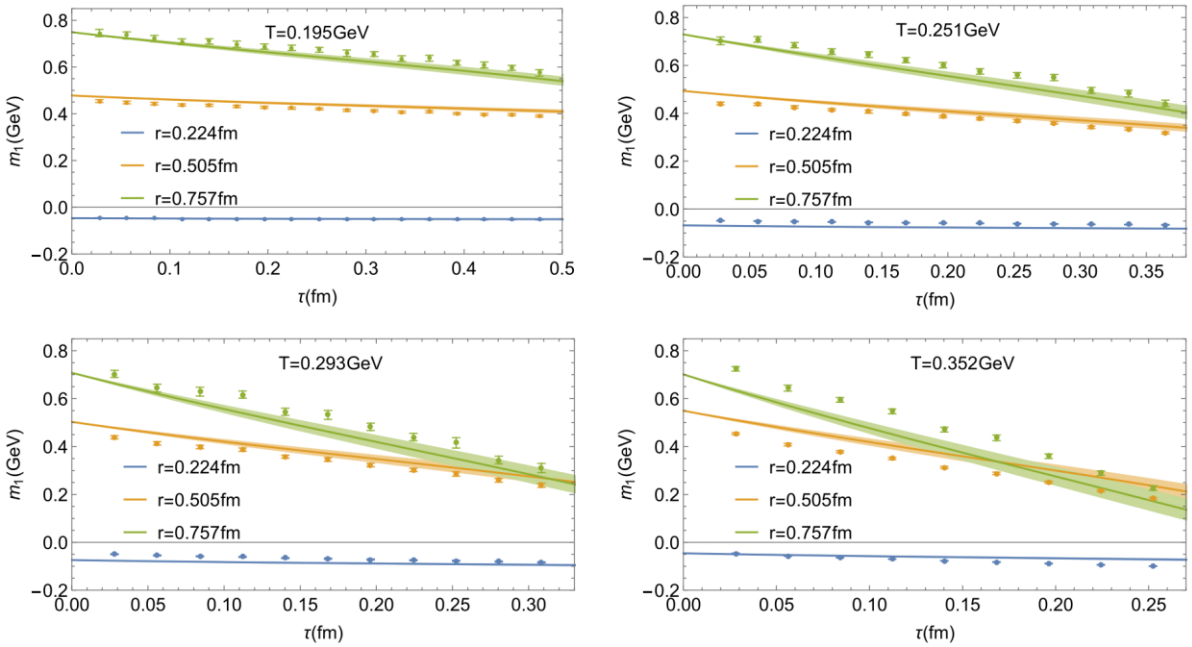

FIG. 1. The first cumulant of WLCs from the self-consistent T-matrix calculations (lines) as a function of imaginary time at different temperatures and distances, compared to the 2+1-flavor lQCD data [7].

bound states and scattering processes. The key input to this approach is the in-medium potential which has been constrained by static heavy-quark (HQ) free energies and Euclidean correlators in previous work [11]. Here we revisit these results using constraints from lQCD data on WLCs and the QGP equation of state [12].

We have found that with an in-medium Cornell potential that is less screened at higher temperatures than previously (specifically for the long-range confining force), one can achieve a good agreement with lQCD data, cf. Fig.1. The underlying in-medium potential, displayed in the left panel of Fig. 2, features remnants of the confining force up to rather large distances. This has significant consequences for the

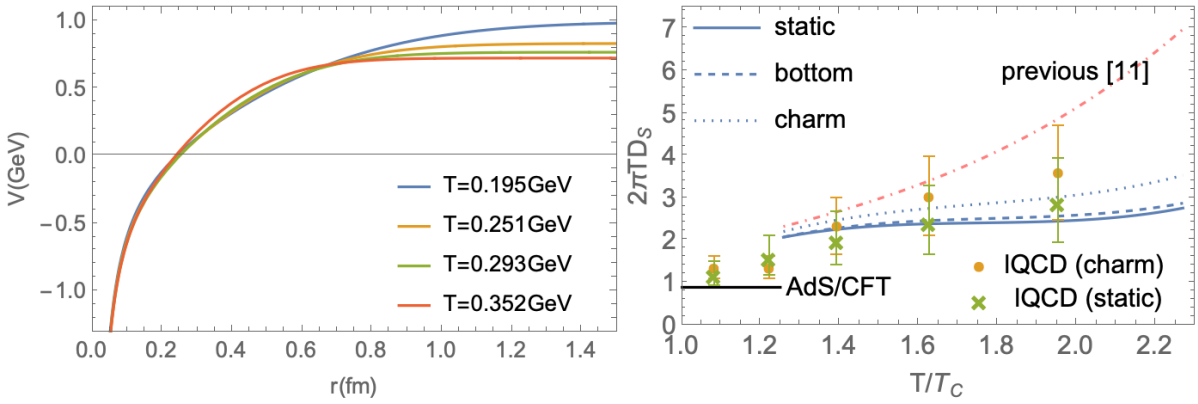

FIG. 2. Left panel: The in-medium potentials used in the T-matrix as a function of distance at different temperatures. Right panel: The spatial diffusion coefficients for charm, bottom and static quarks in comparison with 2+1-flavor lattice data [13,14]. The free energy-based results are from Ref. [11].

thermal relaxation rate, A(ρ,T) of heavy quarks, which shows a stronger temperature dependence than in our previous results based on HQ free energies. On the other hand, the predicted HQ spatial diffusion coefficient, which relates to the zero-momentum limit of the relaxation rate as $D_S = T/(M_Q A(0))$, exhibits a weaker T-dependence, in good agreement with recent lQCD results, cf. right panel in Fig. 2. Applications of these results to phenomenological studies in heavy-ion collisions are underway.

[1] F. Prino and R. Rapp, J. Phys. G **43**, 093002 (2016), 1603.00529.
[2] M. He, H. van Hees, and R. Rapp, Prog. Part. Nucl. Phys. **130**, 104020 (2023), 2204.09299.
[3] A. Beraudo *et al.*, Nucl. Phys. **A979**, 21 (2018), 1803.03824.
[4] R. Rapp, D. Blaschke, and P. Crochet, Prog. Part. Nucl. Phys. **65**, 209 (2010), 0807.2470.
[5] L. Kluberg and H. Satz, Landolt-Börnstein **23**, 372 (2010), 0901.3831.
[6] P. Braun-Munzinger and J. Stachel, Landolt-Börnstein **23**, 424 (2010), 0901.2500.
[7] D. Bala *et al.* (HotQCD), Phys. Rev. D **105**, 054513 (2022), 2110.11659.
[8] M. Mannarelli and R. Rapp, Phys. Rev. C **72**, 064905 (2005), hep-ph/0505080.
[9] F. Riek and R. Rapp, New J. Phys. **13**, 045007 (2011), 1012.0019.
[10] Z. Tang and R. Rapp, Phys. Rev. C. **108**(4), 044906 (2023).
[11] S. Y. F. Liu and R. Rapp, Phys. Rev. C **97**, 034918 (2018), 1711.03282.
[12] A. Bazavov *et al.* (HotQCD), Phys. Rev. D **90**, 094503 (2014), 1407.6387.
[13] L. Altenkort *et al.*, Phys. Rev. Lett. **130**(23), 231902 (2023); L. Altenkort *et al.*, Phys. Rev. Lett. **132**(5), 051902 (2024).

SECTION IV

SUPERCONDUCTING CYCLOTRON, INSTRUMENTATION AND RIB UPGRADE

K500 operations and development

G.J. Kim, B.T. Roeder, F.P. Abegglen, H.L. Clark, L. Gathings, D.P. May, and G. Tabacaru

Introduction

During the April 2023 to March 2024 reporting period a total of 6 different beams, including 4 newly developed beams were used for experiments. The SEE program and the radioactive beams are treated separately in the progress report.

Ion Sources

Both the ECR1 and ECR4 ion sources were available for the K500 operation. The ECR3 ion source was also available; in addition to its main role as the Charge Breeding ECR (CBECR) ion source for radioactive beams, it was used for the production of 47 AMeV zinc beam in March 2024. ECR4 was the main ion source for K500. However, having a second ion source in ECR1, it allowed us to prepare the source for some metal beams which would take longer than a few hours to get ready. Beams of ^{54}Fe and ^{58}Fe were produced from ECR1 using the High Temp Oven. However the iron beam intensities were not strong from ECR1, so the same ^{54}Fe and ^{58}Fe beams were produced by the sputtering method from ECR4. From Nov. 2023, the SEE beams has been prioritized for ECR1.

Cyclotron Beams

Four new beams that were developed for experiments are: 7.5 AMeV $^{54}Fe^{8+}$, 11.5 AMeV $^{56}Fe^{10+}$, and 11.5 AMeV $^{58}Fe^{11+}$, and 47 AMeV $^{64}Zn^{25+}$. 47 AMeV $^{64}Zn^{23+}$ beam was developed and used from 1996 to 2002, however in order to reduce the RF and the deflector conditioning time, the 25+ charge state was selected. The $^{64}Zn^{25+}$ beam was obtained with ECR3, a rod of natural zinc was placed near entrance of ECR3 and was sputtered to produce the beam. Initially, ECR1 was tried with an enriched ^{64}Zn sample loaded into the High Temp Oven, however the beam current from ECR1 was just too weak.

Operations

For the period April 1, 2023 through March 31, 2024, the operational time is summarized in Table I.

Table I. 2023-2024 Operational Time

Time	Hrs	%Time
Science	1224	14
SEE Line	4511	52
Beam Development	532	6
Unscheduled Maintenance	237	3
Scheduled Maintenance	2232	25
Total	8736	100

K150 Operations and development 2023-2024

B.T. Roeder, G.J. Kim, F. Abegglen, H. Clark, L. Gathings, D.P. May, H.I. Park and H. Peeler

The operation of the K150 cyclotron continued this year, providing beams to the science program, SEE line users, and the astatine 211 production program. For the reporting period 4/23-3/24, we logged over 5416 of beam on-target and 1472 hours of beam development as shown in Table I. Included in the beam on-target time was 4968 hours for in-house science experiments and astatine production and 448 hours for SEE line testing.

TABLE I. 2023-2024 operational time for the K150 cyclotron

Time	Hours	% Time
Beam on Target	5416	62%
Beam Development	1472	17%
Scheduled Maintenance	1760	20%
Unscheduled Maintenance	88	1%
Total	8736	100%

The active users of the K150 beams were the light ion guide (LIG) group, Yennello, Folden, Rogachev and Adsley groups. There was one external group, Professor Sobotka from Washington University in St. Louis, that used a beam for a MARS experiment.

The LIG group ran 5 experimental campaigns using proton beams with intensities of up to 12 μA and energies ranging from 10 to 23 MeV. Producing these beams has been relatively easy with the continued operation of the H^- ion source. The ion source output is regulated with the arc discharge current, and only a few amps are necessary to produce the needed beam. The injection efficiency of the beam continues to be good and the extraction efficiency through the carbon stripper foil continues to be high, often 80-90%. However, the beam size after extraction is somewhat large, and not all of the beam can be transported to the LIG target. Nevertheless, once the edges of the beam are removed with the collimators, transmission of the beam from FC02 to FC23 downstream of the LIG gas cell is often 90-100%. The highlight of this year's LIG runs was the production and re-acceleration of ^{89}Nb and ^{89}Zr with the ^{90}Zr(p,2n) and ^{90}Zr(p,d) reactions. These efforts are described in a separate report.

The astatine 211 production program also is continuing to use the beam regularly. This reporting year, there were 9 separate production runs. Each beam consisted of $^4He^{1+}$ beam at 7.2 MeV/u and with intensities between 8 to 13 μA on target. A typical irradiation of the bismuth production target lasts overnight and has a total run time of 14-16 hours. The beam tune for the ^{4}He beam has become relatively routine and can often be optimized within 4-6 hours. However, small improvements to the beam tuning have been made, and this year a new record intensity of 20 μA extracted to FC02 was obtained. It should be noted that this result was observed on a day where there was particularly good vacuum reading ($7.6*10^{-7}$) on the cyclotron ion gauge.

High intensity metal ion beams are being developed with ECR2 and the K150 cyclotron with the MIVOC method. This year, iron and titanium beams were developed. A new coupling flange and fixture were tested such that the metal vapor could flow into the ion source through the side of the plasma chamber where the oven and sputtering fixture would normally be mounted. For the iron beam test, natural ferrocene was used and up to 38 μA of $^{56}Fe^{10+}$ was observed from ECR2. (Trimethyl)pentamethylcyclopentadienyltitanium(IV) was employed for the Ti beam test. Up to 18 μA of $^{48}Ti^{11+}$ was observed from ECR2, which led to about 200 nA of beam extracted from the cyclotron on FC02. The transmission of the $^{48}Ti^{11+}$ beam through the cyclotron for the high main magnet settings necessary for 6.5 MeV/u beam will be improved in subsequent runs. Further details about the MIVOC tests are given in a separate report.

Finally, beginning in January 2024, the existing H^- source was dismounted and replaced with a new filament ion source manufactured by D-Pace Inc. [1]. The new filament ion source can provide both positive and negative hydrogen ions as well as positive ^3He and ^4He ions. Installation of this new ion source took place from January-March 2023 and commissioning of the new source will continue in the coming year.

[1] Positive/Negative Filament Ion Source, Model # ISV.F-100, D-Pace Inc. – https://www.d-pace.com/?e=363

Texas A&M Cyclotron Radiation Effects Facility
April 1, 2023 – March 31, 2024

H.L. Clark, G. Avila, V. Horvat, B. Hyman, M. Kennas, G. Kim, H. Park, C. Parker,
B. Roeder, G. Tabacaru and E. Wilkinson

The activity of the Radiation Effects Facility (REF) increased substantially from last year and was the highest reported year ever. In this reporting period, the facility was used for 4,386 hours, which is a 19% increase over the hours of 2022-2023. Users of the facility (and hours used) over the past year were:

Table 1. Radiation Effects Facility usage by commercial and government customers for this and previous reporting years.

Reporting Year	Total Hours	Commercial Hours (%)	Government Hours (%)
2023-2024	4,386	3,581 (82%)	805 (18%)
2022-2023	3,684	2,991 (81%)	693 (19%)
2021-2022	3,852	3,122 (81%)	730 (19%)
2020-2021	3,300	2,435 (74%)	865 (26%)
2019-2020	3,982	2,862 (72%)	1120 (28%)
2018-2019	3,678	2,939 (80%)	739 (20%)
2017-2018	3,681	2,622 (71%)	1,059 (29%)
2016-2017	3,355	2,501 (75%)	854 (25%)
2015-2016	3,042	2,326 (76%)	716 (24%)
2014-2015	3,024	1,975 (65%)	1,049 (35%)
2013-2014	2,399	1,517 (63%)	882 (37%)
2012-2013	2,626	1,856 (71%)	770 (29%)
2011-2012	2,673	1,630 (61%)	1,043 (39%)
2010-2011	3,042	1,922 (63%)	1,121 (37%)
2009-2010	2,551	1,692 (66%)	859 (34%)
2008-2009	2,600	1,828 (70%)	772 (30%)
2007-2008	2,373	1,482 (62%)	891 (38%)
2006-2007	2,498	1,608 (64%)	890 (36%)
2005-2006	2,314	1,314 (57%)	1,000 (43%)
2004-2005	2,012	1,421 (71%)	591 (29%)
2003-2004	1,474	785 (53%)	689 (47%)
2002-2003	1,851	1,242 (67%)	609 (33%)
2001-2002	1,327	757 (57%)	570 (43%)
2000-2001	1,500	941 (63%)	559 (37%)
1999-2000	548	418 (76%)	131 (24%)
1998-1999	389	171 (44%)	218 (56%)
1997-1998	434	210 (48%)	224 (52%)
1996-1997	560	276 (49%)	284 (51%)
1995-1996	141	58 (41%)	83 (59%)

Northrop Grumman (276), Renesas (260), Lockheed Martin (227), Texas Instruments (234), Honeywell (233), RTS (228), Raytheon (216), Scientic (198.5), Sandia (188), Boeing (177), Navy Crane (164), AFRL (160), Draper (147), Infineon (130), EPC Space (112), Frontgrade (104), SEAKR (80), Trusted Semiconductor (80), VPT Inc (80), Thales Alenia Space (72), Vanderbilt (64), Johns Hopkins (56), Troxel Engineering (56), Aerospace (48), BroadCom (48), Space X (48), Blue Origin (40), Crane AE (40), NASA GSFC (40), NASA JSC (37.5), Analog Devices (35), L3Harris (32), NASA JPL (32), Signal Analysis (32), UT Dallas (32), Axiom Space (26), Amazon (24), Malin Space (24), Milanowski (24), Millennium (24), T2 Research (24), BAE Systems (16), Cisco (16), GSI Technology (16), Microchip (16), QualComm (16), Teledyne (16), Trystine (16), VPT RAD (16), Avalanche (14), General Dynamics (14), Volta Space (13), SMU (12), Astranis (8), Colorado University (8), JD Instruments (8), Aria Labs (8), Los Alamos (8), NuTrek (8), and TAMU Physics (4). Malin Space and Volta Space were new users.

Table I compares the facility usage by commercial and government customers. While commercial hours still dominate, the ratio from this reporting year (82% to 18%) is similar to the usage in the most recent reporting periods (see Fig 1). Commercial usage increased by 20% and was the highest commercial usage ever. Government usage increased by 16% but was still low compared to earlier reporting periods.

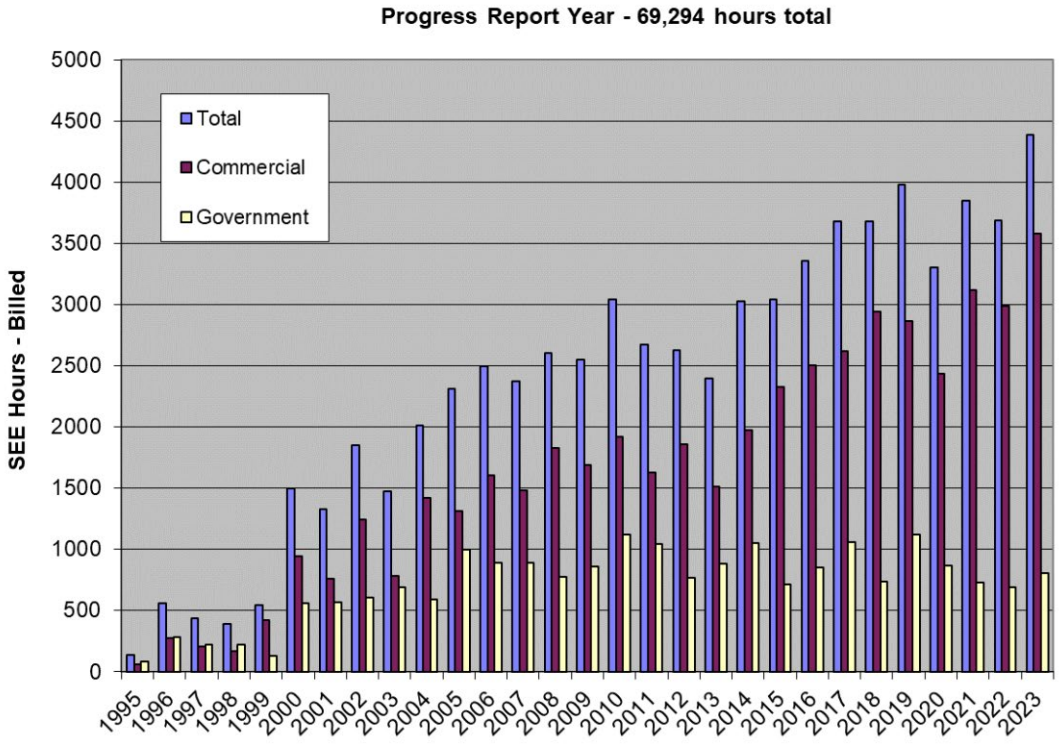

FIG. 1. Radiation Effects Facility usage by commercial and government customers for this and previous reporting years. While commercial hours still dominate, the ratio from this reporting year (82% to 18%) is similar compared to usage from prior reporting periods. Usage hours increased significantly from last year's reporting period (by 19%) was the highest amount in history. 69,294 hours have been billed since the start of the project in 1995.

The 15 MeV/u ions were the most utilized and especially 15 MeV/u Ag and Au. No new beams were added to the K500 cyclotron SEELine users list. Much of the testing conducted at the facility continues to be for defense systems by both government and commercial agencies. We had three foreign users at the facility: Thales Alenia Space-Spain and France (72 hours), Teledyne-Canada (16 hours) and Volta Space-Canada (13 hours).

Recent progress on the light ion guide project

G. Tabacaru, V. Kolhinen, J. Ärje, D.P. May, A. Saastamoinen, F.P. Abegglen, L.N. Gathings, G.J. Kim, S. Molitor, and B.T. Roeder

The Light Ion Guide Project continued to be developed at our facility [1]. The focus was on the optimization of the overall efficiency. Several experiments were conducted using proton beam and ^{114}Cd and ^{90}Zr target. A mobile section of the Sextupole Ion Guide (SPIG) was used to check the production of the radioactive ions: ^{114}In and ^{90}Nb.

The main factors contributing to the optimization of the production of the radioactive ions are: pressure in the gas cell (or flow of Helium), the resonant frequency where the SPIG operates, the proton beam intensity, and various settings of the voltages on the vacuum barriers and the voltage applied to the gas cell. In Fig. 1 is presented a beta decay spectrum of the ^{114}In produced using protons with energy of 10.5 MeV and intensity of 6 μA.

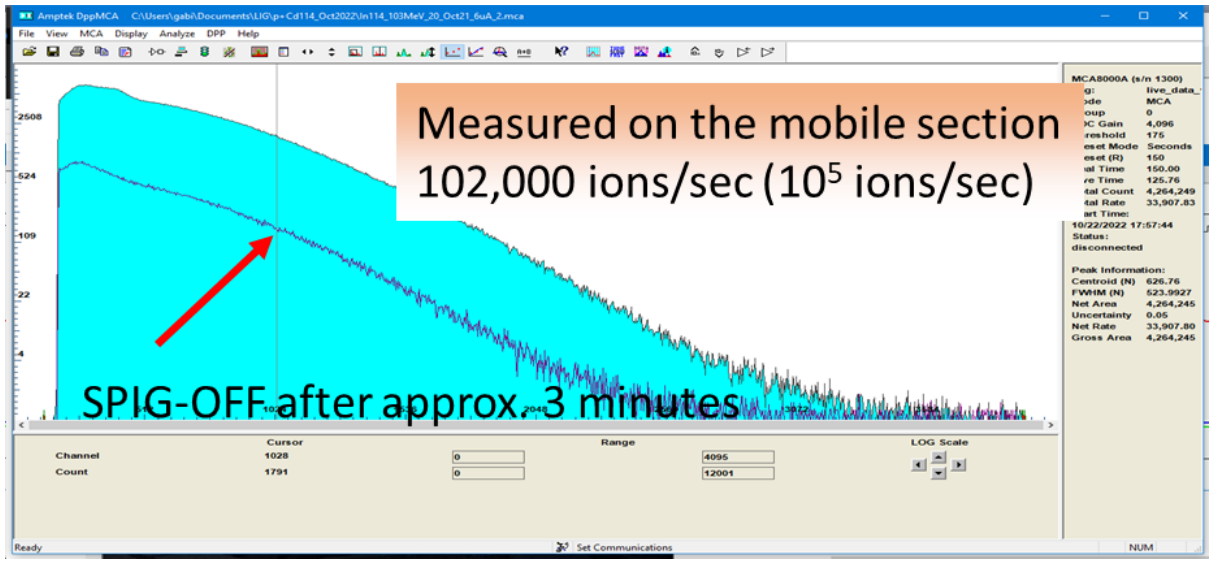

FIG.1. ^{114}In beta decay spectrum. Approximately 10^5 ions/sec were produced.

After the optimization the charge breeding tuning starts and various charge states are analyzed. We focused our efforts on the 19+, 20+ and 21+ charge states of ^{114}In. Based on our measurements we found out the following efficiencies respectively: 2.9%, 2.4% and 1.9%. In order to find the other charge states efficiencies, we have to do in depth measurements and for each charge state a different pilot beam needs to be tuned.

Another interesting result was found: the production of the radioactive ions does not scale with the proton beam intensity. In Fig. 2 the graph showed that increasing the beam intensity from 6 μA to 8 μA does not increase the production of the radioactive ions with 33 %.

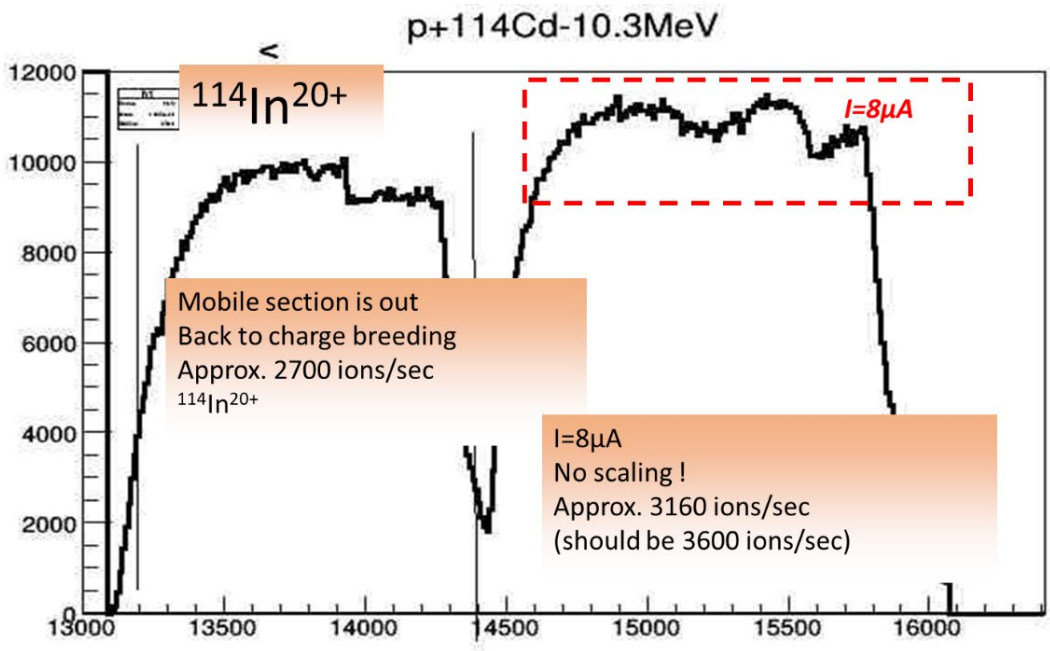

FIG. 2. Production of ^{114}In for 6 μA and 8 μA.

[1] G. Tabacaru *et al.*, *Progress in Research*, Cyclotron Institute, Texas A&M University (2020-2021), p. V-9.

Installation and commissioning of the D-Pace ion source on the K150 cyclotron

B.T. Roeder, G. Tabacaru, H.I. Park, S. Molitor, S. Schmidt, S. Melanson[1] and A. George[1]
[1]*D-Pace Inc., 305-625 Front St., Nelson, BC, Canada*

This year, the pre-existing H^- ion source, the prototype LIISA source from JYFL [1] for the K150 cyclotron has been replaced by a similar, but more versatile ion source from D-Pace Inc. The Positive/Negative Filament Ion Source [2], licensed from TRIUMF lab in Canada, is a direct current, volume cusp source. This ion source is capable of producing both positive and negative ^1H and ^2H ions, as well as $^3He^+$ and $^4He^+$ ions. The previous H^- ion source was not able to produce positive ion beams without significant mechanical modifications to the extraction electrodes. By contrast, the D-Pace ion source can be switched from positive to negative ion extraction and vise-versa by changing the polarity of a few high voltage power supplies and adding voltage to the electron suppression electrode. Thus, the D-Pace ion source can easily provide positive and negative ions at high intensity since the modifications needed to change the polarity of the ions are external to the ion source.

The pre-existing H^- ion source was dismounted in January 2024. A new support structure was constructed to hold the additional weight of the new ion source. The Positive/Negative Filament Ion Source consists of 1) a plasma chamber containing a tantalum filament for heating the plasma and associated extraction electrodes, 2) a diagnostic box containing additional electrodes, an X-Y steering magnet, flanges for mounting turbo pumps and other diagnostic tools such as a faraday cup and an emittance scanner. A picture of the new ion source and its support structure is shown in Fig 1.

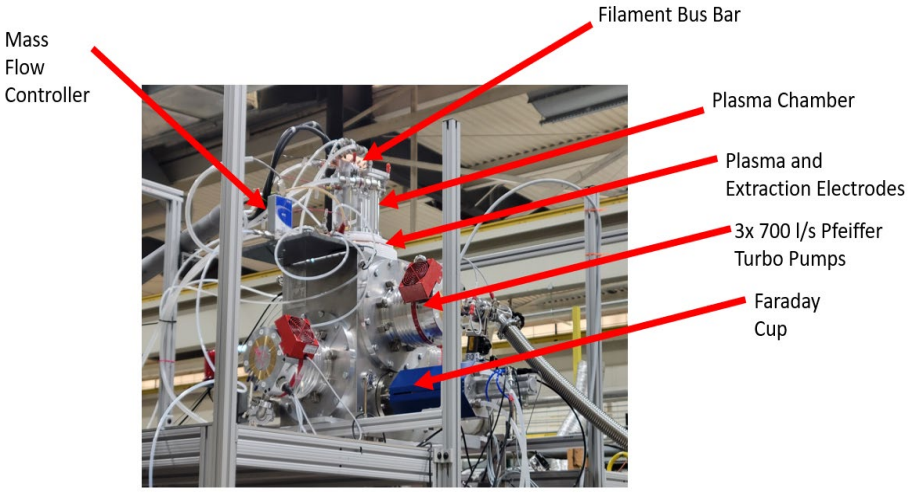

FIG. 1. The Positive/Negative Filament Ion Source as installed above the K150 cyclotron.

Installation of the new ion source was relatively straight-forward and only required small modifications to the support structure for alignment. A MKS mass flow controller was added to the gas inlet line to control the gas flow into the ion source more precisely than in the previous ion source. Control of the gas flow has been shown previously to affect the ion source intensity and emittance. The associated power supplies and electronic connections to the ion source were also modified, as suggested

by the D-Pace Inc. staff. These modifications allowed operation of the ion source in both positive and negative ion mode, and also fixed a polarity issue with the bias of the arc voltage and the plasma electrode that had existed in the pre-existing H^- source.

As of March 2024, the new ion source has been installed and commissioning will continue in the coming year. H^- beam with intensities up to 20 μA have been accelerated and extracted (as H^+) from the K150 cyclotron. $^4He^+$ beam with intensity up to 9 μA has also been accelerated and extracted from the cyclotron.

The high intensity light-ion beams from the new ion source will benefit the basic research and applied science programs by providing reliable, stable hydrogen and helium beams for future projects.

[1] H.L. Clark *et al.*, *Progress in Research*, Cyclotron Institute, Texas A&M University (2009-2010), p. V-6, http://cyclotron.tamu.edu/progress-reports/2009-2010/.
[2] S. Melanson *et al.*, J. Phys. Conf. Ser. **2743**, 012038 (2024).

Improved calculations of the cross sections for atomic electron removal

V. Horvat

The ECPSSR theory provides a framework for calculations of the cross sections for atomic electron removal by means of direct ionization [1] and by atomic electron transfer from the target to the projectile via non-radiative electron capture [2]. It is based on the Plain Wave Born Approximation (for the direct ionization) and the Oppenheimer-Brinkman-Kramers approximation (for the electron capture), but it includes corrections due to projectile energy loss (E), Coulomb deflection of the projectile (C), perturbation of electron's stationary state (PSS) due to polarization and binding effects, as well as relativity (R). PSS is described in terms of increased target electron binding (B) due to the presence of the projectile in the vicinity of the target nucleus, and (for direct ionization only) polarization of the target electron cloud (P) while projectile is outside the electron's shell radius. These calculations became straightforward following the release of Fortran program named ERCS08 [3], which was bundled with a companion program ERCS08w that provided a graphical user interface (GUI) under Microsoft Windows operating system. ERCS08w made it easy to quickly prepare the input file, run the main program, as well as view and analyze the output. It also made it easy to setup for calculations in inverse kinematics (*i.e.* ionization of projectile ions by target atoms or ions). Besides the GUI, ERCS08 is unique due to its capability of calculating individual contributions of various effects to the electron removal cross sections, which makes it straightforward to assess the importance of each effect in a given collision regime.

Several modifications of the ECPSSR theory have been suggested or endorsed by one of its authors (G. Lapicki). These modifications are sometimes explicitly named (for example, eCPSSR, eCUSR, ReCPSSShsR, etc.). Original descriptions of some of these modifications were not sufficiently explicit and/or contained incorrect equations, which resulted in their inadequate implementation in the ERCS08 code.

Consequently, an updated version of the ERCS08 program was developed and released [4]. The names of the program and its GUI companion were changed to ERCS24 and ERCS24w, respectively. The numbers indicate the year of release, while the letters stand for Electron Removal Cross Sections.

Fortran remained the programming language of choice, in order to make the program more portable and easier to customize by a large community of physicists. However, some modifications of the code were necessary in order to comply with the requirements and standards of the currently used compilers. Specifically, GNU FORTRAN compiler became a standard because it is widely available at no charge. Even though the ERCS08 source code could be successfully compiled by GNU FORTRAN compiler and linked without any errors or warnings, problems related to standard input and output did occur at run time. These problems are corrected in the current version of the program (ERCS24), as tested by the latest available versions of the compiler (gFortran 13.2.0-32 and 13.2.0-64) [5].

The updated windows graphics user interface program (ERCS24w) was compiled as a 64-bit application using the latest freely available version of the Microsoft™ Visual Studio (VS 2020) [6].

Most importantly, the erroneous expressions of ECPSSR cross sections for *K*- and *L*-shell ionization by relativistic proton projectiles [7] were replaced by the correct ones [8]. Accuracy of the results was verified by reproducing the data from Fig. 4 of Ref. [7]. Furthermore, the erroneous expressions for limits of integration of the electron transition form factor [9] were corrected as suggested by Šmit and

Lapicki [10]. Accuracy of the results was verified by reproducing the data from Table 2 of Ref. [10]. This correction primarily affects calculations for collisions in the adiabatic regime. In the notation of Refs. [3, 10], the correct limits of integration of the electron transition form factor over scaled square of the momentum transfer (Q) and energy transfer (W) are

$$Q_a = \mu_R^2 y^R \Theta^2 \left[1 - \sqrt{1 - 1/(\mu_R \Theta y^R n_2^2)}\right]^2 ,$$

$$Q_b = \mu_R^2 y^R \Theta^2 \left[1 + \sqrt{1 - 1/(\mu_R \Theta y^R n_2^2)}\right]^2 ,$$

$$W_a = \Theta / n_2^2 \text{ , and}$$

$$W_Q = 2\sqrt{Q y^R \Theta^2} - Q/\mu_R ,$$

where $\Theta = \zeta_s \theta_s$, $y^R = m_s{}^R y = m_s{}^R \eta_s / \Theta^2 = \eta_s{}^R / \Theta^2$, and $\mu_R = \mu / m_s{}^R$.

In addition, values of the fundamental physical quantities used in the calculations were updated and are now taken from the most recent recommended set currently available [11].

[1] W. Brandt, G. Lapicki, Phys. Rev. A **23**, 1717 (1981).

[2] G. Lapicki, F.D. McDaniel, Phys. Rev. A **22**, 1896 (1980), Erratum in Phys. Rev. A **23**, 975 (1981).

[3] V. Horvat, Comput. Phys. Commun. **180**, 995 (2009).

[4] V. Horvat, Comput. Phys. Commun. **299**, 109147 (2024).

[5] https://gcc.gnu.org/ (accessed 26 January 2024).

[6] https://visualstudio.microsoft.com/downloads/ (accessed 26 January 2024).

[7] G. Lapicki, J. Phys. B **41**, 115201 (2008).

[8] S. Cipolla, Comput. Phys. Commun. **180**, 1716 (2009).

[9] G. Lapicki, J. Phys. B **20**, L633 (1987).

[10] Ž. Šmit and G. Lapicki, J. Phys. B **47**, 055203 (2014).

[11] Eite Tiesinga, Peter J. Mohr, David B. Newell, and Barry N. Taylor, Rev. Mod. Phys. **93**, 025010 (2021).

Computing at the cyclotron institute (CI) for 2023-2024

R. Burch, J. Gauthier, K. Hagel and Y.-W. Lui

Over the past year, the Cyclotron Institute's Scientific Compute Group (CI-SCG) has been dedicated to improving the institute's compute capacity. We've also been testing infrastructure to enable High Availability (HA) services for critical operations.

To do this, we added compute nodes and infrastructure to grow our compute capabilities and enhance our infrastructure for critical services.

Computers

The High Performance Research Computing (HPRC) group at Texas A&M University generously donated three full racks of computers to the Cyclotron Institute. These servers were previously part of the decommissioned HPRC ADA cluster. The CI-SCG expanded the institute's compute capacity by repurposing these racks. This expansion involves three racks, each containing six crates, with each crate housing twelve compute blades. Our existing compute capacity supports approximately 1200 job slots. The additional servers could provide an additional 5800 job slots if all servers are operational, representing a fivefold increase. The CI-SCG team is diligently integrating these servers into our infrastructure.

For the operating system installation, we deployed the Rocky Linux 8.x Operating System (OS) on all active compute blades. The installation process utilized Zero-Touch Provisioning, specifically leveraging the Preboot Execution Environment (PXE) Boot and our Infrastructure as Code (IaC) approach. Despite power and cooling constraints, we installed the OS crate by crate, enabling progress even before full power and cooling availability. We seamlessly integrated these servers into our metrics and observability system to monitor their performance and health, ensuring efficient operation. As power and cooling became available, we moved the three racks into the server room. Currently, twelve out of eighteen crates from these racks are in production, yielding 4024 additional job slots, resulting in a total of 5224 slots — a fourfold increase in compute capacity.

High Availability Services Environment

Our initiative to develop infrastructure for HA services is still in the testing phase. HA services are crucial for maintaining an acceptable level of service, even in the presence of faults and operational challenges. As our primary objective, we aim to minimize service interruptions and enhance reliability.

The implementation involves creating dedicated environments for development, testing, production, and backup. For our HA services, we've set up a three-manager-node, three-worker-node environment using FlatCar Linux for the OS and Docker Swarm for container management and operations. This setup ensures continuous availability of critical services. By leveraging Flatcar Linux and Docker Swarm, we establish a secure, scalable, and efficient infrastructure. This platform supports both development and productions activities side-by-side and allows rigorous testing. Our efforts enhance

operational efficiency and anticipate a robust foundation for scaling and accommodating new services. Regular backup testing strengthens disaster recovery capabilities and contributes to overall business resilience.

To date, we have successfully deployed our Signage system in production and development modes on our test infrastructure. The Signage system plays a crucial role in communicating important information to our users. Additionally, we have deployed our LDAP service in this test infrastructure. LDAP provides centralized authentication and directory services, ensuring secure access to institute's resources and is critical to the usage of its compute infrastructure.

Cyclotron Institute Server computer Updates

We coded a graphical user interface application to more efficiently manage the Cyclotron computer user accounts. This GUI is written in Python, can create and modify LDAP entries, add user home directories and create logical volumes on the file server. The code can also pull information about existing users and logical volumes and allows to extend the volumes if users need more space. The application has been called CycAG (Cyclotron Account Generator). A second and simpler GUI has also been built, but unlike CycAG, it can't do any modifications and can only be used to search and display user information from the LDAP server. We named this second application CLS (Cyclotron LDAP Search).

Since CAS (Central Authentication Service) is now considered a legacy [1] protocol by TAMU Technology Services, we took the decision to set up the Cyclotron Institute web server with one of the more modern authentication protocols that are currently used by TAMU. We are now using OpenIDC [2] (also known as OpenID Connect) through Microsoft Azure to authenticate our users on most of our restricted webpages. We expect the CAS replacement to be fully completed on our web server by the end of 2024.

[1] Legacy: outdated computing system, hardware or software that is still in use.
[2] OpenIDC: it is an authentication standard built on top of OAuth 2.0.

Radioisotopes production using lasers: from basic science to applications

M. R. D. Rodrigues,[1] A. Bonasera,[1,2*] M. Scisciò,[3] J. A. Pérez-Hernández,[4] M. Ehret,[4] F. Filippi,[3] P. L. Andreoli,[3] M. Huault,[5] H. Larreur,[5,6,7] D. Singappuli,[6] D. Molloy,[7,8] D. Raffestin,[6] M. Alonzo,[3] G. G. Rapisarda,[2,9] D. Lattuada,[2,10] G. L. Guardo,[2] C. Verona,[11] Fe. Consoli,[2] G. Petringa,[2] A. McNamee,[8] M. La Cognata,[2] S. Palmerini,[12,13] T. Carriere,[6] M. Cipriani,[3] G. Di Giorgio,[3] G. Cristofari,[3] R. De Angelis,[3] G. A. P. Cirrone,[2] D. Margarone,[8,14] L. Giuffrida,[2,14] D. Batani,[6] P. Nicolai,[6] K. Batani,[15] R. Lera,[4] L. Volpe,[4,16] D. Giulietti,[17] S. Agarwal,[18] M. Krupka,[18,19] S. Singh,[18,19] and Fa. Consoli[3**]

[1]*Cyclotron Institute, Texas A&M University, College Station, Texas*

[2]*Laboratori Nazionali del Sud, Istituto Nazionale di Fisica Nucleare (LNS-INFN), Catania, Italy*

[3]*ENEA, Fusion and Technologies for Nuclear Safety and Security Department-C, Frascati, Italy*

[4]*CLPU (Centro de Láseres Pulsados), Villamayor, Spain*

[5]*Universidad de Salamanca, Salamanca, Spain*

[6]*Université de Bordeaux, CNRS, CEA, CELIA (Centre Lasers Intenses et Applications), Talence, France*

[7]*HB11 Energy Holdings Pty, Freshwater, NSW, Australia*

[8]*Queen's University Belfast, School of Mathematics and Physics, Belfast, UK*

[9]*Dipartimento di Fisica e Astronomia "E. Majorana", Università di Catania, Catania, Italy.*

[10]*Facoltà di Ingegneria e Architettura, Università degli Studi di Enna "Kore", Enna, Italy*

[11]*Dipartimento di Ingegneria Industriale, Università di Roma "Tor Vergata", Roma, Italy*

[12]*Dipartimento di Fisica e Geologia, Università degli Studi di Perugia, Perugia, Italy*

[13]*Istituto Nazionale di Fisica Nucleare, sezione di Perugia, Perugia, Italy*

[14]*ELI Beamlines Facility, The Extreme Light Infrastructure ERIC, Dolni Brezany, Czech Republic*

[15]*IPPLM Institute of Plasma Physics and Laser Microfusion, Warsaw, Poland*

[16]*ETSIA, Universidad Politécnica de Madrid, Madrid, Spain*

[17]*Dipartimento Fisica, "E. Fermi", Università di Pisa and INFN, Pisa, Italy*

[18]*FZU-Institute of Physics of Czech Academy of Sciences, Prague, Czech Republic*

[19]*Institute of Plasma Physics of Czech Academy of Sciences, Prague, Czech Republic*

Laser technologies have advanced significantly with the understanding of Chirped Pulse Amplification (CPA), which allows energetic laser beams to be compressed to tens of femtoseconds (fs) pulse durations and focused to a few micrometers (μm). Protons with energies of tens of MeV can be accelerated using methods such as Target Normal Sheath Acceleration (TNSA) and focused on secondary targets. Under these conditions, nuclear reactions can occur, producing radioisotopes relevant for medical purposes. High repetition lasers can produce sufficient isotopes for medical applications, making this approach competitive with conventional methods that rely on accelerators.

The production of the ^{67}Cu, ^{63}Zn, ^{18}F, and ^{11}C were investigated [1] at the 1-petawatt (PW) laser facility at Vega III in Salamanca, Spain. These radionuclides are used in positron emission tomography (PET) and other applications. The reactions ^{10}B(p,α)^{7}Be and ^{70}Zn(p,4n)^{67}Ga were also measured to further constrain proton distributions at different angles and the reaction ^{11}B(p,α)^{8}Be, which is relevant for energy production. The nuclear reaction products were investigated using the pitcher-catcher method, with

protons produced by an aluminum target and impinging on various targets in both the forward and backward directions relative to the laser.

Angular distributions of radioisotopes in the forward (with respect to the laser direction) and backward directions were measured using a High Purity Germanium Detector (HPGE). Our results, presented in detail in Rodrigues et al. [1], are reasonably reproduced by numerical estimates following the approach of Kimura et al. [2]. The theoretical production of different nuclei was also estimated and assumptions for cross sections were made in energy regions where they have not been measured. The TNSA mechanism should be studied in more detail and adjusted to various physical scenarios. In particular, the role of electrons must be clarified and, if possible, used to favor nuclear reactions in the plasma. This may be crucial if this method is applied to neutron less reaction energy production. The predictions in Table I from ref. [1] are confirmed by the experimental data. The reaction $^{11}B(p,\alpha)^{8}Be$ will be discussed in more detail in a new publication [3]. The values obtained [1] are too small for self-sustained reactions, and the catcher may need to be compressed [4,5].

Laser technologies are mature enough to compete with accelerators for production. While costs for construction, space, maintenance, etc., may attest to their competitiveness, the results suggest that this may be a winning technology.

[1] M. R. D. Rodrigues *et al.*, Matter Radiat. Extremes **9**, 037203 (2024); https://doi.org/10.1063/5.0196909.

[2] S. Kimura and A. Bonasera, Nucl. Instrum. Methods Phys. Res. A637, 164 (2011); doi: 10.1016/j.nima.2011.02.043

[3] F. Consoli *et al.*, in preparation.

[4] M. J. Huang, H. J. Quevedo, G. Zhang and A. Bonasera, Nuclear Physics News **29**, 9 (2019), doi: 10.1080/10619127.2019.1603555.

[5] G. Zhang *et al.*, Phys. Lett. A **383**, 2285 (2019); doi: 10.1016/j.physleta.2019.04.048.

Progress on the GOLIATH upgrade for the He6-CRES experiment

D. McClain, B. Diaz, M. Ellis, M. Holloway, V. Iacob, D. Melconian, and K.E. Stonum

The Gas Operated Large Ion-Bunch Atomic Trap for He6-CRES (GOLIATH) radiofrequency quadrupole (RFQ) was designed to be a large throughput ion trap to supply ion bunches to the He6-CRES experiment in order to combat energy dependent losses without sacrificing statistics. In preparation for upcoming commissioning tests for GOLIATH, the TAMUTRAP beamline has been altered into a test bench centered on the high voltage crate that houses the RFQ. These alterations include downsizing the beamline, removal of the TAMUTRAP RFQ, construction of GOLIATH, characterization of two new microchannel plates with delay-line position readout, and the design of their requisite mounts.

Reducing the size of the beamline as seen in Fig. 1 allows us to minimize losses due to space-charge and misalignments, while also reducing the load on our vacuum pumps. With the RFQ having

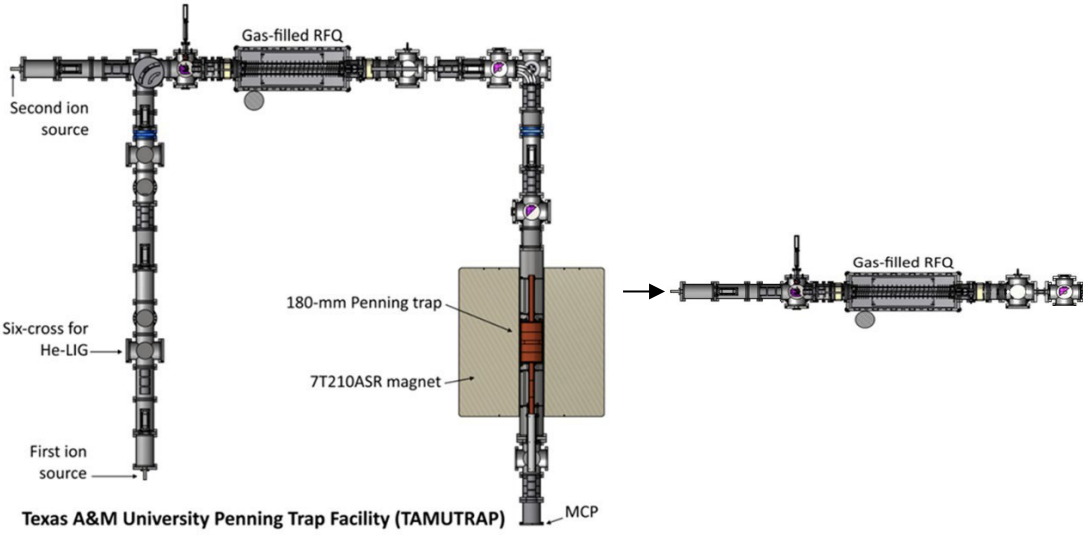

FIG. **1**. Aerial depiction of the TAMUTRAP beamline [1] (left) which has been repurposed to be the smaller GOLIATH test bench (right).

a very small acceptance window and no diagnostic tools until further down the beamline, the TAMUTRAP RFQ was removed and temporarily replaced with a Faraday cup to confirm beam acceptance. This works both in preparation for GOLIATH, which was designed to fit in the same box, despite being bigger in all aspects aside from the footprint as shown in Fig. 2.

Along with the design and alignment changes to the beamline, the detectors in use have been upgraded to 40 mm diameter delay-line anode MCPs for precision timing and position readout. With resolutions of 0.05 mm and 0.2 ns, these detectors will take an integral part in the commissioning of GOLIATH as we attempt to tune to the constraints of a radius of 3.17 mm and time spread of < 1 μs that will make it possible to trap in the upcoming Penning trap.

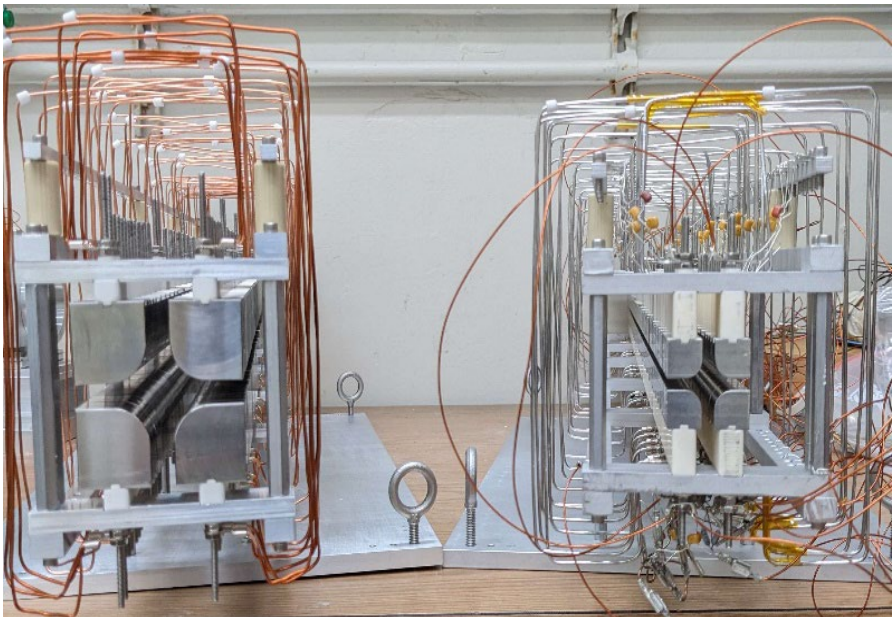

FIG. 2. GOLIATH (left) compared to the smaller TAMUTRAP RFQ (right).

With all components of GOLIATH gathered, commissioning tests are expected to take place this year. Following commissioning tests of GOLIATH at Texas A&M, it will be delivered to the University of Washington. Once there, the results of the tests will be crucial in the development of the beamline as we transition from a gaseous source to an ion source.

[1] V.S. Kolhinen *et al.*, *Progress in Research*, Cyclotron Institute, Texas A&M University (2019-2020), p. IV-101.

Continuing development of compact MWPC detectors for TRINAT experiments

B.M. Vargas-Calderon, V.E. Iacob, J. Klimo, D. McClain, and D. Melconian

As we prepare for further runs of the TRINAT experiment, work continues on developing position sensitive multiwire proportional counter (MWPC) detectors to replace the current 300 μm-thick double-sided Si-strip (DSSSD) ΔE-detectors making up part of the current β telescope assembly. The significant energy loss (~100 keV) and backscattering incurred by the DSSSDs represent a limiting systematic of the current iteration of TRINAT β-decay experiments. Work is in progress on a revision of the MWPC design from last year [1], incorporating onboard charge-sensitive shaping preamplifiers to achieve greater signal strength and fidelity.

Revised MWPC detector design

The wire chamber topology of the revised design will feature two anode wire planes and three planar cathodes, spaced at a distance of 4 mm. Similarly to the previous design, the revised MWPC will be constructed as a stack of PCB frames, supporting the anode and cathode electrodes and occupying a cylindrical form factor. The PCB frame elements will range in thickness from 0.5 mm to 2 mm, with the full stack occupying a total height of 16 mm, an improvement in form factor over the previous design which stood at 26 mm in height. This will allow for an improvement in the solid angle spanned by the scintillator behind each MWPC. Fig. 1 shows a 3D model of the layers comprising the MWPC.

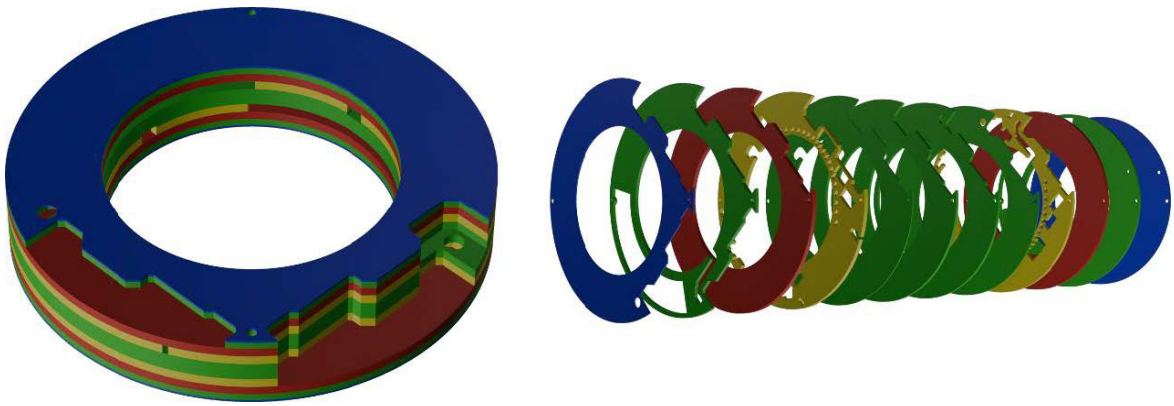

FIG. 1. CAD drawing of the revised MWPC design. On the left is shown the assembled view, while the right shows an exploded view of the various PCB

Per-channel preamplifiers

The PCB frame supporting each anode wire-plane will also hold a set of twenty charge-sensitive shaping pre-amplifier channels, with each pre-amplifier receiving input from one of the twenty wires supported by each anode layer. These pre-amplifiers will be embedded within the PCB frame layers upon

the assembly of the MWPC, reducing the effect on signal-to-noise ratio of any noise introduced outside of the detector. The pre-amplifier circuit topology and a fabricated pre-amplifier circuit is shown in Fig.2.

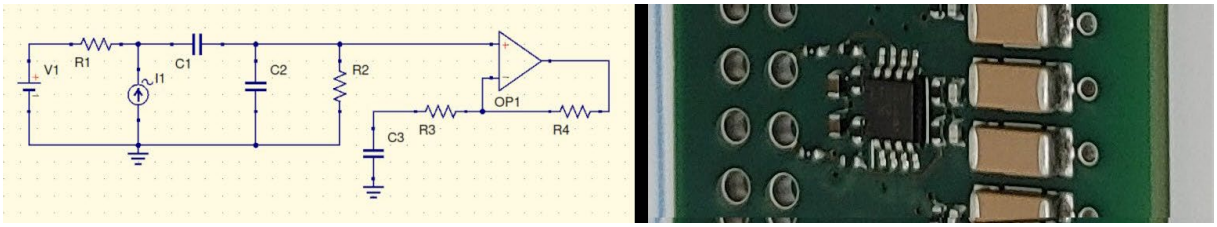

FIG. 2. Per-channel preamplifier circuit design (left) and fabricated testboard (right).

The output of each charge-sensitive shaping pre-amplifier will leave the detector through its own 50Ω cable. Thus, from two anode layers containing twenty wires each, forty output channels will be supplied by each detector. The preamplifier outputs are matched to the 50Ω line impedance, reducing any reflections along the signal pathway.

Anode PCBs

To accommodate the twenty anode wires, charge-sensitive shaping pre-amplifier channels, and 50Ω output channels, each anode PCB frame will be a 6-layer PCB containing high-voltage supply electronics for the anode wires, solders pads on front and back for the 265 SMD components which comprise the charge-sensitive shaping pre-amplifier circuits, and four layers of signal routing along curved 50Ω traces to the output connectors. A CAD rendering of one of these anode frames is shown in Fig. 3.

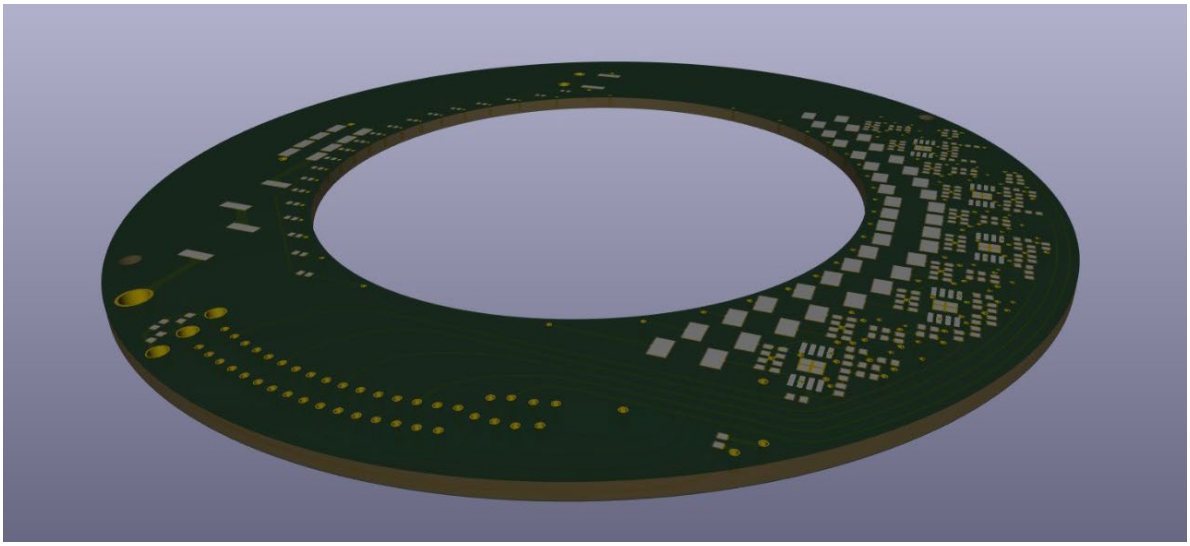

FIG. 3. CAD rendering of the lower anode PCB frame.

The design process for this revised MWPC is nearly complete and we expect to have the new MWPC detectors fabricated and assembled by the end of the year.

[1] J. Klimo *et al.*, *Progress in Research*, Cyclotron Institute, Texas A&M University (2022-2023), P. IV-29.

Pypperpot simulation and analysis software for beam diagnostics

D. McClain, M. Holloway, V. Iacob, D. Melconian, M. Parnell, and K.E. Stonum

Following it's inception last year as a simple code [1], Pypperpot has evolved into a user friendly software created to aid in the design and analysis of pepper-pots, a powerful beam diagnostic tool. The area of the position-momentum phase space of the beam is called the emittance, and can be measured using a pepper-pot. Following Liouville's theorem, barring non-conservative forces, the emittance of a beam will remain constant [2]. Though the space-charge effect is non-conservative, the effect is minimal across short distances. Because of this, a compact pepper-pot system must be created and deployed at target sites, but due to the energy dependent efficiency of a given pepper-pot mask, each mask has a range of emittances it is sensitive to. Therefore, the simulation portion of Pypperpot allows for beam generation, as shown in Fig. 1, as well as trajectory calculations through a designed mask to test the acceptance range of a mask before manufacturing. Generated beams can be saved for testing through multiple masks, and trajectories can be saved as images for analysis.

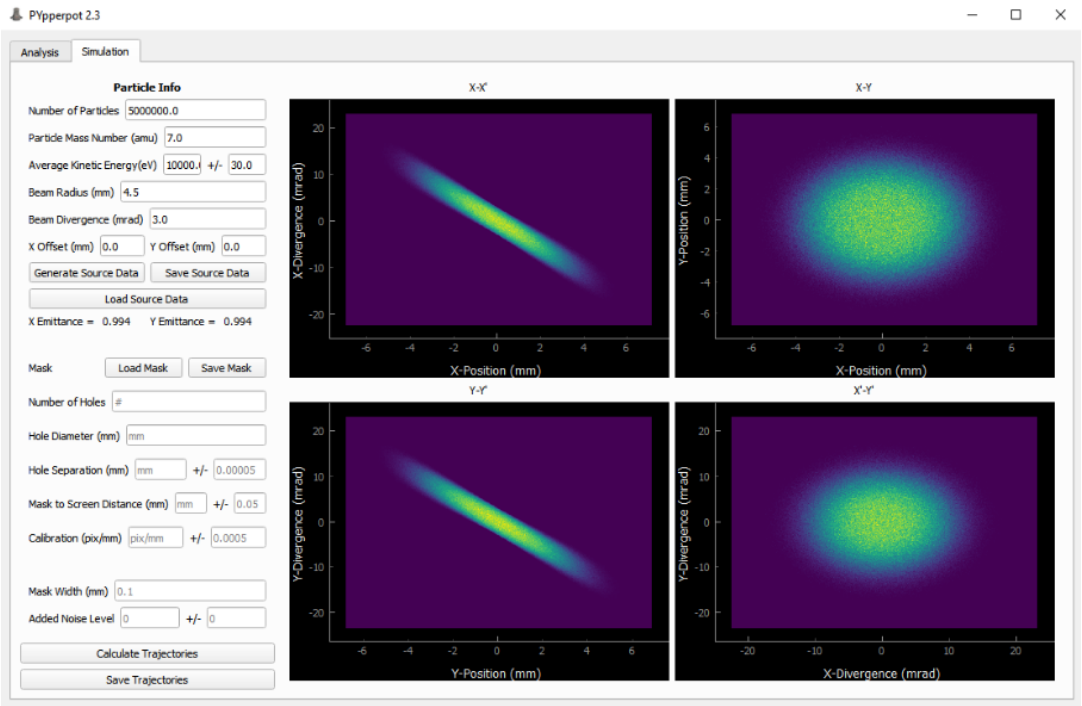

FIG. 1. Pypperpot's simulation tab showing a simulated beam depicting the X-Y phase space

Following the simulation, there is a separate analysis tab that reads in pepper-pot data as images or matrices. When information from the mask is supplied, the user has the ability to tune the algorithm that senses the peaks in the image to make sure their data is accurately fit. The data is then fit peak by peak and the phase space for the beam is displayed along with the measured emittance as shown in Fig. 2. Because the emittance formula was originally derived for a slit mask and extended to the pepper-pot the formula was for measuring projections as either row or column of the mask [3]. To make Pypperpot hole-

number agnostic, the peak-by-peak fit was preferred, and required the disentangling of each peak from the projection, as done in [4], in the equations for emittance. With a simulated mask recently found to be sensitive to the region of requirement for both the Light-ion guide Separator for Texas A&M's Rare isotope beams (LSTAR) [5] and the Gas Operated Large Ion-bunch Atomic Trap for He6CRES (GOLIATH), tests of the emittance on these beamlines using Pypperpot will hopefully be conducted soon.

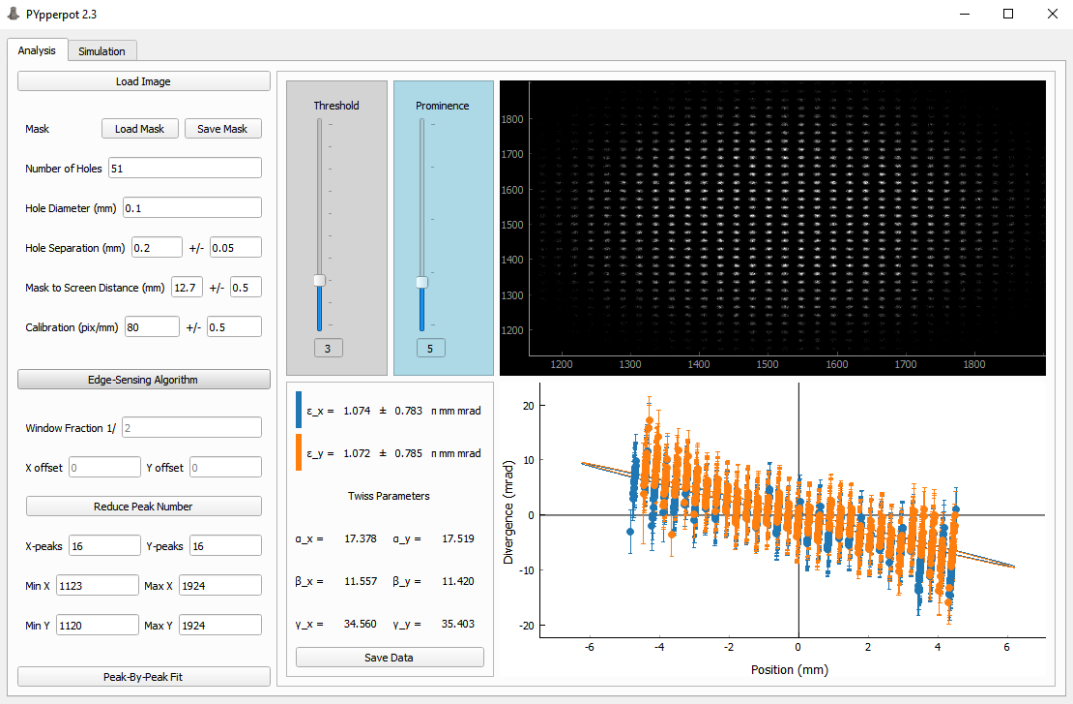

FIG. 2. Pypperpot's Analysis tab depicting a pepperpot image and the resulting emittance and phase space

[1] D. McClain *et al.*, *Progress in Research*, Cyclotron Institute, Texas A&M University (2022-2023), p.IV-37.

[2] J.W. Gibbs, Proceedings of the American Association for the Advancement of Science. (1848).

[3] M. Zhang, No. FNAL-TM-1988. Fermi National Accelerator Lab.(FNAL), Batavia, IL, United States (1996).

[4] K. Pearson, Philosophical Transactions of the Royal Society of London. (A.) **185**, 71 (1894).

[5] D. Melconian *et al.*, *Progress in Research*, Cyclotron Institute, Texas A&M University (2021-2022), p. IV-61.

Update on the He-LIG and LSTAR projects to produce RIB for TAMUTRAP

D. Melconian, J. Klimo, M. Holloway, D. McClain, G.P.A. Berg,[1] M. Couder,[1] and M. Brodeur[1]
[1]*University of Notre Dame, Notre Dame, Indiana*

We continue to develop a ^{3}**He**-based **l**ight-**i**on **g**uide (He-LIG) system, complementing the existing (proton-driven) *p*-LIG system, to increase RIB production at the CI using the high intensity of the K150 cyclotron. The **l**ight-ion guide **s**eparator for **T**exas **A**&M's K150 **r**are isotope beams (LSTAR) will transport and purify the RIBs produced by the He-LIG.

Most of our effort continues to be on the construction of LSTAR as the new graduate student, M. Holloway, gets caught up on his thesis project, the He-LIG gas cell and transport to the separator. In April of 2024, we ordered the two dipoles and electrostatic elements from Danfysik. After iterating with their technical staff, they have come up with the concept design, shown in Fig. 1. Field calculations of the quadrupoles (*Q*), quad-plus-octupoles (*Q*+oct), sextupoles (*S*), 24-rod mulitpole (*M*) and dipoles (*B*) they designed all meet our specifications. With the concept design milestone reached, they are now proceeding with the final design as they begin procuring the raw material (particularly the iron for the dipoles) and subcontract production of the electrostatic elements. If all goes well, Danfysik expects to ship the separator components to TAMU by the summer of 2025.

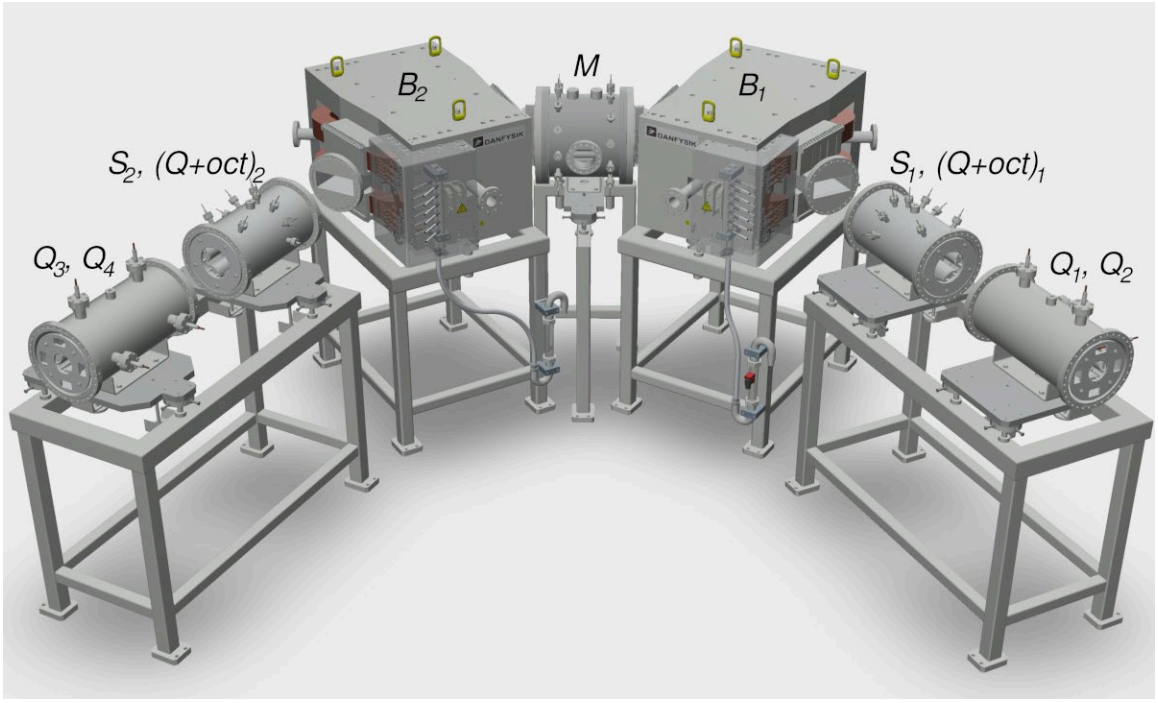

FIG. 1. Danfysik's CAD drawing of their concept design of LSTAR.

In addition to working on the concept design with Danfysik, we have submitted a paper to Nuclear Instrumentation and Methods A, "*LSTAR – An isotope separator for expanding radioactive ion beam production at the Cyclotron Institute, Texas A&M University,*" which describes the layout, ion-

optical design, and specifications of LSTAR. We are in the process of addressing comments from the referees and expect it to be published by the end of summer.

In anticipation of the separator arriving by next summer, we are updating our design of the He-LIG and preparing to install the new (delayed by a year) *p*/He-LIG chamber (see Fig. 2 and Ref. [1]). Our prototype gas cell worked very well, however it leaked a lot of helium, so we are redesigning it to have indium seals; this will lead to better vacuum outside the gas cell for ion transport, and also be a more efficient use of helium. We also need to update the SPIG transport following the gas cell to be curved to accommodate the new design of LSTAR (2x62.5° horizontal instead of the original 2x45° vertical [2]). The new gas cell should be ready for testing this fall. We are also eagerly anticipating the arrival of a new post-doctoral researcher, Dr. Graeme Morgan, this summer who will help lead commissioning of the new gas cell. He will also lead the effort, in collaboration with the *p*-LIG and operations groups, to prepare Cave 5 for installation of the *p*/He-LIG chamber and LSTAR. This will be no easy task as large shielding blocks need to be removed, large roots blowers need to be repositioned, and the HV platform needs to be upgraded to reach 70 kV. Significant planning and organization are required to minimize the disruptions to the *p*-LIG re-accelerated RIB developments [3].

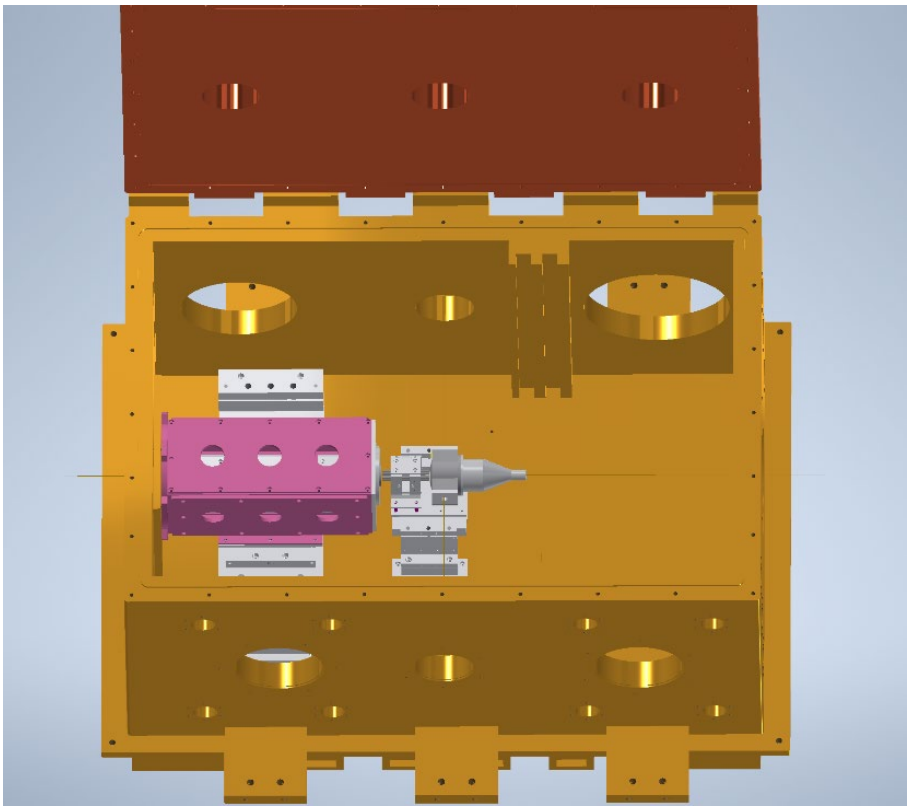

FIG. 2. p/He-LIG chamber in the He-LIG configuration. The required amendments to our prototype are indium seals to reduce gas leakage, and curved SPIGs outside of the box (to the left) to transport beam to the entrance of LSTAR.

[1] P.D. Shilding *et al.*, *Progress in Research*, Cyclotron Institute, Texas A&M University (2020-2021), p. V-68.

[2] G. Chubarian *et al.*, *Progress in Research*, Cyclotron Institute, Texas A&M University (2019-2020), p. IV-93.
[3] G. Tabacaru *et al.*, *Progress in Research*, Cyclotron Institute, Texas A&M University (2023-2024), p. IV-7.

Development of MIVOC beams for the ECR2 ion source

B.T. Roeder, H.I. Park, B. Gall[1] and J. Arje
[1]*Université de Strasbourg, CNRS, IPHC, Strasbourg, UMR7178, 67037, France*

This year, the development of metal ions beams produced with the Metal Ion Volatile Compounds (MIVOC) method [1] continued. The MIVOC method consists of introducing a molecular compound containing a metal atom into the ion source and then ionizing the metal to produce beam. The advantages of MIVOC are that the metal ion beams can be produced at medium to high intensity at near room temperature without the need for an oven, and the MIVOC fixtures are easy and fast to reload, if necessary, during the course of an experiment. Another advantage is that the preparation time for the MIVOC vs. the conventional oven method is much faster. The disadvantages of MIVOC are that the compounds are difficult to prepare and transport (although many of them are available commercially) and the carbon from the molecules pollutes the ion source over time. This carbon contamination degrades the ability of the ion source to produce high charge states. Despite the disadvantages, the MIVOC method has been shown to work well for a variety of metal ion beams [1].

The MIVOC method can be used to produce many metal ion beams for the transition and rare-earth metals that would otherwise require a high-temp oven. To date, titanium beam with the compound (Trimethyl)pentamethylcyclopentadienyltitanium(IV) (Cp^*TiMe_3) and iron beam with the compound Ferrocene ($(C_5H_5)_2Fe$) have been produced at the Cyclotron Institute. Boron beam has been produced with m-Carborane. Vanadium, nickel, and chromium beams are also possible with MIVOC and may be tried here in the future.

The setup for MIVOC is as follows, as advised by Professor B. Gall. About 0.5g-2g of MIVOC compound, usually in the form of a fine powder, is placed into a glass vial. The vial is connected to a calibrated gas dosing valve, such as the Pfeiffer EVN 116. The dosing valve is then connected to a flange mounted on the side of the ECR ion sources. The glass vial is isolated from the ion source high voltage. A custom Peltier cooler and control box, also provided by Professor B. Gall and the University of Strasbourg, can be mounted to the glass vail to control the temperature and thus allows control of the vaporization rate of the material. A picture showing the setup for the MIVOC fixture on the side of ECR2 is shown in Fig 1.

To develop the MIVOC technique for metal beam production, first Ferrocene was tried. About 2g of Ferrocene from Strem Chemical [2] was introduced into the glass vial of the MIVOC fixture and mounted to the side of ECR2. After pumping the ion source overnight, first the temperature of the vial was reduced to 5° C with the Peltier cooler. Then, the EVN dosing valve was slowly opened and ECR output scans were recorded to measure the production of the ^{56}Fe charge states. At low flow rates (EVN 116 valve settings 500-600), it was possible to observe high charge states up to $^{56}Fe^{16+}$. As the flow rate increased (up to EVN 116 valve setting 775), the charge state distribution shifted toward lower chargestates and became peaked around $^{56}Fe^{10+}$ and $^{56}Fe^{11+}$. It was also observed that by adjusting the temperature of the Peltier cooler between 5° C and 17° C (room temp) that the intensity and distribution of the charge states could be controlled. Lower temperatures favored higher charge states whereas higher

temperatures allowed for the maximum intensity of the lower charge states. A typical ECR2 scan, optimized for $^{56}Fe^{13+}$, is shown in Fig 2. The best results were obtained for $^{56}Fe^{13+}$ at 8° C, where about 20μA were measured at the ion source output, and for $^{56}Fe^{10+}$ at 12° C, where about 43 μA was observed.

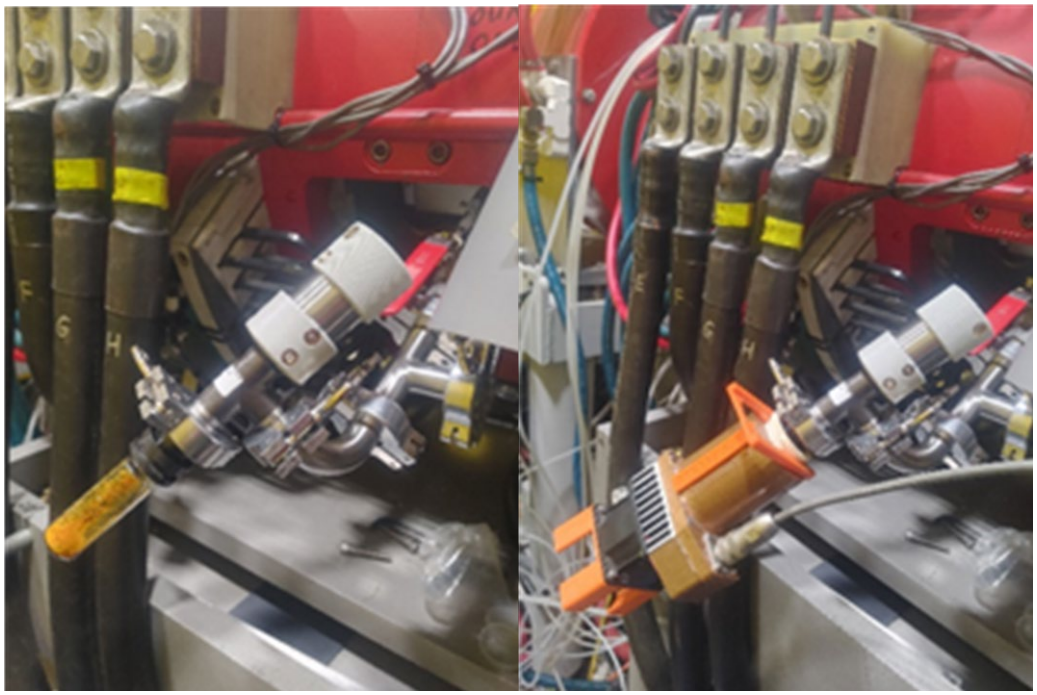

FIG. 1. The MIVOC fixture setup on the side of ECR2. The left picture shows the Ferrocene in the glass vial connected to the EVN 16 dosing valve, which is then connected to the ion source. The right picture shows the Peltier cooler installed, encasing the glass vial in the complete setup.

Future work with the Ferrocene includes also testing the iron beam production on ECR4 to see if similar results can be obtained.

Next, the (Trimethyl)pentamethylcyclopentadienyltitanium(IV) compound (Cp^*TiMe_3), also obtained from Strem Chemical, was tried to produce titanium beam. This compound is more difficult to work with than Ferrocene. It is heat, light, and moisture sensitive. It is best transferred into the glass vial of the MIVOC fixture under argon atmosphere in a glove box and in dim or red background lighting. Once the fixture is mounted to the ion source, it is ideally kept cool at 5° C or less until ready for use. For the test, about 1.5g of Cp^*TiMe_3 was loaded into the glass vial, the EVN 116 valve was opened to 810 (close to fully open), and the temperature was varied with the Peltier cooler from 5° C up to 17° C. A typical ECR2 scan from the test is shown in Fig. 3 with the ion source optimized for $^{48}Ti^{11+}$. With the EVN 116 valve at 810 and the temperature at about 15° C, about 18 μA of $^{48}Ti^{11+}$ was extracted from ECR2. About 2 μA of $^{48}Ti^{13+}$ was also observed.

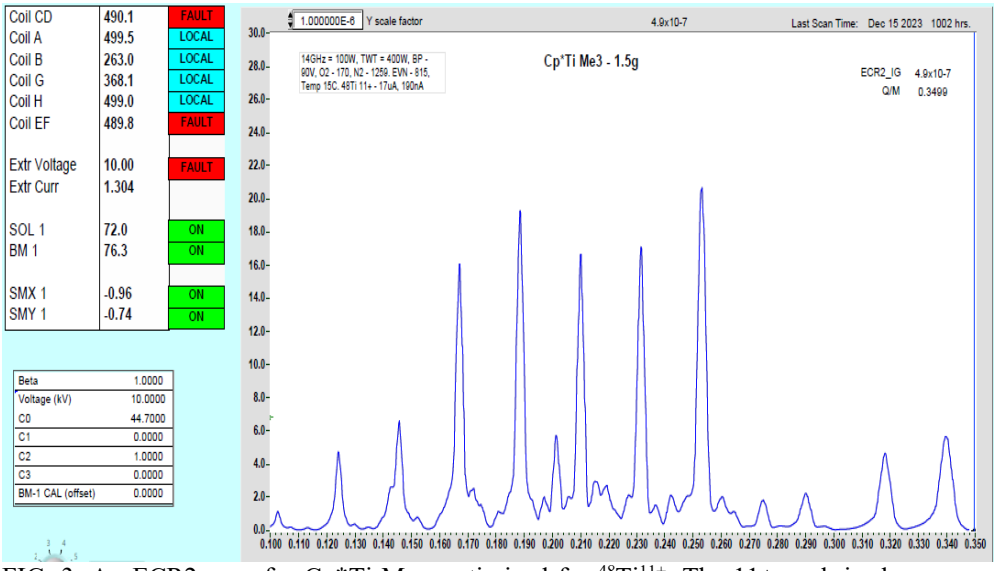

FIG. 3. An ECR2 scan for Cp*Ti Me_3, optimized for $^{48}Ti^{11+}$. The 11+ peak is shown near q/m=0.229 on the X-axis.

^{48}Ti beam produced with Cp*TiMe_3 was delivered for experiments for Professor Folden's group. Future experiments with ^{50}Ti enriched Cp*TiMe_3, and metal beams produced with other MIVOC compounds, are planned in the coming years.

[1] S.L. Bogomolov *et al.*, Phys. Part. and Nucl. Lett. **12**, 824 (2015).
[2] Strem Chemical, www.strem.com

^{6}HeCRES beta monitor design

D. McClain, M. Holloway, V. Iacob, D. Melconian, and B.M. Vargas-Calderon

The ^{6}HeCRES experiment utilizes the cyclotron radiation emission spectroscopy (CRES) technique to measure the β spectrum of ^{6}He and ^{19}Ne. Due to a fixed detector frequency bandwidth, we measure the cyclotron radiation, which is emits when a charged particle precesses in a magnetic field, at different magnetic fields to scan the whole spectrum. The cyclotron frequency, f, of an electron is dependent on the kinetic energy E_e of the electron in a magnetic field B according to

$$f = \frac{1}{2\pi}\frac{eB}{m_e + E_e}$$

Where e is the electron charge and m_e is the rest mass of the electron. The change in magnetic field shifts the energies detectable within our frequency bandwidth and we take slices of the beta spectrum as seen in Fig. 1.

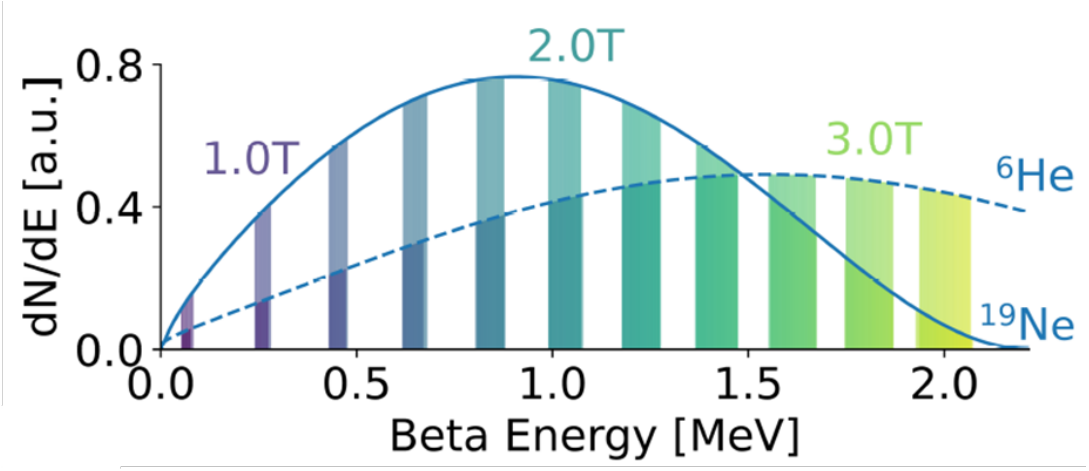

FIG.1. Beta spectrum of ^{6}He and ^{19}Ne within the 18-19 GHz frequency bandwidth for various magnetic fields.

The reconstruction of the beta spectrum requires the normalization of these slices by the number of decays that occurred during their measurement. To fufill this need we utilize an external beta monitor to measure the rate of decays over the length of the run. The rate represents the activity of the gaseous isotopes being pumped to the decay cell, as the monitor lies along the path of the gas to the decay volume. Thus we can normalize our experimental results to the monitor's rate. Previously, three designs of the beta monitor were used, a three detector veto design used to normalize the rate to a known radioactive source, an E-ΔE telescope that is able to reject gammas, and a small scintillator attached to four silicon photomultipliers (SiPMs) that is expected to achieve a greater efficiency, but must be shielded to reject external triggers. Since the beta monitor resides near the experiments large magnet, fringe fields cause uncertainties to the efficiency at the 10^{-3} level, comparable to the precision required in the search for new physics, that can be limited by reducing distance from source to detector. Because of this, Texas

A&M and the University of Washington have each designed new monitors to replace the issues of the old. Because the monitor exists outside of vacuum, limiting the distance from the vacuum seal window is the primary issue to overcome.

The Texas A&M beta monitor is an E-ΔE telescope that is designed to reside in a bucket that mounts directly to the beamline and holds the detector at the window to minimize this distance. The bucket design, shown in Fig. 2., allows for tunable position of the two scintillators, and has a cutout of the top to hold the photomultiplier tube (PMT) such that the ΔE scintillator lies in contact with the

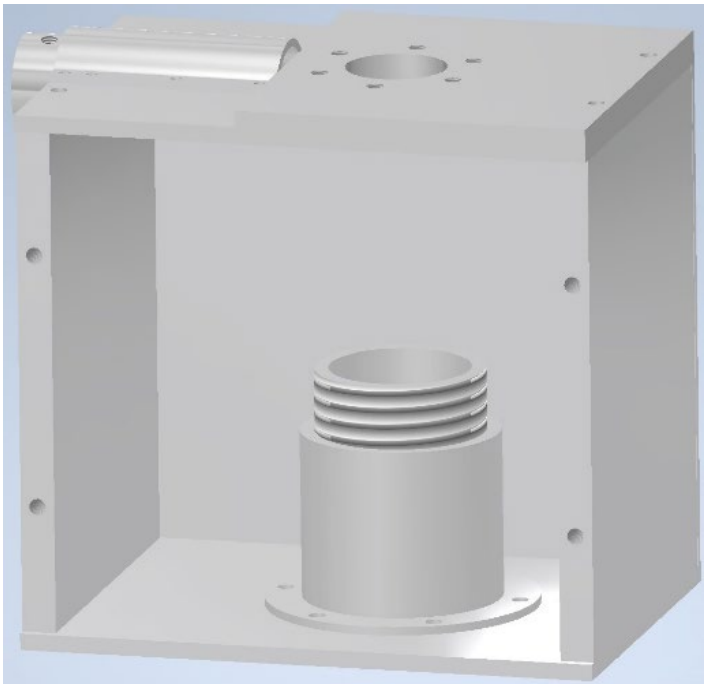

FIG.2. CAD design of the PMT Bucket that will house the beta monitor.

vacuum port. The beta monitor will also employ a temperature stabilizer circuit to prevent variations in gain, and thus detector efficiency across the duration of the experiment. The new design, along with the new detector from the University of Washington will be utilized to confirm the source stability, and the more successful model will be used during future gaseous CRES experiments.

Development of an electron cyclotron emission imaging system

L.E. Henderson, C.A. Gagliardi, H.L. Clark, and D. May

Fabrication of the electron cyclotron emission imaging system for the Cyclotron Institute's electron cyclotron resonance ion sources (ECRIS) has proceeded over the past year and is nearing completion. This has included mechanical construction and electronics fabrication, but much of the recent work has focused on completing the optical components of the system.

Fabrication processes for both ceramic (Magnesium Aluminate) and plastic (standard-grade PLA) microwave lenses have been developed and put into practice over the past year. The PLA lenses can be directly 3D-printed in ready-to-use sections that are later glued together. 3D-printed PLA master positives and mother molds, parametrically generated in OpenSCAD, are being used to create silicone molds that cast ceramic lens sections from Aremco's Ceramacast 575-N. Simple lenses like the primary lens in Fig. 1 can be molded only using a master positive, but a more complex mold is shown in shown in Fig 2 along with molded lens sections it produced.

FIG. 1. Prototype primary optic lens in non-magnetic fixturing.

Design procedures and codes have been refined to reduce optical aberrations and better match lenses to produce high numerical aperture microwave optical systems. The theoretical development has also included anti-reflection coatings which can be 3D-printed from PLA for both ceramic and PLA lenses.

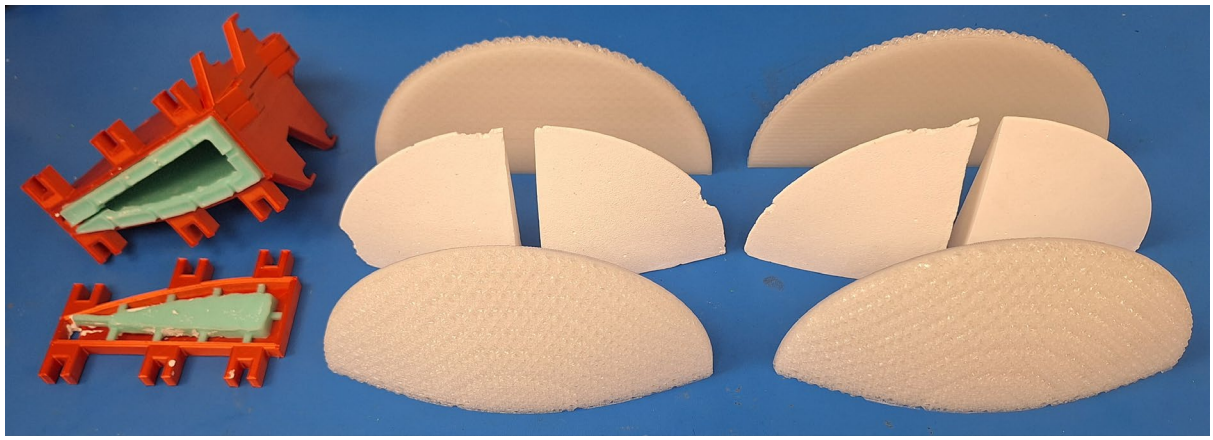

FIG. 1. Silicone mold, cast ceramic lens quarters, and 3D-printed anti-reflection coatings in an unassembled state.

Finding a suitable fabrication method for the long alumina waveguides that will transport the image away from the plasma chamber has proven to be a challenge, but there is promise in the current approach to cutting and metallizing the alumina rods and we hope to report success very soon.

In order to supplement available material data, a simple material characterization method using a known-shape prism of an unknown index material was demonstrated and put into use. What the method lacks in precision it makes up for in simplicity and broad frequency applicability, and the precision achieved was found to be sufficient for current purposes anyways. The prism method has also proven useful for quickly validating intuitions about how the refractive index of 3D-printed structures should vary as the infill of the structure is changed. Examples of such prisms are shown in Fig. 3.

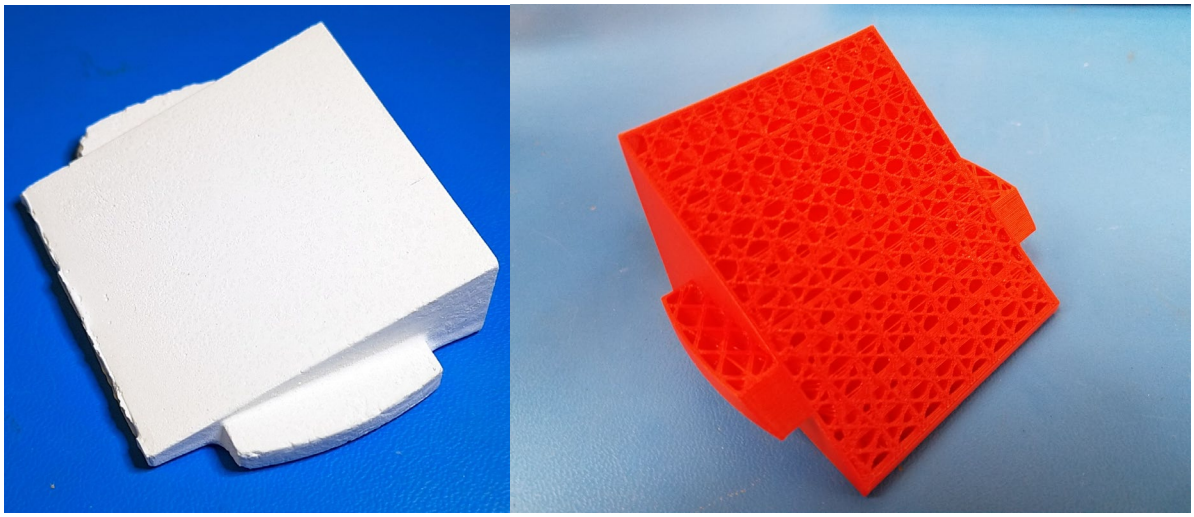

FIG. 3. Examples of prisms used to characterize refractive index for (left) Aremco Ceramacast 575-N and (right) standard-grade PLA with varied infill.

MARS status report for 2023-2024

B.T. Roeder

This year, we continued the program of providing rare isotope beams (RIBs) for the physics program at the Cyclotron Institute at Texas A&M University with the Momentum Achromat Recoil Separator (MARS) [1]. The MARS beam line was utilized in 7 separate runs for various experiments. 3 of these experiments involved rare isotope beams (RIBs).

A summary of the RIBs produced this year is given in Table I. A ^{11}Be beam was produced for Professor Rogachev's group for a test of the new TexNAAM detector. There was a ^{14}O beam made for an experiment with Professor Lee Sobotka's group from Washington University in St. Louis (WUSTL). Finally, there was a brief run with ^{58}Co to test the "Z" separation capabilities of the Oak Ridge Ion Chamber with Professor Yennello's group. Details of these experiments are provided in separate reports.

TABLE I. Summary of MARS RIBs for 2023-2024.

RIB beam	**Reaction**	**Production Rate (eV/nC)**	**Purity**	**Intensity on Target (est.)**
^{11}Be	^{13}C+^{9}Be at 30 MeV/u (Frag.)	281 eV/nC	~78%	~4*10^{4} p/s
^{14}O	^{1}H(^{14}N,^{14}O)n (Transfer) at 17 MeV/u	293 eV/nC	~75%	2*10^{5} p/s
^{58}Co^{25+}	^{1}H(^{58}Fe,^{58}Co)n at 11.5 MeV/u (Transfer)	330 eV/nC	~50%	~10^{3} p/s

The other 4 experiments with MARS involved measurements with stable beams and are not reported here, with the exception of the ^{48}Ti+^{48}Ti measurement led by Dr. A. Bonasera in collaboration with Professor G. Souliotis. In this measurement, beam-like fragments from nucleon transfer reactions were measured. The analysis of these data are ongoing and further, similar experiments are planned in the coming year.

[1] R.E. Tribble, R.H. Burch and C.A. Gagliardi, Nucl. Instrum. and Meth. **A285**, 441 (1989).

A study of the Two-Frequency Effect in ECR2 ion source

H.I. Park, D.P. May, L. Gathings, F.P. Abegglen, G.J. Kim, and B.T. Roeder

Our efforts have continued to improve the performance of the 14.5 GHz electron cyclotron resonance (ECR) ion source, ECR2. Our primary focus is the study of whether a true two-frequency plasma heating effect can be identified in ECR2, leading to the extraction of more intense, higher charge state ions for acceleration in the K150 cyclotron.

The advantage of simultaneously injecting microwaves of two separated frequencies for plasma heating was first demonstrated by the Lawrence Berkeley National Laboratory (LBNL) group on their advanced ECR ion source (AECR), which operated at 14 GHz (the primary frequency) and 10 GHz (the second frequency) [1]. By comparison with the best results obtained with single-frequency (14 GHz) heating, their measurements performed with two-frequency (14+10 GHz) heating showed that the overall charge state distribution shifted to higher charge states, production of the high charge state ions increased by a factor of 2-5 or higher, and the plasma stability improved. These experimental results strongly support the idea that an increased number of resonance surfaces (instead of one) leads to an enhancement of source performance.

Following the approach taken by the LBNL group, we have used the standard 14.5 GHz microwave injection from a 2.25 kW klystron and the second microwave injection from a 0.5 kW traveling wave tube amplifier (TWTA) with a normal operating range of 11–13 GHz to produce highly charged ions in a two-frequency heating mode. Running both transmitters gives hints of better performance of ECR2 at comparable microwave power levels, but not to the same extent as reported for the AECR. This has motivated us to explore a wide range of second frequencies as well as to experiment with magnetic field configurations and microwave power levels for optimization.

The minimum-B magnetic field configuration, formed by a superposition of an axial mirror field, one with a central minimum, and a radial hexapole field, whose zero coincides with the axis of the source, is a critical component of the ECR2 to confine the plasma and to provide the resonant electron heating. The field increases in all directions away from the center of the source. If two microwaves at different frequencies are launched into the source, the magnetic field configuration needs to be adjusted to produce two well-separated ECR surfaces within the minimum-B field and a quiescent plasma condition can be created to allow high charge states to develop. Consequently, it is important to experimentally determine the strength of the minimum field, B_{MIN}, relative to the resonance field, B_{ECR}, expressed as $B_{ECR} = f_{ECR}/28$ where B_{ECR} is in Tesla and f_{ECR} is the microwave frequency in GHz.

Prior to measurements of B_{MIN} with only the TWTA transmitter in operation, the POISSON design model was used to simulate the axial mirror fields of ECR2 for different coils settings. Table 1 shows calculated results for fields at the injection (B_{INJ}), center (B_{MIN}), and extraction (B_{EXT}) of the plasma chamber as well as microwave frequency calculated for the condition of the absolute minimum confinement defined by the ratio of B_{MIN} to B_{ECR} to be equal to unity. These calculated results determined the TWTA frequency range to be varied between 8.5 and 10 GHz for measurements.

TABLE 1. Axial magnetic fields at the injection (B_{INJ}), center (B_{MIN}), and extraction (B_{EXT}) of the plasma chamber as calculated with the POISSON code. In the calculations two middle coils are varied from 250 A to 500 A in increments of 50 A, while the outermost six coils are held at 500 A.

Six Coils at 500 A				
Two Mid Coils [A]	B_{INJ} [T]	B_{MIN} [T]	B_{EXT} [T]	f_{ECR} at B_{MIN} [GHz]
500	1.8360	0.3551	0.9005	9.94
450	1.8197	0.3397	0.8865	9.51
400	1.8032	0.3243	0.8724	9.08
350	1.7866	0.3089	0.8583	8.65
300	1.7698	0.2935	0.8442	8.22
250	1.7528	0.2780	0.8300	7.78

We tested these calculated results experimentally by varying the TWTA frequencies at low microwave powers and/or by adjusting the two middle coils until a small plasma was ignited. Currently analysis is in progress to evaluate how good the agreement is between the measured and calculated B_{MIN}. If the results turn out to be consistent, then the axial mirror fields simulated with the POISSON code can serve as a guide to find the optimum operating frequencies of the TWTA for the two-frequency heating technique.

[1] Z.Q. Xie and C.M. Lyneis, Rev. Sci. Instrum. **66**, 4218 (1995).

Recent development of re-accelerated rare isotope beams from the light-ion guide

B.T. Roeder, G.J. Kim, and G. Tabacaru

This year, the development of re-accelerated rare isotope beams (RIBs) from the light ion guide (LIG) continued. Two mass regions were investigated. First, a mass-89 radioactive cocktail beam composed of ^{89}Zr and ^{89}Nb was tested since relatively high intensities were achieved from the LIG. Following the successful re-acceleration of the mass-89 RIBs with the K500 cyclotron in July 2023, a mass-105 RIB containing ^{105}In, ^{105}Cd and ^{105}Ag was prepared with the LIG in April 2024. After re-acceleration by the K500 cyclotron, the mass-105 RIB was used in the first experiment with re-accelerated beam at the Cyclotron Institute to measure ^{105}In+p and ^{105}Cd+p elastic scattering. Some preliminary results from this experiment are given in a separate report [1].

For the mass-89 RIB in July 2023, a 22 MeV proton beam from the K150 cyclotron bombarded an enriched ^{90}Zr target at the light-ion guide target chamber. Proton beam intensities up to 10μA were used. The ^{89}Nb and ^{89}Zr ions produced from the p+^{90}Zr reactions were stopped in helium gas and transported through the light ion guide to the charge-breeding ECR ion source. In the CB-ECR, the ^{89}Nb and ^{89}Zr were charge-bred up to charge state 19^{+} and then transported to the cyclotron for re-acceleration. Due to the low intensity of the mass-89 RIB, the K500 cyclotron and beam optics tune were first optimized with a $^{14}N^{3+}$ pilot beam at 15 MeV/u. Once completed, the K500 radiofrequency (RF) was re-tuned -32.3 kHz lower (from 12.6453 MHz to 12.6130 MHz) to account for charge-to-mass (q/m) difference between 14N3+ ions and the mass-89 RIB ions.

Following this slight RF frequency change, the mass-89 RIBs were accelerated by the K500 cyclotron to 15 MeV/u and transported to the MARS target chamber. In the chamber, a ΔE-E silicon detector telescope, composed of an 81.6 μm "ΔE" and a 2002 μm "E" silicon surface barrier detectors, was mounted at 0° with respect to the beam to measure and identify the RIB ions with the energy loss technique. The response of ΔE-E silicon detectors was calibrated prior to the experiment with a 15 MeV/u ^{84}Kr beam, also accelerated by the K500 cyclotron. The signals from the silicon telescope were amplified with a CAEN 1422A preamplifier with gain 1mV/MeV and the signals were digitized with a CAEN 5780 desktop digitizer. The data were recorded and could be displayed during the experimental runs with the CoMPASS software package.

When the K500 cyclotron RF frequency was changed to 12.6130 MHz, the mass-89 RIBs immediately appeared in the spectra measured by the ΔE-E silicon detector telescope. The initial beam rates were about 66 ion/s for $^{89}Nb^{19+}$ and about 12 ions/s for $^{89}Zr^{19+}$. Various optimizations were carried out, including adjusting the proton beam intensity, optimizing the cyclotron buncher and dees, adjusting slightly the CB-ECR extraction voltage, tuning the LIG and CB-ECR parameters, and scanning the K500 RF frequency to see how the ion transmission changed. Among these changes, increasing the proton beam intensity to 8μA and optimizing the K500 dees and radiofrequency produced the largest improvements. After optimization, the best beam rate obtained for $^{89}Nb^{19+}$ was 100 ions/s and about 20 ions/s for $^{89}Zr^{19+}$. A small amount of $^{89}Y^{19+}$ was also present in the beam. A spectrum from the mass-89 RIB measurements is shown in Fig. 1.

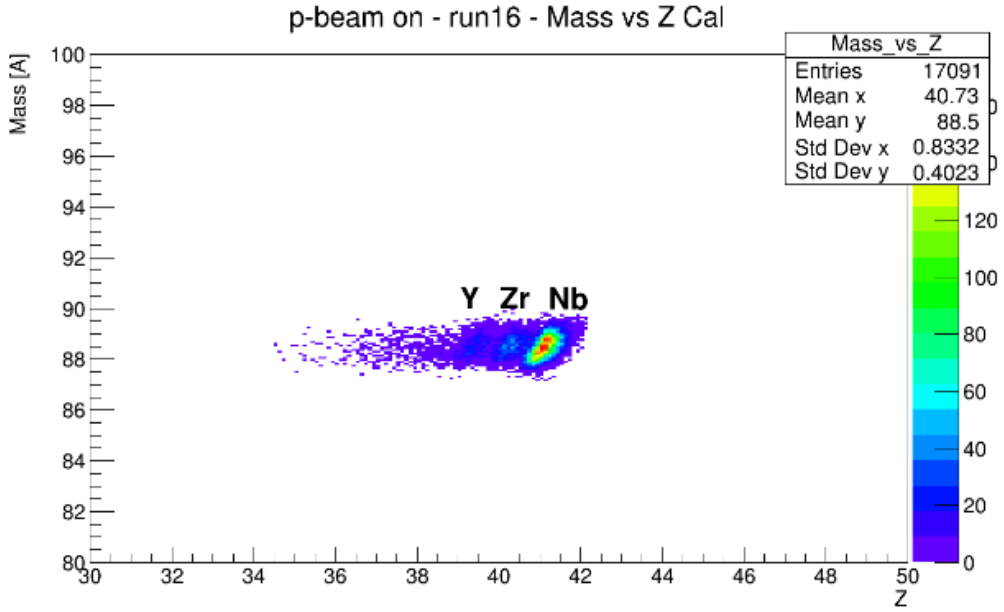

FIG. 1. Results from the mass-89 RIB tune as measured with the ΔE-E silicon detector telescope. The measured energy losses for ions were calibrated in this spectrum to illustrate the mass and proton number of the ions.

For the mass-105 RIB in April 2024, a 22 MeV proton beam from the K150 cyclotron bombarded an enriched ^{106}Cd target at the light ion guide target chamber. Proton intensities up to 12μA were used. The mass-105 RIB ions (^{105}In,^{105}Cd and ^{105}Ag) were stopped in helium gas and transported to the CB-ECR where they were charge-bred up to charge states 22+, and 19+. For the first part of the experiment, the K500 cyclotron and beam optics were tuned with a $^{86}Kr^{18+}$ pilot beam at 15 MeV/u. Then, the RF was changed from 12.6453 MHz to 12.6550 MHz to accelerate the mass-105 RIBs in charge state 22+. The resulting accelerated ions were detected and identified with the same ΔE-E silicon detector telescope and associated data acquisition electronics used for the ^{89}Nb/^{89}Zr development run, except this time the detector telescope was mounted in the BEam Analysis STation (BEAST) chamber in cave 3 [2]. The BEAST chamber was mounted just upstream of the experimental chamber. A picture of the setup in this case is shown in Fig. 2. The maximum mass-105 RIB rates measured were about 6 ions/s of $^{105}In^{22+}$ and about 12 ions/s of $^{105}Cd^{22+}$. $^{105}Ag^{22+}$ was also present at a very low rate. The $^{86}Kr^{18+}$ pilot beam also could not be eliminated by the cyclotron RF change and was still visible on the detector at a rate of about 12 ions/s.

Later in the experiment, a higher rate for the mass-105 RIB ions was desired. It was found that the CB-ECR was producing more of the RIB ions in the 19+ charge state. So, the cyclotron was re-tuned with an $^{83}Kr^{15+}$ pilot beam at 12 MeV/u. In this case, the K500 RF was changed from 11.3666 MHz (pilot beam) to 11.37775 MHz (mass-105 RIBs). The latter RF was chosen to

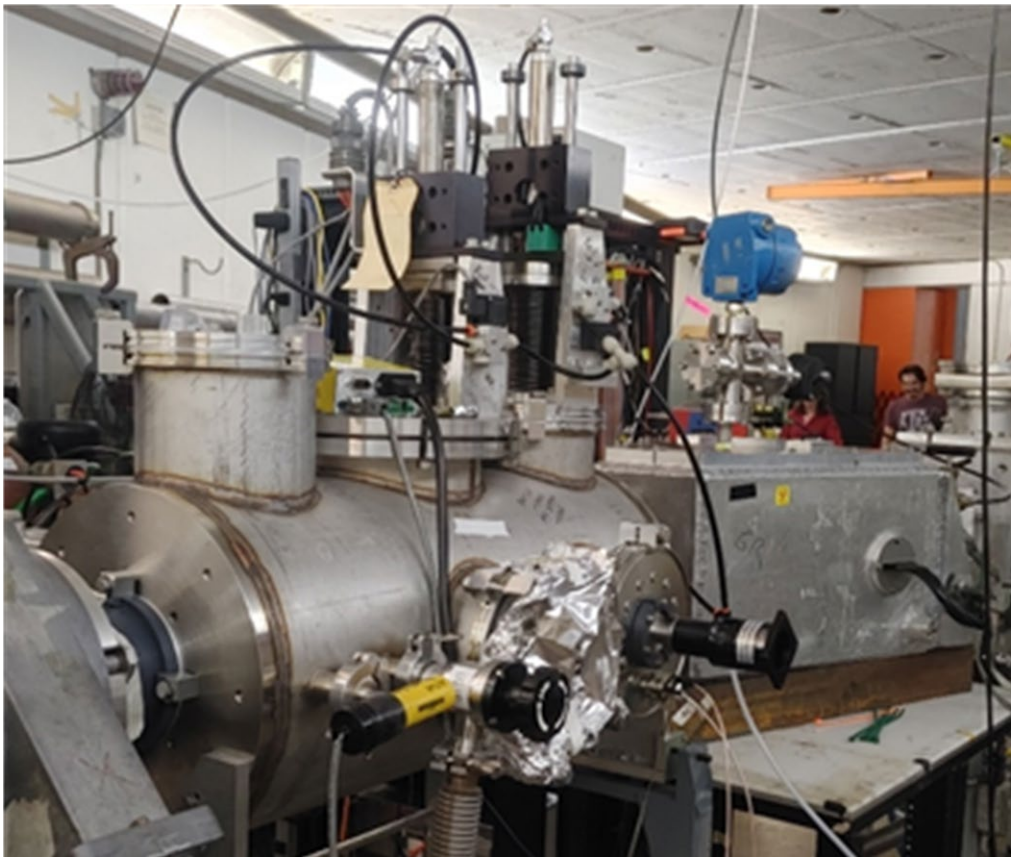

FIG. 2. Picture of the experimental setup for the Mass-105 RIB run. The BEAST chamber with the tuning detectors for the Mass-105 RIB is shown on the left and the experiment chamber is shown downstream on the right of the picture.

optimize the transmission of $^{105}In^{19+}$, which was the RIB of the highest interest for the experimenters. For most of the experiment, the mass-105 RIB rates were about 20 ions/s for $^{105}In^{19+}$ and about 50-60 ions/s for $^{105}Cd^{19+}$, as measured with the silicon detector in the BEAST chamber. This result is expected because the production cross section is expected to be about 4 times higher for ^{105}Cd vs. ^{105}In [3], even though the cyclotron tune was optimized for $^{105}In^{19+}$. However, near the end of the experiment, it was found that the rate of $^{105}In^{19+}$ could be optimized even further by gating directly on the $^{105}In^{19+}$ in the CoMPASS data acquisition software and tuning the cyclotron dees and buncher on the gated event rate. With this technique, the best rate obtained for $^{105}In^{19+}$ was 35 ions/s, which also came with 70 ions/s of $^{105}Cd^{19+}$ and 20 ions/s of $^{105}Ag^{19+}$. A spectrum showing the optimized tune for the mass-105 RIB is shown in Fig. 3. Some stable mass-94, mass-116 and mass-127 contamination was also present in the beam at a very low rate (< few counts/sec). These ions arise from residues in the CB-ECR plasma chamber, as has been noted in previous LIG runs [4]. In total, the experiment ran for about 2 weeks.

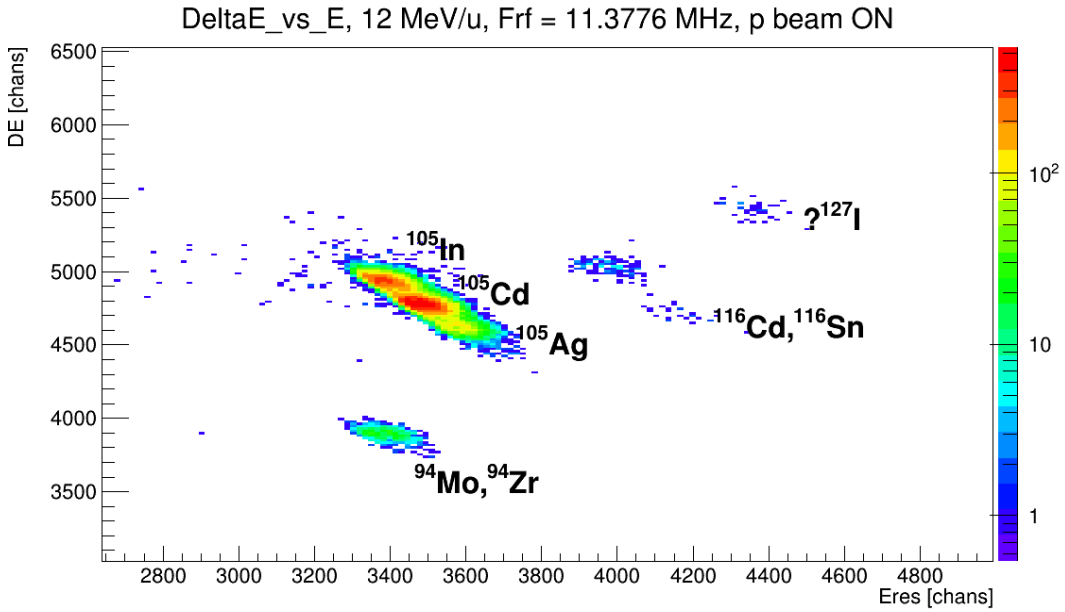

FIG. 3. Spectrum showing the composition of the Mass-105 RIB cocktail beam as measured by the silicon detector telescope in the BEAST chamber in a 300s test run. Mass-94, mass-116 and mass-127 contaminants from the ion source were also present at very low rate.

In conclusion, two new re-accelerated rare isotope beam cocktails were prepared by the light ion guide and re-accelerated by the K500 cyclotron. In both cases, the maximum total RIB rates obtained were around 100 ions/s and were mostly limited by the production cross sections and the CB-ECR charge-breeding efficiency. The mass-105 beam cocktail containing ^{105}In, ^{105}Cd and ^{105}Ag was used for an elastic scattering experiment that lasted 2 weeks. Further developments to improve the beam intensities and to produce other re-accelerated rare isotope beams are planned for the coming year.

[1] M. Barbui *et al. Progress in Research*, Cyclotron Institute, Texas A&M University (2023-2024), p. I-??;http://cyclotron.tamu.edu/progress-reports/2023-2024/SECTION I.html.

[2] B.T. Roeder *et al.*, *Progress in Research*, Cyclotron Institute, Texas A&M University (2019-2020), P. IV-13; http://cyclotron.tamu.edu/progress-reports/2019-2020/SECTION IV.html.

[3] *TENDL-2017*, https://tendl.web.psi.ch/tendl_2017/tendl2017.html.

[4] B.T. Roeder et al., *Progress in Research*, Cyclotron Institute, Texas A&M University (2018-2019), p. IV-23, http://cyclotron.tamu.edu/progress-reports/2018-2019/SECTION IV.html.

SECTION V

PUBLICATIONS

PAPERS PUBLISHED
April 1, 2023– March 31, 2024

***R*-matrix analysis of ^{22}Ne states populated in ^{18}O(α,α) resonant elastic scattering**, A.K. Nurmukh anbetova, V.Z. Goldberg, A. Volya, D.K. Nauruzbayev, G.E. Serikbayeva and G.V. Rogachev, Phys. Rev. C 109, 024607 (2024).

Unveiling the dynamics of little-bang nucleosynthesis, K. J. Sun, R. Wang, C. M. Ko, Y. G. Ma, and C. Sen, Nature Commun. **15**, 1975 (2024).

Characterization and application of alkanethiolate self-assembled monolayers on Au-coated chips for Ir(IV) and Rh(III) sorption, Vira Zakusilova, Evgeny E. Tereshatov, Maria Boltoeva and Charles M. Folden, III, Applied Surface Science **642**, 158356 (2024).

Dense nuclear matter equation of state from heavy-ion collisions, Agnieszka Sorensen, Kshitij Agarwal, Kyle W. Brown, Zbigniew Chajęcki, Pawel Danielewicz, Christian Drischler, Stefano Gandolfi, Jeremy W. Holt*, Matthias Kaminski, Che Ming Ko, Rohit Kumar, Bao-An Li, William G. Lynch, Alan B. McIntosh, William G. Newton, Scott Pratt, Oleh Savchuk, Maria Stefaniak, Ingo Tews, Manyee Betty Tsang, Ramona Vogt, Hermann Wolter, Hanna Zbroszczyk, Navid Abbasi, Jörg Aichelin, Anton Andronic, Steffen A. Bass, Francesco Becattini, David Blaschke, Markus Bleicher, Christoph Blume, Elena Bratkovskaya, B. Alex Brown, David A. Brown, Alberto Camaiani, Giovanni Casini, Katerina Chatziioannou, Abdelouahad Chbihi, Maria Colonna, Mircea Dan Cozma, Veronica Dexheimer, Xin Dong, Travis Dore, Lipei Du, José A. Dueñas, Hannah Elfner, Wojciech Florkowski, Yuki Fujimoto, Richard J. Furnstahl, Alexandra Gade, Tetyana Galatyuk, Charles Gale, Frank Geurts, Fabiana Gramegna, Sašo Grozdanov, Kris Hagel, Steven P. Harris, Wick Haxton, Ulrich Heinz, Michal P. Heller, Or Hen, Heiko Hergert, Norbert Herrmann, Huan Zhong Huang, Xu-Guang Huang, Natsumi Ikeno, Gabriele Inghirami, Jakub Jankowski, Jiangyong Jia, José C. Jiménez, Joseph Kapusta, Behruz Kardan, Iurii Karpenko, Declan Keane, Dmitri Kharzeev, Andrej Kugler, Arnaud {Le Fèvre}, Dean Lee, Hong Liu, Michael A. Lisa, William J. Llope, Ivano Lombardo, Manuel Lorenz, Tommaso Marchi, Larry McLerran, Ulrich Mosel, Anton Motornenko, Berndt Müller, Paolo Napolitani, Joseph B. Natowitz, Witold Nazarewicz, Jorge Noronha, Jacquelyn Noronha-Hostler, Grażyna Odyniec, Panagiota Papakonstantinou, Zuzana Paulínyová, Jorge Piekarewicz, Robert D. Pisarski, Christopher Plumberg, Madappa Prakash, Jørgen Randrup, Claudia Ratti, Peter Rau, Sanjay Reddy, Hans-Rudolf Schmidt, Paolo Russotto, Radoslaw Ryblewski, Andreas Schäfer, Björn Schenke, Srimoyee Sen, Peter Senger, Richard Seto, Chun Shen, Bradley Sherrill, Mayank Singh, Vladimir Skokov, Michał Spaliński, Jan Steinheimer, Mikhail Stephanov, Joachim Stroth, Christian Sturm, Kai-Jia Sun, Aihong Tang, Giorgio Torrieri, Wolfgang Trautmann, Giuseppe Verde, Volodymyr Vovchenko, Ryoichi Wada, Fuqiang Wang, Gang Wang, Klaus Werner, Nu Xu, Zhang-Bu Xu, Ho-Ung Yee, Sherry Yennello and Yi Yin, Prog. Part. and Nucl. Phys. **134**, 104080 (2024).

Fine structure of the isoscalar giant monopole resonance in ^{58}Ni, ^{90}Zr, ^{120}Sn, and ^{208}Pb, A. Bahini, P. von Neumann-Cosel, J. Carter, I.T. Usman, N.N. Arsenyev, A.P. Severyukhin, E. Litvinova, R.W. Fearick, R. Neveling, P. Adsley, N. Botha, J.W. Brümmer, L.M. Donaldson, S. Jongile, T.C. Khumalo, M.B. Latif, K.C.W. Li, P.Z. Mabika, P.T. Molema, C.S. Moodley, S.D. Olorunfunmi, P. Papka, L. Pellegri, B. Rebeiro, E. Sideras-Haddad, F.D. Smit, S. Triambak, M. Wiedeking and J.J. van Zyl, Phys. Rev. C **109**, 014325 (2024).

Longitudinal and transverse spin transfer to Λ and $\bar{\Lambda}$ hyperons in polarized p+p collisions at $\sqrt{s}$=200 GeV, M. I. Abdulhamid, D. M. Anderson, J. Atchison, C. A. Gagliardi, A. Hamed, T. Lin, X. Liu, Y. Liu, S. Mioduszewski, N. R. Sahoo and R. E. Tribble, Phys. Rev. D **109**, 012004 (2024).

Radiative decay branching ratio of the Hoyle state, Zifeng Luo, M. Barbui, J. Bishop, G. Chubarian, V. Z. Goldberg, E. Harris, E. Koshchiy, C. E. Parker, M. Roosa, A. Saastamoinen, D. P. Scriven and G. V. Rogachev, Phys. Rev. C **109**, 025801 (2024).

Understanding the total width of the 3_1^- state in ^{12}C, K. C. W. Li, R. Neveling, P. Adsley*, H. Fujita, P. Papka, F. D. Smit, J. W. Brümmer, L. M. Donaldson, M. N. Harakeh, Tz. Kokalova, E. Nikolskii, W. Paulsen, L. Pellegri, S. Siem and M. Wiedeking, Phys. Rev. C **109**, 015806 (2024).

2023

Many-body expansion for light nuclear systems, Theodore Depastas, George A. Souliotis, Demeter Tzeli, and Sotiris S. Xantheas, Phys. Rev. C **107**, 044004 (2023)

Search for QCD critical point with light nuclei, Che Ming Ko, Nucl. Sci. Tech. **34**, 81 (2023).

α-cluster microscopic study of ^{12}C+^{12}C fusion toward the zero energy limit, T. Depastas, S. T. Sun, H. Zheng and A. Bonasera, Phys. Rev. C **108**, 035806 (2023).

^{138}Ba(d,α) Study of States in ^{136}Cs: Implications for New Physics Searches with Xenon Detectors, B. M. Rebeiro, S. Triambak, P. E. Garrett, G. C. Ball, B. A. Brown, J. Menéndez, B. Romeo, P. Adsley*, B. G. Lenardo, R. Lindsay, V. Bildstein, C. Burbadge, R. Coleman, A. Diaz Varela, R. Dubey, T. Faestermann, R. Hertenberger, M. Kamil, K. G. Leach, C. Natzke, J. C. Nzobadila Ondze, A. Radich, E. Rand and H. -F. Wirth, Phys. Rev. Lett. **131**, 052501 (2023).

Behavior of astatine and bismuth in non-conventional solvents: Extraction into imidazolium-based ionic liquid and methyl anthranilate with active pharmaceuticals binary mixtures from nitric acid media, Evgeny E. Tereshatov, Jonathan D. Burns, Amy L. Vonder Haar, Steven J. Schultz, Lauren A. McIntosh, Gabriel C. Tabacaru, Laura A. McCann, Geoffrey Avila, Andrew Hannaman, Ashley Hood, Kylie N. Lofton, Mallory A. McCarthy, Maxwell Sorensen and Sherry J. Yennello, Sep. Purif. Technol **326**, 124715 (2023).

Determination of asymptotic normalization coefficients for the channel $^{16}O \rightarrow \alpha + ^{12}C$: excited states $^{16}O(0^+;6.05\ MeV)$, L.D. Blokhintsev, A.S. Kadyrov, A.M. Mukhamedzhanov and D.A. Savin, The Eur. Phys. J. A **59**, 4 (2023).

Determination of the astrophysical factor of the $^{3}He(\alpha,\gamma)^{7}Be$ down to zero energy using the asymptotic normalization coefficient method, M. La Cognata, G.G. Kiss, R. Yarmukhamedov, K.I. Tursunmakhatov, I. Wiedenhöver, L.T. Baby, S. Cherubini, A. Cvetinović, G. D'Agata, P. Figuera, G.L. Guardo, M. Gulino, S. Hayakawa, I. Indelicato, L. Lamia, M. Lattuada, F. Mudò, S. Palmerini, R.G. Pizzone, G.G. Rapisarda, S. Romano, M.L. Sergi, R. Spartá, C. Spitaleri, O. Trippella, A. Tumino, M. Anastasiou, S.A. Kuvin, N. Rijal, B. Schmidt, S.B. Igamov, S.B. Sakuta, Zs. Fülöp, Gy. Gyürky, T. Szücs, Z. Halász, E. Somorjai, Z. Hons, J. Mrazek, R.E. Tribble and A.M. Mukhamedzhanov, 28th International Nuclear Physics Conference (INPC 2022), J. Phys. Conf. Series **2586**, 012093 (2023) IOP Publishing, 2023 Cape Town South Africa.

Determining the nuclear temperature dependence on source neutron-proton asymmetry in heavy-ion reactions at intermediate energy, Guofeng Qu, Y. Huang, Hua Zheng, Xing-Quan Liu, R. Wada, Wei-Ping Lin, Meirong Huang, Jifeng Han, Pei-Pei Ren, Zhenlei Yang, Xin Zhang and Qiangzhong Leng, Chinese Physics C **47**, 054002 (2023).

Elliptic flow of heavy-flavor decay electrons in Au+Au collisions at $\sqrt{s_{NN}}$ = 27 and 54.4 GeV at RHIC, M.I. Abdulhamid, D.M. Anderson, J. Atchison, C.A. Gagliardi, A. Hamed, T. Lin, X. Liu, Y. Liu, S. Mioduszewski, N.R. Sahoo and R.E. Tribble, Phys. Lett. B **844**, 138071 (2023).

Energy dependence of intermittency for charged hadrons in Au + Au collisions at RHIC, M.I. Abdulhamid, D.M. Anderson, J. Atchison, C.A. Gagliardi, A. Hamed, T. Lin, X. Liu, Y. Liu, S. Mioduszewski, N.R. Sahoo and R E. Tribble, Phys. Lett. B **845**, 138165 (2023).

Entanglement entropy, single-particle occupation probabilities, and short-range correlations, A. Bulgac, Phys. Rev. C **107**, L061602 (2023)

Event-by-event antideuteron multiplicity fluctuation in Pb + Pb collisions at $\sqrt{s_{NN}}$ =5.01 TeV, Kai-Jia Sun and Che Ming Ko, Phys. Lett. B **840**, 137864 (2023).

Examination of how properties of a fissioning system impact isomeric yield ratios of the fragments, D. Gjestvang, J.N. Wilson, A. Al-Adili, S. Siem, Z. Gao, J. Randrup, D. Thisse, M. Lebois, N. Jovančević, R. Canavan, M. Rudigier, D. Etasse, R.-B. Gerst, E. Adamska, P. Adsley, A. Algora, C. Belvedere, J. Benito, G. Benzoni, A. Blazhev, A. Boso, S. Bottoni, M. Bunce, R. Chakma, N. Cieplicka-Oryńczak, S. Courtin, M.L. Cortés, P. Davies, C. Delafosse, M. Fallot, B. Fornal, L. Fraile, A. Gottardo, V. Guadilla, G. Häfner, K. Hauschild, M. Heine, C. Henrich, I. Homm, F. Ibrahim, Ł.W. Iskra, P. Ivanov, S. Jazrawi, A. Korgul, P. Koseoglou, T. Kröll, T. Kurtukian-Nieto, S. Leoni, J. Ljungvall, A. Lopez-Martens, R. Lozeva, I. Matea, K.

Miernik, J. Nemer, S. Oberstedt, W. Paulsen, M. Piersa-Silkowska, Y. Popovitch, C. Porzio, L. Qi, P.H. Regan, K. Rezynkina, V. Sánchez-Tembleque, C. Schmitt, P.-A. Söderström, C. Sürder, G. Tocabens, V. Vedia, D. Verney, N. Warr, B. Wasilewska, J. Wiederhold, M. Yavahchova and S. Ziliani, Phys. Rev. C **108**, 064602 (2023).

Examining the justification for the introduction of a fermion localization function, A. Bulgac, Phys. Rev. C **108**, L051303 (2023).

Excited hadron channels in hadronization, R. J. Fries, J. Purcell, M. Kordell and C. M. Ko, Proceedings of Science 438, 132 (2023).

Expanding RIB capabilities at the Cyclotron Institute: ^{3}He-LIG production with an isobar separator LSTAR, D. Melconian, G.P.A. Berg, P.D. Shidling, M. Couder, M. Brodeur, G. Chubarian, V.E. Iacob, J. Klimo and G. Tabacaru Proceedings of the XIX International Conference on Electromagnetic Isotope Separators and Related Topics (EMIS 2022), IBS/RISP, Daejeon Korea, 3–7 October 2022, Nucl. Instrum Methods Phys. Res. B **541**, 99 (2023).

First observation of cyclotron radiation from MeV-scale $e\pm$ following nuclear β decay, W. Byron, H. Harrington, R.J. Taylor, W. DeGraw, N. Buzinsky, B. Dodson, M. Fertl, A. García, G. Garvey, B. Graner, M. Guigue, L. Hayen, X. Huyan, K.S. Khaw, K. Knutsen, D. McClain, D. Melconian, P. Müller, E. Novitski, N.S. Oblath, R.G.H. Robertson, G. Rybka, G. Savard, E. Smith, D.D. Stancil, M. Sternberg, D. W. Storm, H.E. Swanson, J.R. Tedeschi, B.A. VanDevender, F.E. Wietfeldt, A.R. Young (He6-CRES Collaboration), Phys. Rev. Lett. **131**, 082502 (2023).

First observation of the $\beta 3\alpha p$ decay of ^{13}O via β-delayed charged-particle spectroscopy, J. Bishop, G.V. Rogachev, S. Ahn, M. Barbui, S.M. Cha, E. Harris, C. Hunt, C.H. Kim, D. Kim, S.H. Kim, E. Koshchiy, Z. Luo, C. Park, C.E. Parker, E. C. Pollacco, B.T. Roeder, M. Roosa, A. Saastamoinen and D. P. Scriven, Phys. Rev. Lett. **130**, 222501 (2023).

FITEVT: A FORTRAN program for arrival-time analysis of nuclear-decay events, Vladimir Horvat, Computer Physics Communications **284**, 108600 (2023)

Global polarization of Λ and $\bar{\Lambda}$ hyperons in Au+Au collisions at $\sqrt{s_{NN}}$ = 19.6 and 27 GeV, M.I. Abdulhamid, D.M. Anderson, J. Atchison, C.A. Gagliardi, A. Hamed, T. Lin, X. Liu, Y. Liu, S. Mioduszewski, N.R. Sahoo and R.E. Tribble, Phys. Rev. C **108**, 014910 (2023).

High event rate analysis technique for the dual-axis duo-lateral position-sensitive silicon detectors of FAUST, A. Hannaman, A.B. McIntosh, K. Hagel, B. Harvey, S. Regener, A. Abbott, J. Gauthier, T. Hankins, Y.-W. Lui, L. McCann, L.A. McIntosh, R. Rider, S. Schultz, M.Q. Sorensen, Z.N. Tobin, R. Wada and S.J. Yennello, Nucl. Instrum. Methods Phys. Res. A **1050**, 168130 (2023).

Ion exchange behavior of astatine and bismuth, Evgeny E. Tereshatov, Jonathan D. Burns, Steven J. Schultz, Brooklyn D. Green, Gabriela A. Picayo, Laura A. McCann, Lauren A. McIntosh, Gabriel C. Tabacaru, Austin Abbott, Matthew Berko, Emily Engelthaler, Kris Hagel, Travis Hankins, Bryan Harvey, Lauren Hoekstra, Kylie Lofton, Sebastian Regener, Robert Rider, Maxwell Sorensen, Alexandra Tabacaru, David Thomas, Justin Tobar, Zachary Tobin and Sherry J. Yennello, New Journal of Chemistry **47**, 12037 (2023).

Isoscalar giant monopole strength in ^{58}Ni, ^{90}Zr, ^{120}Sn, and ^{208}Pb, A. Bahini, R. Neveling, P. von Neumann-Cosel, J. Carter, I.T. Usman, P. Adsley, N. Botha, J.W. Brümmer, L.M. Donaldson, S. Jongile, T.C. Khumalo, M.B. Latif, K.C.W. Li, P.Z. Mabika, P.T. Molema, C.S. Moodley, S.D. Olorunfunmi, P. Papka, L. Pellegri, B. Rebeiro, E. Sideras-Haddad, F.D. Smit, S. Triambak, M. Wiedeking and J.J. van Zyl, Phys. Rev. C **107**, 034312 (2023).

Kinetic approach of light-nuclei production in intermediate-energy heavy-ion collisions, Rui Wang, Yu-Gang Ma, Lie-Wen Chen, Che Ming Ko, Kai-Jia Sun and Zhen Zhang, Phys. Rev. C **108**, L031601 (2023).

Measurement of electrons from open heavy-flavor hadron decays in Au+Au collisions at $\sqrt{s_{NN}}$ = 200~GeV with the STAR detector, and M. I. Abdulhamid, D.M. Anderson, J. Atchison, C.A. Gagliardi, A. Hamed, T. Lin, X. Liu, Y. Liu, S. Mioduszewski, N.R. Sahoo and R.E. Tribble, J. High Energy Phys. **2023**, 176 (2023).

Measurements of dielectron production in Au+Au collisions at $\sqrt{s_{NN}}$ =27, 39, and 62.4 GeV from the STAR experiment, M.I. Abdulhamid, D.M. Anderson, J. Atchison, C.A. Gagliardi, A. Hamed, T. Lin, X. Liu, Y. Liu, S. Mioduszewski, N.R. Sahoo and R.E. Tribble, Phys. Rev. C **107**, L061901 (2023).

Measurement of sequential Υ suppression in Au+Au collisions at $\sqrt{s_{NN}}$ = 200 GeV with the STAR experiment, B.E. Aboona, D.M. Anderson, J. Atchison, C.A. Gagliardi, A. Hamed, T. Lin, X. Liu, Y. Liu, S. Mioduszewski, N.R. Sahoo and R.E. Tribble, Phys. Rev. Lett. **130**, 112301 (2023).

Measures of complexity and entanglement in many-fermion systems, A. Bulgac, M. Kafker and I. Abdurrahman, Phys. Rev. C **107**, 044318 (2023).

Mechanism of astatine and bismuth sorption on extraction chromatography resins from nitric acid media, Evgeny E. Tereshatov, Jonathan D. Burns, Steven J. Schultz, Brooklyn D. Green, Gabriela A. Picayo, Laura A. McCann, Lauren A. McIntosh, Gabriel C. Tabacaru, Austin Abbott, Matthew Berko, Emily Engelthaler, Kris Hagel, Travis Hankins, Bryan Harvey, Lauren Hoekstra, Kylie Lofton, Sebastian Regener, Robert Rider, Maxwell Sorensen, Alexandra Tabacaru, David Thomas, Justin Tobar, Zachary Tobin and Sherry J. Yennello, Chem. Eng. J. **464**, 142742 (2023).

Menthol-Based eutectic solvent for indium and thallium partition from hydrochloric acid media, E. E. Tereshatov, M. F. Volia and C. M. Folden, III, J. Mol. Liq. **391**, 123339 (2023)

New developments in fission studies within the time-dependent density functional theory framework, A. Bulgac, 15th International Conference on Nuclear Data for Science and Technology (ND2022) Sacramento, CA, Eur. Phys. J. Web of Conf. **284**, 04001 (2023).

Noise signal identification in time projection chamber data using deep learning model, C. H. Kim, S. Ahn, K. Y. Chae, J. Hooker and G. V. Rogachev, Nucl. Instrum. Methods Phys. Res. **A1048**, 168025 (2023).

Nondestructive and destructive assay for forensics characterization of weapons-grade plutonium produced in LEU irradiated in a thermal neutron spectrum, Sean P. Martinson, Jenna R. Garcia, Isaac W. Haynes, Simrun P. Saini, Elisan R. Wagner, Grace R. Long, Charles M. Folden, III and Sunil S. Chirayath, Ann. Nucl. Energy **183**, 109645 (2023).

Nuclear level density in the statistical semiclassical micro-macroscopic approach, A. G. Magner, and A.I. Sanzhur, S. N. Fedotkin, A. I. Levon, U. V. Grygoriev, and S. Shlomo, Nucl. Phys. At. Energy **24**, 175 (2023).

Optical potentials for the rare-isotope beam era, C. Hebborn, F. M. Nunes, G. Potel, W. H. Dickhoff, J. W. Holt, M. C. Atkinson, R. B. Baker, C. Barbieri, G. Blanchon, M. Burrows, R. Capote, P. Danielewicz, M. Dupuis, Ch Elster, J. E. Escher, L. Hlophe, A. Idini, H. Jayatissa, B. P. Kay, K. Kravvaris, J. J. Manfredi, A. Mercenne, B. Morillon, G. Perdikakis, C. D. Pruitt, G. H. Sargsyan, I. J. Thompson, M. Vorabbi and T. R. Whitehead, J. Phys. G **50**, 060501 (2023).

Production of ^{99}Mo in inverse kinematics heavy ion reactions, Marcia Regina Dias Rodrigues, Justin Mabiala, Victor E. Iacob, Ninel Nica, Brian Roeder, Gabriel Tabacaru, Kang Wang, Jedidiah Romo, Dustin Scriven, Nolan Tenpas, Georgios A. Souliotis and Aldo Bonasera, Radiat. Phys. Chem. **212**, 111162 (2023).

Production, isolation, and shipment of clinically relevant quantities of astatine-211: A simple and efficient approach to increasing supply, Lauren A. McIntosh, Jonathan D. Burns, Evgeny E. Tereshatov, Riccardo Muzzioli, Kris Hagel, Noimat A. Jinadu, Laura A. McCann, Gabriela A. Picayo, Federica Pisaneschi, David Piwnica-Worms, Steven J. Schultz, Gabriel C. Tabacaru, Austin Abbott, Brooklyn Green, Travis Hankins, Andrew Hannaman, Bryan Harvey, Kylie Lofton, Robert Rider, Maxwell Sorensen, Alexandra Tabacaru, Zachary Tobin and Sherry J. Yennello, Nucl. Med. Biol. **126-127**, 108387 (2023).

Proton 0.01 MeV resonance width and low-energy S factor of p+10B fusion, A. M. Mukhamedzhanov, Phys. Rev. C **108**, 054603 (2023).

Proton decays from α-unbound states in ^{22}Mg and the ^{18}Ne(α,p_0)^{21}Na cross section, J. W. Brümmer, P. Adsley, T. Rauscher, F. D. Smit, C. P. Brits, M. Köhne, N. A. Khumalo, K. C. W. Li, D. J. Marín-Lámbarri, N. J. Mukwevho, F. Nemulodi, R. Neveling, P. Papka, L. Pellegri, V. Pesudo, B. M. Rebeiro, G. F. Steyn and W. Yahia-Cherif, Phys. Rev. C **107**, 055802 (2023)

Reaction dynamics and in-medium nucleon-nucleon cross section with ^{12}C+^{1}H at 95~MeV/nucleon, G. Tian, Z. Chen, R. Wada, X. Liu, W. Lin, M. Huang, H. Zheng, Q. Hu, R. Han, F. Shi, X. Zhang, B. Liu and H. Sun, Phys. Rev. C **107**, 044602 (2023).

Restoring original signals from pile-up using deep learning, C. H. Kim, S. Ahn, K. Y. Chae, J. Hooker and G. V. Rogachev, Nucl. Instrum. Methods Phys. Res. **A1055**, 168492 (2023).

Search for an s-wave resonance in ^{7}Li just above the proton-decay threshold, N. Dronchi, J. Berkman, R. J. Charity, J. M. Elson, L. G. Sobotka, A. G. Thomas, A. Saastamoinen, M. Barbui, J. Bishop, C. E. Parker, B. T. Roeder, G. V. Rogachev, D. P. Scriven, S. T. Marley and R. M. Shaffer, Phys. Rev. C **107**, L061303 (2023).

Search for the chiral magnetic effect in Au + Au collisions at $\sqrt{s_{NN}}$ = 27 GeV with the STAR forward event plane detectors, B. E. Aboona, D. M. Anderson, J. Atchison, C. A. Gagliardi, A. Hamed, T. Lin, X. Liu, Y. Liu, S. Mioduszewski, N. R. Sahoo and R. E. Tribble, Phys. Lett. B **839**, 137779 (2023).

Searching for QCD critical point with light nuclei, Che Ming Ko, Nuclear Science and Techniques (NST) **34**, 80 (2023).

Searching for resonance states in ^{22}Ne(p,γ)^{23}Na, D. P. Carrasco-Rojas, M. Williams, P. Adsley, L. Lamia, B. Bastin, T. Faestermann, C. Fougères, F. Hammache, D. S. Harrouz, R. Hertenberger, M. La Cognata, A. Meyer, F. de Oliveira Santos, S. Palmerini, R. G. Pizzone, S. Romano, N. de Séréville, A. Tumino and H. -F. Wirth, Phys. Rev. C **108**, 045802 (2023).

Semimicroscopic description of isoscalar giant multipole resonances in medium-mass closed-shell nuclei, M. L. Gorelik, S. Shlomo, B. A. Tulupov and M. H. Urin, Phys. Rev. C **108**, 014328 (2023).

Semirelativistic antisymmetrized molecular dynamics for the production of energetic neutrons in intermediate-energy heavy-ion reactions, Q. Hu, G. Y. Tian, R. Wada, X. Q. Liu, W. P. Lin, H. Zheng, Y. P. Zhang, Z. Q. Chen, R. Han and M. R. Huang, Phys. Rev. C **108**, 054907 (2023).

Spatial orientation of the fission fragment intrinsic spins and their correlations, G. Scamps, I. Abdurrahman, M. Kafker, A. Bulgac and I. Stetcu, Phys. Rev. C **108**, L061602 (2023).

Spectroscopy of ^{13}Be through isobaric analog states in ^{13}B, C. Hunt, S. Ahn, J. Bishop, E. Koshchiy, E. Aboud, M. Alcorta, A. Bosh, K. Hahn, S. Han, C. E. Parker, E. C. Pollacco, B. T. Roeder, M. Roosa, S. Upadhyayula, A. S. Volya and G. V. Rogachev, Phys. Rev. C **108**, L051606 (2023).

S**tudy of N=50 gap evolution around Z=32: new structure information for ^{82}Ge**, D. Thisse, M. Lebois, D. Verney, J. N. Wilson, N. Jovančević, M. Rudigier, R. Canavan, D. Etasse, P. Adsley*, A. Algora, M. Babo, K. Belvedere, J. Benito, G. Benzoni, A. Blazhev, A. Boso, S. Bottoni, M. Bunce, R. Chakma, N. Cieplicka-Oryńczak, S. Courtin, M. L. Cortés, P. Davies, C. Delafosse, M. Fallot, B. Fornal, L. Fraile, D. Gjestvang, A. Gottardo, V. Guadilla, R. -B. Gerst, G. Häfner, K. Hauschild, M. Heine, C. Henrich, I. Homm, J. Hommet, F. Ibrahim, Ł. W. Iskra, P. Ivanov, S. Jazrawi, A. Korgul, P. Koseoglou, T. Kröll, T. Kurtukian-Nieto, L. Le Meur, S. Leoni, J. Ljungvall, A. Lopez-Martens, R. Lozeva, I. Matea, K. Miernik, J. Nemer, S. Oberstedt, W. Paulsen, M. Piersa-Silkowska, W. Poklepa, Y. Popovitch, C. Porzio, L. Qi, D. Ralet, P. H. Regan, D. Reygadas-Tello, K. Rezynkina, V. Sánchez-Tembleque, S. Siem, C. Schmitt, P. -A. Söderström, K. Solak, C. Sürder, G. Tocabens, V. Vedia, N. Warr, B. Wasilewska, J. Wiederhold, M. Yavahchova, F. Zeiser and S. Ziliani, Eur. Phys. J. A **59**, 153 (2023).

Thermodynamic properties at kinetic freeze-out in Au+Au and Cu+Cu collisions at RHIC using the Tsallis distribution, W.H. Wu, J.Q. Tao, H. Zheng, W.C. Zhang, X.Q. Liu, L.L. Zhu, A. Bonasera, Nucl. Sci. Tech. **34**, 151 (2023).

Pseudorapidity distributions of charged particles in asymmetric collisions using Tsallis thermodynamics, J.Q. Tao, H.B. He, H. Zheng, W.C. Zhang, X.Q. Liu, L.L. Zhu, A. Bonasera, Nucl. Sci. Tech. **34**, 172 (2023).

SECTION VI

APPENDIX

TALKS PRESENTED
April 1, 2023 – March 31, 2024

Heavy ion collisions: tool for studying strong-interaction matter, ***C M. Ko****, Colloquium, Institute of Physics, Academia Sinica, Taipei, Taiwan (March 2024).*

Hadronic effects on Lambda polarization, ***C. M. Ko****,* ***Invited Talk****, ExHIC-p Workshop on Polarization Phenomena in Nuclear Collisions, Taipei, Taiwan (March 2024).*

DAPPER and Triton Beams, **A. McIntosh**, **Talk**, Trotin 2024, Florida State University, Tallahassee, Florida (March 2024).

Nucleon-Nucleon Bremsstrahlung in Fermi-Energy Heavy-Ion Collisions, **T. Onyango**, **Talk**, Stewardships Science Academic Programs Symposium, college station, Texas (February 2024)

Forward Analysis of 58Fe's Photon Strength Function With The DAPPER Array, **M. Sorensen, Talk**, SSAP, Washington, D.C. (February 2024).

Preliminary Analysis towards ^{55}Fe Photon Strength Function using ^{54}Fe(d, p)^{55}Fe reactions with DAPPER, **A. Alvarez**, **Talk**, Stewardship Science Academic Programs, Arlington, Virgina (February 2024).

^{6}He-CRES: Recent progress and future plans, **D. Melconian**, **Invited Talk**, XLV Symposium on Nuclear Physics, Cocoyoc, Morelos, Mexico (January 2024).

2023

Precise half-life measurement of ^{29}P, **V. Iacob**, **Talk**, 6th Joint Meeting of the APS Division of Nuclear Physics and the Physical Society of Japan, Waikoloa Village, HawaiiI, United States (November 2023).

Survival of Excited, Heavy Compound Nuclei, **C. Folden III**, **Talk**, 6th Joint Meeting of the APS Division of Nuclear Physics and the Physical Society of Japan, Waikoloa, Hawaii (November 2023).

Cross section measurement for ^{149}Tb production, **A. McIntosh**, **Talk**, Meeting of the Division of Nuclear Physics of the American Physical Society, Wikoloa, Hawaii, (November 2023).

Progress on the Extraction of ^{58}Fe's Photon Strength Function with the DAPPER Array Using the Forward Method, **M. Sorensen**, **Talk**, American Physical Society, Wikoloa, Hawaii, (November 2023).

Nuclear Forensic Analysis of Manhattan Project Plutonium, **C. Folden III**, **Invited Talk**, Southwest Regional Meeting of the American Chemical Society, Oklahoma City, Oklahoma (November 2024).

Signatures of Short-Range Correlations in Intermediate Energy Heavy Ion Collisions, **K. Hagel**, **Invited Talk**, Workshop on Particles Correllations and Femtoscopy 2023, INFN, Sezione di Catania and Laboratori Nazionali del Sud (LNS), Physics and Astronomy Department "E. Majorana" of the University of Catania, Catania, Italy (November 2023).

Nuclear Forensic Analysis of Manhattan Project Plutonium, **C. Folden III**, **Talk**, 66th Radiobioassay & Radiochemical Measurements Conference, West Palm Beach, Florida (November 2023).

Nuclear Forensic Analysis of Manhattan Project Plutonium, **C. Folden III**, **Invited Talk**, Southeast Regional Meeting of the American Chemical Society, Durham, North Carolina (October 2023).

Normalizing flows for Monte Carlo importance sampling and quantum many-body calculations, **J. Holt, Invited Talk**, Fall 2023 meeting of TSAPS, TSAAPT, and Zone 13 of the SPS, San Angelo, Texas (October 2023).

The STAR Forward Upgrade, **C. Gagliardi**, **Invited Talk**, 25th International Spin Physics Symposium (SPIN 2023), Duke University, Durham, North Carolina (September 2023)

Experiments with Texas Active Target Detector on Rare Isotope Beams, **Y. Koshchiy**, **Talk**, XXXVII Mazurian Lakes Conference on Physics September 7, 2023, Warsaw, Poland (September 2023).

Status of Texas A&M - Cyclotron Institute USNDP Evaluation Center, **N. Nica**, **Invited Talk**, Nuclear Data Advisory Committee Meeting, National Nuclear Data Center, Brookhaven National Laboratory, Upton, New York (September 2023).

Quark recombination: past results, recent developments and future perspectives, **C. M. Ko**, **Invited Talk**, *International Workshop on Past, Present and Future of High-Energy Heavy-Ion Physics, China Central Normal University, Wuhan, China (September 2023).*

Reflection on works with Chinese Aggies, **C. M. Ko, Invited Talk,** *International Mini-Workshop on Heavy-Ion Collisions and Phase Structure of Nuclear Matter, Fudan University, Shanghai, China (July 2023).*

Transport model for nuclear symmetry energy study, **C. M. Ko, Invited Talk***, The International Symposium on Physics of Unstable Nuclei 2023, Phu Quoc Island, Vietnam, (May 2023).*

Mechanism of astatine and bismuth sorption on extraction chromatography resins from nitric acid media, **E. Tereshatov**, **Talk**, ACS Fall 2023, San Francisco, California (August 2023).

Heavy Element Capabilities at Texas A&M University, **C. Folden III**, **Invited Talk**, Low-Energy Community Virtual Meeting, East Lansing, Michigan (August 2023).

Photon Strength Function of ^{58}Fe using the Oslo and Shape Methods, **A. Abbott**, **Talk**, 2023 CENTAUR SAC Meeting, Los Alamos National Laboratory, Los Alamos, New Mexico (August 2023).

Nucleon-Nucleon Bremsstrahlung in Heavy-Ion Collisions at Fermi Energies, **T. Onyango**, **Talk**, Scientific Advisory Committee meeting for CENTAUR, Los Alamos National Laboratory, Los Alamos, New Mexico (August 2023).

(Not) Understanding globular cluster pollution through nuclear reactions, **P. Adsley**, **Invited Seminar**, *Surrey Nuclear Seminar, University of Surrey, Guildford, United Kingdom* (August 2023).

Microscopic many-body theory for hot and dense matter 2, **J. Holt**, **Invited Talk**, Special Nuclear Physics Lecture Series, Yonsei University, Seoul, South Korea (June 2023).

Microscopic many-body theory for hot and dense matter 1, **J. Holt**, **Invited Talk**, Special Nuclear Physics Lecture Series, Yonsei University, Seoul, South Korea (June 2023).

First observation of the β3αp decay of 13O via β-delayed charged-particle spectroscopy, **J. Bishop**, **Talk**, PROCON2023, Warsaw, Poland (June 2023).

Medical radioisotope production using inverse kinematics, **M. Dias Rodrigues**, **Talk**, Advances in Radioactive Isotope Science conference (ARIS 2023), Avignon, France

Preliminary Forward Analysis on ^{58}Fe's Photon Strength Function using DAPPER, **M. Sorensen**, **Talk**, Nuclear Chemistry GRC, Colby Sawyer, New London, New Hampshire (June 2023).

TexAT and TeBAT: a multitude of experiments, **J. Bishop**, **Invited Talk**, TPC2023, College Station, Texas (May 2023).

Microscopic optical potentials for the FRIB era, **J. Holt**, **Invited Talk**, FRIB TA Topical Program: Theoretical Justifications and Motivations for Early High-Profile FRIB Experiments, East Lansing, Michigan (May 2023).

Texas A&M University Master's Program in Radiation Effects, **C. Parker**, **Invited Talk**, SEE Symposium and MAPLD Combined Workshop, La Jolla, California May 2023).

DAPPER TPC, **A. McIntosh**, **Invited Talk**, TPC 2023, College Station, Texas (May 2023).

Mixtures of active pharmaceuticals for studying behavior of medical radioisotopes, **E. Tereshatov**, **Talk**, 3rd International Conference on Radioanalytical and Nuclear Chemistry, Budapest, Hungary (May 2023).

alpha-cluster structure of ^{18}Ne, **M. Barbui**, **Talk**, ANL Physics Division Seminar, Argonne National Laboratory, Lemont, Illinois (May 2023).

Heavy Element Research at Texas A&M University, **C.Folden**, **Invited Talk**, 20th Workshop on [a] Recoil Separator for Superheavy Element Chemistry & Physics, Darmstadt, Germany (April 2023).

Neutron-upscattering enhancement of the triple-alpha process, **J. Bishop**, **Talk**, APS April Meeting, Minneapolis, Minnesota (April 2023).

Exploring sub-barrier fusion reactions, **A. Bonasera**, **Invited Talk**, SDSS-V/IReNA Science Festival, Institute of Astronomy, KU Leuven., Leuven, Belgium (April 2023).

RESEARCH PERSONNEL AND ENGINEERING STAFF

April 1, 2023 - March 31, 2024

Faculty and Research Group Leaders

Adsley, Philip – Asst. Professor of Physics
Bonasera, Aldo – Senior Scientist
Christian, Gregory – Adjunct Professor
Fries, Rainer – Professor of Physics
Folden, Charles M., III – Professor of Chemistry
Gagliardi, Carl A. – Professor of Physics
Hardy, John C. – Professor Emeritus
Holt, Jeremy – Asst. Professor of Physics
Ko, Che Ming – Professor of Physics
Melconian, Dan – Professor of Physics
Mioduszewski, Saskia – Professor of Physics
Natowitz, J. B. – Professor Emeritus
Rapp, Ralf – Professor of Physics
Rogachev, Grigory – Professor of Physics and Department Head of Physics and Astronomy
Shlomo, Shalom – Senior Scientist
Tribble, Robert E. – Professor Emeritus
Yennello, Sherry J. – Professor of Chemistry, Bright Chair, Director
Youngblood, Dave H. – Professor Emeritus
Zhanov, Akram M. – Senior Scientist – Retired 1/1/2024

Research Staff

Ärje, Juha – Research Scientist
Barbui, Marina – Asst. Research Scientist
Bishop, Jack – Asst. Research Scientist – To 6/1/2023
Chubaryan, Grigor – Research Scientist, Retired
Clark, Henry – Accelerator Physicist (50%)
Gauthier, Jerome – Asst. Research Scientist
Goldberg, Vladilen – Research Scientist, Retired
Hagel, John C. – Research Scientist (50%)
Horvat, Vladimir – Research Scientist (50%)
Iacob, Victor – Research Scientist
Kennas, Miltiadis – Research Associate
Koshchiy, Yevgen – Assoc. Research Scientist
Lui, Yiu-Wing – Research Scientist
McIntosh, Alan – Assoc. Res. Scientist
McIntosh, Lauren – Asst. Research Scientist
Nica, Ninel – Assoc. Research Scientist
Rodrigues, Marcia Dias – Asst. Research Scientist
Sahoo, Nihar – From 11/1/2023 To 1/19/2024
Tereshatov, Evgeny – Assoc. Research Scientist

Accelerator Physics and Radiation Line Staff

Avila, Geoffrey – Research Assistant
Clark, Henry – Accelerator Physicist (50%)
Horvat, Vladimir – Research Scientist (50%)
Hyman, Bruce – Research Associate
Kennas, Miltiadis – Research Associate
Kim, George – Accelerator Physicist
May, Don – Senior Accelerator Physicist
Roeder, Brian – Accelerator Physicist
Park, Hyo-In – Accelerator Physicist
Parker, Cody – Accelerator Physicist – To 3/15/2024
Saastamoinen, Antti (50%) – To 10/27/2022
Tabacaru, Gabriel – Accelerator Physicist

Computer Systems Staff

Burch, Jr. Robert – Lead Microcomputer/LAN Administrator
Hagel, John C. – Research Scientist (50%)
Gauthier, Jerome
Lui, Yiu-Wing

Engineering Staff

Molitor, Stephen – Senior Mechanical Engineer
Olsen, Robert – Senior Mechanical Engineer

Postdoctoral Research Associates

Kilmo, Jozef – To 10/31/2023
Kolhinen, Veli Sakari – To 7/31/2023
Zakusilova, Vera
Zelga, Kamila – To 4/30/2023

STUDENTS

April 1, 2023 – March 31, 2024

Graduate Students and Research Assistants

Abbott, Austin
Aboona, Bassam
Alafa, Alex
Alvarez, Arthur
Amberger, Ryan
Bartsch, Robert
Bukowski, Anna – From Spring 2024
Cook, Titeana – From 2/1/2024
Depastas, Theodoros
Fentress, Andrew – From 10/2022
Friendenberg, David
Hankins, Travis
Hannaman, Andy – To 6/30/2023
Harris, Emily
Haynes, Isaac
Henderson, Lawrence
Holloway, Matthew
Hood, Stephen – From Spring 2024 To 5/31/2024
Kirkland, Amelia
Krishn, Tharun – From Spring 2024
Liu, Yanfang
Lopez, Jamie – From Summer 2024
McCain, David
Mildon, Jordan
Nasser, Morgan – To 8/18/2023
Onyango, Thomas
Robicheaux, Stephen
Roosa, Michael
Santucci, John
Sarver, Issac – To Spring 2023
Schultz, Steven
Scriven, Dustin – To 12/31/2023
Sengupta, Arjun
Settlemyre, Thomas – To 12/31/2023
Shin, Eunkyoung
Skinner, Tristin – From Spring 2024
Sorensen, Maxwell
Tang, Zhanduo
Tobar, Justin
Tobin, Zachary
Tyler, Jace
Vargas–Calderon, Brayden
Wellons, Benjamin
Wen, Pengshen

Undergraduates and Student Technicians

Ascione, Alexander – To 5/9/2023
Diaz, Briana – To summer 2024
Gallegos, Rachel – To 5/1/2023
Green, Brooklyn – To summer 2024
Jeske, Colby – To 5/1/2023
Kovacs, Isabel – From 2/4/2022
Martin, Alyssa – To 3/7/2024
Reuter, Madison

ORGANIZATIONAL CHART - CYCLOTRON INSTITUTE

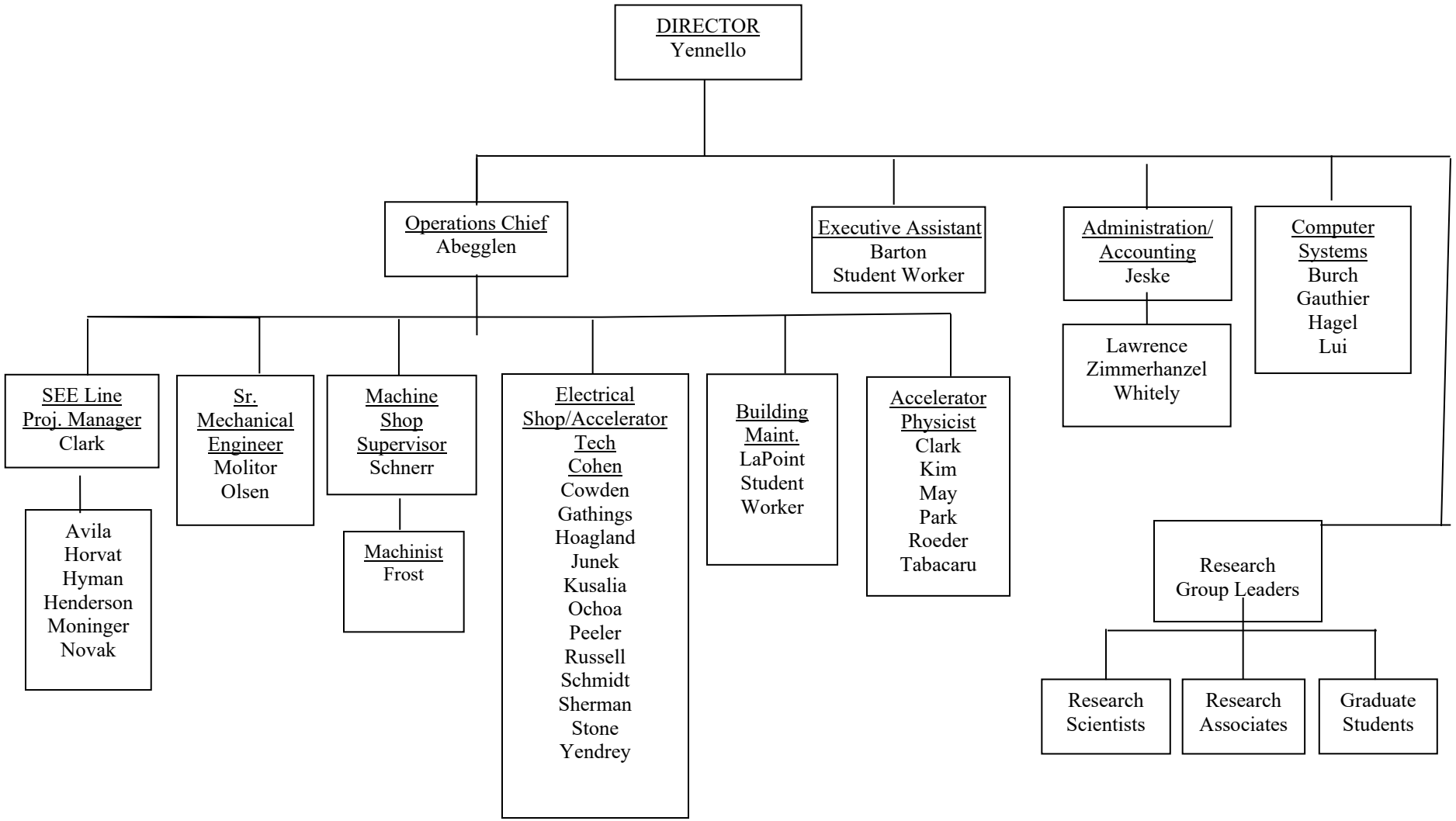

STUDENTS WHO RECEIVED GRADUATE DEGREES
FROM THESIS WORK CONDUCTED
AT
THE CYCLOTRON INSTITUTE

April 1, 2023 – March 31, 2024

Name	Year	Thesis Title	Advisor	Present Position
Thomas Onyango	2023	*Nucleon-nucleon Bremsstrahlung in heavy-ion collisions at Fermi energy*	R. Rapp	NA
Stefania Dede	2023	*NA*	G. Christian/ S.J. Yennello	Postdoctoral researcher At Los Alamos National Laboratory, New Mexico
Andrew Hannaman	2023	*Experimental search for toroidal high-spin isomers in collisions of $^{28}Si+ ^{12}C$ at 35 Mev/nucleon using FAUST*	S.J. Yennello	Ion Implant Engineer at Texas Instruments, Allen Texas
Stephen Robicheaux			R. Fries	
Isaac Sarver	2023	*Momentum dependence of Quakonia spectral function in Quark-Gluon plasma*	R. Rapp	NA
Arun Sengupta	2024		R. Fries	Associate at Goldman Sachs
Tommy Settlemyre	2023	*Pair production in strong fields*	Aldo Bonasera	NA

INSTITUTE COLLOQUIA AND SEMINARS

April 1, 2023 - March 31, 2024

2023

April 5	Professor Alexander Volya, Department of Physics Florida State University Tallahassee, Florida 32306	*Order and Chaos in Mesoscopic Nuclear Physics*
April 27	Dr. Siegfried S. Hecker, Professor of the Practice in Nuclear Engineering and Distinguished Faculty Fellow in the Center for Nuclear Security Science and Policy Initiatives (NSSPI), Texas A&M University, College Station, Texas 77843	*Nuclear Solutions Institute Colloquium: North Korea's Sixty-Year Odyssey to a Nuclear Arsenal*
June 7	Professor Jorge A. Munoz, Jr. Department of Physics, The University of Texas at El Paso (UTEP), El Paso, Texas 79968	*Computational Thinking and Close Mentoring in Nuclear Physics Education and Training*
June 20	Dr. Eric Aboud Critical Engineer and Postdoctoral Researcher, Lawrence Livermore National laboratory, Livermore, California 94550-9234	*Integral Experiments for Nuclear Criticality at Lawrence Livermore National Laboratory*
July 13	Dr. Kiana Setoodehnia, Research Staff Scientist, Duke University/Triangle Universities, Nuclear Laboratory Durham, North Carolina 27708	*Current Status of SECAR: A Recoil Separator for Nuclear Astrophysics Experiments at FRIB*
August 10	Dr. Patrick Steinegger, Assistant Professor of Radiochemistry, Laboratory of Inorganic Chemistry, Department of Chemistry and Applied Biosciences, ETH Zuich, Switzerland	*The chemical characterization of superheavy elements (Z > 103)*
August 15	Dr. Robert Eichler, Joint professorship PSI/UniBern University of Bern, Bern, Switzerland	*Recent and future Swiss radionuclide production for science*

August 31	David Kahl,	*Investigation of Nuclear Reactions with Magnetic Spectrometers*
September 5	Dr. Sylvie Hudan,, Senior Scientist, Indian University, Bloomington, Indiana 47405	*Impact of neutron excess on near-barrier fusion in* $^{16\text{-}20}O + {}^{12}C$
September 11	Michael Story, Ph.D. Vice-Chair, Department of Radiation Oncology, Chief, Division of Molecular Radiation Biology, Director, Pre-clinical Radiation Core Facility, David A. Pistenmaa, M.D., Ph.D. Distinguished Chair in Radiation Oncology, University of Texas, Southwestern Medical Center, Dallas, Texas 75390	*The return of carbon ion radiotherapy to the United States: Will this $233M bet pay off?*
October 10	Dr. George Zimba, Post Doc, Facility for Rare Isotope Beams (FRIB) Michigan State University, East Lansing, Michigan 48824	*Isospin breaking in the upper fp-shell nuclei: In-beam spectroscopy of A = 78 T = 1 nuclei via recoil-double-β and recoil-β tagging methods*
October 12	Mr. Rahul Jain, Graduate Research Assistant Facility for Rare Isotope Beams Michigan State University, East Lansing, Michigan 48824	*Heating and cooling of accreting neutron star crusts*
October 24	Janilee Benitez, Principal Engineering Associate, MARS-D Project Manager ECR Group, 88-Inch Cyclotron, Lawrence Berkeley National Laboratory, Berkeley, California 94720	*Development of Electron Cyclotron Resonance Ion Sources at LBNL's 88-Inch Cyclotron*
October 26	Deepa Thomas, Assistant Professor, The University of Texas at Austin, Austin, Texas 78767	*Exploring QCD in Extreme Conditions*

November 7	Dr. Cheuk-Yin Wong, Distinguished Senior Physicist, Oak Ridge National Laboratory (ORNL), Oak Ridge, Tennessee 37830	*On the question of quark confinement in the QED interaction*
November 14	Professor Dean Lee, Department of Physics, Facility for Rare Isotope Beams (FRIB) Michigan State University, East Lansing, Michigan 48824	*Nuclear Lattice Simulations for Nuclear Structure and Thermodynamics*
November 15	Professor Filomena Nunes, Department of Physics and Astronomy, Facility for Rare Isotope Beams, Michigan State University, East Lansing, Michigan 48824	*BAR: Bayesian Analyses of Reactions*
November 20	Rebecca (Becca) Hoerres, Ph.D. candidate, Department of Chemistry, The University of Missouri, Columbia, Missouri 65211	*Development of [^{99m}Tc]Tc- and [^{186}Re]Re-tricarbonyl metal complexes with TACN-based chelators for radiopharmaceutical applications*
November 21	Dr. Jonathan Morrell, Post-doctoral Research Associate, Los Alamos National Laboratory, Los Alamos, New Mexico 87545	*Understanding Pre-Equilibrium Physics for Isotope Production*

2024

January 10	Dr. Armand Bahini, Post-doctoral researcher, iThemba laboratory for Accelerator based Sciences (LABS), Somerset West 7129, South Africa	*Study of the isoscalar giant monopole resonance (ISGMR) at iThemba LABS*
January 17	Rajkumar Santra, Visiting Fellow, Variable Energy Cyclotron Center (VECC), India	*Nine things every faculty and staff should know about title IX (and civil rights!) at Texas A&M University*
January 23	S. Shahina, Ph.D. Candidate, University of Notre Dame, Notre Dame, Indiana 46556	*Stellar neutron sources for the s-process nucleosynthesis*

January 31	Tyler Wheeler, Graduate Research Assistant, Facility for Rare Isotope Beams, Michigan State University Laboratory, East Lansing, Michigan 48824	*Measuring the $^{15}O(\alpha, \gamma)^{19}Ne$ Reaction Rate in Type I X-ray Bursts using ^{20}Mg β-decay*
February 6	Xinyi Wang, Graduate Student, Michigan State University, East lansing, Michigan 48824	*Locating the first $p_{1/2}$- state in ^{13}Be*
February 6	James DeBoer, Associate Research Faculty, University of Notre Dame, Notre Dame, Indiana 46556	*Another (α,n) measurement from the University of Notre Dame, the $^{13}C(\alpha,n)^{16}O$ reaction*
February 27	Dr. Paul Ellison, Assistant Professor of Medical Physics, School of Medicine and Public Health, Health Sciences Learning Center, University of Wisconsin, Madison, WI 53705	*Cyclotron production, radiochemical synthesis, and biological evaluation of theranostic radiopharmaceuticals*
February 29	Nathaniel Pogue, Accelerator Physics Group Leader, National Security Engineering Division (NSED) Lawrence Livermore National Lab (LLNL), Livermore, California 94550	*LIAs - The Powerful Accelerators you have never heard of, that are enabling US Science and Security*
March 5	Chloe Hebborn, Assistant Professor, Facility for Rare Isotope Beams, Michigan State University, East Lansing, Michigan 48824	*Ab initio prediction of $\alpha(d,\gamma)^{6}Li$ and impact of the ^{6}Li properties onto α -induced reactions of astrophysical interest*
March 12	Dr. Heshani jayatissa, Postdoctoral Researcher, Los Alamos National laboratory, Los Alamos, New Mexico 87545	*Understanding the nucleosynthesis flow in type-I x-ray bursts using a direct measurement of an α-capture reaction on ^{22}Mg*
March 18	Rebeka Lubna, Facility for Rare Isotope Beams, Michigan State University, East Lansing, Michigan 48824	*Probing the Evolution in Nuclear Structure around N = 20*

March 19	Dr. Gregory Potel, Staff Scientist, Lawrence Livermore National Laboratory, Livermore, California 94550-9234	*The Optical Potential: From Structure to Reactions and Back Again*
March 25	Veronika Mocko, Research Scientist, Los Alamos National Laboratory, Los Alamos, New Mexico 87545	*From R&D to large scale production of a new PET radionuclide Ce-134*
March 27	Jonas Karthein, Massachusetts Institute of Technology Cambridge, Massachusetts 02139	*Unknown Electroweak Nuclear Properties From Single Molecular Ions*